Block Copolymer Nanolithography

by

Cong Jin

A thesis submitted in partial fulfillment of the requirements for the degree of

Doctor of Philosophy

Department of Chemistry
University of Alberta

Abstract

The development of photolithography has been the main driving force of the semiconductor industry to keep pace with Moore's Law for over five decades. The theoretical resolution limit of state-of-the-art 193 nm photolithography is about 36 nm (half pitch). By integrating multiple patterning technologies, the semiconductor industry has now successfully extended the resolution of photolithography to 14 nm half-pitch. Innovative and cost-effective patterning technologies need to be developed for sub-14 nm patterning. Directed self-assembly, referred to as DSA, of block copolymers is a patterning technology that is able to form 5 - 200 nm patterns spontaneously, at low cost. It is one of two potential solutions for low cost sub-20 nm half-pitch lines and spaces patterning, in 2017, and one of four potential solutions for sub-14 nm half-pitch patterns by 2019, according to the International Technology Roadmap for Semiconductors, 2015 edition. Moreover, directed self-assembly of block copolymers has already been demonstrated on 300 mm wafers, and a fully automatic lithography system for finFET, bit patterned media, and contact hole applications.

This thesis is divided into two parts. The first part deals with understanding the

annealing process of block copolymer self-assembly, the critical step in which the actual nanoscale phase segregation takes place. First, the mechanism of microwave annealing of block copolymers on silicon was studied and elucidated. In this work, it was discovered that the semiconductor itself is the source of heating and not the polymer, contrary to the reports in the literature. In the next phase of this part of thesis, a new solvent flow annealing system with *in situ* laser reflectometry and an optical microscope was developed. By integrating a feedback loop, this system is able to control the swelling/deswelling rate, degree of swelling, and annealing time to accurately control the annealing conditions to eliminate the formation of dewetting or double layers, leading to much improved reproducibility. Multi-step swelling and deswelling in an individual process run have also been demonstrated.

In the second part of the thesis, the concept of density multiplication was examined. Density doubled and tripled dot patterns are studied, as a means of creating more complex patterns that could be attained with single step annealing. The quality of the resulting dot patterns was analyzed and a theoretical model was developed to predict the quality of density doubled and tripled patterns using only two parameters obtained from single layer patterns. As an intriguing extension of this work, the orientational relationship between sequentially deposited BCP dot patterns with different pitches was investigated. From large scale helium-ion microscope images, it was found that preferential orientations, or Moiré patterns, are formed, which is determined by the pitch ratio and dot size.

Preface

This thesis is arranged into 6 chapters. Chapter 1 overviews basic concepts in BCP self-assembly and its future applications in the semiconductor industry. Chapter 2 investigates the mechanism of BCP microphase segregation in microwave annealing. Chapter 3 introduces a new solvent vapor flow annealing system and investigates the morphology evolution of BCP thin film in both nano- and microscale during the annealing process. Chapter 4 introduces a sequential annealing process to enable an increase of the native pattern density of a given dot-forming BCPs up to a factor of three. Chapter 5 studies Moiré patterns obtained from sequential annealing of two different dot-forming BCPs. Finally, Chapter 6 summarises this thesis and proposes several directions of future study.

The work presented in Chapter 2 has been published as Cong Jin, Jeffrey N. Murphy, Kenneth D. Harris, Jillian M. Buriak, "Deconvoluting the Mechanism of Microwave Annealing of Block Copolymer Thin Films" *ACS Nano*, vol. 8, issue 4, 3979–3991. I designed and conducted all the experiments, wrote the initial text draft, analyzed the data, and prepared all the figures. Dr. Jeffrey N. Murphy wrote the algorithm for defect analysis. All authors contributed to discussion and text

editing.

The work presented in Chapter 3 has been published as Cong Jin, Brian C. Olsen, Erik J. Luber, Jillian M. Buriak, "Nanopatterning *via* Solvent Vapor Annealing of Block Copolymer Thin Films." *Chem. Mater*, vol. 29, issue 1, 176-188. I conducted all the experiments, analyzed the data, wrote most of the initial text draft, and prepared most of the figures. The solvent vapor flow annealing system was designed and assembled by Dr. Erik J. Luber and Brian C. Olsen. The control software and technical description of the annealing system were written by Brian C. Olsen. He also prepared the functional flow diagram, the schematics of solvent annealing systems, and cross section draw of parts in the flow controlled solvent vapor annealing system. All authors contributed to discussion and text editing.

The work presented in Chapter 4 was published Cong Jin, Brian C. Olsen, Nathanael L.Y. Wu. Erik J. Luber, J. M. Buriak, "Sequential Nanopatterned Block Copolymer Self-Assembly on Surfaces." *Langmuir*, vol. 32, issue 23, 5890-5898. The initial concept was studied in a preliminary fashion by Dr. Nathanael L.Y. Wu. For this paper, I carried out the experiments. Dr. Erik J. Luber, Brian C. Olsen, and I wrote the initial text draft, analyzed data, and prepared all the figures. Dr. Erik J. Luber, Brian C. Olsen developed the image analysis procedure and conducted the theoretical simulation. All authors contributed to discussion and text editing.

The work presented in Chapter 5, except the section: "Influence of the Bottom Layer Pitch'', has been published as Cong Jin, Brian C. Olsen, Erik J. Luber,

Jillian M. Buriak, "Preferential Alignment of Incommensurate Block Copolymer Dot Arrays Forming Moiré Superstructures." *ACS Nano*, vol. 11, issue 3, 3237-3246. I carried out the experiments, wrote the initial text draft. Dr. Erik J. Luber, Brian C. Olsen, and I analyzed the data and prepared all the figures. Dr. Erik J. Luber and Brian C. Olsen wrote the code for HIM image analysis. All authors contributed to discussion and text editing. The work presented in section: "Influence of the Bottom Layer Pitch" is unpublished. I conducted all the experiments, wrote the text, analyzed data, and prepared all the figures. Prof. Jillian M. Buriak, Dr. Erik J. Luber, and Brian C. Olsen contributed in optimizing EBL patterns. Prof. Jillian M. Buriak contributed to figure preparation.

Acknowledgements

Six years ago, when I was a third-year undergraduate student at the Zhejiang University, I could not imagine that I would finish a Ph.D. degree in Canada. My English was so poor that I could not even write a paragraph with a few hundred words. Six years later, I am sitting here in my office at the University of Alberta writing my Ph.D. thesis. Looking back, I am grateful for so many awesome people around me. I couldn't have gotten this far without their help.

First of all, I would like to express my deepest thanks to my supervisor, Professor Dr. Jillian Buriak. Her passion and knowledge for science have greatly supported me to conquer every challenge in my research. I am also grateful that, with her support and encouragement, I was able to attend various conferences and workshops where I met great researchers from all over the world. In addition, I would like to thank my committee: Dr. Eric Rivard and Dr. Michael Serpe, and Faculty members in the Chemistry Department: Dr. Steven Bergens, Dr. Arthur Mar, Dr. Robert Campbell, Dr. Mark McDermott, and Dr. Jonathan Veinot for their valuable guidance and support. I would also like to express my gratitude to Dr. Liang Li, who introduced me to this Ph.D. program and helped me a lot with my application.

I would also like to thank Buriak group members for providing a cooperative and fun atmosphere and useful suggestions and discussions on my research projects: Tate Hauger, Dr. Peter Kalisvaart, Dr. Erik Luber, Kelli Luber, Brian Olsen, Jennifer Ozdoba, Dr. Bing Cao, Mahmoud Almadhoun, Chris Fetterly, Dan Yang, Gayashani Ginige, Minjia Hu, Chengcheng Rao, Hao Wang, Hezhen Xie, Dr. Binbin Yu, Dr. Lei Chen, Dr. Delwar Sikder, Dr. Gang He, Dr. Xiaoming He, Dr. Hosnay Mobarok, Minkyu Kang, Dr. Ibrahim Al-Rafia, Dr. Lawrence Huck, Dr. Fenglin Liu, Dr. Jeffrey Murphy, Dr. Jeremy Bau, Dr.

Nathanael Wu, Dr. Brian Worfolk, Dr. Xiaojiang Zhang, Dr. Kenneth Harris, Yaqi Tu, Sung Eun Cho, and Miriam Fenniri. For the majority of the work in this thesis I was fortunate enough to collaborate with Dr. Xiaojiang Zhang, Dr. Nathanael Wu, Dr. Kenneth Harris, Dr. Jeffrey Murphy, Brian Olsen, and Dr. Erik Luber. I am especially thankful for their help and guidance. I would also like to thank Kelli Luber, Gayashani Ginge, Tate Hauger, Chris Fetterly, Dr. Erik Luber, Miriam Fenniri, and Regina Sinelnikov for providing useful suggestions to improve this thesis manuscript. Thanks to all my friends here in Canada for making this five-year journey so enjoyable.

I would also like to thank NINT staff: Paul Concepcion, Dr. Kai Cui, Mike O'Toole, Rob Indoe, and Tim Patrie, as well as Nanofab staff: Dr. Eric Flaim, Dr. Aaron Hryciw, Peng Li, Stephanie Bozic, Glenn Elaschuk, Melissa Hawrelechko, Dr. Anqiang He, Scott Munro, and Les Schowalter for instrument training and technical support. The scholarships and awards from the University of Alberta and Alberta Innovates have also generously facilitated my research.

Finally, I would like to thank my parents and grandparents for their unconditional love and support. Thanks to my sister, You Jin, who has made my life so fun since we were very young and helps to take care of my parents and grandparents when I am away. I am lucky to have met Jingwen Niu here, and I thank her for friendship, love, and care.

Contents

List of Figures

List of Figures

List of Figures

List of Tables

List of Tables

List of Symbols

Symbol	Meaning [units]
T_g	Glass transition temperature [°C]
T_{ODT}	Order-disorder transition temperature
χ	Flory-Huggins parameter
f	Volume fraction
N	Degree of polymerization
D	Degree of swelling
L_0	Dot pitch [nm]
M_n	Number average molecular weight [g/mol]
k	$\times 10^3$ [kg/mol]
d_0	Mean Dot Diameter
$\sigma_{\bar{\epsilon}}$	Standard deviation of hydrostatic strain
T	Temperature [°C]
t	Time [s]
H	Transfer function

List of Abbreviations

Abbreviation	Meaning
CD	Critical dimension
AFM	Atomic force microscopy
SEM	Scanning electron microscopy
HIM	Helium ion microscopy
RIE	Reactive ion etching
GISAXS	Grazing incidence small-angle X-ray scattering
PDI	Polydispersity index
ODT	Order disorder transition temperature
FFT	Fast Fourier transform
ITO	Indium tin oxide
-b-	*-block-*
PS	Polystyrene
PMMA	Poly(methyl methacrylate)
PDMS	Polydimethylsiloxane
BCP	Block copolymer
PEO	Polyethylene oxide
P2VP	Poly(2-vinylpyridine)
PPO	Poly(propylene oxide)
PI	Polyisoprene
PB	Polybutadiene
PMAPOSS	Poly(maleimide isobutyl POSS)
POSS	Polyhedral oligomeric silsesquioxane
PFS	Polyferrocenylsilane
HSQ	Hydrogen silsesquioxane
THF	Tetrahydrofuran

List of Abbreviations

Abbreviation	Meaning
D (T)	Diffusivity
PID	Proportional–integral–derivative
KDE	Kernel density estimation
ITRS	International technology roadmap for semiconductors
EBL	Electron bean lithography
HSQ	Hydrogen silsequioxane
SADP	Self-aligned double patterning
SAQP	Self-aligned quadruple patterning
Td	Teradot

1

Introduction

The purpose of this chapter is to give a brief introduction to the challenges in current lithography technology and to describe the basic principles of block copolymer (BCP) self-assembly and its applications in the semiconductor industry. This chapter will start with discussing challenges of the state-of-the-art 193 nm photolithography in sub-20 nm (half pitch) patterning and potential solutions. Next, this chapter will introduce computational and experimental studies of the phase segregation of BCPs, and followed by a discussion of the recent development of directed self-assembly of BCP thin films and its application in finFET, bit patterned media, and contact hole fabrication. Finally, this chapter will conclude with a brief summary and future research directions of BCP self-assembly for patterning applications in the semiconductor industry.

1.1 Moore's Law and Lithography Challenges

In 1965, Intel's co-founder Gordon Moore made his famous prediction, Moore's law.[42] It predicted that the transistor density of a chip would double in every 18 months. As transistors become smaller, computers run faster and consume less energy.[43] Owing to the rapid development of photolithography technology, the semiconductor industry has marched at the pace of Moore's Law for over five decades. The general concept of photolithography, shown in Figure 1.1, uses light (generally UV light) to transfer the pattern from a mask to photoresist films. After exposure, photoresist layers will either become cross-linked (negative photoresist) or decompose (positive photoresist) under light irradiation.[44] The pattern can then be developed by washing away unexposed areas of negative photoresist or exposed areas of positive photoresist.[44]

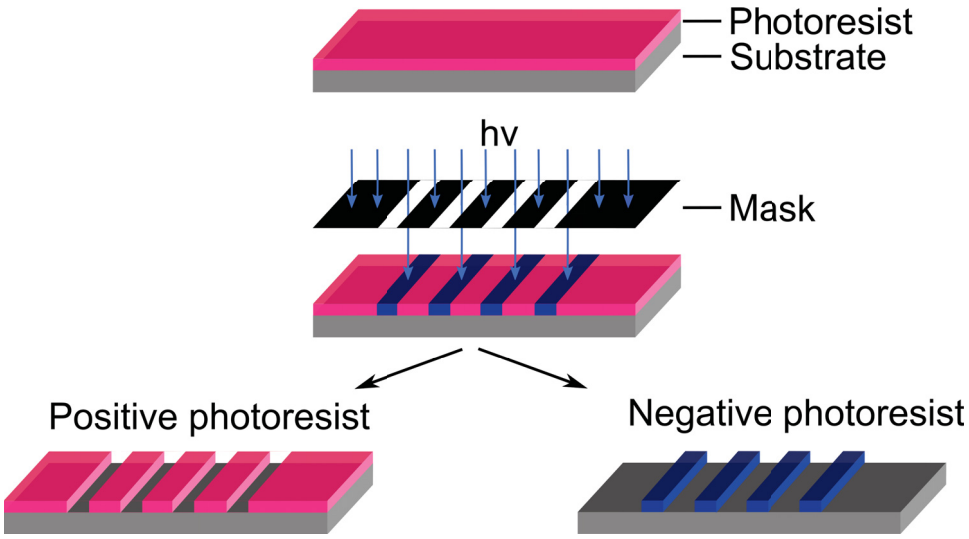

Figure 1.1: *Schematic representation of the photolighography process.*

In order to keep the trend of Moore's law, advanced innovations have been applied to improve the resolution of photolithography. The resolution of photolithography can be described by the Rayleigh equation 1.1.1,

$$CD = k \cdot \frac{\lambda}{NA} \tag{1.1.1}$$

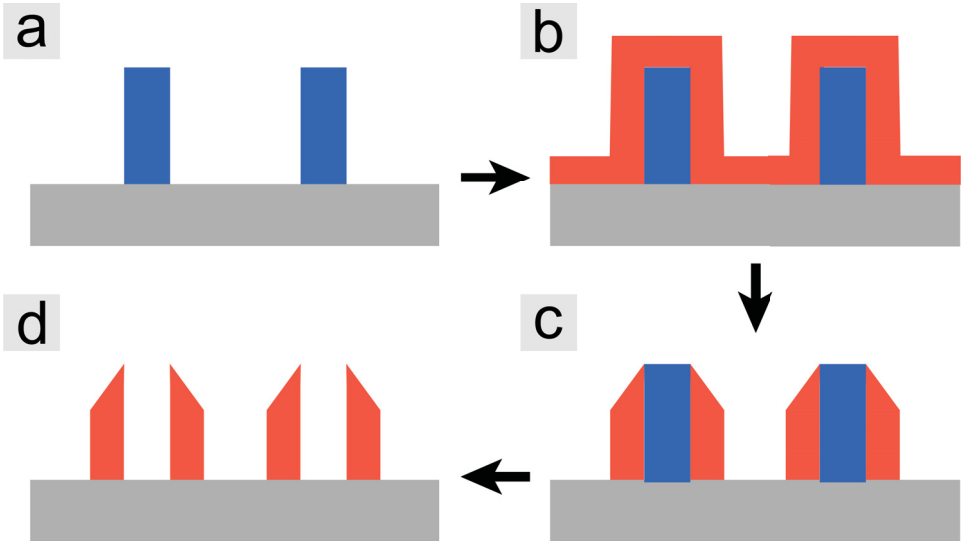

Figure 1.2: *Schematic representation of self-aligned double patterning (SADP) process. (a) Original sacrificial pattern. (b) Spacer deposition. (c) Spacer etching. (d) Sacrificial pattern is etched, leading to the double density pattern.*

where CD is the critical dimension, equal to 2 $\times$ half pitch, λ is the wavelength of the light source, NA is the aperture number of the projection optics, and the k is a process related coefficient.[45] Decreasing of the wavelength of light source, λ, is a preferable way to decrease the critical dimension that can be printed from photolithography, according to Equation 1.1.1. In the last couple decades, the wavelengths of photolithography light sources has been changed from the G-line of mercury arc lamps (436 nm) to ArF excimer lasers (193 nm).[46] However, in 2004, the semiconductor industry abandoned the development of the F_2 excimer laser (157 nm) due to economic and technological issues[47] and planned to develop a lithography technology at a wavelength of 13.5 nm (so-called "extreme ultraviolet lithography" or EUVL) to prolong Moore's law for another two decades.[48] At the same time, the semiconductor industry is struggling to extend the resolution of 193 nm photolithography from 130 nm down to around 36 nm with a complex optical system (lower k) and liquid immersion technology (higher NA). The application of multiple patterning methods have enabled the extension of the

resolution of photolithography down to 14 nm half pitch.[49] The most widely used multiple patterning method is the self-aligned double patterning (SADP) (Figure 1.2).[50, 51] Two SADP processes, also called self-aligned quadruple patterning (SAQP) processes are required to achieve 14 nm half pitch patterning. Due to the delay of EUV, photolithography with SAQP or even octuple patterning might be extended for sub-11 nm even sub-7 nm half pitch patterning, according to the 2015 International Road Map of Semiconductor (ITRS 2015).[49] Along with EUVL, directed self-assembly (DSA) of BCPs is another candidate that may potentially be used in sub-14 nm high volume production in 2019 to reduce the cost of current patterning processes.[52–56]

Directed self-assembly of BCPs, also called BCP nanolithography, is a technology that takes advantage of the self-assembly properties of BCPs to economically achieve high-resolution nanopatterns. BCPs are a type of polymer that have two or more different homopolymer segments (blocks) that are connected by covalent bonds, and are able to form nanopatterns with feature sizes ranging from 5 - 200 nm.[57] In order to form useful patterns, top-down patterning technology, such as photolithography, is required to guide the phase segregation of BCPs, as well as to accelerate the self-assembly process and to improve the pattern quality. This next generation patterning approach has attracted enormous attention from the semiconductor industry as it is high resolution, high versatility, and low cost.[52, 53] As proposed by ITRS as a candidate of next-generation lithography technology in 2005,[58] DSA has made huge progress toward semiconductor fabrication. As shown in Figure 1.3, all 7 features required for integrated circuit fabrication have been demonstrated by DSA.

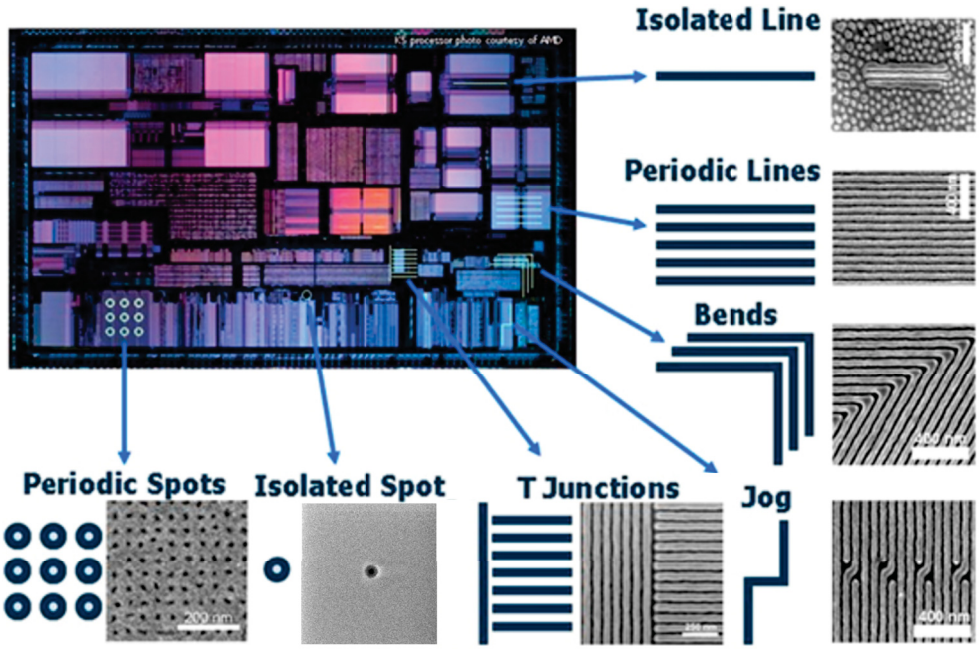

Figure 1.3: *Patterns required for integrated circuit fabrication and patterns demonstrated with directed self-assembly of BCPs. The SEM micrograph of the isolated dot is from ref. [1] Reprinted with permission from ref. [1]. Copyright © 2017 SPIE. The remaining images are from ref. [2]. Reprinted with permission from ref. [2]. Copyright © 2011 Cambridge University Press.*

1.2 Block Copolymer Self-Assembly

1.2.1 Polymer Basics

A polymer is a type of macromolecule consisting of many repeating units. It is one of the most versatile materials and can be found everywhere in our daily lives from natural polymers, like DNA, proteins, and plant fibers, to synthesized polymers which make up common products such as water bottles, cell phone cases, car tires, and medicines. Varieties of methods have been developed to synthesize functional polymers. Generally, they can be divided into two categories: step-growth polymerization and chain-growth polymerization. In step-growth polymerization, reactions take place in an unselective manner between functional groups of bi-functional or multi-functional monomers. In contrast, in chain-growth polymerization, reactions only occur at the end of polymer chains. In terms of polymer molecular structures, polymers can be divided into homopolymers and copolymers. If a polymer is made of only one type of repeat unit, it is called a homopolymer. On the other hand, if a polymer contains more than one type of repeat unit, it is called a copolymer. For example, polystyrene (PS), which is synthesized from styrene monomers, is a homopolymer. Acrylonitrile butadiene styrene (as known as ABS), which is made from three different monomers: acrylonitrile, 1,3-butadiene, and styrene, is a copolymer.

Number average molecular weight (M_n), weight average molecular weight (M_w), polydispersity index (*PDI*), glass transition temperature (T_g), and melting temperature (T_m), are important parameters of a polymer. Unlike small molecule synthesis, polymers are synthesized from 100 to over 100,000 monomers. The polymerization reaction happens randomly in a reaction matrix and hence the resulting product is a mixture of polymer molecules with different molecular weights. As a result, in polymer science, average molecular weights are used, and are commonly defined as follows:

Number average molecular weight (M_n):

$$\overline{M}_n = \frac{\sum_{i=1}^{N} M_i N_i}{\sum_{i=1}^{N} N_i}$$

Weight average molecular weight (M_w):

$$\overline{M}_w = \frac{\sum_{i=1}^{N} {M_i}^2 N_i}{\sum_{i=1}^{N} M_i N_i}$$

where N_i is the number of polymers with molecular weight of M_i. Both M_n and M_w can be determined by gel permeation chromatography and size exclusion chromatography. The weight average molecular weight, M_w, is more sensitive to the high molecular portion of the given polymer sample and represents its mechanical or bulk property. The number average molecular weight, M_n, represents the average polymer chain length and is more closely related to the molecular or chemical properties of a given polymer. The polydispersity index (*PDI*) of a polymer sample is given by:

$$PDI = M_w/M_n$$

where *PDI* is a value greater than 1. It measures the distribution of molecular weight in a polymer sample. As *PDI* approaches 1, the length of polymer molecules is more uniform. Polymers synthesized *via* conventional step-growth polymerization and chain-growth polymerization usually result in high *PDI*. Living polymerization, a special type of chain-growth polymerization, is able to yield polymers with a low *PDI* and a controlled molecular weight.[59]

The glass transition temperature, T_g, refers to a temperature when a polymer transitions from a brittle state to a rubbery state upon heating. At the molecular level, below T_g, polymer chains have no freedom to move around. When the temperature reaches T_g, however, polymer chains are able to move around in the polymer matrix.

The melting temperature, T_m, refers to the temperature when the polymer transitions from a crystalline state to a melting state upon heating. Every polymer has a T_g, but not all of them have T_m, as some polymers have no crystalline portion. T_g is a very important parameter in terms of the application of a polymer material. For example, the polymers used to make Petri dishes require high T_g as they need to be hard at room temperature. On the other hand, the polymer materials that used to make space suits require super low T_g, as the space temperature will drop to around -160 °C, and the space suit needs to stay flexible.[60]

1.2.2 Block Copolymers

Block copolymers (BCPs) are a type of copolymer with two or more chemically distinct homopolymer segments (blocks) that are connected *via* covalent bonds. The first BCP, polystyrene-*block*-poly(methyl methacrylate) (PS-*b*-PMMA), was synthesized by Dunn and Melville in 1952.[61] The main purpose of synthesizing this type of copolymer was to obtain unique properties that differ from random copolymers and homopolymer mixtures. After that, a number of methods have been developed to synthesize new BCPs or to improve the quality of synthesized BCPs.[62–65] The first BCP product was commercialized in 1954.[66, 67] It was a poly(ethylene oxide)-*block*-poly(propylene oxide)-*block*-poly(ethylene oxide) (PEO-*b*-PPO-*b*-PEO) linear triblock copolymer, which was a surfactant, called Pluronics. After six decades of development, BCPs have found applications in thermoplastic elastomers,[68] cosmetics,[69] drug delivery,[70] and catheters for angioplasty.[71] Since 1990, owing to their microphase segregation properties, BCPs have attracted much attention in nanoresearch as nanostructured membrane,[72, 73] nanocomposities,[74] surface patterning,[75, 76] and lithography.[53, 77]

Along with the development of organic synthetic chemistry, a large variety of BCPs has been reported. Generally, BCPs can be divided into different categories in

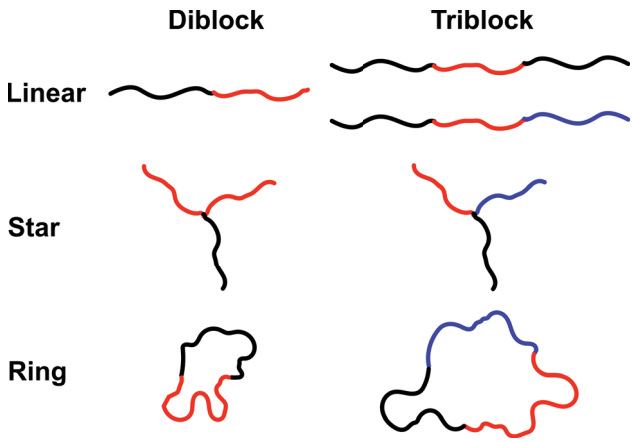

Figure 1.4: *Examples of common BCP architectures.*

terms of the number of blocks (*i.e* diblock copolymer, triblock copolymer) and how they are arranged between each other (*i.e.* linear, star, and ring), shown in Figure 1.4. Among these BCP architectures, the linear diblock copolymer is the simplest and the most well studied. Discussions in the following section will be mainly focused on theoretical and experimental research of linear diblock copolymers. Hence, in the following text, the term BCP refers to linear diblock copolymers.

Sequential addition of monomers with living polymerization is a common way to synthesize BCPs with defined structures. For example, an A-B diblock copolymer can be synthesized by adding the monomer B into a reaction system when monomer A is fully consumed. The chain length of each block can be controlled by adjusting the ratio between monomers and initiators or reaction time. Other synthetic strategies such as coupling two or more homopolymer chains *via* the functional group on the end have also been reported.

1.2.3 Phase Behavior in Bulk

Microphase separation is a unique phenomenon of BCPs and hence gives BCPs distinct properties comparing to related random copolymers or homopolymer

mixtures. This phenomenon originates from the incompatibility between homopolymer segments or blocks. The pioneer theory of BCP microphase separation was proposed by Meier in early 1970s.[78] In his theory, the morphology of a BCP could be determined by comparing the free energy change, ΔG, between random BCP molecule mixtures and ordered BCP morphologies. Later, Helfand and co-workers firstly applied self-consistent mean field theory (SCMF) to study microphase separation.[79] This version of SCMF assumes a strong segregation force between two domains, also called the strong segregation limit (SSL), and has successfully predicted equilibrium morphologies and order-order transitions between two morphologies, which agrees with experimental results. In order to understand order-disorder transition of BCP microphase separation, Leiber proposed the random-phase approximation method to study BCP models with a weak segregation force (called a weak segregation limit or WSL).[80]

Figure 1.5a is a typical bulk phase diagram of an A-B diblock copolymer that is predicted by SCFM. In SCFM, only three parameters of a BCP are considered:

1. Flory-Huggins interaction parameter,

$$\chi_{AB} = \frac{z}{kT}\left(\varepsilon_{AB} - \frac{1}{2}\left(\varepsilon_{AA} + \varepsilon_{BB}\right)\right)$$

where z is the coordination number and ε_{AB}, ε_{AA}, and ε_{BB} are the interaction energies between segment A and segment B, in between segment A, and in between segment B, respectively.

2. Degree of polymerization,

$$N = N_A + N_B$$

where N_A is the number of repeat units in block A, and N_B is the number of repeat units in block B.

3. Volume fraction,

$$f_A = N_A/N$$

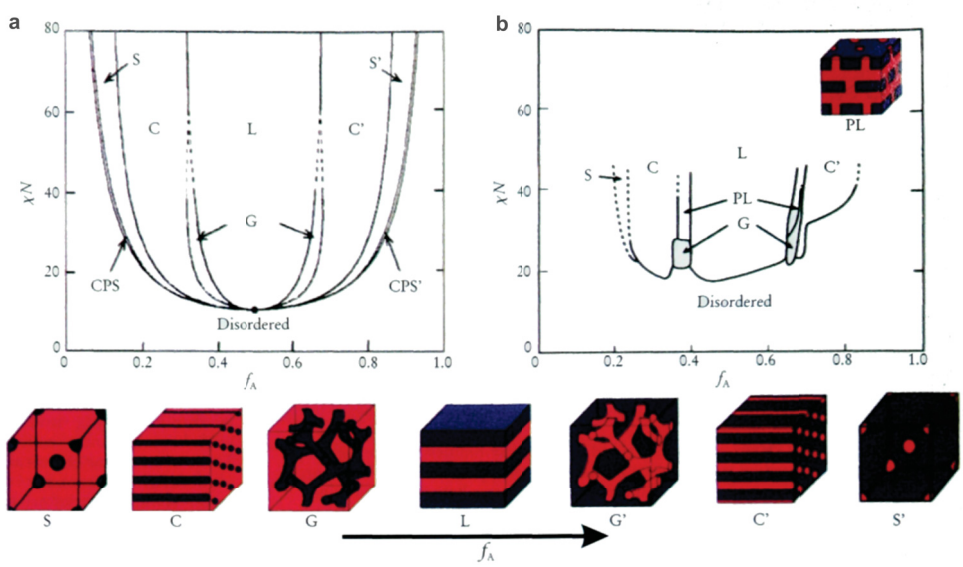

Figure 1.5: *Phase diagram of a diblock copolymer. (a) Theoretical phase diagram of a diblock copolymer obtained from self-consistent mean-field theory. (b) Experimental phase diagram of a polystyrene-block-polyisoprene (PS-b-PI). (Bottom) Equilibrium structure of a diblock copolymer as the volume fraction of one block (f_A) increases. Reproduced from [3], with the permission of the American Institute of Physics.*

According to Flory-Huggins theory, the entropy contribution to the free energy decreases as the length of BCP (N) increase. The enthalpy contribution to the free energy is proportional to χ. As a result, the product of χN is used to describe the phase behavior of a given BCP. The predicted phase diagram is plotted using the product of χN as the y-axis, and volume fraction of block A, f_A, as the x-axis. As shown in Figure 1.5a, the minimum segregation force (χN) for microphase formation is 10.5. As block A and block B are identical in simulation, this phase diagram has a mirror symmetry at $f_A = 0.5$. For the same χN value, the equilibrium phases at f_A and $1 - f_A$ share the same structure, but with inverted composition. When $\chi N \geq 10.5$, as the volume fraction of block A increases, the ordered equilibrium phase may change from close-packed spheres (CPS), body-centered cubic spheres (S), hexagonal packed cylinders (C), gyroids (G), lamellar (L), inverted gyroids (G'), invert body-centered cubic spheres (S') to invert close-packed spheres (CPS'). Among these equilibrium structures, the CPS or GPS' only appear in a very narrow region in the order-disorder transition boundary, and the G or G' phase appears at a weak segregation region ($10.5 < \chi N < 60$). Figure 1.5b shows an experimental phase diagram of polystyrene-*block*-polyisoprene (PS-*b*-PI). Similar to the theoretical phase diagram, the experimental phase diagram shows all major equilibrium phases, which appear at similar positions of phase diagram, compared to the theoretical one. There are several major discrepancies between the experimental phase diagram and the theoretical phase diagram. Firstly, the experimental phase diagram is not symmetric. Secondly, the experimental phase diagram shows a new perforated lamellar (PL) between C phase and L phase at higher χN in stead of G or G' phases. Lastly, the S' and CPS (or CPS') are not observed in experiment. These discrepancies are mainly due to the limitation of SCFM, where the chemistry and size of two different repeat units are all ignored. In addition, the interaction parameter (such as ε_{AB}, ε_{AA}, and ε_{BB}) in real samples may not match the value used in simulation.

Although the theory does not perfectly match the experimental results, it has dramatically benefited the synthesis and application of BCPs in self-assembly.

Even for the simplest BCPs, diblock copolymers, there are infinite combinations of homopolymer segments and molecular weights of each block. With the help of theoretical BCP phase diagram, researchers are able to design the chemistry, molecular weight, and volume fraction of BCPs to form specific nanopatterns or domain size. For example, in order to achieve lamellar structures, a BCP needs to be symmetric, with the volume fraction of one block around 0.5. The degree of polymerization should be larger than $10.5/\chi$ in order to achieve the ordered equilibrium structures and the equilibrium pitch size (L_0) of a BCP can also be estimated according to the equation obtained from SCFM: $L_0 \approx aN^{2/3}\chi^{1/6}$, where a is the statistical segment length. In order to achieve very small microphase segregated domains (small L_0), BCPs with high χ value but low N need to be developed.[81]

1.2.4 Phase Behavior in Thin Films

For a lithographic application, BCPs need to be spin-cast onto substrates to form thin films. The nanopatterns in BCP thin films can then serve as sacrificial masks for patterning application.[82] As BCPs are confined in a thin film state (generally 10 nm to 100 nm thick), their phase diagrams become more complicated compared to the bulk state, as the film thickness, substrate surface topography or/and chemistry, and air-BCP interface all contribute to the resulting morphologies.[83]

The theoretical and experimental research of BCP thin films started in the early 1980s. In 1979, Thomas and O'Malley reported that the surface morphology of spin-cast polystyrene-*block*-poly(ethylene oxide) (PS-*b*-PEO) film was different from its bulk morphology.[84] Later, Hasegawa and Hashimoto observed a similar phenomenon at the air-BCP interface of a lamellar-forming polystyrene-*block*-polyisoprene (PS-*b*-PI).[85] In 1987, Fredrickson studied the surface ordering of a diblock copolymer thin film with a mean field theory at the weak segregation limit regime.[86] Two years later, Anastasiadis *et al.* also reported the surface-induced

ordering of a lamellar-forming polystyrene-*block*-poly(methyl methacrylate) (PS-*b*-PMMA) with neutron reflectivity.[87] Later, more sophisticated studies of BCP thin films were carried out by Magerle and co-workers by combining experimental results with computer simulations (Figure 1.6). In this research, they measured the morphologies of a self-assembled polystyrene-*block*-polybutadiene-*block*-polystyrene (PS-*b*-PB-*b*-PS) triblock copolymer thin film with a scanning force microscope and found that film thickness strongly influences BCP phase segregation. If the film is too thin, there is no phase segregation and forming of a wetting layer. Bulk phase morphology of the BCP, such as single layer cylinders patterns and double layer cylinder patterns, appear at terraces with a film thickness of 30 nm and 60 nm, respectively. New morphologies such as perpendicular cylinders ($C_{\perp}$) and perforated lamellars (PL) only appear at transition areas between wetting layers, single layers, and double layers.

Li and co-workers' SCFT study gives more insight into the phase segregation of BCP thin films.[5] Figure 1.7 shows a theoretical phase diagram of an A-B diblock copolymer ($\chi N = 20$) that is confined between two rigid surfaces (attracting the B block). By changing the volume fraction of block A (f_A) and film thickness (w), 20 different phases were obtained. Generally, these phases are related to four major types of equilibrium phases in bulk: body-centered cubic sphere (S), hexagonal packed cylinder (C), gyroid (G), and lamellar (L), and they all appear in a similar volume fraction region of the related bulk phase diagram. The perforated lamellar (PL) appears in the thin film instead of the gyroid (G) phase in bulk. Interestingly, this result matched Magerle and co-workers' experimental result ($f_A \approx 0.3$), shown in Figure 1.6.[4] However, some of these phases were not be able to be observed in the experimental study, in which case a BCP thin film is confined by one rigid surface and the thickness of the BCP thin film can rearrange to form more stable phases. As a result, BCP thin film thickness needs to perfectly match with the domain spacing in order to form a uniform, large scale nanopattern.[88] Too thin or too thick of a film will lead to the formation of wetting layers, terraces, and metastable phases at transition areas (see Chapter 3 for a more

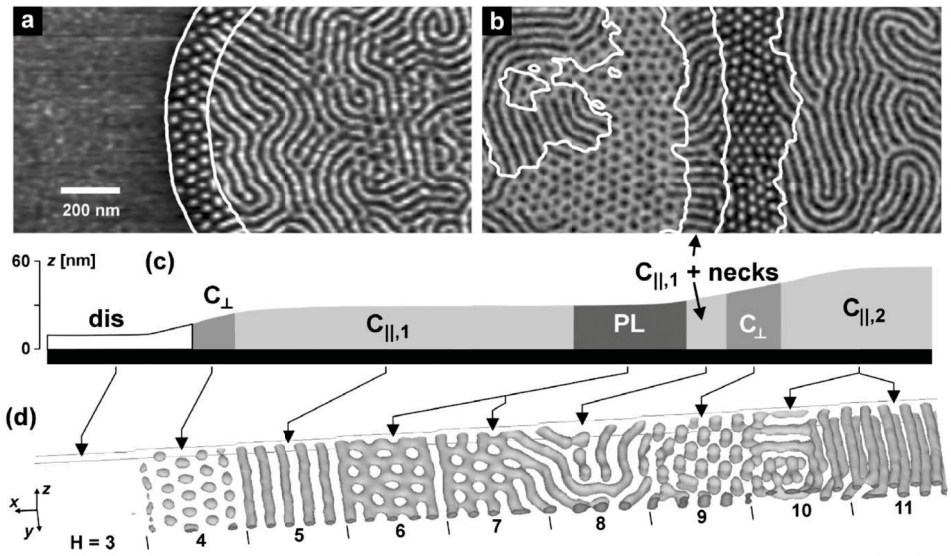

Figure 1.6: *Influence of film thickness on the BCP morphology. (a-b) A scanning force microscope phase image of a polystyrene-block-polybutadiene-block-polystyrene (PS-b-PB-b-PS) triblock copolymer thin film on silicon substrate. (c) The height profile of phase image in (a,b). (d) The simulated morphology for related film thickness. Reprinted with permission from ref. [4]. Copyright © 2002 American Physical Society.*

detailed discussion).[27, 89]

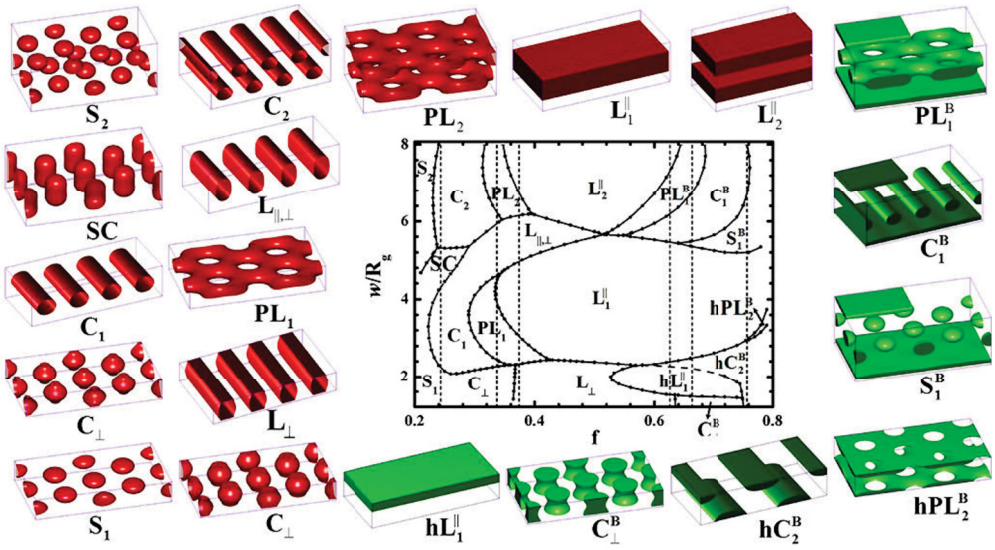

Figure 1.7: *Theoretical phase diagram of an AB diblock copolymer ($\chi N = 20$) confined in a thin film. Reprinted with permission from ref. [5]. Copyright © 2013 American Chemical Society.*

Generally, an untreated substrate surface always prefers to interact with one block of a BCP. As shown in Figure 1.8a, two different substrate surfaces attract different blocks of a lamellar-forming BCP, which leads to different arrangements of parallel lamellar structures. On the other hand, if a substrate is treated to interact with two blocks of a BCP equally, a so called 'neutral wetting surface', perpendicular lamellar can be achieved (Figure 1.8b). In the lithographic application, a neutral wetting surface for lamellar-forming BCPs is favored in order to get parallel line patterns. As for cylinder-forming BCPs, a preferential wetting surface can lead to horizontal cylinder patterns and a neutral wetting surface can drive the formation of perpendicular cylinder patterns. The surface treatment can be generally carried out by grafting end-group functionalized polymers[90–92] and self-assembled monolayers (SAMs).[93, 94] Similar to the substrate-BCP interface, adjusting the interaction on the air-BCP interface can also help to control the resulting nanopatterns. Willson and co-workers developed a top-coating polymer,

which enables to the tuning of the morphology of high-χ BCPs from parallel lamellar phases to perpendicular lamellar phases.[95, 96].

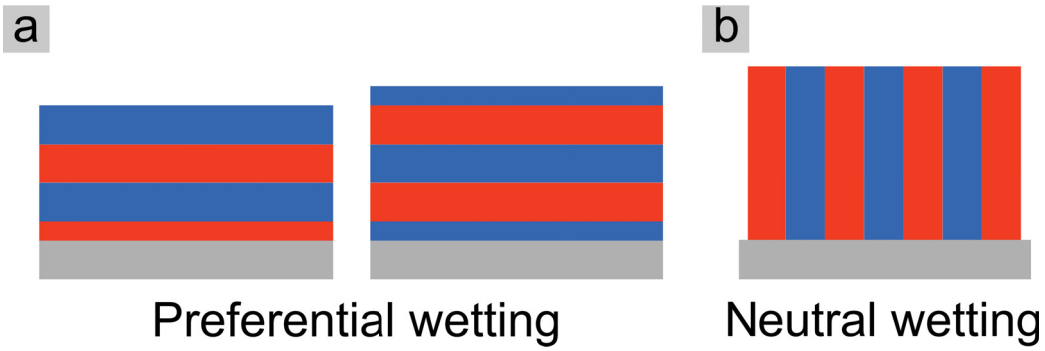

Figure 1.8: *Schematic of a lamellar-forming BCP on preferential wetting surface (a) and neutral surface (b).*

1.2.5 Annealing

The key to driving the BCP thin film self-assembly process is the annealing step, during which the BCPs undergo nanoscale phase segregation.[57, 82] The BCP of interest is typically dissolved in a good solvent to form a diluted solution and spin-coated onto a substrate in order to produce smooth thin films of controlled thicknesses. The substrate surface should be cleaned beforehand in an appropriate manner, with perhaps additional functionalization with a brush layer, or other chemical methods.[96–99] As-spun films are kinetically trapped in a disordered state due to fast evaporation of the solvent, and they represent the starting point for self-assembly. Two basic techniques for annealing of BCP thin films are thermal annealing and solvent vapor annealing. Other annealing methods like microwave annealing with/without solvent,[21, 100] solvothermal annealing,[23] laser annealing,[101–103] zone annealing,[104] or solvent immersion[105] are all based on one or both basic annealing methods. Briefly, the mechanism of annealing is improving chain mobility to promote a self-assembly process into a reasonable time scale (seconds to days). In this section, the annealing approach, mechanism,

advantages, and drawbacks of two basic annealing methods will be discussed.

Thermal Annealing

Thermal annealing involves the heating of BCP thin films on a substrate to a temperature above the glass transition temperature, T_g, and below the order-disorder transition temperature (T_{ODT}), to enhance polymer diffusivity.[106–110] The T_{ODT} is a temperature when BCP nanostructures disappear and form a homogeneous mixture. Experimentally, it can be measured from dynamic temperature sweep experiments.[111] It can also be estimated from the temperature dependent Flory-Huggins interaction parameter, χ (Equation 1.2.1) and the minimum segregation strength, $\chi N \geq 10.5$.[112]

$$\chi = \frac{\alpha}{T} + \beta \tag{1.2.1}$$

where α and β are all constant (α is enthalpic contribution, and β is entropic contribution) and T is absolute temperature.[113]

The thermal energy increases the mobility of the BCP chains. With sufficient time, BCPs are able to reach lower energy configurations. For each BCP, the optimal annealing conditions will differ as they depend upon the chain lengths, volume fraction of each block, the χ parameter, film thickness, and treatment of the substrate surface.[6, 8, 106, 114, 115] Thermal annealing is usually performed in a vacuum or in an inert gas atmosphere to avoid oxidation and decomposition of the organic polymer. Apparatus for thermal annealing includes the use of a vacuum oven, a hot plate in an inert atmosphere glove box, or a tube furnace with either vacuum or inert gas flow. Temperatures are generally in the range of 120-250 °C, and the time required is on the order of hours-to-days.[11, 106, 107, 115, 116] Welander *et al.* studied the kinetics of the thermal annealing process of a lamellar PS-*b*-PMMA on a chemical patterned surface in a nitrogen glovebox. Figure 1.9 shows the semi-log plot of annealing time t versus inverse annealing temperature $1/T$. The inserted SEM micrographs show the morphologies of PS-*b*-PMMA thin films when

defects start to disappear and when defects have all disappeared at each annealing temperature. The BCP diffusivity $D(T)$ can be described as Equation 1.2.2.

$$D(T) = A \times exp^{-\frac{\Delta E_a}{RT}} \tag{1.2.2}$$

Where A is a constant, ΔE_a is the activation energy of a BCP, R is ideal gas constant, T is absolute temperature. As the $D(T)$ is proportional to the annealing time $1/t$, the relationship between annealing temperature T and related annealing time t can be described as:

$$\ln t = \frac{\Delta E_a}{RT} + B \tag{1.2.3}$$

where B is constant. The slope of the fitting line in Figure 1.9 is $\frac{\Delta E_a}{R}$. The linear fitting line suggests the annealing time will decrease as the annealing temperature increase and sub-1 min annealing could be done with annealing temperature at 280 °C.

It has been recently reported that thin films of BCPs can be successfully annealed in an ambient atmosphere (air) *via* fast heating approaches (seconds to minutes) such as microwave heating,[21, 26, 100, 117, 118] photothermal laser heating,[25, 101–103] and rapid thermal annealing.[119, 120] Additionally, thermal annealing has the advantage of being compatible with current patterning processes in the semiconductor industry, such as spin-casting, baking, and etching process.[120]

BCPs with a high-χ value are particularly interesting to the semiconductor industry as it can provide sub-10 nm resolution patterning, low line width roughness, and low line edge roughness.[96, 121] However, high-χ BCPs are difficult to be annealed thermally in any reasonable annealing time due to low diffusivity (Equation 1.2.2). As a result, much higher annealing temperatures are required, which can result in thermal decomposition of BCP blocks or can cause unwanted changes in the substrate.[113, 122–125] In addition, thermal annealing also has

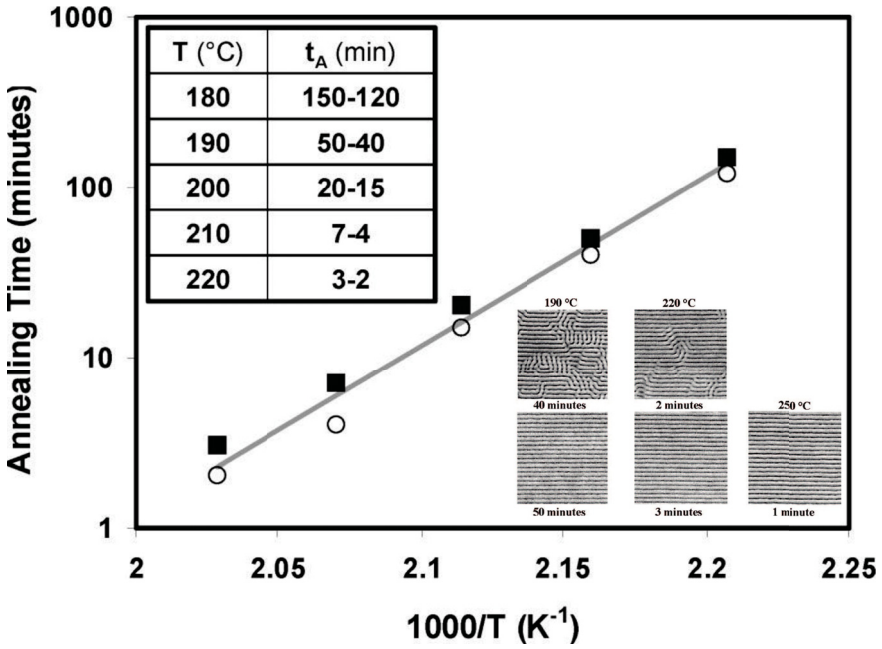

Figure 1.9: *Scatter diagram of annealing time and annealing temperature and fitting line. ■ and ◯ indicated the time when the defect of BCP start to decrease and a defect free pattern is formed, respectively. Upper left is the data table of the plot. Lower right shows for SEM micrographs of PS-b-PMMA thin film in two annealing test. Reprinted with permission from ref. [6]. Copyright © 2008 American Chemical Society.*

difficulties in annealing BCPs with large molecular weight due to the chain entanglement. [126]

Solvent Vapor Annealing

The basic principle of solvent vapor annealing is simply the exposure of a BCP thin film to a solvent vapor; if the solvent has a similar value of the Hildebrand solubility parameter with one or more of the blocks (often referred to as a 'good' solvent), the polymer layer absorbs the solvent and swells, resulting in a thicker film. Within the swollen film, the free volume of BCP chains increases as the solvent molecules act as a plasticizer, which lowers the glass transition temperature and increase the polymer chain mobility. The solvent vapor annealing was proposed by Thomas and co-workers in 1998 as an alternative annealing method.[128] They noted that the order of solvent vapor annealed polystyrene-*block*-polybutadiene-*block*-polystyrene (PS-*b*-PB-*b*-PS) triblock copolymer thin films was improved compared to those annealed thermally. The same year, Libera and co-workers studied the influence of solvent evaporation in the long-range order and orientation of cylinder-forming PS-*b*-PB-*b*-PS triblock copolymer nanopatterns.[129] The solvent annealing method became increasingly popular after Fukunaga, Russell and co-workers demonstrated that long-range order of lamellar and cylindrical structures was achieved *via* solvent vapor annealing.[130–132] Since these early reports of solvent vapor annealing, this approach has been widely used for many BCP systems.[7]

Unlike thermal annealing, BCP solvent vapor annealing is a complex process. Due to shielding of one or more of the blocks by solvent, the effective Flory-Huggins interaction parameter of swollen BCP decreases ($\chi_{eff} = \chi(1 - f)$, where the f is the volume fraction of solvent in swollen BCP thin film). On the other hand, the volume fraction of a block (or homopolymer segment-solvent mixture), $f_{swollen}$, in the BCP thin film can increase, decrease, or stay constant during the annealing process by selecting specific annealing solvents. Additionally, solvent vapor also

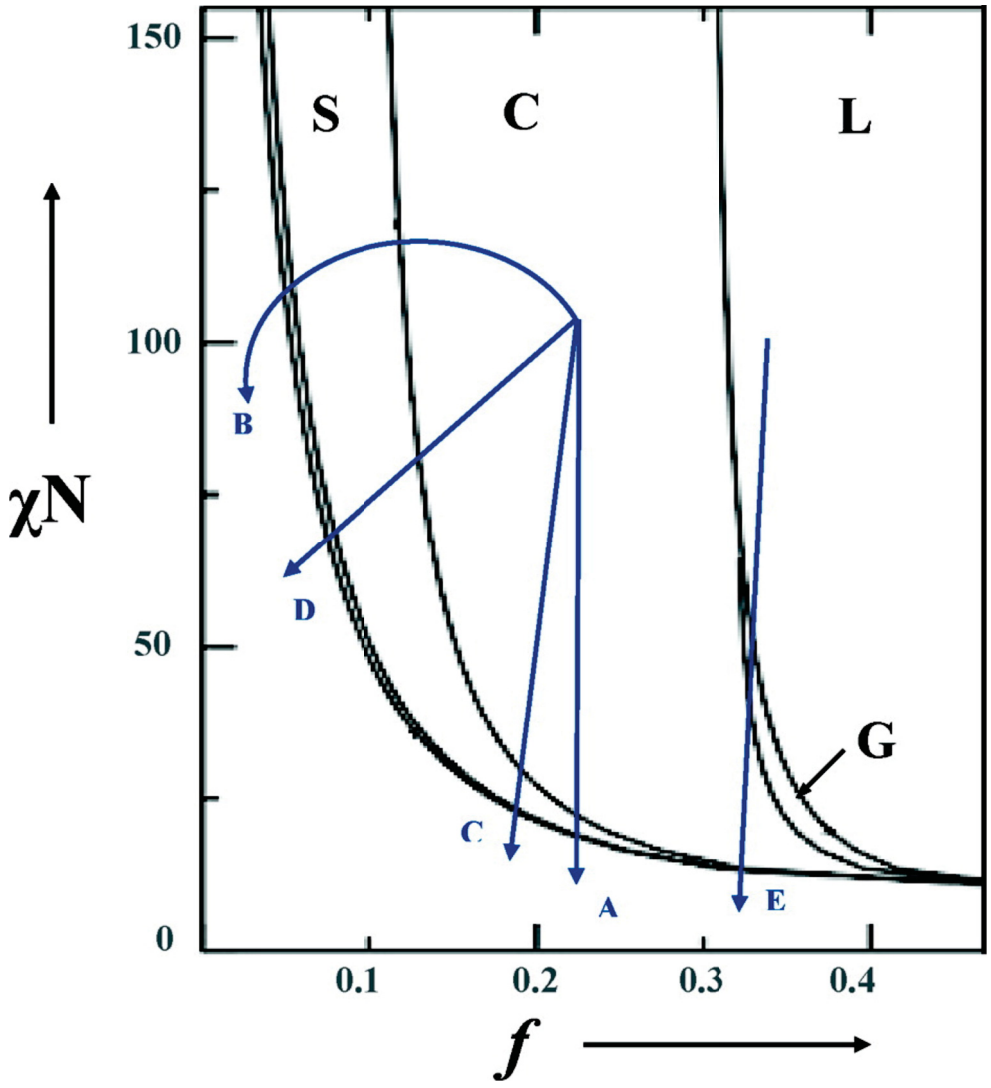

Figure 1.10: *Schematic of the trajectories of two polystyrene-block-poly(4-vinylpyridine) (PS-b-P4VP) / 2-(4'-hydroxybenzeneazo)benzoic acid annealed in non-selective solvent (A), strongly PS selective solvent (B), chloroform vapor (C, E), 1,4-dioxane vapors (D). Reprinted with permission from ref. [7]. Copyright © 2010 American Chemical Society.*

changes the polymer-substrate, polymer-air interaction, and film thickness. Hence, the pitch of the resulting pattern ($L_o \propto \chi_{eff}^{1/6}$) will be different from its native pitch. In some extreme cases, a given BCP could access non-equilibrium morphology with the selection of a different annealing solvent and degree of swelling, D (the film thickness of the swollen BCP thin film divided by its initial film thickness).[83, 133–138] Figure 1.10 shows the trajectory of morphology evolution of polystyrene-*block*-poly(4-vinylpyridine) (PS-*b*-P4VP) / 2-(4'-hydroxybenzeneazo)benzoic acid annealed in different solvent.[7]

Solvent vapor annealing is incredibly versatile because of the availability of a wide range of solvents with different solubility parameters, vapor pressures, and other characteristics that can be used. It has been widely used to anneal BCPs with a high χ parameter, high molecular weight, and low thermal stability. Various solvent vapor annealing apparatus have been developed to precisely control and monitor the micro- and/or nano-scale morphology evolution during the annealing process (see Chapter 3 for more discussion). It has been demonstrated that solvent vapor annealing could anneal BCP thin films on a 300 mm wafer in a sub-1 minute time scale.[105] When combined with a thermal heating process, such as hot plate or microwave irradiation (called solvothermal annealing), this type of hybrid annealing approach showed a much shorter annealing time, low defect density, low line edge roughness, and line width roughness.[21, 22, 100, 139, 140]

1.3 Directed Self-Assembly

Self-assembly of BCPs on a free surface leads to the formation of randomly oriented BCP nanopatterns. In order to control the orientation of BCP nanopatterns to form highly oriented and defect free patterns, an external force can be applied during the process of BCP self-assembly. This type of alignment method is called directed self-assembly (DSA).[83] DSA methods, such as shear force,[103] zone annealing,[104] and a electric field[141] can be used to induce large-

scale ordered patterns. However, these methods have difficulty in fabricating complex nanopatterns in a micro-, or even a nanometer range that is required for semiconductor fabrication. DSA approaches using chemical (chemical epitaxy) or topological features (graphoepitaxy) patterned surfaces to induce self-assembly of BCP thin films are the most favorable methods for the semiconductor industry (Figure 1.11).[16, 20, 142] Chemical epitaxy and graphoepitaxy not only can induce long-range order of BCP thin film self-assembly,[8, 107, 108, 143] but also can guide BCP thin films to form complex nanopatterns that are essential for integrated circuit fabrication, including bends,[106] jogs,[12] T-junctions,[12] and square arrays.[144, 145]

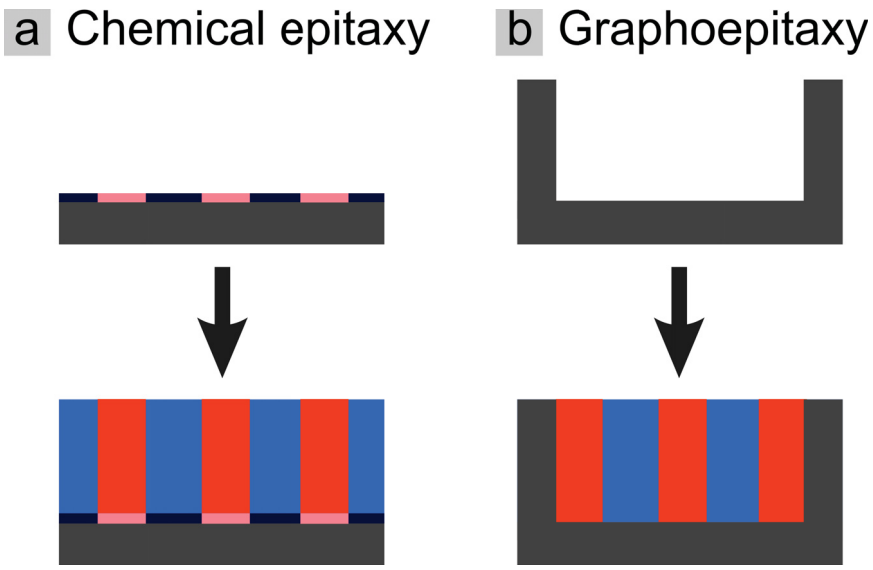

Figure 1.11: *Schematic of chemical epitaxy (a) and graphoepitaxy (b).*

1.3.1 Graphoepitaxy

Graphoepitaxy refers to a type of approach that uses topographic patterns on the substrate to confine BCP thin film self-assembly. These type of guiding patterns can be fabricated by conventional photolithography, nanoimprint lithography, and electron beam lithography (EBL).[16, 20, 142] The pitch of the resulting

topographic patterns needs to perfectly match the native pitch of a given BCP. It gives a lateral orientation control in BCP thin films during the self-assembly process and can be used to direct the self-assembly of BCPs with any kind of morphology.

Ross and co-workers developed a graphoepitaxy approach by using silica pillar array patterns to induce the alignment of dot-forming PS-*b*-PDMS thin films.[8] The silica pillars were fabricated by EBL with accurate position and size control. The self-assembly of PS-*b*-PDMS thin films on an unpatterned silicon substrate resulted in a polycrystalline dot pattern with multiple domains (Figure 1.12a). With hexagonal silica pattern guiding patterns (bright spots in Figure 1.12b), a defect-free and perfectly aligned BCP dot grain was obtained. These types of EBL patterned silica pillars can also be used to align line-forming PS-*b*-PDMS BCPs. By placing the silica pillars arrays with a spacing commensurate with the native pitch of the BCP, defect free parallel line arrays and complex nanopatterns with bends, junctions, and parallel lines were also demonstrated.[9, 10]

Buriak and co-workers demonstrated DSA of cylinder-forming PS-*b*-P2VPs in 35-nm deep trenches.[11] Parallel line patterns were obtained from rectangular shaped and triangular shaped trenches (Figure 1.13a and b) and concentric circles were obtained in perfect circular trench (Figure 1.13c). Interestingly, if a defect was present in a circular trench, a 'ying-yang' pattern was formed instead of concentric circles (Figure 1.13d). It has been also reported that trench or wall patterns can also be used to induce the self-assembly of BCPs to form long-range order dot,[16, 23] lamellar,[146] and perforated lamellae patterns.[146]

1.3.2 Chemical Epitaxy

Chemical epitaxy is a type of approach that uses a chemically patterned surface to induce self-assembly of BCP thin films. The chemical patterns are usually obtained by grafting polymers or small molecules onto specific areas or by selectively oxidizing homogeneous chemical modified surface. As chemical epitaxy only

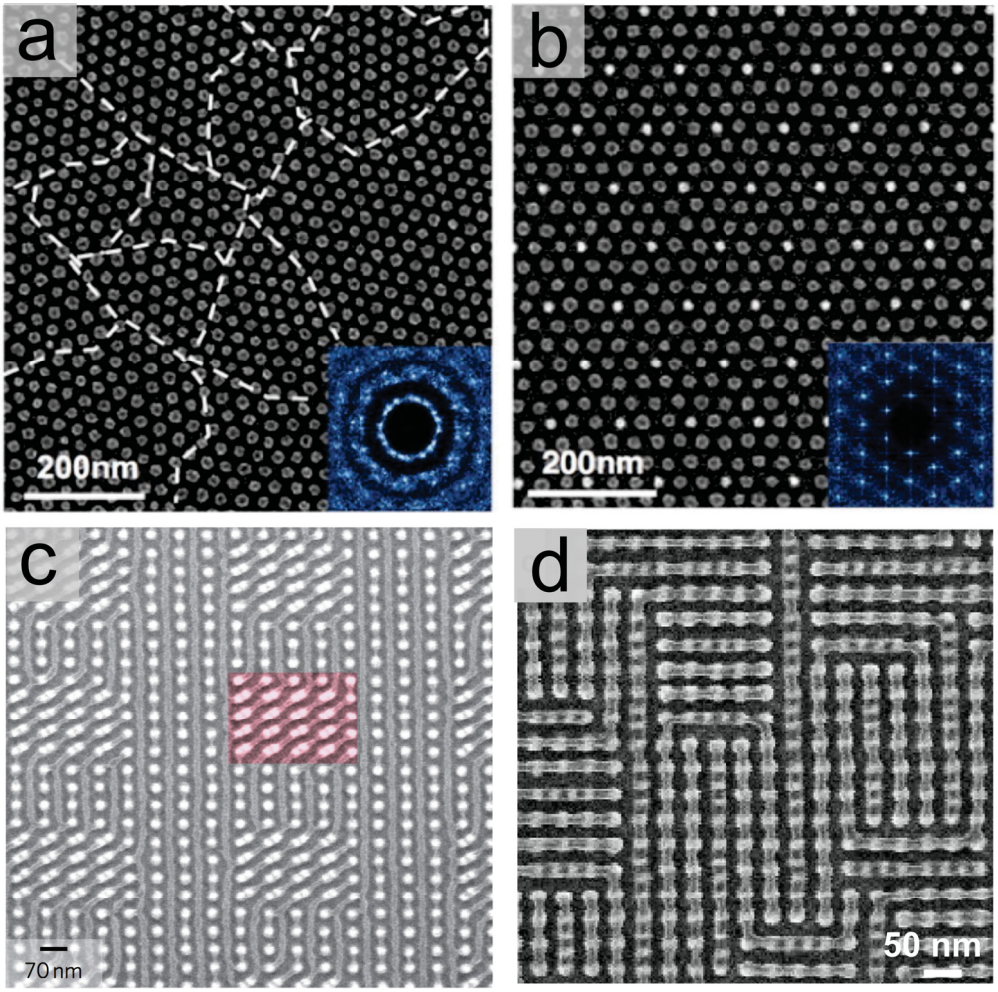

Figure 1.12: *SEM micrographs of a dot-forming PS-b-PDMS thin film self-assembled on flat silicon substrate (a) and silica posts array on a patterned silicon substrate (b). Insert: 2DFFT. Reprinted with permission from ref. [8]. Copyright © 2008 American Association for the Advancement of Science. (c) Diagonal line arrays surrounded by a parallel line array formed by annealing a cylinder-forming PS-b-PDMS on silica pillar template (white dots). Reprinted with permission from ref. [9]. Copyright © 2010 Rights Managed by Nature Publishing Group. (d) Complex patterns with bends and terminations formed by annealing a cylinder-forming PS-b-PDMS on silica pillar templates. Reprinted with permission from ref. [10]. Copyright © 2014 Rights Managed by Nature Publishing Group.*

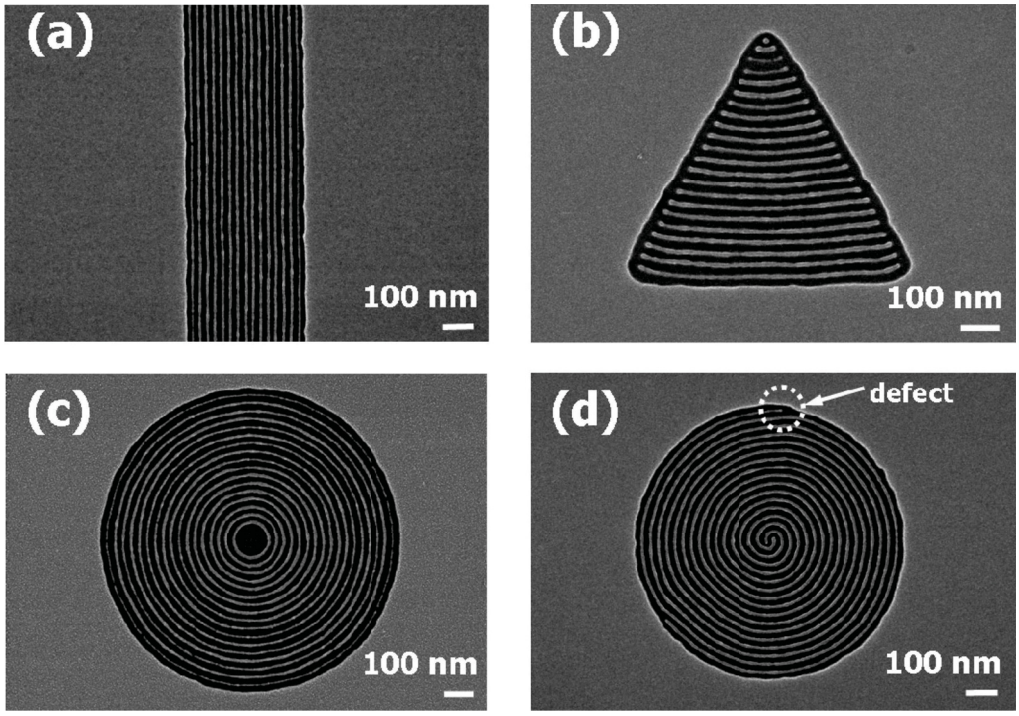

Figure 1.13: *SEM micrographs of aligned platinum nanopatterns converted from line-forming PS-b-P2VP annealed in rectangular (a), rectangular (b), and circular (c, d) trenches. Reprinted with permission from ref. [11]. Copyright © 2008 American Chemical Society.*

controls the surface potential, it is mainly used to direct lamellar- and cylinder-forming BCPs, where both BCP block domains can appear at the polymer-substrate interface. Parallel line patterns, hexagonal dot patterns, and other complex patterns can also be achieved *via* chemical epitaxy with proper guiding patterns.

Nealey and co-workers first reported a surface patterning strategy enabling the direct self-assembly of lamellar-forming PS-*b*-PMMA thin films to form defect free, oriented parallel line patterns over a 5 μm $\times$ 5 μm area.[107] The chemical strips were fabricated by selective oxidation of a monolayer of phenylethyltrichlorosilane (PETS) that self-assembled on a silicon substrate. During annealing, the PMMA block of the BCP wet the oxidized PETS monolayer area, and the PS block wet the unoxidized PETS monolayer surface. The quality of the resulting lamellar pattern highly depended on the pitch of of underlying chemical strips. The defect free pattern was obtained only when the pitch of chemical strip matched the BCP pitch. Later, the authors extended this chemical pattern epitaxy method to induce the formation of complex BCP patterns such as bends with angles from 135 to 45 °,[106], isolated lines,[12] isolated jogs,[12] T-junctions arrays (Figure 1.14).[12]

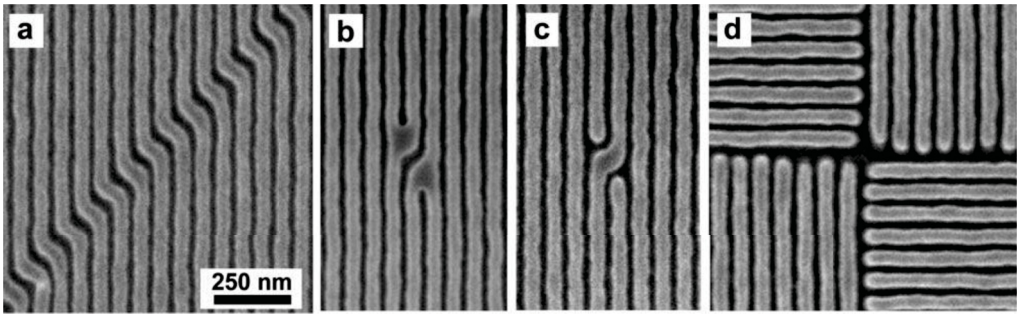

Figure 1.14: *SEM micrographs of (a) jog array, (b,c) isolated jogs, and (d) T-junctions fabricated by self-assemble PS-b-PMMA on a chemically patterned surface. Reprinted with permission from ref. [12]. Copyright © 2007 American Chemical Society.*

Chemical epitaxy can also be used to fabricate defect-free hexagonal packed dot patterns with density up to 1 Teradot/in^2 with cylinder forming PS-*b*-PMMA thin

films.[108] The chemical patterns were hexagonally packed circular spots grafted with oxidized PS polymer brushes. It selectively wet PMMA blocks in BCPs. Density tripled BCP nanopattern was achieved. It is also reported that square dot patterns can also be achieved by annealing cylinder-forming BCPs on chemical pattern with square-packed dot arrays.[144]

1.4 Pattern Transfer

As for lithography applications, self-assembled BCP thin films are used as a sacrificial mask. Morphologies of BCP thin films need to be transferred to the underlying substrate for device fabrication. Plasma etching, also called dry etching, is widely used to selectively remove one type of domain in self-assembled BCP thin films.[147] It utilizes chemical reactive ions and radicals to remove materials on a surface at low pressure. Different etching rates between different domains in BCP thin films provide an etching contrast. For example, as shown in Figure 1.15, the etching speed of PS domains in CHF_3/O_2 plasma is slower than that of PMMA domains. The PS trench structure was formed after 120 s of etching with complete removal of PMMA domains and partial removal of PS domains. The PS trenches can then be further etched down using a silicon selective plasma, such as CF_4 plasma. Inorganic-organic BCPs, such as PDMS containing BCPs (PS-*b*-PDMS, P2VP-*b*-PDMS), oligomeric silsesquioxane containing BCPs (PS-*b*-PMAPOSS),[148] and polyferrocenylsilane (PFS) containing BCPs (PI-*b*-PS-*b*-PFS),[149, 150] have all shown much improved etching contrast and edge roughness compared with that of PS-*b*-PMMA. The inorganic containing domains are more resistant to oxygen plasma compared with organic domains. After oxygen plasma, the PDMS and POSS containing domains are converted to silica nanostructures and the PFS containing domains forming nanostructures of iron and silicon oxides.

In order to enhance the etching contrast of organic BCPs, a variety of strategies have been developed. For PS-*b*-P2VP and PS-*b*-P4VP, a process called

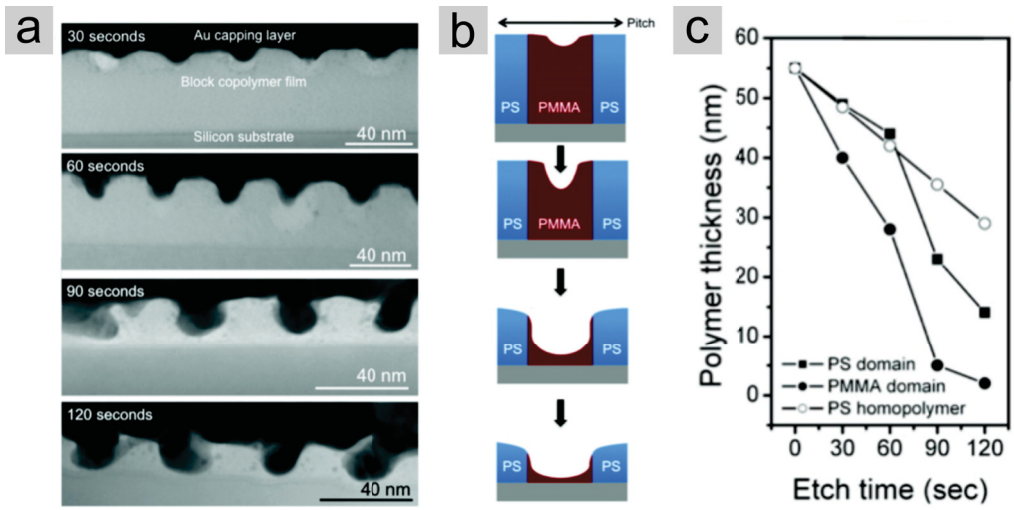

Figure 1.15: *(a) Cross-sectional TEM micrographs and (b) schematic representation of PS-b-PMMA lamellar structure during CHF_3/O_2 plasma etching period. (c) A plot of the film thickness of PMMA domain, PS domain, and PS homopolymer versus etching time. Reprinted with permission from ref. [13]. Copyright © 2010 American Chemical Society.*

metallization has been demonstrated by Buriak and co-workers.[11, 14] In this process, self-assembled PS-*b*-P2VP and PS-*b*-P4VP thin films were first immersed into aqueous solutions of anionic metal salts and followed by plasma etching to form metallic nanostructures (Figure 1.16). When immersed in a metal salt solution, the anionic metal complex loaded into the protonated P2VP and P4VP by electrostatic force (Figure 1.16a). The plasma simultaneously removed the BCP and reduced metal salt complexes to metals (Figure 1.16b and c). Ordered Au, Pd, Pt, Fe, Co, Cu, and Ni nanostructures were obtained. Self-assembled PS-*b*-P4VP thin films can also be converted to metal oxide (Al_2O_3 and Fe_3O_4) nanostructures.[151] Similar to the metallization process, iron nitrate or aluminium nitrate ethanol solutions were used to load metal ions into P4VP domain and followed by UV/O_3 treatment, during which BCPs were all removed and metal ions were all converted to metal oxides. The resulting Al_2O_3 and Fe_3O_4 nanopatterns were used as an etching stop in silicon etching and silicon fin structures with about 10 nm in width were fabricated.

Atomic Layer Deposition is also used to enhance the etching contrast of PS-*b*-PMMA thin films.[152–154] In this process, metal precursors (*i.e.* $Al(CH_3)_3$, $TiCl_4$, $Zn(CH_2CH_3)_2$), and water vapor were sequentially introduced into a reaction chamber for several cycles. Metal precursors reacted with carbonyl groups on PMMA and led to the formation of metal oxides in PMMA domains. The PS-*b*-PMMA thin film was then removed by oxygen plasma to obtain metal oxide nanostructures.

In addition, the PMMA domains in PS-*b*-PMMA thin films can be selectively removed by UV (usually 254 nm) irradiation in vacuum followed by washing with acetic acid solution or an organic solvent.[155–157] During UV irradiation, PS domains are crosslinked and PMMA domains are decomposed. Moreover, the polybutadiene (PB) domains in PS-*b*-PB thin films can be selectively degraded and removed when exposed to ozone.[147]

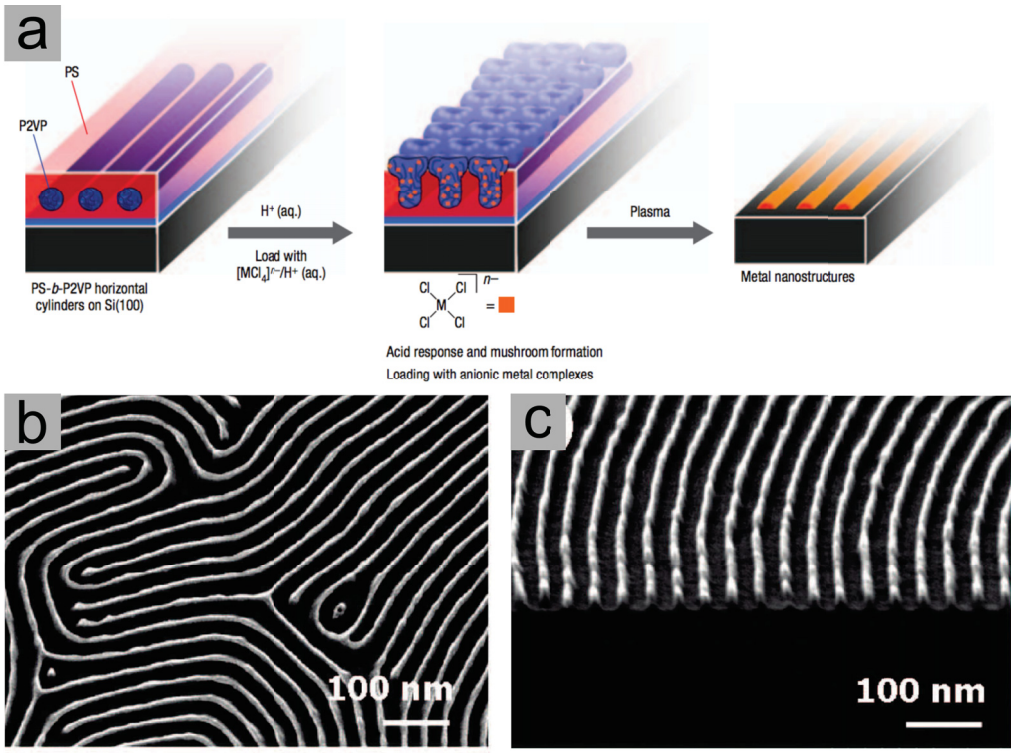

Figure 1.16: *(a) Schematic of metalization process. Reprinted with permission from ref. [14]. Copyright © 2007 Rights Managed by Nature Publishing Group. (b,c) Top-down and cross-sectional SEM micrographs of Pt nanostructures converted from a cylinder-forming PS-b-P2VP thin film. Reprinted with permission from ref. [11]. Copyright © 2008 American Chemical Society.*

1.5 Applications

The capabilities of density multiplication and defect rectification of BCPs are of interest to the semiconductor industry as an extension option for top down lithography.[108, 158] Various works of integrating this technology with conventional 193 nm photolithography on 300 mm wafers have been reported.[18, 158–160]

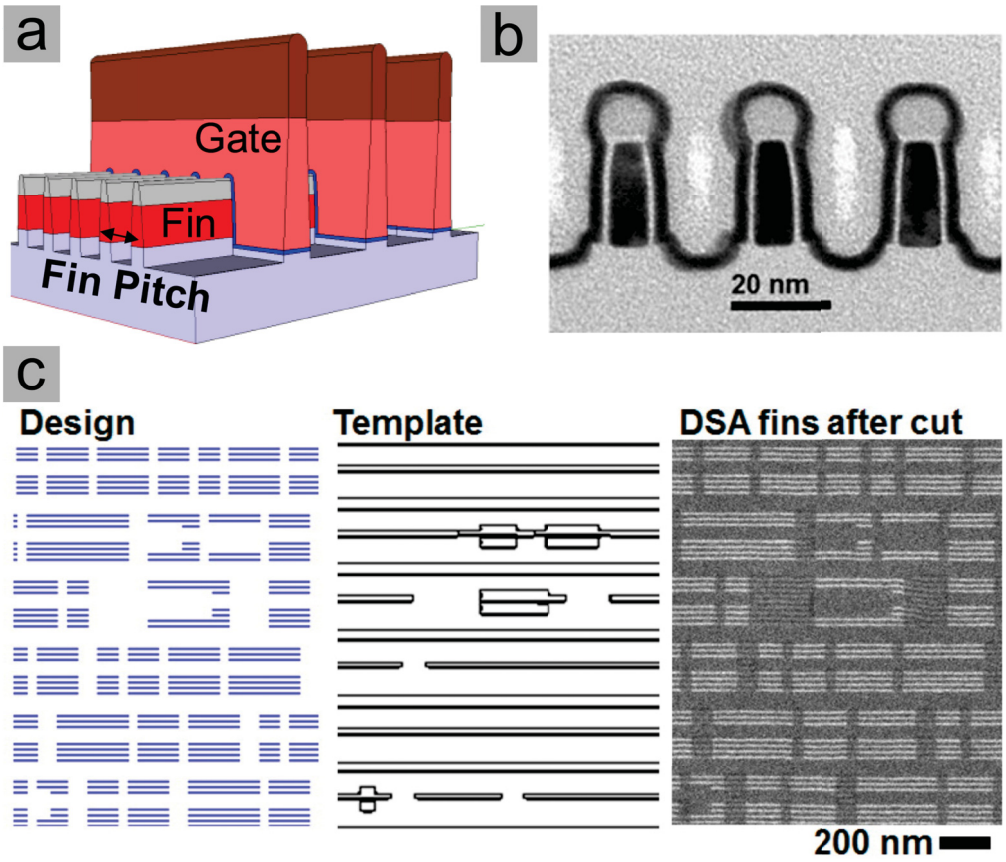

Figure 1.17: *(a) Schematic of finFET structure. (b) Cross-sectional TEM micrograph of 29-nm pitch fins fabricated from BCP self-assembly. (c) Schematic of fin design, DSA template design, and SEM micrographs of fin structure after DSA and pattern transfer. Reprinted with permission from ref. [15]. Copyright © 2008 American Chemical Society.*

1.5.1 FinFET

FinFET (fin field effect transistor) is a new type of transistor architecture with thin silicon fin structures wrapped by gate electrodes (Figure 1.17a). Compared to conventional CMOS (complementary metal–oxide–semiconductor) transistors, finFETs are smaller in size (sub-20 nm), have better performance, and lower energy consumption.[161] FinFET devices consist of multiple closely packed straight channels, which can be fabricated by DSA of lamellar- or cylinder-forming BCPs at low cost and high resolution. The idea of integrating BCP self-assembly into finFET fabrication was first proposed by Black from IBM in 2005.[162] Fin structures with 40 nm in pitch were fabricated by DSA of a cylinder-forming PS-*b*-PMMA. In 2014, Tsai and co-workers from IBM reported the first functional finFET transistor with a 29-nm pitch fins fabricated by directed self-assembly of lamellar-forming PS-*b*-PMMA (Figure 1.17).[15]. PS-*b*-PMMA thin films were deposited and thermally annealed on silica guiding patterns fabricated by EBL. The resulting devices with 10-nm thick and 20-nm tall silicon fins showed reasonable performance. DSA of PS-*b*-PMMA thin films have also been demonstrated in fabrication of finFET devices on 300 mm wafers integrated with 193 nm photographically and standard semiconductor fabrication process.[159, 160] High aspect ratio fin structures with 10 nm in width and 100 nm in height were fabricated.[160] Recently, silica fin structures fabricated *via* DSA of a high-χ BCP, PS-*b*-PDMS, showed improved resolution (24 nm pitch), low line edge roughness, lower line width roughness.[163]

1.5.2 Bit Patterned Media

Bit patterned media is an innovative data storage technology that uses magnetic nanodot arrays to store data.[164] It shows much higher storage capacity with up to 300 Td/in^2 oppose to 1 Td/in^2 at the theoretical limitation in conventional hard disk drives.[165] DSA of BCPs is a cost-effective approach to fabricate patterned media with high resolution. The pioneer work was reported by Ruiz and co-workers form

HGST in 2010, where they fabricated 0.5 teradot/in^2 and 1 teradot/in^2 hexagonally packed magnetic dot arrays for bit pattern media applications.[166] These dots were templated from PS-*b*-PMMA thin films with perpendicular hexagonally packed cylinder patterns which showed narrow magnetic switching field distribution. A variety of approaches have been developed to pattern dot arrays with BCP nanopatterns, including using hexagonally packed sphere-forming BCPs,[31–33] and perpendicular cylinder-forming BCPs.[32]. In 2014, Xiao and co-workers from Seagate demonstrated the first functional bit patterned media fabricated by using directed self-assembly of BCPs. Nanoimprint lithography was used to generate templates for PS-*b*-PDMS to form functional dot patterns. Bit patterned media with theoretical capacity up to 5 Td/in^2 was fabricated. A fully functional 1 Td/in^2 bit patterned media was tested and showed low bit error rate of $2^{2.43}$.[16]

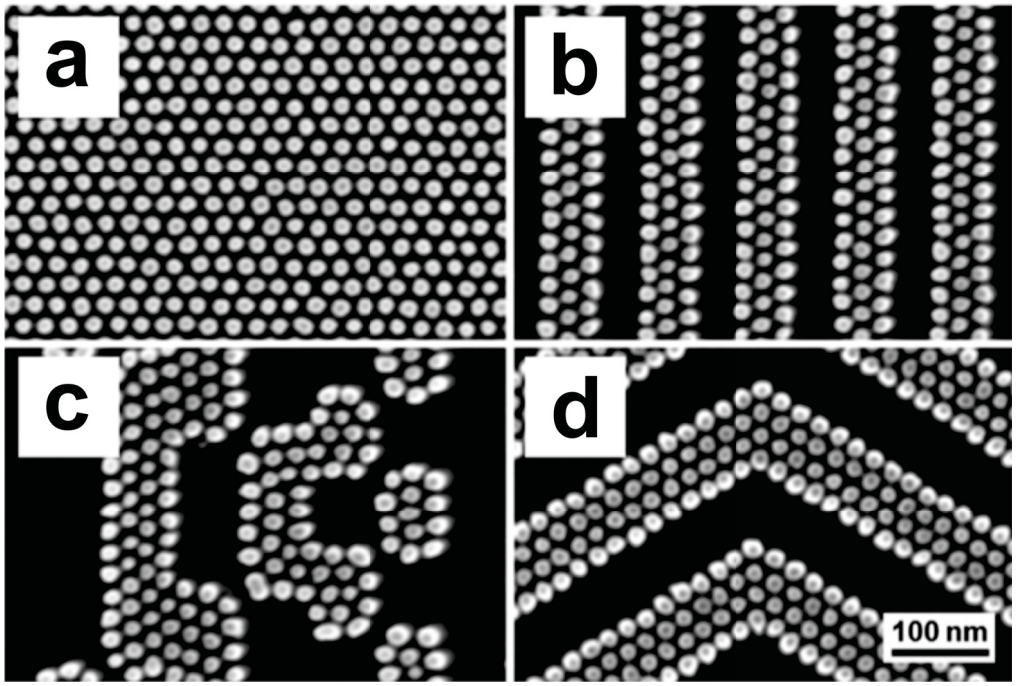

Figure 1.18: *SEM micrographs of self-assembled PS-b-PDMS thin film directed by nanoimprint lithography pattern. Reprinted with permission from ref. [16]. Copyright © 2014 American Chemical Society.*

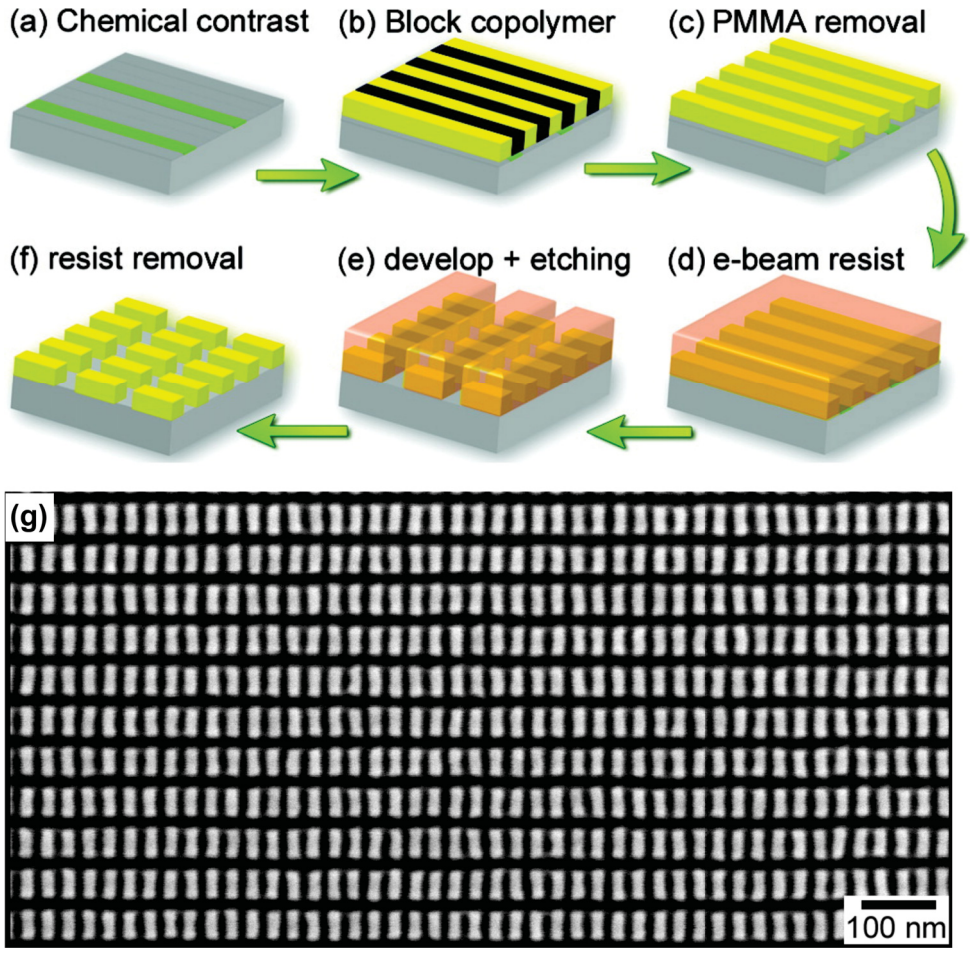

Figure 1.19: *(a-f) Schematic representation of rectangular bit fabrication process. (g) SEM micrograph of rectangular PS domains. Reprinted with permission from ref. [17]. Copyright © 2011 American Chemical Society.*

However, bit patterned media with a densely packed nanodot array may lead to challenging device fabrication as the reading and writing head needs to be smaller than the track width to ensure correct data reading and writing.[17, 167, 168] In order to avoid this problem, rectangular shape bit arrays with elongated along cross-track direction were proposed. Two patterning strategies, which involve BCP self-assembly, have been suggested. The first method was combined directed self-assembly of a BCP and selective etching.[17] The fabrication process is shown in Figure 1.19a-f). A lamellar-forming PS-*b*-PMMA thin film was directed by sparse chemical line patterns to form a perpendicular lamellar pattern with a pitch of 27 nm. Then the PMMA domains were selectively removed. After that, a new positive photoresist was applied, followed by perpendicular EBL writing and etching.The resulting rectangular bits were 27 nm $\times$ 54 nm and showed high uniformity. The second method involved directed self-assembly of BCPs and double imprint processes.[168] Briefly, two sub-master masks with radial and circumferential patterns were fabricated by directed self-assembly of BCP thin films separately. Then, nanopatterns on these two sub-master masks were printed onto a master mask to form a rectangular pattern. Finally, rectangular bit patterns were obtained by imprinting the nanopattern from the final master mask. The aspect ratio of the rectangular bit could be adjusted by changing PS-*b*-PMMAs used in sub-master mask fabrication. A rectangular bit array with 27 nm $\times$ 41 nm in bit size and 0.58 Td/in^2 was demonstrated.

1.5.3 Contact Hole Shrink

The contact hole is a type of key patterning element in integrated circuit fabrication. It comprises hole patterns drilled through the dielectric layer and filled with metal to connect underlying electrodes in transistors (gates, grains, and sources) and metal wiring layers. By combining with double or quadruple patterning technology, 193i photolithography is able to improve the resolution line patterns from about 40 nm to around 14 nm. As the size of the transistor feature keeps

shrinking, hole patterns remain a challenge for conventional lithography to match the resolution of transistors.[169] Graphoepitaxy of cylinder-forming BCPs in hole-shape temples have been proposed to be a potential solution for high-resolution closely packed contact hole pattern fabrication. As demonstrated in Figure 1.20, hole guiding patterns with 50 - 100 nm in diameter were fabricated by EBL or 193i photolithography.[18] The holes were then filled with a cylinder-forming PS-*b*-PMMA and followed by thermal annealing. The PS-*b*-PMMA formed a perpendicular single cylinder pattern with PMMA domain inside surrounded by PS domain. Then PMMA domains were etched away and shrunk hole patterns were transferred onto the substrate. The resulting holes showed 15 - 20 nm in diameter and improved size uniformity.

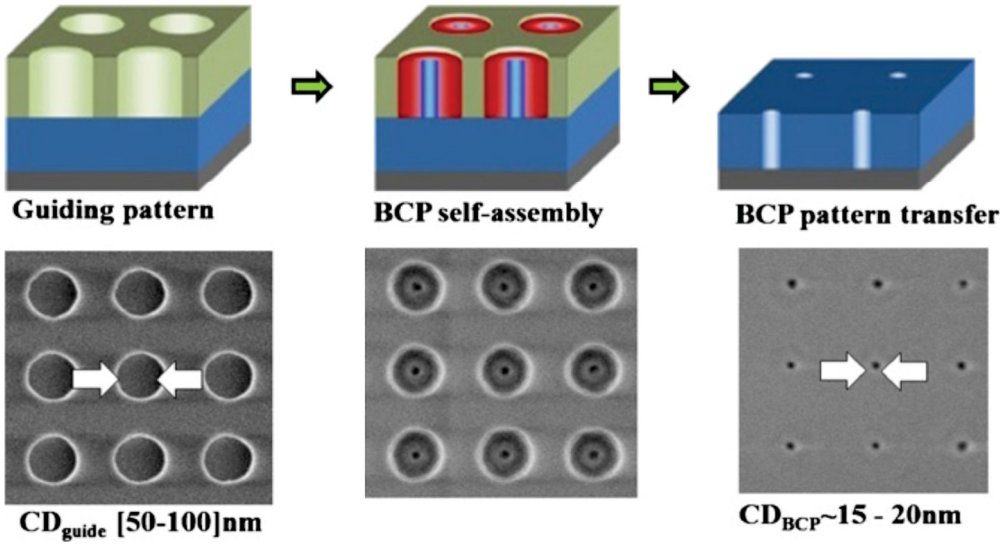

Figure 1.20: *Schematic representation and related top-down SEM micrographs of contact hole shrink process with BCP self-assembly. Reprinted with permission from ref. [18]. Copyright © 2014 Japan Society of Applied Physics.*

By changing the shape and size of template holes, complex high-resolution hole patterns were be obtained.[19, 20] As shown in Figure 1.21a, 126 nm × 126 nm square holes led to the formation of 4-hole square lattice patterns. Two or three close packed hole patterns were directed by rectangular hole guiding patterns with a size of

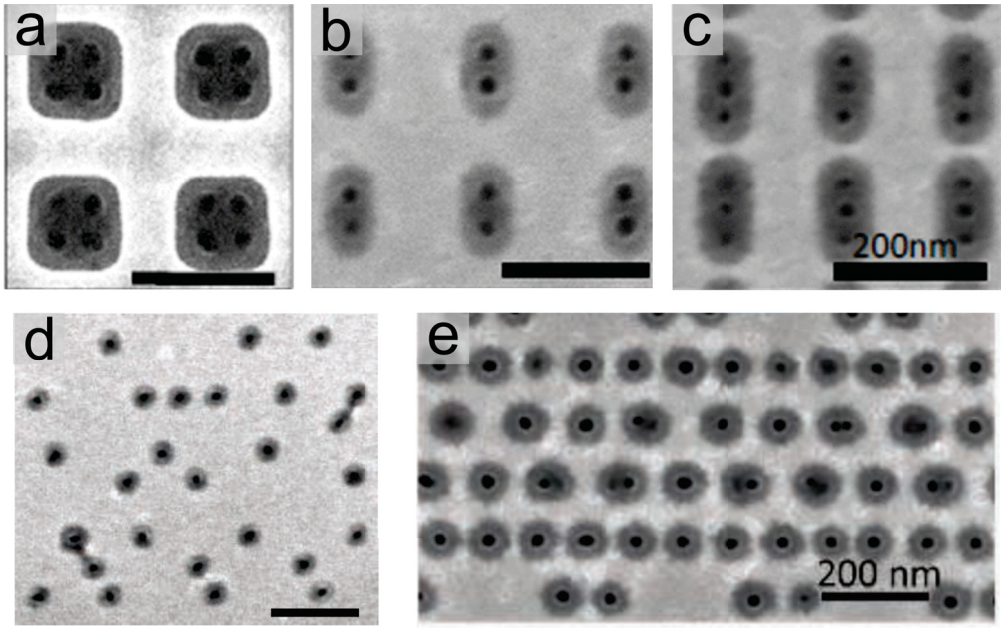

Figure 1.21: *Top-down SEM micrographs of (a) 4 holes in square templates, (b) 2 holes in rectangular templates, and (c) 3 holes in rectangular templates fabricated with BCP self-assembly. Reprinted with permission from ref. [19]. Copyright © 2014 IEEE. (d, e) Complex comtact hole patterns for 22 nm random logic circuits fabricated with BCP self-assembly. Schematic representation and related top-down SEM micrographs of contact hole shrink process with BCP self-assembly. Reprinted with permission from ref. [20]. Copyright © 2012 WILEY□VCH Verlag GmbH & Co. KGaA, Weinheim*

60 nm × 110 nm and 70 nm × 145 nm, respectively.[19] Additionally, contact hole patterns that met the current integrated circuit standard were successfully fabricated with BCP self-assembly, shown in Figure 1.21d and e.[19, 20]

1.6 Summaries and outlook

In summary, BCP self-assembly has shown its potential as a cost-effective approach for high volume production of sub-14 nm patterning. This technology has already been demonstrated on industry standard 300 mm wafers integrated with a 193 nm photolithography process and fully automatic lithography system.[159, 160] Compared to top-down patterning technologies, BCP self-assembly has the advantage of fabricating high-resolution close-packed periodic patterns, such as parallel fin structures and magnetic dot arrays in bit pattern media.

The semiconductor industry has successfully reached 14 nm half pitch resolution with state-of-the-art 193 nm photolithography and multiple patterning (SAQP or SAOP). This approach will be extended to sub-7 nm half pitch patterning if the next generation lithography (*i .e* EUVL, BCP self-assembly, electron beam lithography, and nanoimprint lithography) does not beat multiple patterning approaches in terms of resolution and cost.[49] BCP self-assembly has a much simpler pattern process in sub-14 nm patterning comparing to SAQP method, which requires ten times more deposition and etching processes in one pattern layer. Additionally, BCP self-assembly can achieve an arbitrary number of density multiplications by varying the size of guiding patterns. However, the line edge roughness and pattern etching contrast remains a challenge for BCP self-assembly.

High-χ BCPs have shown much higher resolution (as small as 5 nm half pitch) as well as lower line edge roughness and line width roughness in thin film self-assembly.[114] A variety of high-χ BCPs have been synthesized. However, currently, PS-*b*-PMMA (low-χ, χ = 0.03)[113] is the most favored in the

semiconductor industry, because PMMA is a commonly used photoresist in the semiconductor industry. The patterning process of PS-*b*-PMMA, such as annealing and PMMA block removal, is fully compatible with current lithography systems. However, most high-χ BCPs require solvent annealing processes, which have not been demonstrated for current semiconductor fabrication. Hence, in order to improve the BCP self-assembly to facilitate sub-14 nm half pitch patterning, a standardized solvent annealing system/procedure for high-χ BCPs needs to be developed.

2

Microwave Thermal Annealing of Block Copolymer Thin Films

This chapter endeavors to uncover the key steps that take place during microwave annealing, which enables the self-assembly of block copolymers (BCPs) to proceed in a rapid manner. Using a fiber optic probe in direct contact with the sample, *in situ* temperature monitoring of the annealing process revealed that the silicon substrate on which the BCP thin film is cast is the dominant source of heating. The influence of doping, sample size, and BCP composition was analyzed to rule out other possible mechanisms. *In situ* temperature monitoring of various polymer samples (PS, P2VP, PMMA, and the BCPs used here) showed that the polymers do not heat to any significant extent on their own with microwave irradiation of this frequency (from a household microwave oven, 2.45 GHz) and power ($\sim$600 W). It was also demonstrated that BCP annealing can be effectively carried out in 60 s on non-microwave responsive substrates, such as highly doped silicon, indium tin oxide (ITO)-coated glass, glass, and Kapton, by placing a piece of high resistivity silicon wafer in contact with the sample. In this configuration, the silicon wafer is termed

the heating element. Annealing of polystyrene-*block*-poly(2-vinylpyridine) (PS-*b*-P2VP) and polystyrene-*block*-polymethylmethacrylate (PS-*b*-PMMA) BCPs into horizontal cylinder structures was shown to take place in under 60 s. Defect densities were calculated and were shown to decrease with higher maximum temperatures. Conflicting results in the literature regarding BCP annealing with microwave are explained in light of the results obtained in this study.

2.1 Recent Development in Block Copolymer Fast Annealing

To prepare well-ordered, self-assembled BCP thin films, annealing is a key step in facilitating the necessary reorganization of nanoscale phase-separated domains that generates the desired morphology. The most commonly used annealing methods are thermal annealing[8, 104, 106, 107, 156, 170–176] and solvent annealing.[28, 122, 130, 131, 155, 177–181] For thermal annealing, BCP thin films are heated to a temperature between the glass transition temperature (T_g) and order disorder transition temperature (T_{ODT}) for an extended period of time to enable plasticization of the polymer chains. In the case of solvent vapor annealing, the BCP film is exposed to a vapor of a compatible solvent, where compatible indicates a solvent in which one or more blocks are soluble.[182] The solvent is absorbed by the BCP blocks, resulting in swelling of the polymer film. Solvent absorption brings about a decrease in the Flory-Huggins interaction parameter [$\chi_{eff} = \chi(1\text{-}f)$], where f is the volume fraction of solvent in swollen BCP film, and owing to the shielding effect of the solvent, polymer chains then have increased mobility, resulting in lowering of the barrier to phase reorganization. The time required for conventional thermal annealing and solvent annealing is on the order of hours or days.[28, 30, 40, 116, 171, 183]

From a practical perspective, the time required for annealing is important for

both commercial applications and research laboratory throughput. The 2007 ITRS roadmap specifically states that the BCP annealing process needs to be complete in under 4 minutes;[184] by 2011, improvements in the time required for annealing were noted by the roadmap, and it stated that "a few minutes $\cdots$ represents a realistic timescale for potential processing applications".[185] As a result, there has been a determined effort to reduce the time required for annealing.[6, 21, 142] For instance, in 2008, Nealey and co-workers demonstrated that PS-*b*-PMMA thin films could be anneales to form well-ordered lamellar patterns on a patterned surface on hot plate at 250 °C within 1 min.[6] In 2010, our group showed that PS-*b*-P2VP and PS-*b*-PMMA thin films could assemble into aligned horizontal cylinders in 60-180 s with microwave-assisted solvothermal annealing in a research grade microwave reactor.[100] One year later, we demonstrated that cheap domestic microwave oven could also be used to attain rapid annealing of PS-*b*-P2VP thin films within 1 minute.[21] In this setup, BCP samples and annealing solvent were sealed in a custom-made Teflon chamber (microwave transparent material) and then 'cooked' by a domestic microwave oven (see Figure 2.1a for detail).[21] In 2012, Jung and co-workers demonstrated a solvothermal approach on conventional hot plate combined with graphoepitaxy, with successfully brought about self-assembly of line patterns from high-χ BCP polystyrene-*block*-polydimethylsiloxane (PS-*b*-PDMS) at 85 °C in 5 minutes (Figure 2.1c).[23] Later, they also annealed PS-*b*-PDMS BCP thin films in the same setup but with binary annealing solvent.[186] Well-ordered BCP nanopatterns could be achieved in just 10 s.[186] In 2012, Karim and co-workers reported a thermal induced gradient soft-shear method for BCP fast annealing in a speed of 12 mm/min.[24] Nanopatterns of centimeter-scale BCP thin films could be aligned along the annealing direction on non-patterned substrate.[24] In 2013, Ross and co-workers combined with graphoepitaxy, sequential solvent vapor flow annealing and thermal annealing to anneal PS-*b*-PDMS thin films (Figure 2.1b).[22] An ordered hexagonal packed dot pattern and a parallel line pattern were obtained in 30 s and in 5 min, respectively. The same year, Perego and co-workers demonstrated a non-graphoepitaxial rapid thermal processing approach

to 250 °C can be applicable to PS-*b*-PMMA thin films, and resulted in fingerprint line patterns in a minimum of 60 s.[119] Recently, Yager and co-workers proposed that laser zone annealing could potentially anneal BCP at sweep speed of 1 mm/s (Figure 2.1e).[25] When incorporating with soft-share, the order of annealed BCP thin film was dramatically improved and BCP horizontal cylinder domains were aligned along the laser sweeping direction without physical or chemical epitaxy patterns.[25, 103] Zelsmann and co-workers showed that by simply blending with commercial plasticizers (dioctylsebacate or diisooctyl adipate), PS-*b*-PDMS could be annealed with just thermal annealing in 30 s at 300 mm wafer scale.[187] There remain, however, questions as to the applicability of conventional thermal annealing, conventional solvent vapor annealing, and other innovative rapid annealing processes in an integrated circuit manufacturing environment; at present, solvent vapor annealing and other innovative annealing setups have not yet been developed within the context of semiconductor processing, and therefore thermal annealing may be more readily adopted.[188]

2.2 Microwave-Assisted Fast Annealing

Microwave-based heating is a subtly different approach towards thermal annealing that has been only superficially explored for BCP annealing. Given its simplicity and speed, microwave annealing merits continued investigation.[185] Microwave heating is well established in industrial, academic, and domestic settings as a rapid, non-classical heating technique.[189–191] It was first used primarily in the food industry in the 1960's, but thereafter, its use rapidly expanded to other large scale manufacturing, including the curing of rubber and wood products, ceramics and semiconductors.[192] Microwave heating is commonly used in academic laboratory settings, since the rate of many reactions can be dramatically increased, often leading to higher yields and product purities.[190, 193, 194] Since microwave irradiation can heat and even melt silicon wafers,[195] the typical substrate used for

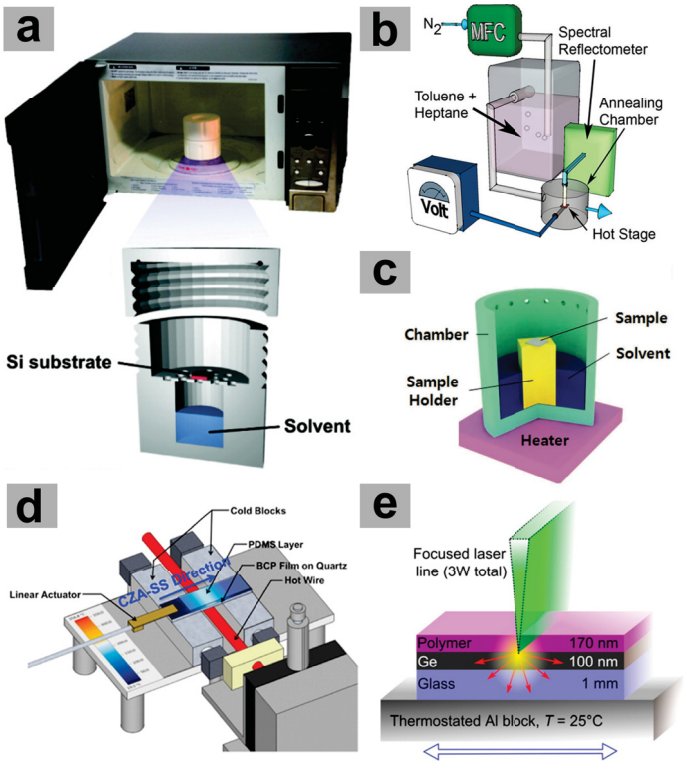

Figure 2.1: *Fast annealing setups. (a) A solvent-assisted microwave annealing setup. Annealing solvent and BCP thin films are sealed in a custom-made Teflon chamber and heated in a domestic microwave oven.[21] Reprinted with permission from ref. [21]. Copyright © 2011 American Chemical Society. (b) A solvothermal annealing setup with binary solvent vapor flow system, hot stage and in situ spectral reflectometry for thickness measurement.[22]. Reprinted with permission from ref. [22]. Copyright © 2013 American Chemical Society. (c) A low temperature solvothermal annealing setup, wherein a stainless steel chamber with solvent reservoir and sample holder is placed on a hot plate.[23] Reprinted with permission from ref. [23]. Copyright © 2012 WILEY-VCH Verlag GmbH & Co. KGaA, Weinheim. (d) A thermally induced gradient soft-shear annealing setup.[24] Reprinted with permission from ref. [24]. Copyright © 2012 American Chemical Society. (e) Schematic of Lase zone annealing process. The heat is generated from the Ge layer via absorbing laser light.[25] Reprinted with permission from ref. [25]. Copyright © 2015 American Chemical Society.*

self-assembly of BCP thin films, our group proposed in 2010 that a research grade microwave oven could be used to anneal BCP thin films on silicon wafers.[100] BCP thin films on silicon wafer shards of known resistivities were sealed in a glass vial, with or without a solvent, and heated in a research grade microwave oven. Analysis of the resulting BCP structures clearly demonstrated that this microwave-assisted solvothermal annealing process dramatically decreased the observed defect density, and reduced the anneal time to only minutes (and, in many cases, to 1 minute).[100] It was demonstrated soon afterwards that an inexpensive domestic microwave oven could also be used to anneal the BCP films, which opened up the annealing technique to any lab.[21] This initial work was followed up by Morris and co-workers who demonstrated that microwave annealing could be applied to fabricate cylinder and perforated lamellar patterns on the order of minutes, also in a research grade microwave reactor, both with and without a solvent.[117, 118]

The mechanism of the microwave annealing process is, at present, disputed, and there are conflicting results that complicate interpretation. The role of the silicon wafer as a source of thermal heating has been questioned, with one group pointing to links between silicon wafer resistivity and annealing rates for the BCP self-assembled nanopatterns (and also to wafer heating evidenced by wax melting experiments),[21, 100] and another group categorically stating that silicon wafer heating cannot account for the observed annealing of BCPs.[117, 118] Further convoluting the matter, two papers showed opposing trends with respect to wafer resistivity and BCP annealing rates and defect densities.[21, 100] In all of the prior work, the *in situ* temperature of the substrate and polymer was not measured, since the research grade microwave ovens rely upon an infrared thermometer that measures the temperature of the glass vial in which the samples are contained, rather than directly measuring the sample temperature itself. There is no reason to assume that the temperature of the glass vial would be the same as a shard of a silicon wafer contained within, given the non-equilibrium, non-isothermal nature of the system, low thermal conductivity of glass, and the poor contact between the shard and the vial.[100, 117, 118] The domestic (kitchen) microwave

ovens are similarly hampered with respect to *in situ* temperature monitoring. BCP annealing is tantalizing in its rapidity and simplicity, but in order to effectively utilize the technique, optimize it, and generalize to different BCPs and substrates, the fundamentals of the mechanism of microwave annealing need to be detailed, deconvoluted, and fully understood. In this work, we use microwave-compatible fiber optic temperature probes to directly measure the temperatures of all the components within the microwave oven in real time. A fluorescence-based fiber optic temperature probe was selected on account of the small heat capacity (0.6 mm diameter with a polyimide tip), microwave compatibility, and fast response time. All materials were analyzed independently, and combined, and the results compared. We confirm the source of heating by decoupling the 'heating element' (those materials that heat up upon microwave irradiation) from the substrate, and we show that an independent microwave-susceptible heating element can be used for an arbitrary composition of BCP thin film and underlying substrate.

2.3 Methods

2.3.1 Materials

PS-*b*-P2VP (23.6k-10.4k, N_{PS}: 225, N_{P2VP}: 98, f_{P2VP} =0.30), PS-*b*-PMMA (45k-20k, N_{PS}: 429, N_{PMMA}: 200, f_{P2VP} = 0.28) and P2VP (154k) were purchased from Polymer Source Inc. Sodium tetrachloroplatinate (II) hydrate, $Na_2PtCl_4 \cdot xH_2O$, was obtained from Strem Chemicals. Concentrated HCl(aq), concentrated H_2SO_4 and acetone were obtained from Caledon Laboratories Ltd. H_2O_2, dichloromethane, PS (192k) and PMMA (120k) were obtained from Sigma-Aldrich. Toluene and isopropanol were obtained from Fisher Scientific. Silicon wafers (thickness: 525 $\pm$ 25 μm) were obtained from University Wafer and WRS Materials, glass substrates were ordered from Fisher Scientific (Catalog No.: 12-550-A3, 25 $\times$ 75 $\times$ 1.0 mm), and ITO-coated glass (sheet resistance: 8-12 Ω/sq) substrates were purchased from

Delta Technologies Ltd. Kapton film (PIT5N/12.7) was purchased from Caplinq.

2.3.2 Substrate Dicing and Cleaning

Silicon wafers were cut to the desired size with a dicing saw (Disco DAD 321). For dicing glass or ITO-coated glass, a Diamond Touch Cutting Saw was used.

Silicon and glass substrates were cleaned using piranha solution: samples were immersed into a 3:1 (v/v) mixture of concentrated sulfuric acid and 30 % hydrogen peroxide(aq) for 15 min, rinsed with ultra-pure water (18.2 MΩ·cm), and dried with a nitrogen stream. For ITO-coated glass pieces, successive 15-min ultrasonication steps in dichloromethane, ultrapure water and isopropanol were applied, and then the substrates were dried with a nitrogen stream. Kapton substrates were rinsed in toluene and acetone, and then dried with a nitrogen stream.

2.3.3 Block Copolymer Thin Film Preparation

Block copolymer powder was dissolved in toluene to make $\sim$1 % w/w solutions. These solutions were then stirred for at least thirty minutes, and then 15 μL volumes were dropped onto clean substrates and spin-coated at 3000 rpm for 15 s under an argon environment. The thicknesses of BCP thin films as determined by ellipsometry were generally $\sim$40 nm.

2.3.4 Microwave Annealing Procedure

Microwave annealing was performed in modified Panasonic microwave ovens (model number NNST651B, purchased from Walmart), using inverter technology to provide constant power, up to 1200 W, varying linearly with power setting, rather than a cycled pulses. A mortar with about 100 g SiC was placed in the left side of the

microwave oven to absorb excess microwave radiation and prevent damage to the microwave oven (Figure 2.2c). A fluorescence-based fiber optic temperature probe (model number PRB-G40-2.0M-ST-C with polyimide tip and calibration to 250 °C and accuracy of ±0.5 °C were obtained from OSENSA Inc.) was inserted through a small hole drilled in the microwave oven and Teflon chamber (see Figure 2.2a-b). Substrates coated with the BCP film and heating element (a high resistivity silicon shard: 1.5 × 1.5 cm^2, p-type, <100>, 525 ± 25 μm thickness, 8.4 Ω·cm) were put into a Teflon annealing chamber (Figure 2.2e-f). The BCP thin film coated substrates were placed on the heating element with the BCP thin film in between them and form a sandwich structure, as shown in Figure 2.2e and f. The chamber was sealed, power level 5 selected (∼600 W), and the microwave oven turned on manually. The microwave oven was manually turned off when the desired temperature was reached. The temperature was monitored and recorded until the wafer had cooled down to around 40 °C.

2.3.5 Metalization

For PS-*b*-P2VP films, a metalization step was employed to improve visualization by scanning electron microscopy (SEM). PS-*b*-P2VP films were immersed in an aqueous platinum salt solution (20 mM Na_2PtCl_4 and 0.250 M HCl) for three hours. The films were then removed from solution, rinsed with ultra-pure water, and dried under a nitrogen stream. The metalized PS-*b*-P2VP samples were then inserted in a Harrick Plasma Cleaner/Sterilizer PDC-32G and treated by oxygen plasma (0.6 Torr, 45 s) to etch the polymer film and to reduce Pt^{2+} to Pt metal. For PS-*b*-PMMA samples, a brief oxygen plasma step (0.6 Torr, 15 s) was used to increase contrast under SEM (Hitachi S-4800) at 15 kV, 20 μA and AFM (Digital Instruments/Veeco, tapping mode under ambient condition).

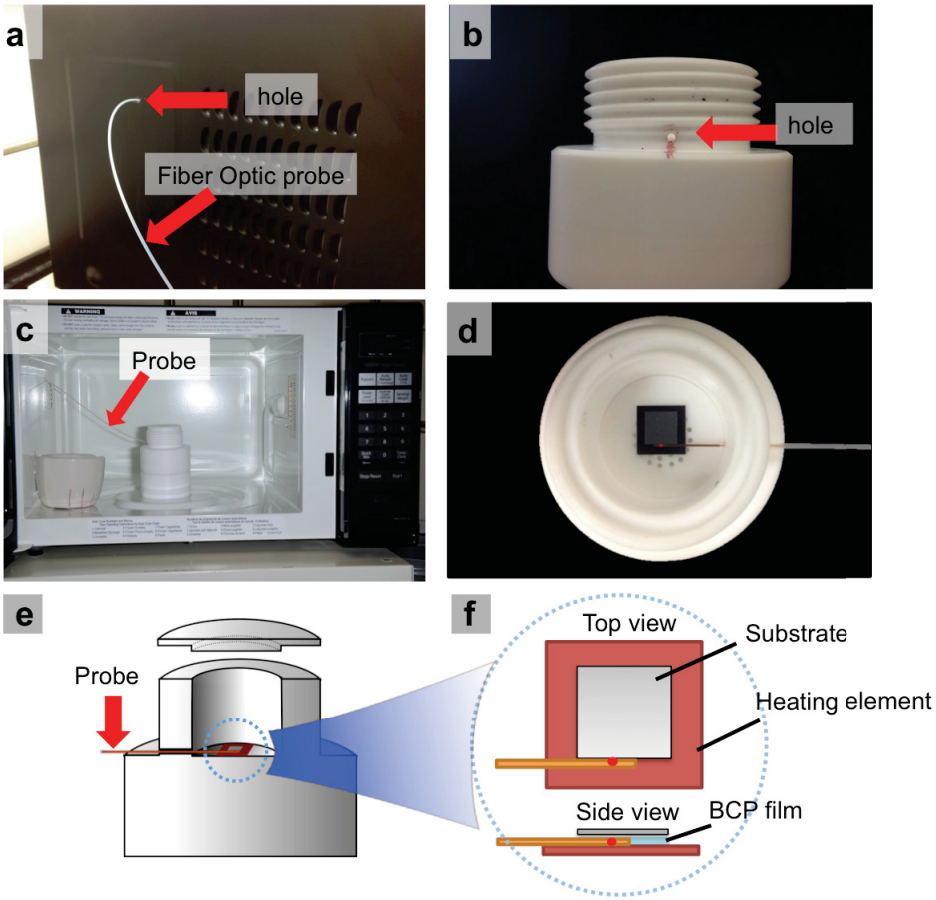

Figure 2.2: *(a) A photograph of the fiber optic probe extending through the back of the domestic microwave oven. (b) A photograph of the annealing chamber, illustrating the hole through which the fiber optic probe enters the chamber. (c) Photograph of the microwave annealing apparatus with a motor, an annealing chamber, and a fiber optic probe. (d) A photograph showing the interior of the annealing chamber with heating element, substrate and temperature probe. (e) Cross-section scheme of the annealing chamber with a sandwich structure and fiber optic probe inserted through the side. (f) Details of the sandwich structure for annealing, including the position of fiber optic probe. Reprinted with permission from ref. [26]. Crown copyright.*

2.4 Heating Profiles of Silicon Wafers in Microwave Irradiation

The fact that silicon wafers can absorb microwave radiation and generate heat has been known for many decades. In the 1980s, a specially designed microwave device (given the name "microwave drill") was created to melt silicon wafers in a spatially defined, localized fashion.[195] This work, and others, built upon the established observation that high resistivity silicon wafers heat more rapidly with microwave irradiation (frequency: 2.45 GHz,[21] 2.856 GHz,[195] and 28 GHz[196]) than low resistivity wafers.[21, 196] For BCP annealing, the relationship between silicon wafer resistivity and geometry, and the heating profiles during irradiation remain unknown. To examine the influence of the resistivity and dopant type over the temperature profile of silicon, wafers of similar thickness (525 $\pm$ 25 μm) but of different resistivities and doping (Table 2.1), were cut into 1.5 $\times$ 1.5 cm^2 pieces. Each silicon piece was placed in a Teflon chamber, and the fiber optic probe was placed in direct physical contact with the silicon for *in situ* monitoring (Figure 2.3). When the wafer temperature reached 200 $\pm$ 3 °C, or the annealing time reached 60 s, the microwave oven was turned off manually. A typical heating profile of a silicon piece (1 $\times$ 1 cm^2 in size, p-type, 525 $\pm$ 25 μm thickness, 6.2 Ω·cm) heated by the domestic microwave oven was plotted in Figure 2.4. The temperature of the silicon wafers did not change in the first 4 s, due to a 4 s lag required to activate the cavity magnetron after the microwave oven was turned on (Figure 2.4). After 4 s, silicon pieces would undergo an increase in temperature until the microwave oven was turned off manually (Figure 2.4).

Figure 2.5 showed heating profiles of 9 silicon chips listed in Table 2.1. High resistivity silicon pieces (ρ>0.6 Ω·cm) could reach 200 °C within 30 s of microwave irradiation, and with this resistivity (or higher), the silicon wafer pieces presented very similar heating curves. Low resistivity wafers ($\rho \leqq$0.6 Ω·cm) could not reach 200 °C with 60 s of microwave irradiation. The initial heating rates of each silicon

Table 2.1: *Resistivity and dopant composition of silicon wafer pieces used for the microwave heating experiments.*

ρ/Ω·cm	11.9	10.5	8.4	6.4	6.4	2.4	0.6	0.016	0.0041
Type	p	n	p	p	n	p	p	p	p
Dopant	B	P	B	B	P	B	B	B	B

piece were calculated from the first 7 s of heating (t = 4-11 s on the temperature profile plot of Figure 2.5), and the results displayed graphically in Figure 2.5b. As can be seen from Figure 2.5, the following trend is apparent: the heating rate increases with greater resistivity, and does not appear to be dependent upon the type of doping (n- and p-type dopants provided similar results).

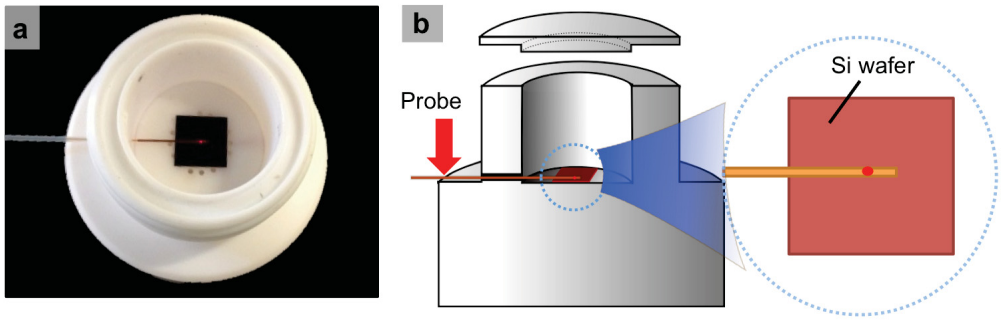

Figure 2.3: *(a) Photograph of the Teflon chamber with fiber optic probe and silicon wafer inside. (b) Cross-sectional drawing of the Teflon chamber with fiber optic probe and silicon wafer. The red dot on the probe is fluorescent ceramic material encased in 0.6 mm diameter polyimide sphere. Reprinted with permission from ref. [26]. Crown copyright.*

While not seemingly of interest, the relationship between wafer size and heating profile must also be understood, particularly with an eye on future scale-up. A 4-inch silicon wafer (p-type, 525 $\pm$ 25 μm thickness) with a resistivity of 6.2 Ω·cm was cut into 2.5 $\times$ 2.5 cm^2, 2 $\times$ 2 cm^2, 1.5 $\times$ 1.5 cm^2, 1 $\times$ 1 cm^2, and 0.5 $\times$ 0.5 cm^2 square pieces. When the wafer temperature reached about 200 $\pm$ 3 °C or the annealing time reached 60 s, the microwave oven was turned off manually.

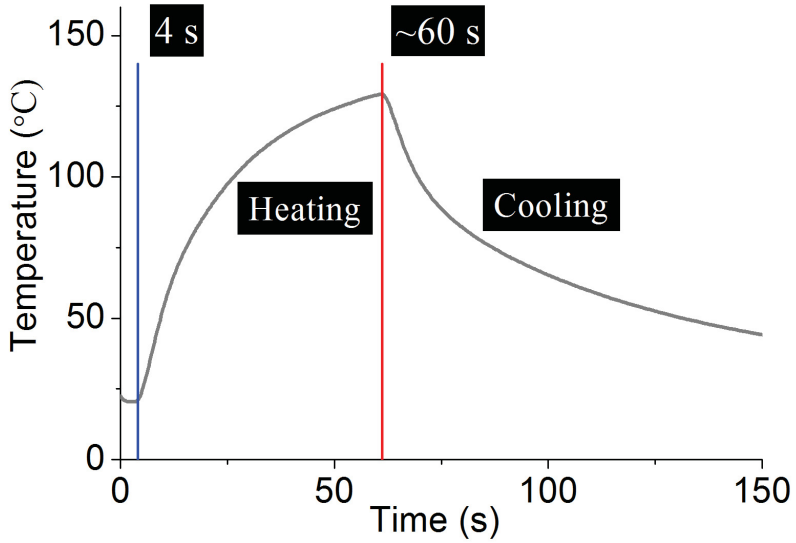

Figure 2.4: *Temperature profile of a 1 × 1 cm^2 silicon wafer shard (p-type, 525 ± 25 μm thickness, 6.2 Ω·cm) heated in a domestic microwave oven for ~60 s. Reprinted with permission from ref. [26]. Crown copyright.*

Table 2.2: *Initial heating rates for different silicon wafers (1.5 × 1.5 cm^2 in size) in the domestic microwave oven.*

Resistivity (Ω·cm)	Type	Heating Rate (°C/s)
11.9	p	16.36 ± 0.15
10.5	n	16.73 ± 0.99
8.4	p	18.83 ± 0.48
6.4	p	15.46 ± 0.22
6.4	n	19.67 ± 0.61
2.4	p	12.65 ± 0.39
0.6	p	5.58 ± 0.33
0.016	p	3.19 ± 0.22
0.0041	p	2.08 ± 0.19

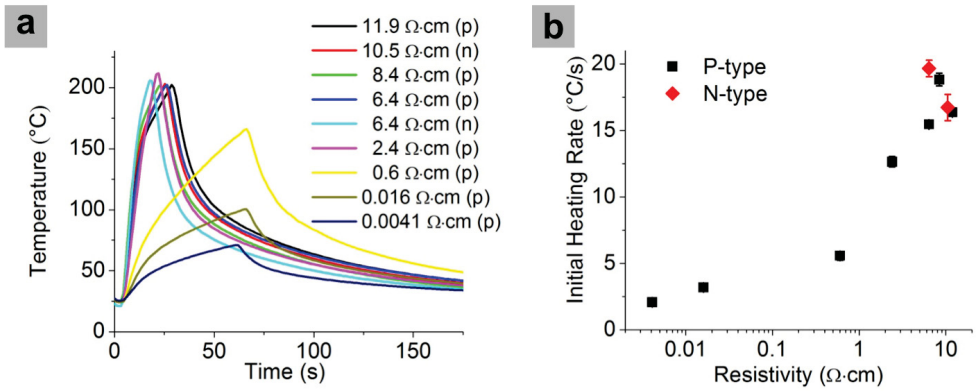

Figure 2.5: *(a) Temperature profiles of 1.5 × 1.5 cm^2 silicon pieces of different resistivities and doping types during microwave irradiation. (b) Plots of initial heating rate (obtained from 4 s to 11 s on each heating profile versus resistivity. Error bars (representing plus and minus one standard deviation) are present on all points in (b), but are mostly invisible (see Table 2.2). Reprinted with permission from ref. [26]. Crown copyright.*

The temperature of the silicon wafer piece was monitored until the temperature dropped to around 40 °C. Temperature profiles of these silicon pieces are plotted in Figure 2.6. The largest piece, the 2.5 × 2.5 cm^2 silicon shard, heated the fastest, reaching 200 °C at the 11 s mark. The 2 × 2 cm^2 sample was similar to the largest piece, reaching 200 °C at the 13 s mark. As the pieces became smaller, the time required to reach 200 °C increased, with the 1.5 × 1.5 cm^2 shard requiring 26 s. The smaller silicon pieces, 1 × 1 cm^2 and 0.5 × 0.5 cm^2, could not reach 200 °C within 60 s. The initial heating rates of each silicon piece were calculated using the temperature profiles from 4-11 s, and they are plotted in Figure 2.6b. This data suggests a linear increase in the initial heating rate as sample size increases from 0.5 × 0.5 cm^2 to 1.5 × 1.5 cm^2, that the linearity does not continue above this size (the rate of temperature increase appears to drop with larger sizes). This observation may point to a heat sink effect, or could be the result of greater likelihood of overlap between the sample and a "hotspot" in the microwave, which occurs at half the wavelength, or 6.1 cm, as sample position was consistent, but not optimized for

maximum heating rate. Samples larger than 2.5 × 2.5 cm^2 are not reported here because they exceed the size of the Teflon chamber.

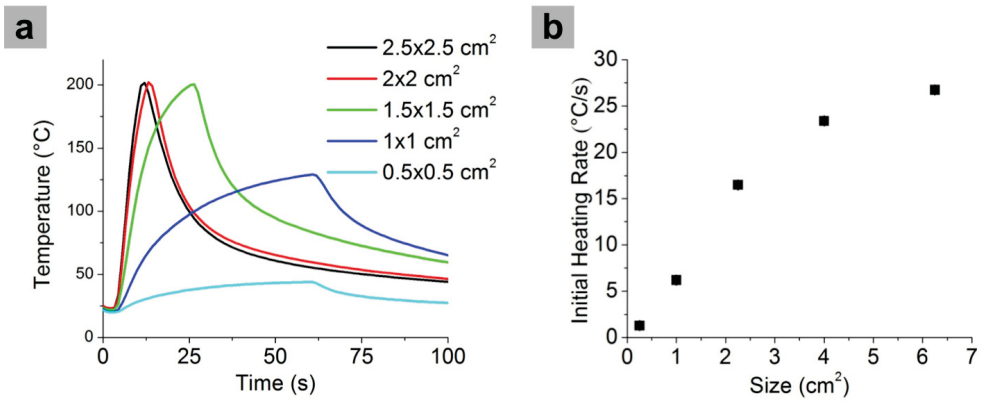

Figure 2.6: *Temperature profiles for different sizes of silicon pieces cut from one silicon wafer (p-type, 525 ± 25 μm thickness, 6.2 Ω·cm). (b) Initial heating rate of silicon pieces versus area, obtained from 4 s to 11 s on each heating profile. Error bars (representing plus and minus one standard deviation) are present on all points in (b), but are mostly invisible (see Table 2.3). Reprinted with permission from ref. [26]. Crown copyright.*

2.5 Heating Profiles of Homopolymers in Microwave Irradiation

It has been postulated that the BCP itself could heat up with microwave irradiation, and therefore act as the heat source that induces nanoscale phase segregation.[117] To understand whether either BCP block absorbs microwave radiation and induces local heating independent of the silicon substrate, five thick films (PS, P2VP, PMMA) and two mixtures (PS + P2VP and PS + PMMA) were drop cast onto low resistivity (p-type, 525 ± 25 μm thickness, 0.0044 Ω·cm, 1 × 1 cm^2) silicon substrates, as shown in Table 2.4. The weight ratios of homopolymers in the two

Table 2.3: *Initial heating rates of silicon pieces of different sizes cut from one silicon wafer (p-type, 525 ± 25 μm thickness, 6.2 Ω·cm).*

Size (cm^2)	Heating Rate (°C/s))
2.5 × 2.5	26.73 ± 0.17
2 × 2	23.39 ± 0.39
1.5 × 1.5	16.47 ± 0.38
1 × 1	6.19 ± 0.35
0.5 × 0.5	1.28 ± 0.11

blend films are close to the weight ratio in PS-*b*-P2VP and PS-*b*-PMMA used in this work. These silicon wafers had already been shown to maintain a relatively static temperature under these conditions. Each homopolymer film was placed in the center of the Teflon chamber in contact with the fiber optic temperature probe, and was irradiated in the microwave oven for around 60 s. The samples coated with homopolymers heated up to about 32 °C within ∼60 s of applied microwave power, which is far below their T_g (about 100 °C) and the temperature expected for successful annealing. Temperature profiles for each homopolymer on silicon, as well as control profiles for the silicon substrate without polymer and the fiber optic temperature probe without either silicon or polymer are plotted in Figure 2.7. Because the homopolymers are poor microwave absorbers, as is consistent with the low dielectric loss tangents for each material (PS, PMMA, P2VP, and also PDMS, Table 2.5),[197] they alone cannot absorb sufficient microwave energy to surpass T_g. The source of the heating must arise from the silicon substrate, if it has a sufficiently high resistivity.

Table 2.4: *Weight and thicknesses of homopolymer and blended films. Film thicknesses were measured with calipers (Mitutoyo Corp. Model: ID-C112EB, 12.7-0.001 mm).*

Homopolymer	Weight (g)	Thickness (mm)
PS	0.1372	2.4 ± 0.1
P2VP	0.1289	2.56 ± 0.06
PMMA	0.1172	1.64 ± 0.08
PS+P2VP[a]	0.2750	5.0 ± 0.2
PS+PMMA[b]	0.2845	4.9 ± 0.4

[a]PS: 70.1 % w/w, and P2VP: 29.9 % w/w.

[b]PS: 69.1 % w/w, and PMMA: 30.9 % w/w.

Table 2.5: *The dielectric constant and loss tangent of PS, P2VP, PMMA and PDMS at 3 GHz.*

Polymer	Dielectric Constant (relative to vacuum)	Loss Tangent
PS	2.55	0.0049
P2VP	2.98	0.0135
PMMA	2.6	0.0057
PDMS	2.65	0.0068

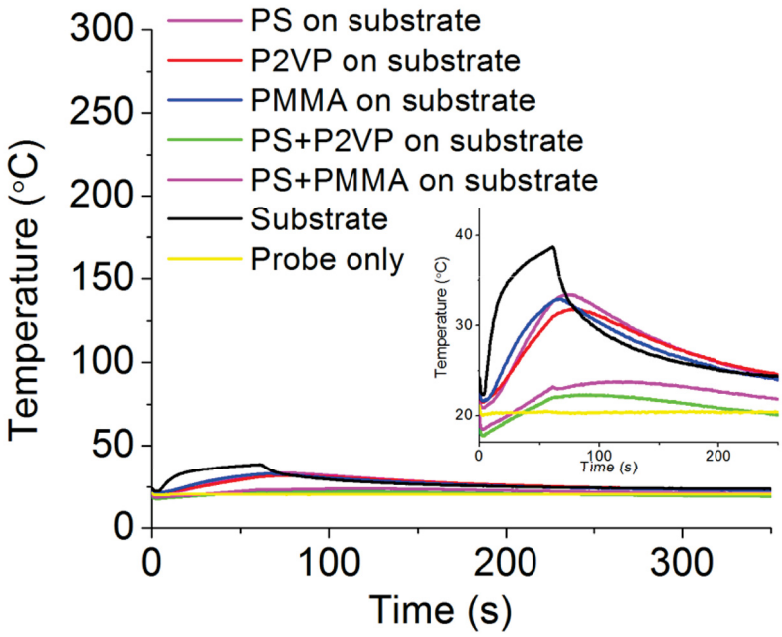

Figure 2.7: *Temperature profiles during microwave irradiation for three thick homopolymer films on low resistivity silicon substrates (0.0044 Ω·cm), two thick polymer blend films also on low resistivity substrates, and control samples of an uncoated substrate and a fiber optic temperature probe. The inset is the same temperature data with a different scale on the y-axis. Reprinted with permission from ref. [26]. Crown copyright.*

2.6 Annealing Block Copolymer Thin Films on Silicon Substrates and Defect Analysis

Since it was determined that the silicon substrate was the source of heating upon microwave irradiation, separate materials were used as microwave heating elements and BCP substrates, as shown schematically in Figure 2.2. The heating element is thus decoupled from the BCP thin film on the substrate , which allows for microwave annealing on any substrate material, including those that are irresponsive to microwaves. To demonstrate this concept, a 1.5 $\times$ 1.5 cm^2 silicon wafer (p-type, <100>, 525 $\pm$ 25 μm thickness, 8.4 Ω·cm) was chosen as the heating element. Figure 2.8 showed that the heating element had great reproducibility in microwave irradiation with all four trials reaching 200 °C at 23 s. Low resistivity silicon wafers (0.0044 Ω·cm) were used as substrates and spin-coated with $\sim$1 % w/w toluene solutions of PS-*b*-P2VP (23.6k-10.4k, PDI = 1.04) and PS-*b*-PMMA (45k-20k, PDI = 1.07) to form thin films about 40 nm in thickness, as measured by ellipsometry. The BCP-coated substrates were then placed on the 1.5 $\times$ 1.5 cm^2 silicon heating element with the BCP thin film between them, forming a sandwich structure (see Figure 2.2). The fiber optic temperature probe was installed in the Teflon chamber and placed in contact with the silicon heating element. During microwave annealing, the microwave oven was again turned off manually once a certain predefined temperature was obtained. With BCP thin film coated sample on top, the heating rate was about 7 s slower in reaching 200 °C than that of the heating element without BCP thin film coated sample (23 s) (Figure 2.9). The temperatures at which the microwave heating was shut off ranged from 160 °C to 240 °C. As control experiments, substrates with the same BCP thin films but no heating element were microwave annealed for 60 s. In those experiments where PS-*b*-P2VP was employed, the annealed BCP template was converted to Pt patterns to improve contrast for SEM imaging.[11, 14, 198] Annealed PS-*b*-PMMA samples required only a brief oxygen plasma treatment to remove part of the PMMA block

to aid visualization by SEM.[108, 144]

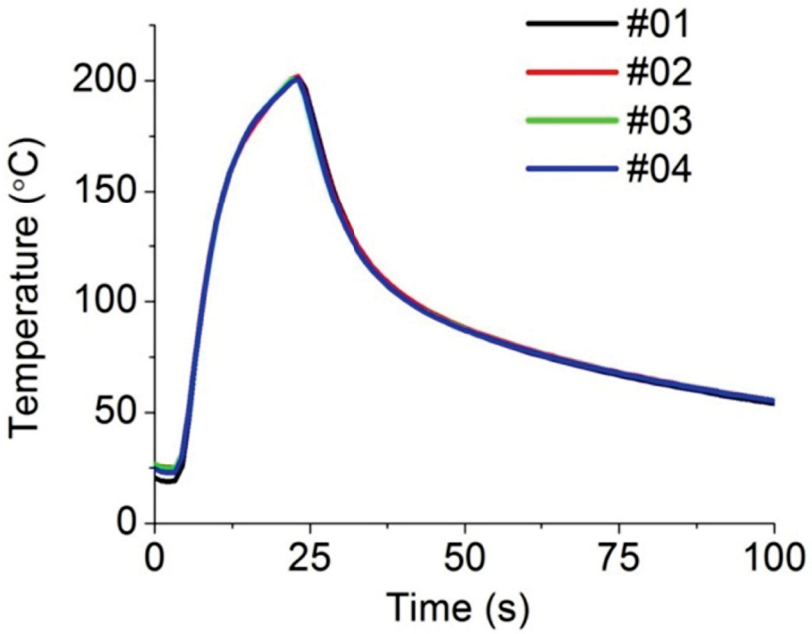

Figure 2.8: *Temperature profiles of the heating element (1.5 × 1.5 cm^2, p-type, <100>, 525 ± 25 μm thickness, 8.4 Ω·cm) used in this work, repeated four times to demonstrate reproducibility. Reprinted with permission from ref. [26]. Crown copyright.*

Figures 2.10 and 2.11 show the SEM micrographs of Pt nanopatterns prepared from PS-*b*-P2VP and PS-*b*-PMMA self-assembled thin films, respectively, annealed at different temperatures. Temperature profiles corresponding to the images in Figures 2.10a-g and 2.11a-g are also provided in Figures 2.10h and 2.11h. Silicon wafers that heat to no appreciable extent upon microwave irradiation (p-type, 1 × 1 cm^2, <100>, 525 ± 25 μm thickness, 0.0044 Ω·cm) were used as substrates for PS-*b*-P2VP and PS-*b*-PMMA thin films (∼40 nm). As can be seen in Figure 2.10b, without the heating element, the BCP is essentially unchanged after 60 s of microwave irradiation as compared to the unannealed sample in Figure 2.10a because the temperature did not exceed 50 °C (Figure 2.10h). With the heating

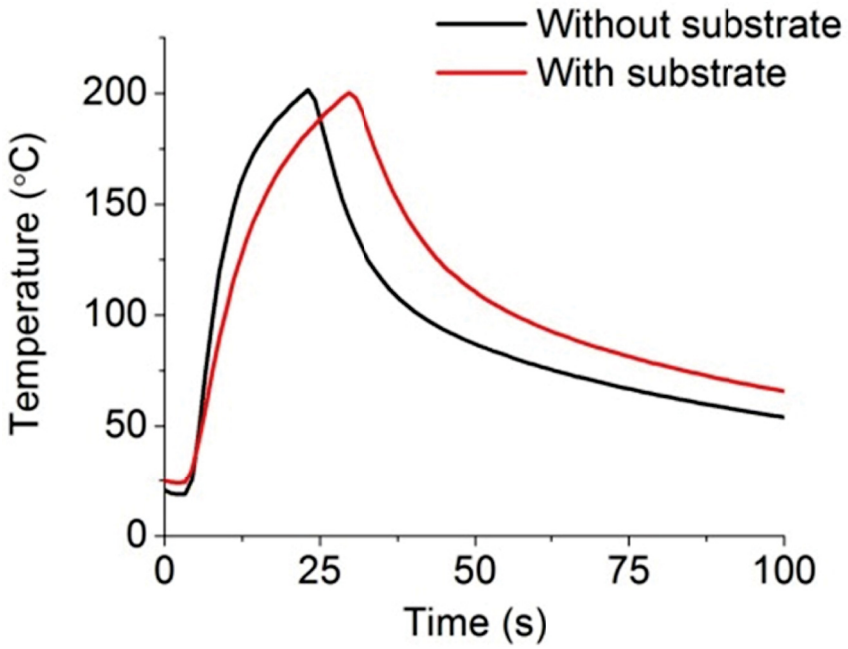

Figure 2.9: *Temperature profiles of the heating element (1.5 × 1.5 cm^2, p-type, <100>, 525 ± 25 μm thickness, 8.4 Ω·cm) with and without a PS-b-P2VP coated substrate (1 × 1 cm^2, p-type, <100>, 525 ± 25 μm thickness, 0.0044 Ω·cm). Reprinted with permission from ref. [26]. Crown copyright.*

element in contact with the microwave-irresponsive heavily-doped silicon substrate, increased ordering of the horizontal cylinders can be seen upon increasing the maximum attained temperature from 160 °C to 240 °C (Figures 2.10c-e). Similar results are observed for the PS-*b*-PMMA films (Figure 2.11). The presence of a heating element results in formation of better ordered horizontal cylinder patterns when the temperature is increased from 160 °C to 240 °C (Figure 2.11g).

Defect density analysis of annealed BCP thin film samples was carried out with the method described in our previous paper.[100] Briefly, a SEM micrograph taken from a BCP sample was manually smoothed and converted to binary image to facilitate automatic defect density analysis (Figure 2.12a-b). Then defects, such as junctions, terminals, and dots, were identified and counted (Figure 2.12c). The defect density of the PS-*b*-P2VP and PS-*b*-PMMS samples shown in Figure 2.10 and 2.11 were calculated and plotted in Figure 2.13. The plots show that the defect density decreases exponentially with maximum annealing temperature. For PS-*b*-P2VP, an ordered pattern with a defect density of 17.6 $\pm$ 1.5 pairs/μm^2 could be obtained by reaching an annealing temperature of 240 °C, which corresponds to 41 s of microwave irradiation. However, the defect densities of PS-*b*-PMMA samples could only be decreased to 49.8 $\pm$ 10.0 pairs/μm^2 when annealed to 240 °C in 43 s. These values exceed the level suggested by the ITRS for commercialization,[199] but are in line with other results obtained without control of orientation (ie, graphoepitaxy) that have been reported in the literature.[100, 119] The annealing process, at this point, is entirely unoptimized, as it is performed on a neutral surface without graphoepitaxy, and modifications, such as tuning of surface properties, would be expected to reduce defect densities further.[100, 170, 200] In addition, more sophisticated heating profiles could be designed to maintain the temperature above T_g, or to carry out multiple rapid anneals to 'exercise out' defects through programmed heating and cooling cycles. One variable that was not specifically controlled is the length of time the BCP films are held above the T_g, as represented by Figure 2.14. Time above T_g refers to the length of time each BCP thin film was above its T_g, as tabulated in Table 2.6. As expected, the time at and above the T_g

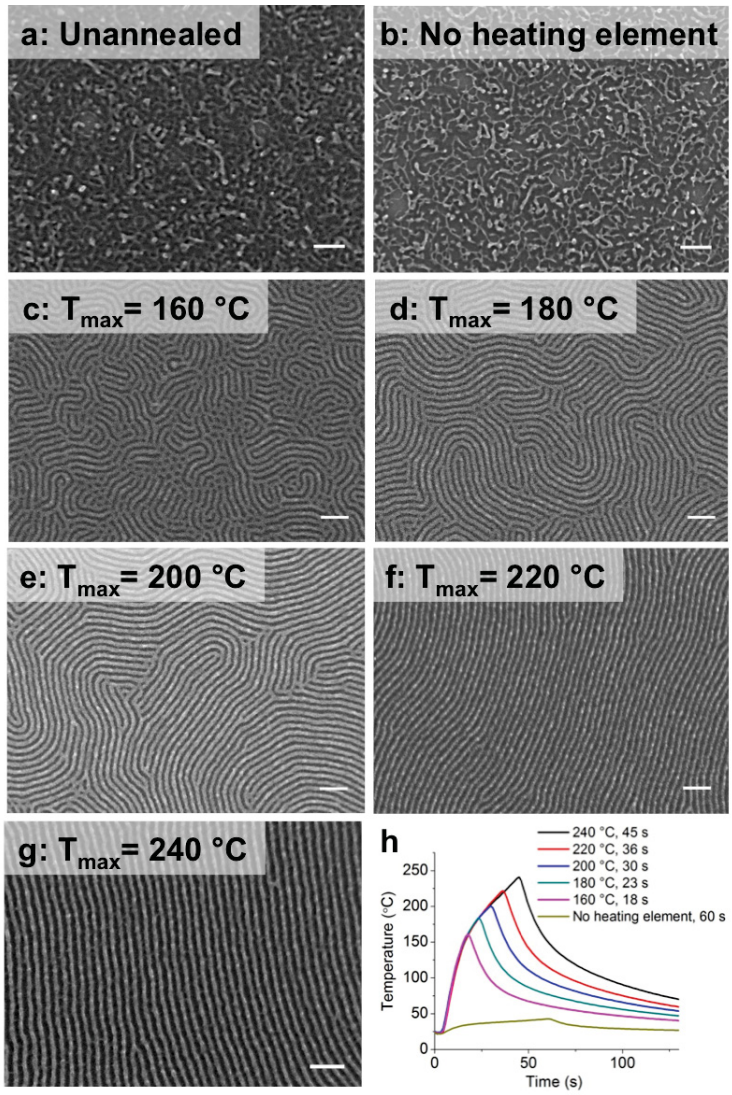

Figure 2.10: *Influence of the temperature of the heating element on the morphology of the PS-b-P2VP thin film. (a) SEM micrograph of Pt features produced using an unannealed PS-b-P2VP thin film for comparison. (b) SEM micrograph of Pt features produced from PS-b-P2VP thin films heated in microwave oven for 60 s without a heating element. (c-g) SEM micrographs of Pt features produced from PS-b-P2VP thin films that had been annealed to 160 °C, 180 °C, 200 °C, 220 °C, and 240 °C, respectively. (h) The temperature profiles for each of these samples. All scale bars are 100 nm. Reprinted with permission from ref. [26]. Crown copyright.*

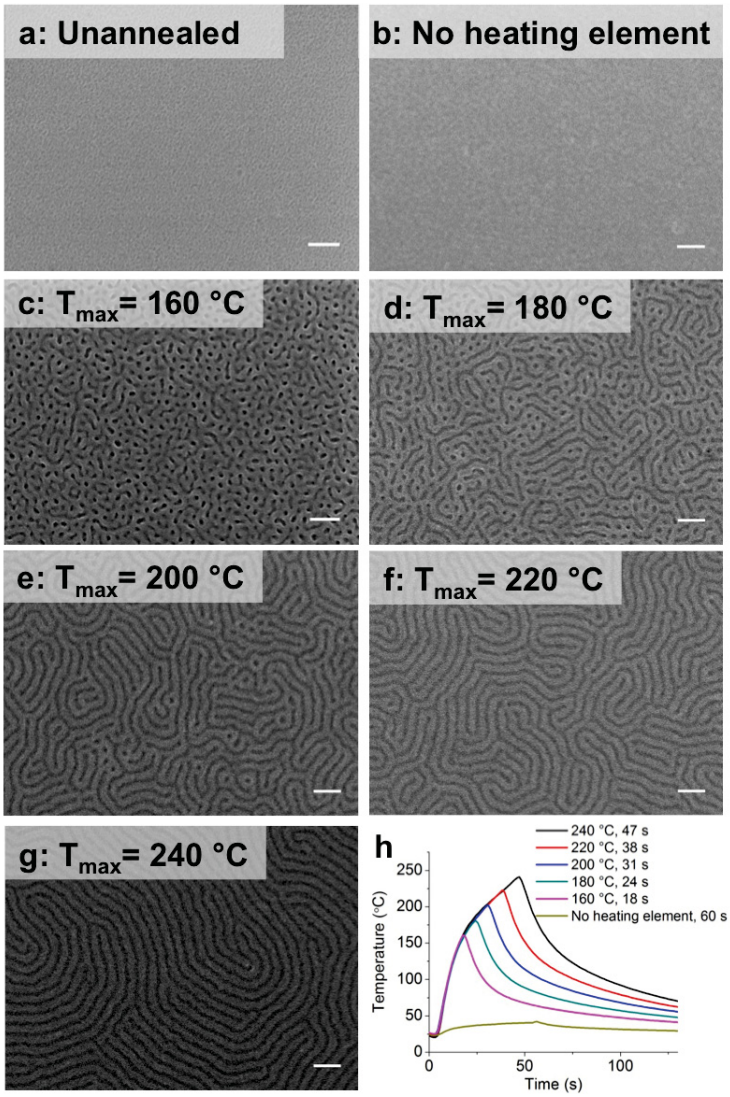

Figure 2.11: *Influence of annealing temperature with and without the heating element on the morphology of the PS-b-PMMA thin film. (a) SEM micrograph of unannealed PS-b-PMMA thin film. (b) SEM micrograph of PS-b-PMMA thin film heated in microwave oven for 60 s without heater. (c-g) SEM micrographs of PS-b-PMMA thin films annealed to 160 °C, 180 °C, 200 °C, 220 °C, and 240 °C, respectively. (h) The temperature profiles for each of these samples. All scale bars are 100 nm. Reprinted with permission from ref. [26]. Crown copyright.*

increases with an increase in the maximum annealing temperature. Controlling the length of time the sample spends above T_g is an important variable that is the subject of future work.

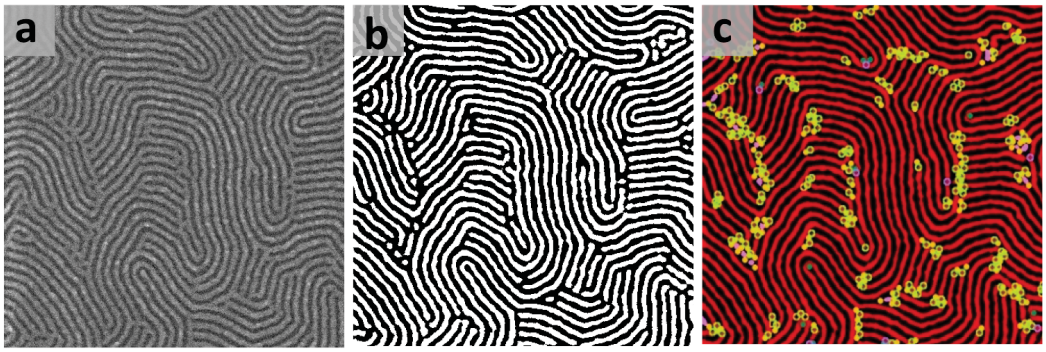

Figure 2.12: *(a) Original SEM micrograph of Pt nanostructures derived from a PS-b-P2VP thin film template. (b) Binary image converted from (a) to facilitate defect density analysis. (c) Image processed using the defect density analysis algorithm. Each material and defect type is indicated by a different color symbol: Pt wires, black; PS wires, red; Pt dots, magenta; junctions of Pt wires, yellow; Terminal points of Pt wires, green; junctions of PS phase, blue; terminal points in PS phase, open yellow-green circles. Reprinted with permission from ref. [26]. Crown copyright.*

Table 2.6: *Time spent above T_g for PS-b-P2VP and PS-b-PMMA thin films on heavily-doped silicon wafer shards annealed to different temperatures.*

T_{max}/ °C		240	220	200	180	160
Time (T_g to T_g)/s	PS-*b*-P2VP	79.9	60.3	46.4	31.2	18.9
	PS-*b*-PMMA	87.2	71.1	53.9	35.6	20.7

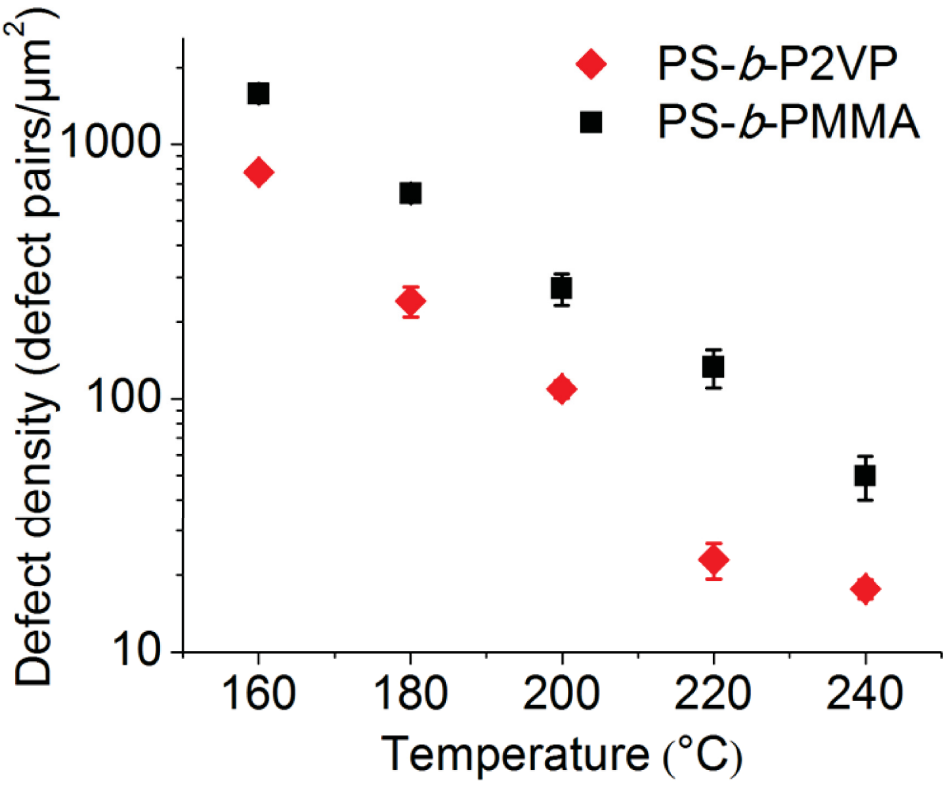

Figure 2.13: *Plot of defect density versus peak annealing temperature for PS-b-P2VP and PS-b-PMMA thin films. Reprinted with permission from ref. [26]. Crown copyright.*

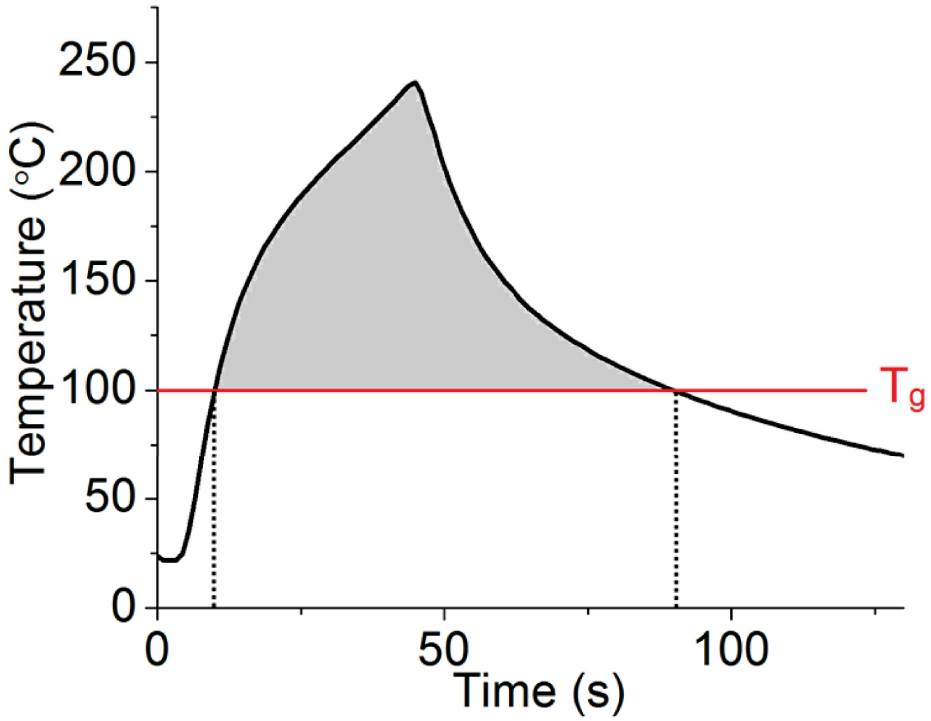

Figure 2.14: *Black line: heating profile for a PS-b-P2VP sample on a low resistivity silicon substrates (0.0044 Ω·cm). Red line: T_g of PS-b-P2VP. The gray area: the time above T_g experienced by the PS-b-P2VP sample. Reprinted with permission from ref. [26]. Crown copyright.*

2.7 Annealing Block Copolymer Thin Films on Non-Silicon Substrates

Because the heating element is decoupled from the BCP thin film (on its own substrate), the use of the heating element should enable the microwave assisted annealing of BCP thin films on non-silicon substrates, such as ITO-coated glass, glass, and Kapton. 40 nm thick PS-*b*-P2VP and PS-*b*-PMMA thin films was coated on ITO-coated glass, glass, and Kapton and heated to 240 °C. The temperature profiles for these three substrates are shown in Figures 2.15 and 2.16 for PS-*b*-P2VP and PS-*b*-PMMA, respectively. As seen in Figures 2.17 and 2.18, BCP thin film annealing and self-assembly is successful on ITO-coated glass, glass, and Kapton, when using the heating element configuration, since the temperature rapidly exceeds the polymer T_g. The ITO-coated glass, glass, and Kapton were cut into 1 × 1 cm^2 pieces in size, and PS-*b*-P2VP and PS-*b*-PMMA thin films (∼40 nm) were spin-coated on these clean substrates in the same fashion as described earlier for silicon surfaces. The temperature of PS-*b*-P2VP thin films on ITO-coated glass reached 45 °C after ∼60 s of microwave irradiation without the heating element, while the glass and Kapton showed no apparent change in temperature (dashed curves in Figures 2.15 and 2.16).

Table 2.7: *Time spent above T_g for PS-b-P2VP and PS-b-PMMA thin films on ITO-coated glass, glass, and Kapton annealed to 240 °C.*

Substrate		ITO-coated glass	Glass	Kapton
Time (T_g to T_g)/s	PS-*b*-P2VP	115.1	90.4	76.8
	PS-*b*-PMMA	113.1	95.7	81.6

The BCP thin film samples were then placed on the same heating element as described previously (1.5 × 1.5 cm^2, p-type, <100>, 525 ± 25 μm thickness, 8.4 Ω·cm). Three PS-*b*-P2VP samples were annealed to 240 °C with a heating element, and the results are shown in Figures 2.17a-c. The corresponding temperature

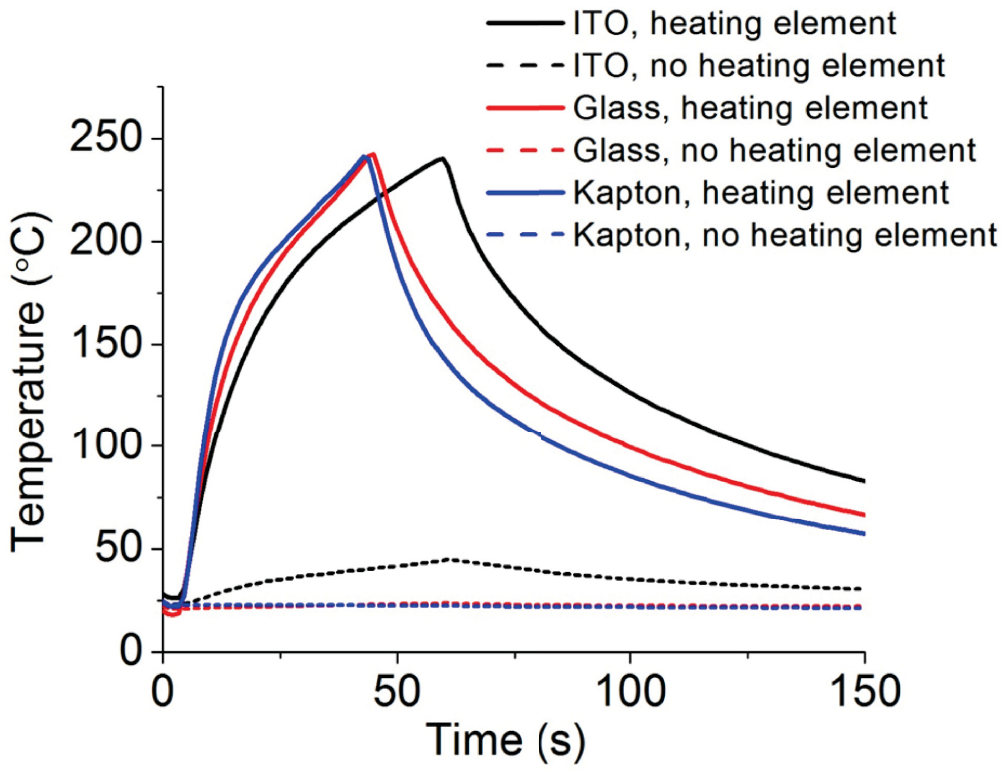

Figure 2.15: *Temperature profiles of PS-b-P2VP thin films coated on ITO-coated glass, glass, and Kapton annealed with and without heating element. Reprinted with permission from ref. [26]. Crown copyright.*

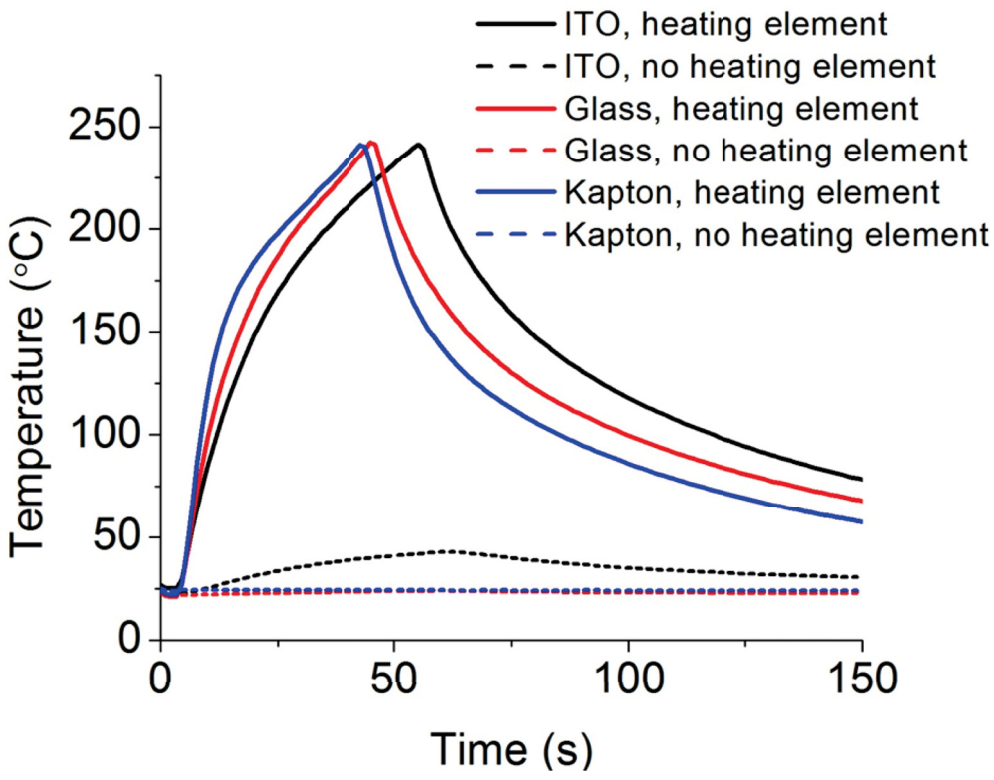

Figure 2.16: *Temperature profiles of PS-b-PMMA thin films coated on ITO-coated glass, glass, and Kapton annealed with and without heating element. Reprinted with permission from ref. [26]. Crown copyright.*

profiles are shown in Figure 2.15. It takes ~20 s longer for PS-*b*-P2VP thin film on ITO-coated glass to reach 240 °C comparing to that of PS-*b*-P2VP films on glass and Kapton (45 s). The time above T_g for the PS-*b*-P2VP thin film coated on ITO-coated glass is longer than that of films on glass and Kapton (Table 2.7). Without the heating element, the appearance of BCP films on ITO-coated glass, glass, and Kapton (Figure 2.17d-f) are not changed after 60 s of microwave irradiation, compared to unannealed samples (Figure 2.17g-i).

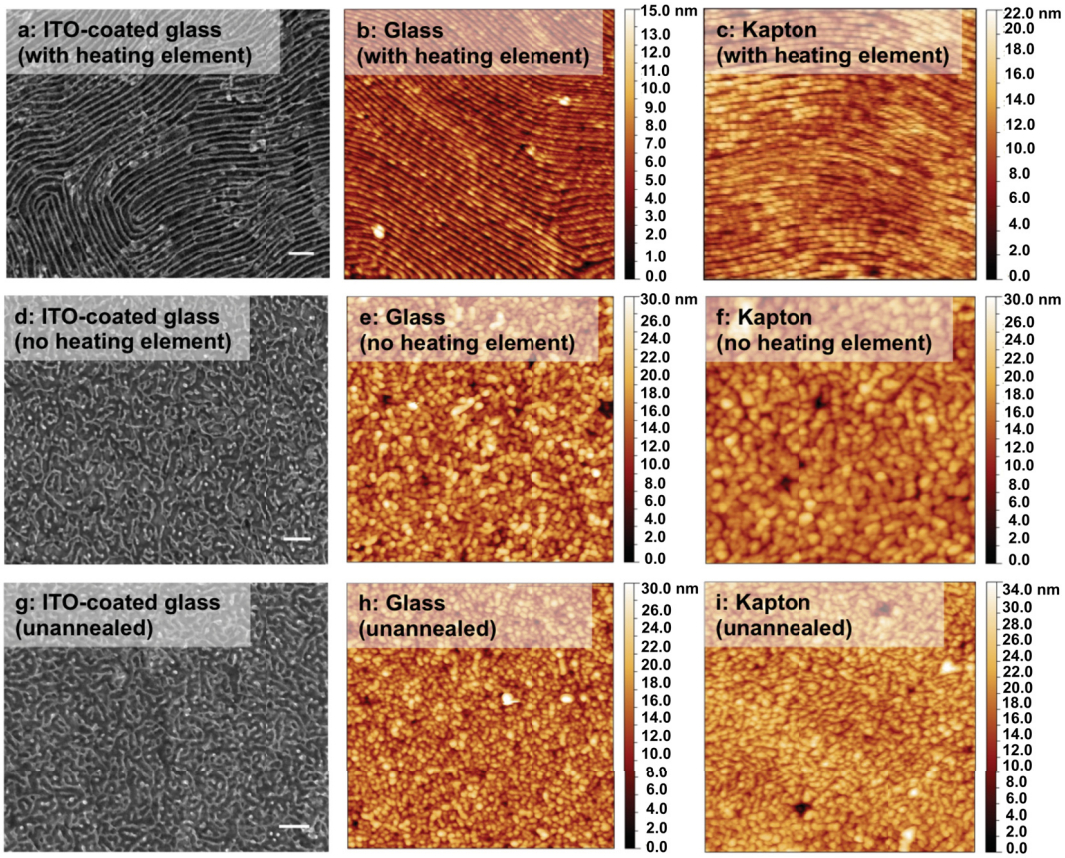

Figure 2.17: *SEM micrographs and AFM micrographs of Pt features prepared from PS-b-P2VP thin films annealed with and without a heating element, and unannealed PS-b-P2VP thin films on ITO-coated glass, glass, and Kapton. All scale bars are 100 nm. The sizes of AFM micrographs are all 1 × 1 μm^2. Reprinted with permission from ref. [26]. Crown copyright.*

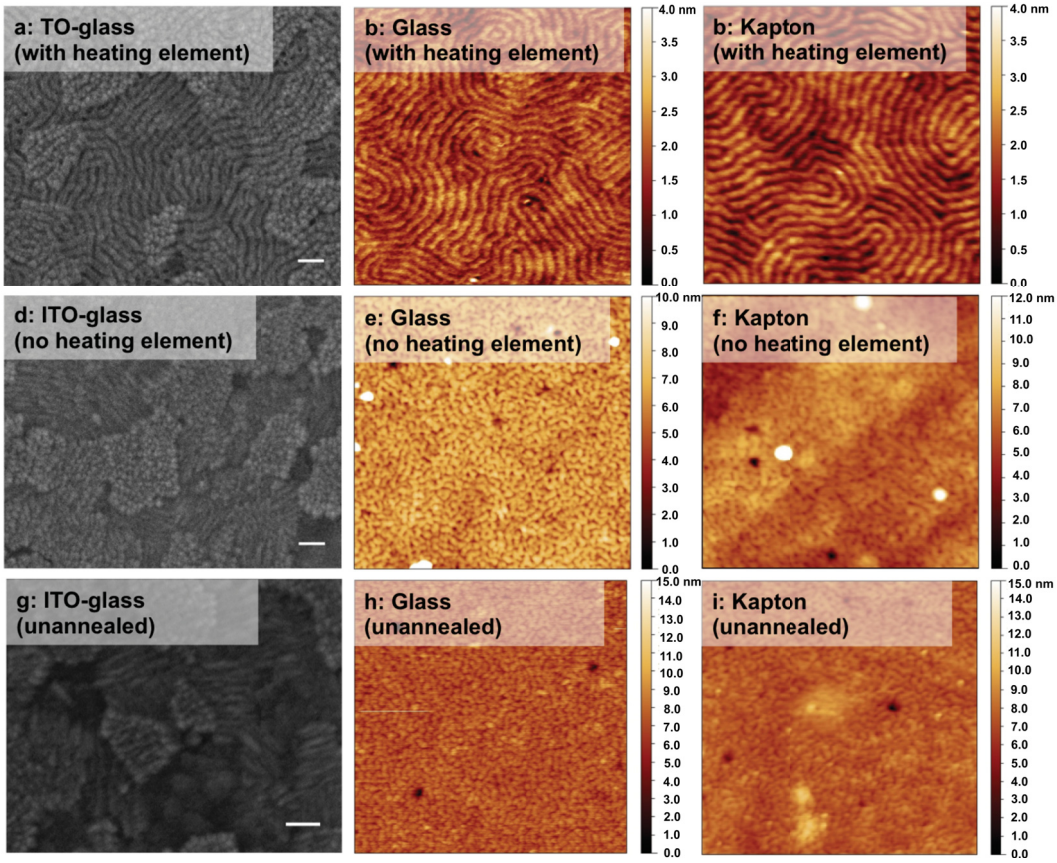

Figure 2.18: *SEM micrographs and AFM micrographs of PS-b-PMMA thin films annealed with heater, without heater and unannealed PS-b-PMMA thin films on ITO-coated glass, glass, and Kapton. All scale bars are 100 nm. The sizes of AFM micrographs are all 1 × 1 μm^2. Reprinted with permission from ref. [26]. Crown copyright.*

Similar results were obtained for PS-*b*-PMMA thin film samples as shown in Figure 2.18; the corresponding temperature profiles are shown in Figure 2.16. Samples were annealed to 240 °C with a heating element, and images of the annealed films are shown in Figures 2.18a-c. About 60 s were required for PS-*b*-PMMA thin films on ITO-coated glass to reach 240 °C, which is about 10 s longer than that of a PS-*b*-PMMA thin film on glass or Kapton (about 45 s). The time above T_g for the PS-*b*-PMMA thin film on ITO-coated glass was also longer than that on glass or Kapton (see Table 2.7). Small regions of a perforated lamellar structure were observed with a PS-*b*-PMMA thin film on ITO-coated glass (Figure 2.20), due to its high surface roughness (Figure 2.19).

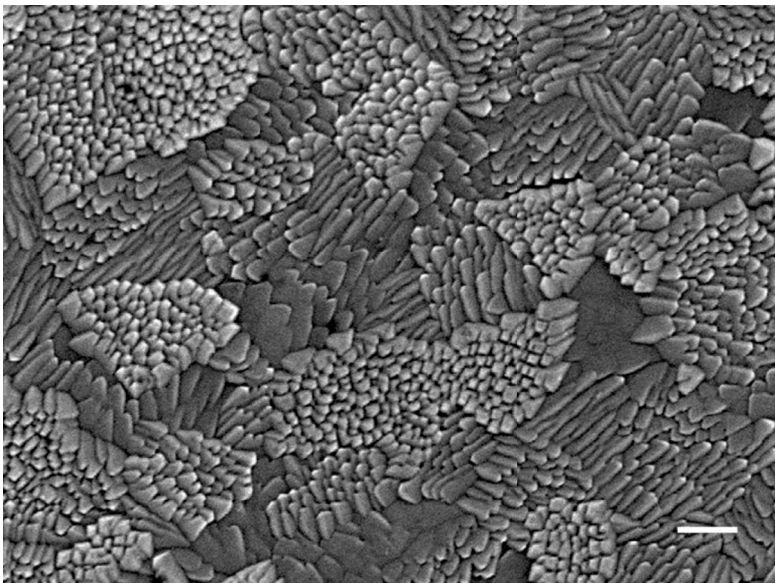

Figure 2.19: *SEM micrograph of clean ITO surface on ITO-coated glass. Scale bar is 100 nm. Reprinted with permission from ref. [26]. Crown copyright.*

2.8 Discussion

To summarize, BCP thin films can be rapidly annealed using microwave irradiation, and this annealing effect appears to be due to heating of a microwave-responsive

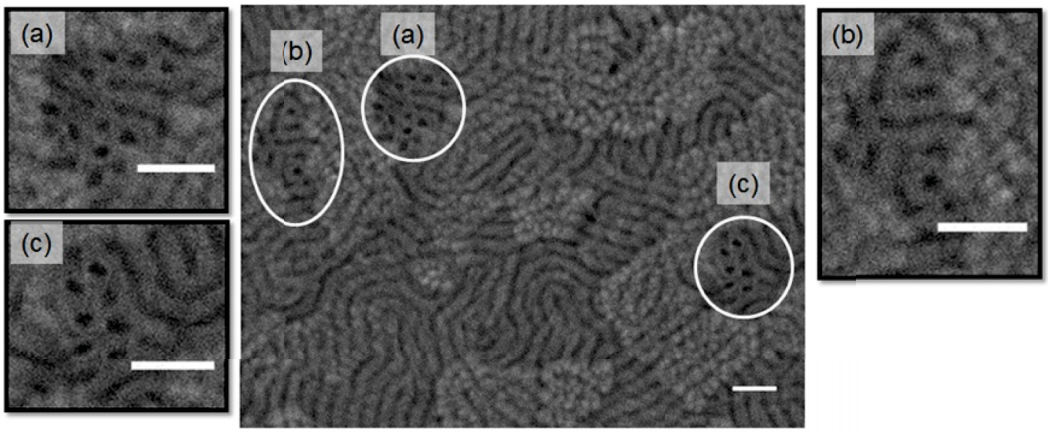

Figure 2.20: *SEM micrographs of perforated lamellar structure observed in PS-b-PMMA thin film on ITO-coated glass. All scale bars are 100 nm. Reprinted with permission from ref. [26]. Crown copyright.*

material with which the sample is in contact. The proposal that a non-thermal microwave effect, possibly related to changes in local electromagnetic fields during the anneal,[191] is responsible for the annealing effect, is implausible, as all available data points to rapid heating of the substrate/heating element under the influence of microwave irradiation as a driving mechanism. In the first report of BCP annealing by our group (2010), it was concluded that defect densities of the resulting BCP samples were lower for low resistivity silicon substrates,[100] which is the opposite of what we observed here. The second report in 2011 showed the opposite effect: high resistivity, faster-heating silicon led to better annealing in a domestic microwave oven, which is what we observe in this work.[21] In this 2011 report, *in situ* melting of paraffin wax experiments demonstrated the relationship between substrate resistivity and thermal output, in some cases even leading to the vaporization of the wax.[21] Finally, there are reports by others that have suggested that heating contributions from the substrate are insignificant, and do not contribute to the annealing process.[117, 118] The discrepancy of results arises, we believe, from the following. In our 2010 paper, sealed glass vessels were used in a research grade microwave reactor, and the programmed temperature profile has an unknown

relationship with the temperature of the wafer contained within.[100] In a research grade microwave reactor, the temperature is measured at the external surface of the glass vial using infrared thermometer, and therefore, it does not necessarily reflect the temperature of objects inside the vial. The research grade reactor also uses a temperature-feedback loop to control the microwave power output. The controller decreases microwave power as the surface temperature of the vial, which in the 2011 paper was in direct thermal contact with the solvent, approaches its target.[21] It must be remembered that the presence of solvent leads to defect densities that are at least one, and in many cases, several orders of magnitude lower than without solvent.[21, 100] When samples are exposed to solvent, the annealing is termed solvothermal, and is a more complex system than simple thermal annealing due to accompanied swelling of the BCP film. In the 2011 microwave paper, a domestic kitchen microwave was used, and the samples were sealed in a Teflon chamber with warm THF.[100] Due to high vapor pressure, the BCP film (on a lightly doped silicon substrate: 10-20 Ω·cm) most likely underwent immediate swelling with solvent after it was placed in the chamber, but before microwave heating could be commenced manually. We conclude that this solvothermal approach is, in fact, a two-stage solvent and thermal annealing process, that begins with solvent annealing, and is followed by solvothermal annealing. While it needs to be determined, the heating of a BCP film swollen with solvent to $T > 200$ °C may completely expel the low-boiling point solvent, at which point the annealing transitions to a predominately thermal process. Parallels may be made to the sequential solvent and thermal annealing process recently described by Kim and co-workers,[126] and by Gotrik and Ross.[22]

2.9 Conclusion

The mechanism of microwave-driven annealing of BCPs to enable self-assembly into nanoscale patterns on surfaces has been elucidated. In this work, it was

demonstrated through use of *in situ* temperature probes in direct contact with the sample surface that the underlying silicon substrate is the key to the rapid heating observed. Lightly doped silicon wafers can reach temperatures in excess of 200 °C in seconds, whereas the BCPs themselves do not heat to any significant extent. The critical role of the silicon wafer was proven by carrying out microwave-induced BCP annealing on non-microwave responsive materials such as glass and Kapton plastic; in this case a separate piece of lightly doped silicon that does rapidly heat with microwave irradiation, termed the heating element, can be used to heat the BCP film and bring about annealing. Because the heating element can be decoupled from the substrate on which the BCP film self-assembly takes place, microwave annealing can thus be considered as a general approach, and may permit spatially defined local heating through the use of a patterned heating element.

3

Solvent Vapor Flow Annealing of Block Copolymer Thin Films

In this chapter, we describe a controlled solvent vapor flow annealing system with integrated *in situ* microscopy and laser reflectometry, as well as a feedback loop that automatically controls the solvent vapor flow rate, based upon real-time calculations of the difference between thickness set point and the observed film thickness. The feedback loop enables precise control of swelling/deswelling of the polymer thin film, the degree of swelling at the dwell period, and preprogrammed complex multi-step annealing processes. The *in situ* microscope provides critical insights into the microscopic morphological evolution of the block copolymer (BCP) thin films during annealing process. This device could be a powerful tool for understanding and optimizing solvent annealing by providing multiple sources of *in situ* information, at both the micro- and nanoscales.

3.1 Apparatus for Solvent Vapor Annealing

As was discussed in Chapter 1, solvent vapor annealing is a versatile annealing method in BCP self-assembly research. A varieties of non-equilibrium, metastable phases could be obtained from the same BCP by changing a annealing solvent, the annealing solvent compositions, and the degree of swelling.[122, 178, 201] In addition, high molecular weight or high-χ BCPs, which are difficult to be thermally annealed due to poor chain mobility, can be annealed *via* solvent vapor annealing approach.[23, 126] Although solvent vapor annealing has been used for almost two decades, there is no standard annealing apparatus or setups, meaning that reproducibility and comparison of results may be difficult.[128] There are three main categories that define the methods for carrying out solvent vapor annealing, shown in Figure 3.1.

The simplest incarnation of the solvent annealing system is a static annealing method that uses a sealed chamber containing a solvent reservoir and the sample of a polymer thin film-on-substrate, held at room temperature, with no additional controls over temperature. This method, termed static or "jar" annealing, is effective, and with practice, can be used to produce self-assembled thin films of BCPs, albeit in a mostly empirical manner (Figure 3.1a). Early versions comprised a beaker or crystallization dish with a flat glass cover, enclosing a vial of solvent and the sample.[34, 129, 130] More recent versions of the static solvent vapor annealing apparatus use a custom-designed chamber with a transparent window that allows for *in situ* ellipsometry or reflectometry to monitor the film thickness during the annealing process, shown in Figure 3.4.[28, 34, 130, 178, 186, 201] The annealing chamber volume, surface area of solvent reservoir, and leakage of solvent vapor annealing chamber all influence the swelling speed and final degree of swelling, and thus *in situ* analysis is critical for reproducibility and to study intermediate degrees of swelling. This type of annealing apparatus has no direct control over the swelling rate during the annealing, and since solvent

vapor annealing is very sensitive to humidity and room temperature fluctuations, precise reproducibility becomes difficult. The annealing results may, therefore be influenced by gross parameters such as the weather, room temperature fluctuations, and seasonal building temperature changes. Figure 3.2 shows two swelling profiles and room temperature profiles during annealing process.[28] The film thickness was obtained *via in situ* ellipsometry. It clearly shows that the BCP film swells when room temperature decreases, and deswells when room temperature increases. In addition, we have found noticeable effects due to heating of the building during the spring and fall, when outside temperatures fluctuate on either side of what is considered 'room temperature'.

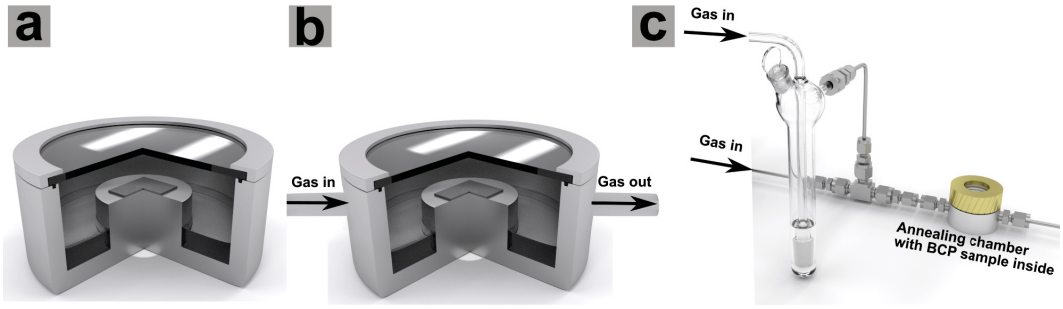

Figure 3.1: *Examples of three different types of solvent vapor annealing apparatus. (a) Static solvent vapor annealing apparatus. (b) Static solvent vapor annealing apparatus with gas flow. (c) Solvent vapor flow annealing apparatus. Reprinted with permission from ref. [27]. Copyright © 2017 American Chemical Society.*

The second general family of solvent vapor annealing apparatus is a static solvent vapor annealing with inert gas flow to adjust the vapor pressure (Figure 3.1b).[123, 148, 202, 203] This feature allows more control over solvent vapor pressure during annealing process, particularly the deswelling process. In static solvent vapor annealing apparatus, when the degree of swelling (D, defined as the ratio of swollen film thickness to initial film thickness) of a BCP thin film reaches its target value, the deswelling process is conducted by simply opening the chamber and releasing solvent vapor. However, in the second general family of solvent vapor annealing, the deswelling process is controlled by flowing different amount of inert

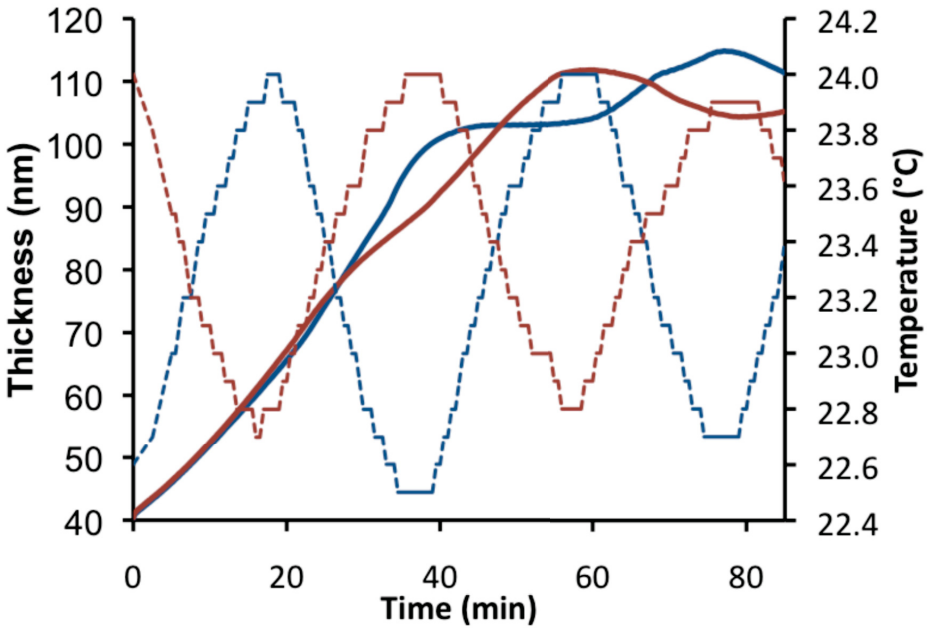

Figure 3.2: *Two swelling profiles (solid line) and their related room temperature profiles (dotted line). The temperature profile and swelling profile from the same trial is plotted in the same color. Reprinted with permission from ref. [28]. Copyright © 2013 American Chemical Society.*

gas and the morphology evolution of the BCP thin film during dewelling process can be studied.[123]

The third family of solvent vapor annealing apparatus is solvent vapor flow annealing, where the solvent vapor is introduced in to annealing chamber by an inert gas going through a solvent bubbler (Figure 3.1c). Usually, they are equipped with a flow control, a purge line, and an *in situ* sample thickness monitoring, which provide a way to control the swelling rate and final degree of swelling of BCP thin film during the annealing process. The first use of solvent vapor flow annealing system, to the best of our knowledge, was carried out by Knoll and co-corkers in 2004, who studied the dependence of morphology on the thickness of the film, of a PS-*b*-PB-*b*-PS triblock copolymer.[29] In 2007, Russell and co-workers followed with a study of cylinder-forming PS-*b*-PLA diblock copolymer in a solvent vapor flow annealing system.[204] Their results revealed that solvent vapor annealing was an effective way to achieve nanopatterns of perpendicular cylinders. They also studied the influence of annealing parameters on the order of cylinder-forming PS-*b*-P4VP thin film using the same setup.[205] The results were promising and showed that longer annealing times with the vapor of a selective solvent (THF, a 'good' solvent for the PS block) can not only improve local order but can also improve the long-range order of the resulting nanopatterns. In 2012, Epps and co-workers used a solvent vapor flow annealing system and showed that the rate of solvent removal from swollen BCP thin films influenced the final morphology.[206] The same year, Ross and co-workers reported a study of the resulting morphology of a PS-*b*-PDMS BCP using a combination of solvents for annealing in a controlled solvent vapor flow annealing system with reflectometry to measure film thickness *in situ*.[122]] In this system, three mass flow controllers were used to adjust flow rates of toluene vapor, n-heptane vapor and pure nitrogen gas, independently. With precise control over solvent vapor pressure and the ratio between the two solvents, this annealing method was shown to reproducibly tune the morphology of a given BCP thin film. When combined with a sufficiently fast quench to terminate the anneal, long-range order was achieved in 30 s.[22] Leighton and co-workers examined

solvent vapor annealing of cylinder-forming PS-*b*-PLA in a custom designed all-metal solvent flow annealing system by incorporating a *in situ* thickness monitor (reflectometry).[207] Thanks to the added capability of the *in situ* thickness monitor, the results obtained using this system showed that there was a narrow window (with respect to the degree of swelling) for the annealing of this cylinder-forming PS-*b*-PLA, which was close to the order-disorder transition condition.

Another variant of solvent vapor flow annealing apparatus uses grazing-incidence small-angle X-ray scattering (GISAXS) to provide *in situ* analysis of the resulting patterning formation in BCP thin film.[208–211] Most recently, Ross and co-workers reported a GISAXS study of polystyrene-*block*-polydimethylsiloxane (PS-*b*-PDMS) thin films in a newly designed controlled solvent vapor flow annealing system.[212] The results shed light on the complex kinetic and thermodynamic factors to play during swelling and deswelling in solvent vapor annealing.

Ellipsometry and reflectometry provide extremely useful *in situ* information regarding thin film thickness and therefore the degree of swelling in the film resulting from solvent uptake. These techniques are most often implemented over large areas (hundreds of micrometer) without lateral resolution, which forces the assumption of a uniform film thickness over that area. However, during the annealing process, the film can become terraced, forming regions of different microstructures with different thicknesses (Figure 3.3).[28, 29, 178, 213] Since these terraced phases are related to the local thickness of the film, data obtained from ellipsometry, reflectometry, or other nonmapping thickness measuring techniques will therefore only be able to return an average or effective thickness over a large area. In order to provide additional information, *ex situ* optical microscopy of thin films can be carried out to complement the *in situ* data, but thin film samples need to be quenched before optical microscopy analysis.

Herein, we describe a solvent vapor flow annealing apparatus with precise control over the degree of film swelling, enabled by feedback control linking *in*

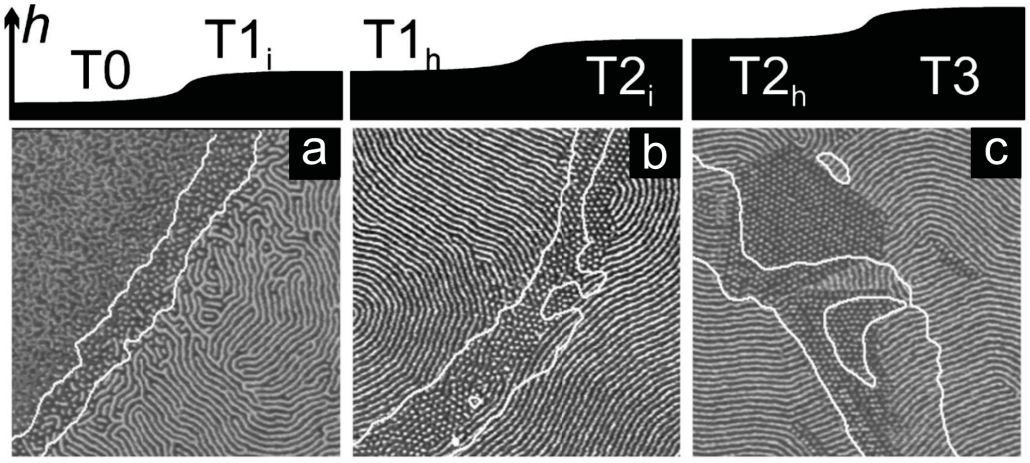

Figure 3.3: *Profile and plan view of terraced phases of a thin film of polystyrene-block-polybutadiene-block-polystyrene (PS-b-PB-b-PS, 14k-73k-15k), showing different morphologies in areas of varying thicknesses. (a−c) AFM phase images of BCP thin films. The drawn white lines are contour lines, and all images are 2 × 2 μm^2. Adapted with permission from ref [29].*

situ monitoring of film thickness with solvent vapor flow. An integrated optical microscope provides additional critical information about macroscale properties of the film (such as micron-scale dewetting and island formation). Feedback control enables precise, dial-in control over the degree of swelling of the film to enable reproducible solvent annealing of BCP thin films. This combination of precise control over thin film annealing, and information obtained from *in situ* optical microscopy together with laser reflectometry enables detailed understanding of solvent vapor annealing of BCP thin films in both nanometer thickness regimes (z-scale), and broad, millimeter-scale areas in the x- and y-directions on the substrate. These insights are useful for rational optimization of annealing procedures for directed self-assembly.

3.2 Methods

3.2.1 Materials

All BCPs and homopolymers used in our group were purchased from Polymer Source Inc. and used as received. The polymers used in this paper were PS-*b*-PDMS (31k-14.5k, PDI = 1.15, N_{PS}: 295, N_{PDMS}: 196, f_{PDMS} = 0.34), PS-*b*-PDMS (22.5k-4.5k, PDI = 1.09, N_{PS}: 214, N_{PDMS}: 61, f_{PDMS} = 0.18) and PS (10k, PDI = 1.09). Toluene was purchased from Fisher Scientific. THF was obtained from Fisher Scientific. Silicon wafers (4 inch, <100>, thickness: 525 $\pm$ 25 μm, p-type, Resistivity: 0.001-0.005 Ω·cm) were purchased from WRS Materials.

3.2.2 Silicon Wafer Dicing and Cleaning

Silicon wafers were diced into 1 cm $\times$ 1 cm squares with a Disco DAD 321 dicing saw. The silicon chips were immersed into a freshly prepared piranha (96 % sulfuric

acid / 30 % hydrogen peroxide solution: 3:1 v/v) solution for 15 min and then washed with DI water and dried in nitrogen stream.

3.2.3 BCP Thin Film Preparation

PS-*b*-PDMS (31k-14.5k), PS-*b*-PDMS (22.5k-4.5k), and PS (10k) were dissolved into toluene to make 1 wt % solution. These solutions were then stirred overnight at room temperature. To make sure there were no insoluble particles in the BCP solution, the BCP solution was filtered through a PTFE filter (0.20 μm pore size) twice before use. PS-*b*-PDMS (31k-14.5k) / 30 wt % PS (10k) was prepared by mixing 1 wt % PS-*b*-PDMS (31k-14.5k) solution and 1 wt % PS (10k) solution at 7:3 v/v (estimated f_PDMS = 0.24. BCP thin films were spin casted by dropping 17 μL of the BCP solution onto piranha-cleaned silicon chips at 6000 rpm [PS-*b*-PDMS (31k-14.5k)/30 wt % PS (10k)] and 8000 rpm [PS-*b*-PDMS (22.5k-4.5k)] for 40 s with a WS-400BZ-6NPP/ 120 LITE spin-coater (Laurell Technologies Corporation). The film thickness was measured by ellipsometry, with film thickness to be around 25 nm for PS-*b*-PDMS (31k-14.5k)/30 wt % PS(10k) and 22 nm for PS-*b*-PDMS (22.5k-4.5k).

3.2.4 Static Solvent Vapor Annealing Procedure

Firstly, a 25-nm-thick PS-*b*-PDMS (31k-14.5k) / 30 wt % PS (10k) thin film sample was placed in the middle of annealing chamber (Figure 3.4). The chamber was then placed on the stage of the ellipsometer (L116S, Gaertner Scientific). The laser was aligned by adjusting the angle and height of the stage to make sure the incident laser passed through the window of the annealing chamber, hit the center of BCP thin film, with reflected laser passing through the second window of the annealing chamber to reach the window of the sensor. After that, 1 mL of THF was transferred in to reservoir and a glass window was placed on top of the annealing chamber and

two screws were used to fix the position of the glass wafer. To try to retain the sealing of the vessel constant, these two screws were twisted on by hand without tightening, and no additional pressure was applied to the glass window. At that point, the ellipsometer was switched on to record film thickness data every 10 seconds. When film thickness reached the degree of swelling of 2.2, the glass window was immediately removed and the sample was immediately removed from the chamber.

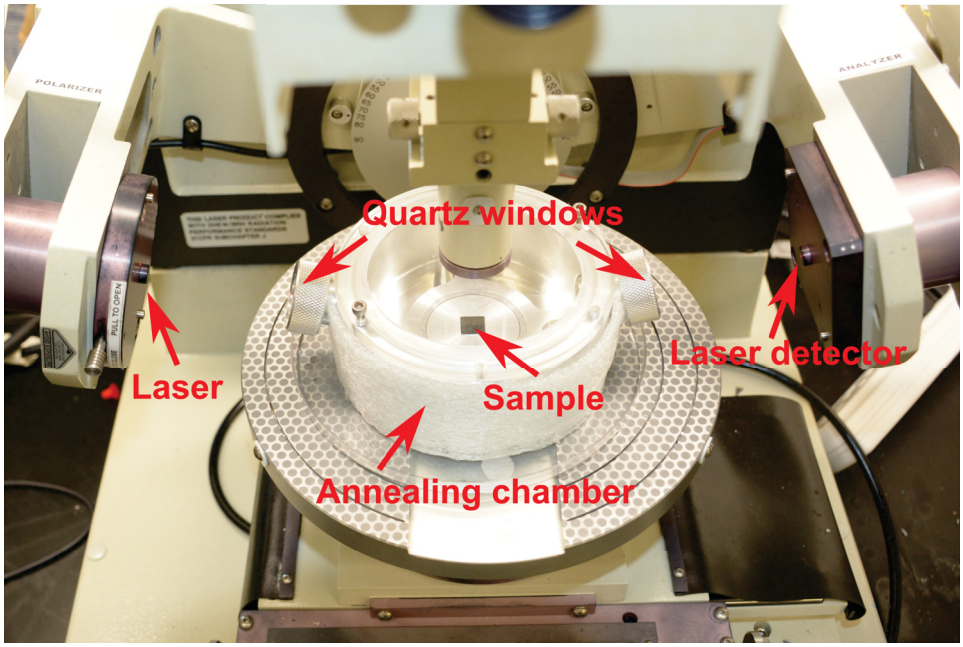

Figure 3.4: *static solvent vapor annealing setup. Reprinted with permission from ref. [27]. Copyright © 2017 American Chemical Society.*

3.2.5 Controlled Solvent Vapor Flow Annealing Procedure

Initially, PS-*b*-PDMS (31k-14.5k) / 30 wt %, PS-*b*-PDMS (22.5k-4.5k) BCP thin film samples were placed in the center of the annealing chamber (Figure 3.5). The perfluoro o-ring was then set in the chamber, followed by a quartz window. Another o-ring was laid on the quartz window and a brass lid was screwed onto the annealing chamber to make sure it was tightly sealed. A homemade 3D printed cap was placed

onto brass lid. The lid was designed to be integrated with a laser and a detector for *in situ* film thickness measurement, and the window for *in situ* film morphology measurement. Multiple marks were marked on the annealing chamber, brass lid, and 3D printed cap to ensure they are placed in the same position at every annealing. Before commencing the annealing program, it was ensured that the bubbler had enough solvent. Initial film thickness (nm), target degree of swelling (D, target film thickness/initial film thickness), dwell time (s), and ramp speed (D/min) were entered into the program. A 20 sccm flow rate of Ar was bubbled into the solvent bubbler, followed by automatic adjustment of the value of another pure Ar flow to control the swelling speed, and final degree of swelling. At the end of annealing, the program automatically stopped the solvent vapor flow and purged the annealing chamber with pure Ar to deswell the BCP thin film.

3.2.6 PS-*b*-PDMS Thin Films Etching Process

The BCP/BCP blend samples mentioned above form hexagonal packed spherical domain structures in annealed single layer films. PS-*b*-PDMS thin film samples were etched with a Plasmalab μEtch with a two-step etching. For PS-*b*-PDMS (31k-14.5k) / 30 wt % PS (10k), step 1, CF_4, 100 mT, 50 w, 8 s; step 2, O_2, 135 mT, 30 w, 60 s. For PS-*b*-PDMS (22.5k-4.5k), step 1, CF_4, 100 mT, 50 w, 8 s; step 2, 80 % O_2/ 20 % CF_4, 150 mT, 30 w, 60 s. The first step was used to remove the PDMS surface wetting layer on BCP thin film and the second step was used to remove the PS and convert the PDMS spherical domains to silica dots.

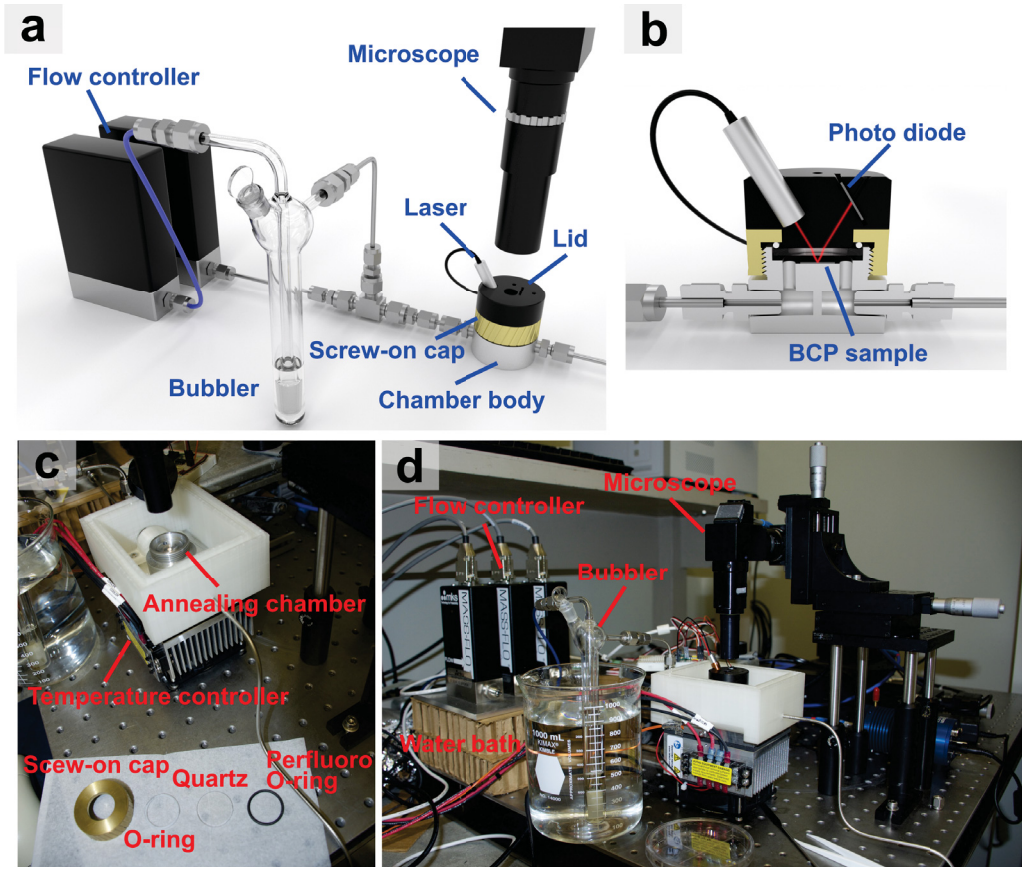

Figure 3.5: *(a)Schematic of controlled solvent vapor flow annealing apparatus. (b) Cross section drawing of the annealing chamber in (a). (c, d) Two photographs of the apparatus. Reprinted with permission from ref. [27]. Copyright © 2017 American Chemical Society.*

3.3 Description of Solvent Vapor Flow Annealing Apparatus

Schematics and photographs of our controlled solvent vapor flow annealing apparatus were shown in Figure 3.5. The sample chamber volume was made as small as possible (less than 1.5 cm^3), which was sufficient to fit a 'standard' BCP thin film sample (1 $\times$ 1 cm^2) and was able to precise control solvent vapor pressure during annealing (Figure 3.5b). Laser reflectometry has been used in other systems to determine film thickness.[122, 210] It is a simple and effective way to determine film thickness in real time to obtain degree of swelling, in BCP thin film. A diode laser and a photodiode were mounted at 30° from normal incidence (Figure 3.5b). This angle accompanied with small apertures prevented additional reflections from the top and bottom of the quartz window. Since it was difficult to reliably determine the absolute intensity of the laser and losses from the optical path from run to run, the transfer function (H) of the system was determined at the start of every run. H was calculated using the expected reflectivity from the optical transfer-matrix method[214] for the initial film thickness, as measured by ellipsometry before the chip was placed in the chamber, and the initial reflected intensity. The transfer-matrix method was used to calculate a table of expected reflectivities for increasing film thickness. The laser reflectivities during annealing were compared to this table to determine the film thickness and subsequently the degree of swelling. The initial optical constants of BCP films were determined by a rule-of-mixtures on the polymer weight ratio and the pure polymer constants. As solvent was absorbed by the film, the optical constants were determined from a rule-of-mixtures on the the degree of swelling in the film and optical constants from the BCP and the pure solvent.

The sample chamber was mounted to a thermoelectric plate capable of both heating and cooling the chamber. The bubbler was immersed in a water bath to help maintain a constant temperature of the solvent. While solvent annealing

at a constant flow, the swelling degree will still fluctuate with room temperature changes. Figure 3.6 shows three different trials of swelling profiles of a 25-nm-thick PS-*b*-PDMS (31k-14.5k) / 30 wt % PS (10k) film on native-oxide-capped silicon annealed at 1.2 sccm of Ar flow mixed with 20 sccm flow of THF-saturated gas from the bubbler, at room temperature. By mixing the PS-*b*-PDMS (31k-14.5k) with an appropriate amount of PS, thin films from this blend yield a hexagonal packed dot pattern upon annealing. The degree of swelling reached ~2.25 soon after exposure to the solvent vapor flow in all three trials. After that, the degree of swelling is quite different between each trials. Two of them dramatically decreased to about 2.1 and another one increased to 2.4 first and then decreased to about 2.3. In addition, there are quite a few fluctuations of the degree of swelling in each trial. This was caused by room temperature difference between each trial, room temperature fluctuation, and cooling of the bubbler after constant bubbling.

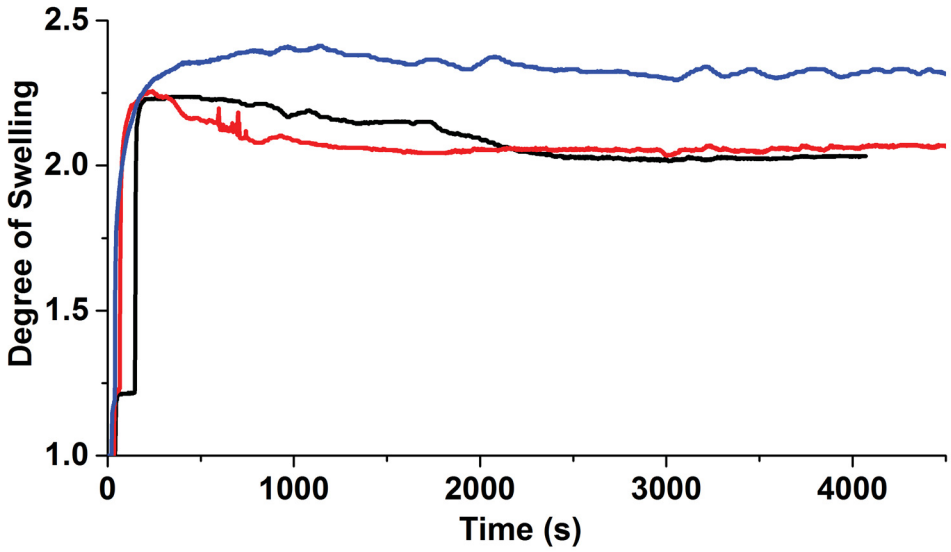

Figure 3.6: *Swelling profiles of three different trials of constant solvent vapor flow annealing at room temperature.The argon flow is 1.2 sccm and the bubbler flow is 20 sccm. Reprinted with permission from ref. [27]. Copyright © 2017 American Chemical Society.*

In order to control the degree of swelling of the polymer film during annealing, a feedback loop linking a precise and responsive thickness measurement technique with solvent vapor flow was developed (Figure 3.7 and 3.5). The argon flow and solvent bubbling flow both started at 20 sccm for several seconds to prime the bubbler before the computer control takes over. The solvent flow was kept at 20 sccm for the duration of annealing process and the argon flow was reduced to increase the partial pressure of solvent in the chamber and swell the film. The solvent flow ratio, defined by the solvent saturated flow from the bubbler over the pure argon flow, was adjusted, using a PID (proportional–integral–derivative) control scheme, against the difference in the current degree of swelling from the set point. In order to allow, one set of PID tuning parameters for most of the swelling degree range, the error from the set point was linearized by fitting a power law. This linearization changes with chamber temperature. In order to allow a small amount of gas to mix evenly with solvent flow and minimize back diffusion, a mixing chamber was designed to inject a small flow of gas into the center of the solvent flow (Figure 3.8). This was achieved using a $1/4$-inch tube tee union and $1/8$-inch to $1/4$-inch bored through tube adapters as seen in Figure 3.8. The control software (BCPID) allowed multiple steps including different ramps and hold times. The acquired data, including film thickness, temperature, and micrographs, was plotted live and logged to a text file. Due to its modular structure, BCPID allowed different or additional, sensors and controllers including but not limited to: flow controllers, thickness measurements and temperature. For example, in future systems, a fiber coupled light source and spectrometer could act as a thickness measurement technique. This software is open source and available at: `https://github.com/bcolsen/BCPID`.

Figure 3.9 shows the degree of swelling profile (red solid line), argon flow profile (blue solid line), PID feedback control signal (green solid line), and pre-programmed swelling profile (black solid line) of another 25-nm-thick PS-*b*-PDMS (31k-14.5k) / 30 wt % PS (10k) film on native-oxide-capped silicon which was annealed using a solvent vapor flow annealing system with feedback loop. The pre-

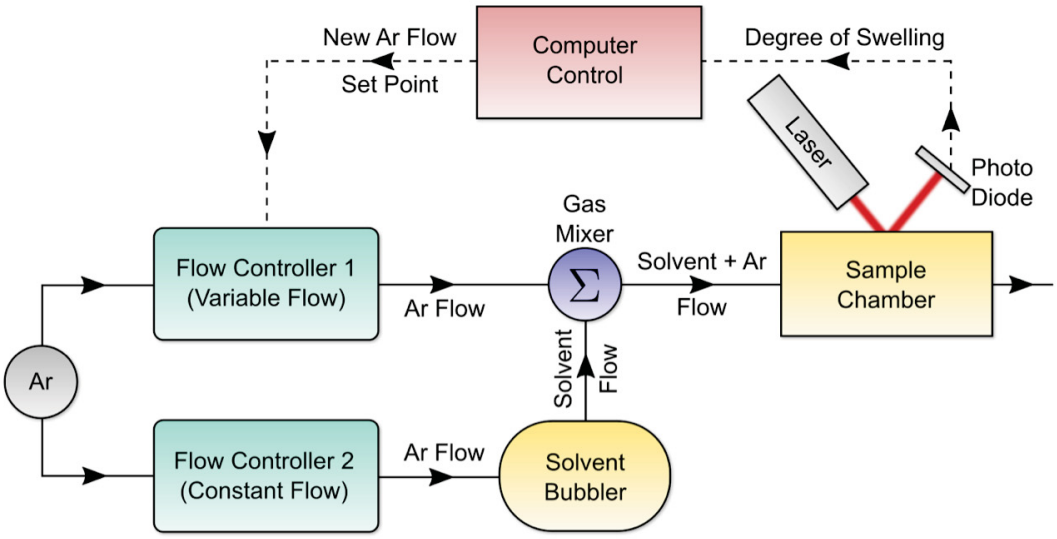

Figure 3.7: *A functional flow diagram of the controlled solvent vapor flow annealing system. Reprinted with permission from ref. [27]. Copyright © 2017 American Chemical Society.*

programmed swelling profile (Figure 3.9a) was set using a rate of 0.3 D/min (D is the degree of swelling, here, the degree of swelling increases 0.3 every minute) ramp to a set point of D equals to 2.20, and then held constant for a prescribed length of time (1500 s). The system was then rapidly purged at the 30-minute mark to arrest the annealing process and kinetically trap the morphology of the swelled BCP thin film. During the annealing process, PDI (green solid line in Figure 3.9b) automatically adjusted the Ar flow according to the degree of swelling and related set point. Figure 3.10a shows four annealing profiles with different set points of D, from 2.05 to 2.20, and Figure 3.10b shows four annealing profiles with different swelling speeds from 0.04 D/min to 0.3 D/min. The degree of swelling can be held precisely ($\pm$0.03) for several hours or more (limited only by the volume of solvent in the bubbler). The volume of the chamber (1.5 cm^3) was designed as small as possible to facilitate rapid deswelling of BCP thin film. It enabled a deswell time of less than 2 seconds at 20 sccm and permit kinetic trapping of the thin film morphology at a precise time (Figures 3.9 and 3.10).

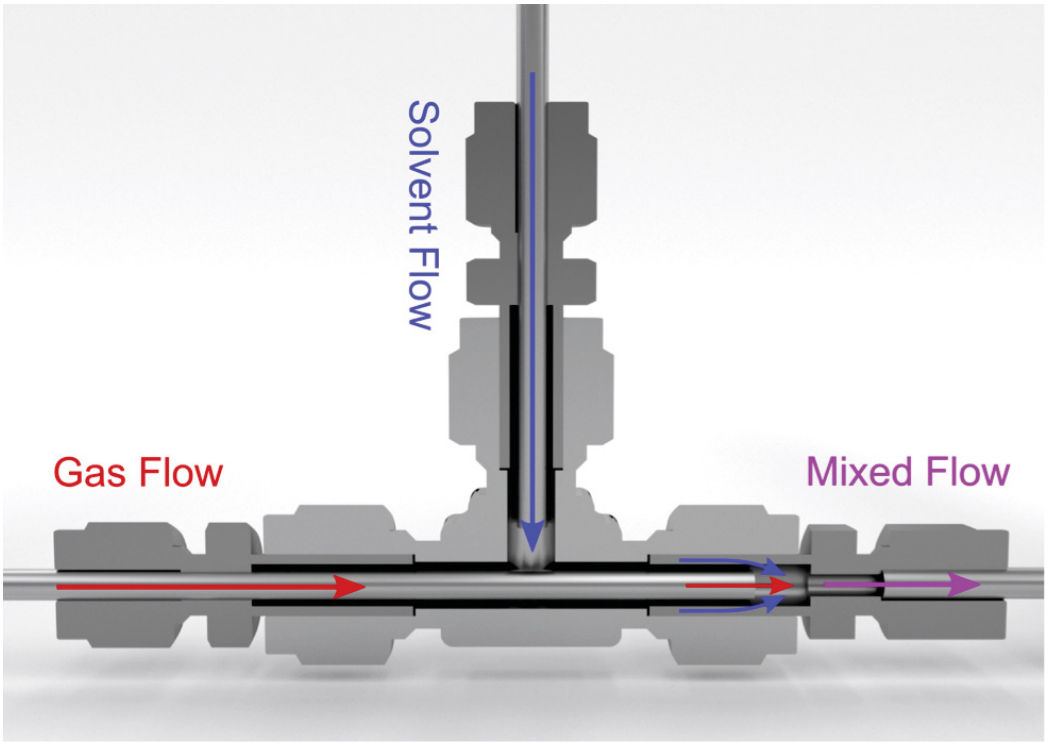

Figure 3.8: *Cross section drawing of the gas mixing section of the controlled solvent vapor flow annealing system. Reprinted with permission from ref. [27]. Copyright © 2017 American Chemical Society.*

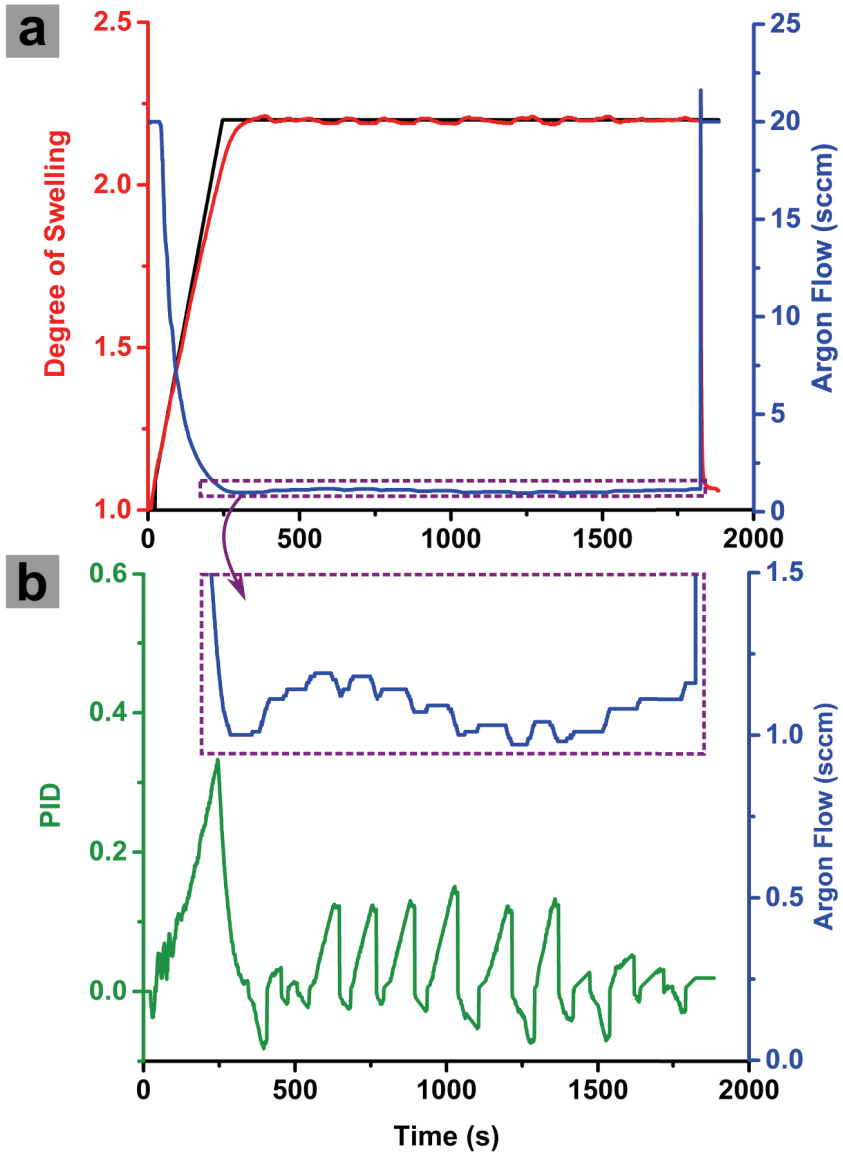

Figure 3.9: *Swelling profile (red solid line), argon flow profile (blue solid line), pro-programmed swelling profile (black solid line) and PID (proportional–integral–derivative) feedback control signal (green solid line) of a feedback controlled solvent vapor flow annealing of a 25-nm-thick PS-b-PDMS (31k-14.5k) / 30 % wt PS (10k) film annealed by THF vapor. Reprinted with permission from ref. [27]. Copyright © 2017 American Chemical Society.*

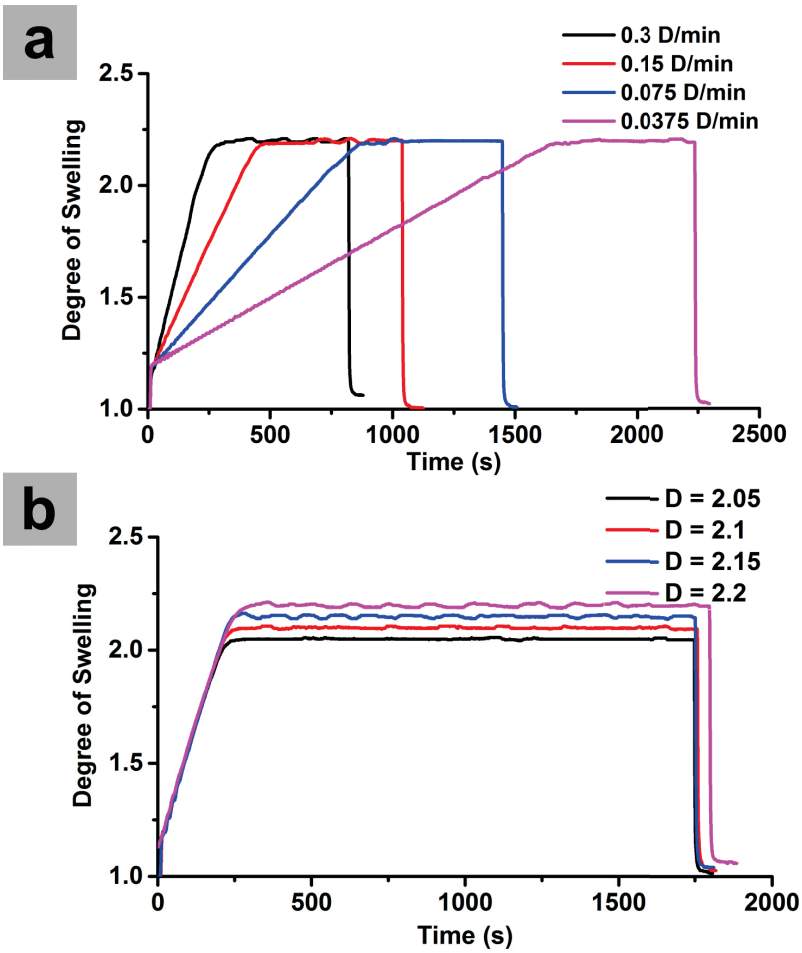

Figure 3.10: *(a) Four swelling profiles with different degrees of swelling, 2.05, 2.10, 2.15, and 2.20, at the same swelling rate (0.3 D/min). The dwell time was set to be 1500 s. (b) Four swelling profiles with the same degree of swelling and dwell time (500 s) but different swelling rates (from 0.300 to 0.04 D/min). The BCP thin film sample were 25-nm-thick PS-b-PDMS (31k-14.5k) / 30 % wt PS (10k) films and annealing solvent was THF. Reprinted with permission from ref. [27]. Copyright © 2017 American Chemical Society.*

To contrast with the swelling profiles that can be obtained with the feedback controlled solvent vapor flow annealing system, Figure 3.11 shows the swelling curve for a 25-nm-thick film of PS-*b*-PDMS (31k-14.5k) / 30 wt % PS (10k) in a static solvent vapor annealing system. The shape of swelling curve was determined by several factors, such as surface area of the solvent, humidity of the ambient air, and temperature of the room. The degree of swelling of the polymer film was monitored *via* ellipsometry, and while a given morphology (or combination of morphologies) was reproducible for a given degree of swelling, the rate of swelling varied from experiment-to-experiment. For example, the dip in the degree of swelling at 3500 s in Figure 3.11 was considered to be the result of a usual room temperature fluctuation of about 2 °C (due to the building temperature control). Figure 3.12 also shows dramatic degree of swelling change (0.8) with annealing temperature from 18°C to 16.5°C on a PS-*b*-PDMS BCP thin film at constant solvent flow annealing. With the feedback loop and temperature control in the flow-controlled system, reproducibility become much less of an issue.

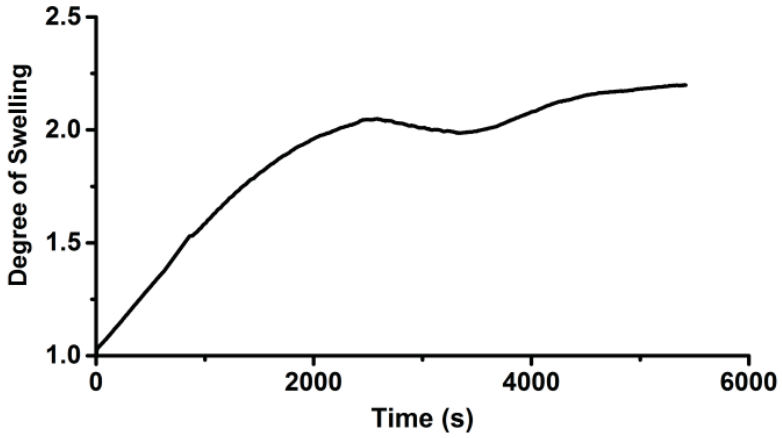

Figure 3.11: *(Swelling profile in a static solvent vapor annealing system of a 25-nm-thick PS-b-PDMS (31k-14.5k) / 30 % wt PS (10k) films in THF vapor. Reprinted with permission from ref. [27]. Copyright © 2017 American Chemical Society.*

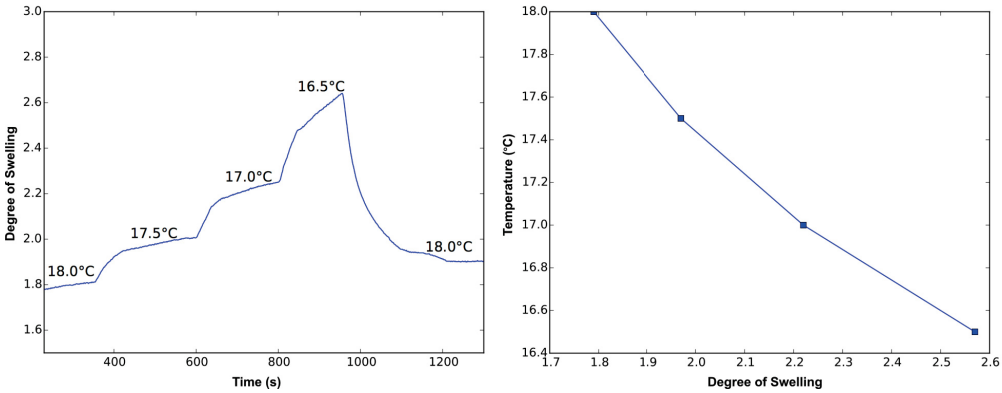

Figure 3.12: *Influence of temperature on the degree of swelling of a thin film of a 26-nm-thick PS-b-PDMS (43k-8.5k) thin film, during THF vapor flow annealing. (a) Swelling profile of the BCP thin film in a constant THF vapor flow. The temperature is controlled by a thermoelectric plate. (b) The relationship of swelling degree and substrate temperature. Reprinted with permission from ref. [27]. Copyright © 2017 American Chemical Society.*

3.4 Controlling and Observing the Degree of Swelling

Thickness of the pre-annealed film is critical not only with respect to the resulting nanoscale morphology, but on the micron-scale as well. Films that are too thin cannot properly self-assemble into single layer spherical domains, and will dewet, leading to formation of regions of thin wetting layers or bare substrate regions (referred to hereafter as a wetting layer in accordance with previous literature).[29] If the sample is too thick, double- and triple-layer regions will result. Lateral nonuniformity in as-spun thickness as well as mass transport due to repeated swelling of the film can result in formation of both wetting layers and multilayers within the same sample. An example, in what was intended to be a monolayer-thin film, is shown in Figure 3.13. In this example, a 25-nm-thick PS-*b*-PDMS (31k-14.5k) / 30 wt % PS (10k) film was solvent annealed, resulting in mostly single-layer films, but the low magnification SEM micrograph, Figure 3.13b, shows some small regions of wetting layers (darkest areas), and double layers (lightest areas).

Figures 3.13c-e show high magnification SEM micrographs of the three different areas for conclusive identification.

From a manufacturing perspective, reproducibility, consistency, and avoidance of wetting layers and multilayers will be critical, particularly across the large area of a 300-mm wafer.[215] Optical microscopy provides real-time measurement of the phase morphology correlated directly with film thickness across large areas of the sample, as shown in Figure 3.14. For future lithographical applications, minimization of large scale defects such as wetting layers and multilayers is critically important. Much remains to be learned about dewetting and double/triple layer formation in single layer BCP annealing, in the context of manufacturing and scale-up. The *in situ* microscopy capability allows for monitoring of the phase morphology during the entirety of the solvent vapor annealing process.

Control software was developed to allow multiple annealing steps, including ramping up and down and dwelling at different degree of swelling (Figure 3.14), enabling cyclic annealing recipes[216] that have recently been suggested to provide a fine degree of control over the self-assembly process. To demonstrate the utility of the integrated optical microscope, coupled with control over the degree of swelling (enabled by the feedback loop), Figure 3.14 demonstrates multi-step annealing. This figure shows a simple three-step annealing process of a 25-nm-thick PS-*b*-PDMS (31k-14.5k) / 30 wt % PS (10k) thin film on a silicon substrate: The first step is a 250 s dwell at a degree of swelling of 2.4; the second step is a decrease in swelling degree to 2.0, which is then held constant for a 150 s; the third step is an increase of the degree of swelling to 2.3, holding this value for 150 s. The ramp rate for all these three steps is 0.3 D/minute, indicated by the solid red line. Far more complicated cycling profiles are, of course, possible. The optical micrographs are shown in images T0-T7 with corresponding times of capture indicated on the annealing curve. The contrast in the optical micrographs is due to thin film interference. At this thickness, thicker films appear darker, and thinner films are lighter. The sharp contrast between the phases is due to the thickness differences

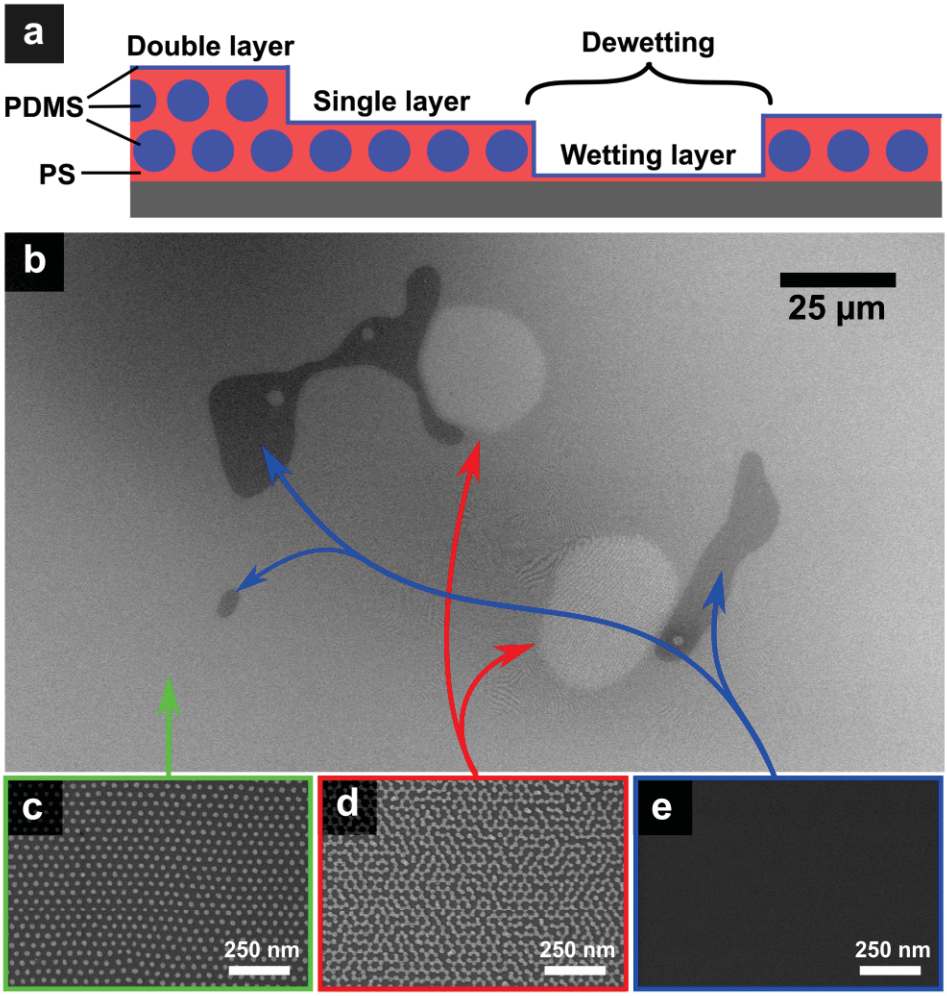

Figure 3.13: *(a) A cross section schematic showing single and double layers, and the wetting layer of an annealed PS-b-PDMS thin film. (b) Low magnification SEM micrograph of a solvent vapor-annealed thin film of PS-b-PDMS following CF_4/O_2 plasma treatment, an established high-fidelity conversion of the PDMS block to silica, accompanied by simultaneous removal of the PS. (d) High magnification SEM micrograph of the majority single layer (hexagonal silica dot pattern). (d) High magnification SEM image of double layer area (honeycomb dot pattern). (e) High magnification SEM micrograph of the area that has undergone dewetting (no polymer pattern seen). Reprinted with permission from ref. [27]. Copyright © 2017 American Chemical Society.*

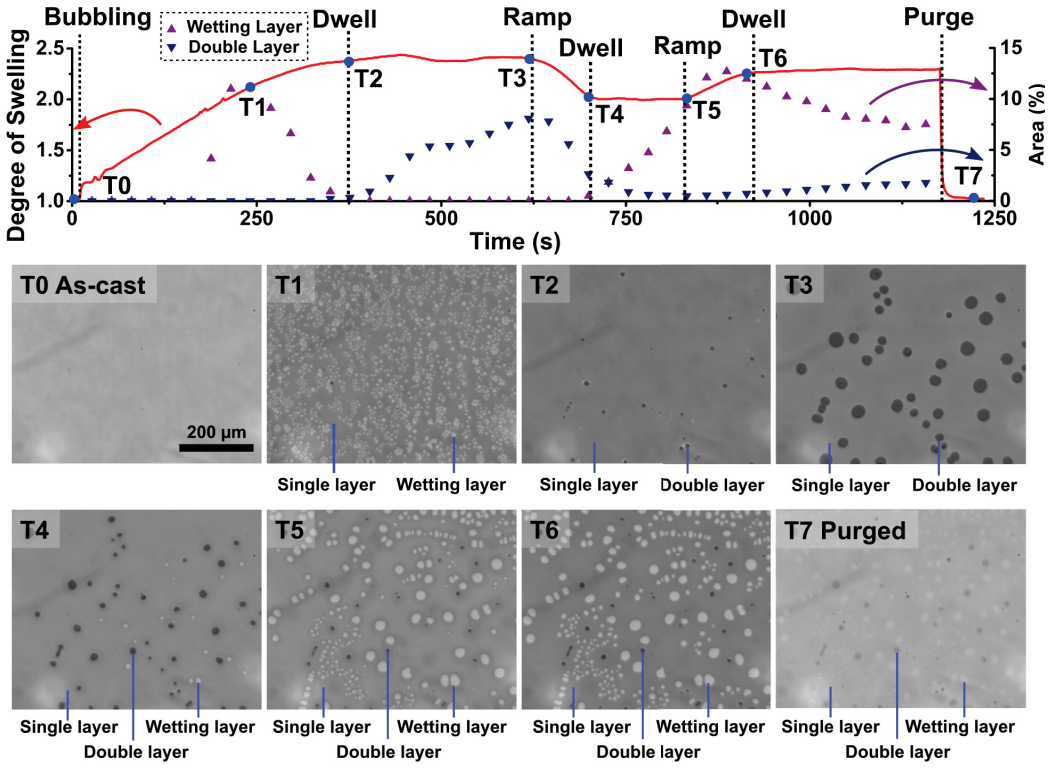

Figure 3.14: *The evolution of the microstructure evolution in a 25-nm-thick PS-b-PDMS (31k-14.5k) / 30 wt % PS (10k) film during a three-step annealing process. See supplementary information for a full video capture of the entire annealing process. Note: the gray line mark at middle left and two whitish spots in every image are due to the contamination of microscope lens. Reprinted with permission from ref. [27]. Copyright © 2017 American Chemical Society.*

between them, Figure 3.13a. The area fraction of regions with a wetting layer (white circular spots in microscope image) and double layer areas (dark circular spots) have been tabulated using threshold and are plotted along the annealing profile. As seen in these optical micrographs, immediately after spin casting, the BCP thin film is relatively uniform, however weak contrast variations are observed across the field of view, which are ascribed to thickness fluctuations of the film. Upon commencing the solvent vapor anneal, the BCP film immediately begins to increase in thickness as it absorbs solvent, from 25 nm at 8.7 s to 29 nm at 13.8 s. Along with the increase in film thickness, non-uniformity of the film thickness begins to increase significantly, as evidenced by the increased contrast between light and dark regions (as seen in the optical micrographs in Figure 3.14). The wetting layers (white circular spots) appear at ∼189 s, and the area fraction of wetting layers increases dramatically from 4.2 % of the total area at 189 s to 11.1 % at 242 s (degree of swelling: 2.1, Figure 3.14T1). The wetting layers then progressively shrink as the BCP thin film continues to swell, and completely disappears at a degree of swelling of 2.4 at 377 s (Figure 3.14T2). At these higher degrees of swelling, double layers (dark circular areas) start to appear, and increase in size during the 250 s dwell, from 0.2 % to 8.1 % (Figure 3.14T3) of the total film area. From T3 (619 s) to T4 (700 s), the degree of swelling of this BCP thin film was then decreased from 2.4 to 2.0, and the double layer area of the thin film decreased from 8.1 % to 2.6 % (Figure 3.14T4). Upon a second stage of dwelling, the area of double layers decreased (from 2.6 % to 0.5 %), and the wetting layers reappeared, increasing from 0.5 % (Figure 3.14T4) to 9.3 % (Figure 6T5) of the total area. The wetting layer area reached its maximum at 888 s (12.7 %, 2.2 degree of swelling) but started to shrink afterward. At the end of the solvent annealing, the BCP thin film was quenched, with a resulting double layer area fraction of 1.8 % and wetting layer area fraction of 7.5 %.

Careful investigation of Figure 3.14 reveals that the area fractions of wetting, single and double layers can change significantly despite maintaining a constant degree of swelling. As mentioned previously, when using an optical interference method without lateral resolution to measure the degree of swelling of a BCP thin

film, it is generally necessary to assume that the film has a uniform thickness over the measurement area. When there are terraced phases present, only an effective thickness is measured resulting in an effective degree of swelling. Therefore, as the film equilibrates to a given degree of swelling set point, the relative fractions of wetting, single and double layers can change while the effective thickness stays constant. This is an important consideration for interpreting *in situ* optical thickness measurements, and highlights the importance of coupling these measurements with optical microscopy.

An example of the utility of the controlled solvent vapor flow annealing system is shown in Figure 3.15, which demonstrates very fast annealing of large ordered areas of a thin film of PS-*b*-PDMS (22.5k-4.5k). The annealing profile, Figure 3.15d, is short, and starts with a pre-programmed swelling profile at a rate of 0.3 D/min to ramp up to D = 1.75. The film was then held constant for 900 s, followed by a purge at time = 1050 s. The annealed thin film was shown to be majority single layer dot pattern, comprised of 11.3-nm-diameter dots with a pitch of 22 nm, within large ordered grains of over 50 μm^2 in area (Figures 3.15a and b). The film has a small quantity of double layer areas, which was determined to be 3.5 % of the total area (Figure 3.15c).

3.5 Conclusions

For nanopatterning *via* BCP self-assembly (directed self-assembly) to be a viable commercial method for nanolithographic applications for semiconductor devices, unprecedented control over the annealing process is required. Detailed, fundamental insights are required to enable the deep understanding required to permit rational optimization. In this paper, we have described apparatus to enable solvent vapor annealing with dial-in feedback control to precisely control the degree of swelling, tailor the swelling profile, and rate of swelling and deswelling of a thin film. The integration of an *in situ* optical microscope provides critical information as to the

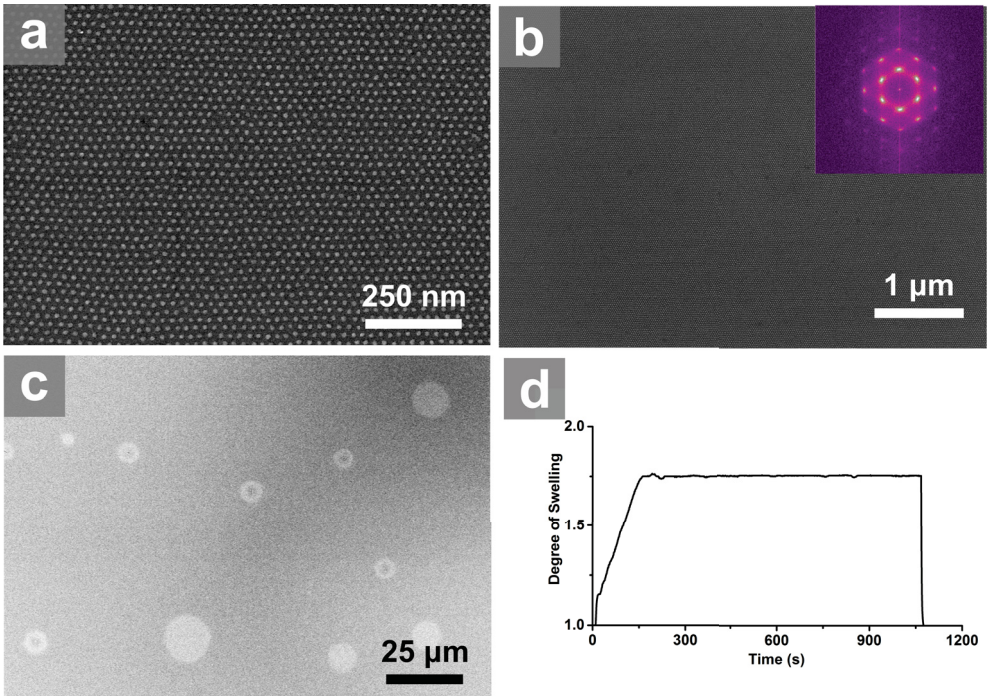

Figure 3.15: *Example of controlled solvent vapor flow annealing of a 22-nm-thick PS-b-PDMS (22.5k-4.5k) thin film. (a) High magnification SEM micrograph of the annealed BCP thin film following CF_4/O_2 plasma treatment. (b) Low magnification SEM micrograph of a BCP grain. The hexagonal pattern can be seen upon expanding (zooming in) on the image. Insert: 2DFFT. (c) Low magnification SEM micrograph of annealed BCP thin film surface with single (majority phase), and double layers (light circles). (d) Swelling profile of the annealing profile. Reprinted with permission from ref. [27]. Copyright © 2017 American Chemical Society.*

evolution of the micromorphology of the film during the anneal, which complements the film thickness data, as formation of terraced phases can and does occur. Because terraced phase formation is reversible, exquisite control over the degree of swelling allows optimization of the solvent vapor annealing, to reach the highest level of desired morphology. This tool can be used by the community to tailor and optimize annealing procedures in a manner that is reproducible, while providing instructive data as to intermediate states along the annealing pathway.

4

Density Doubling/Tripling of Block Copolymer Dot Patterns

In this chapter, we demonstrate sequential patterning of highly ordered silica dots arrays to yield density-doubled and tripled dot patterns, derived from a well-established family of high-χ BCPs, PS-*b*-PDMS (polystyrene-*block*-polydimethylsiloxane). The spacing of the hexagonal nanopatterns was systematically tuned by blending with a homopolymer, and the quality of these density multiplied patterns, measured as the fraction of dots that are distinct and separate, was fully quantified and modeled.

4.1 Density Multiplication of BCP Bottom-Up Self-Assembly

For a given BCP thin film, the resulting nanopattern is determined by the material constraints of the polymer and the processing conditions.[217] Significant efforts have focused on the production of high-density nanopatterns with sub-20 nm spacing, with great attention devoted to the development of small diblock copolymers comprising two immiscible blocks, as defined by a large Flory-Huggins interaction parameter, χ.[8, 114, 121, 218–220] Because the spacing of a given self-assembled BCP nanopattern is generally dependent upon its degree of polymerization, N, and the segregation strength of a polymer depends on the product χN, the self-assembly of high-density nanopatterns requires BCPs with higher χ to offset the lower N.[83] Recently, the development of BCPs with small N and large χ has proven to be a fruitful approach towards making high density BCP arrays.[95, 121, 219, 220] Without the use of lithographically defined guiding features or prepatterned substrates, well-defined control and implementation of these new polymers as templates for high fidelity pattern transfer is challenging, in part due to poor segregation of the two short blocks.[55, 77]

The concept of density multiplication of BCP self-assembly has seen some attention, as summarized by four examples. Spatz and co-workers used a two-step BCP-based approach for making mixed metal gold and titania hexagonal dot arrangements.[221] Kim and co-workers showed that metal dot and line patterns produced from BCP self-assembly could be treated with a second BCP self-assembly step to produce more complex patterns, and while the results are very promising, detailed quantification and analysis were not carried out.[198] A one-step conversion of a BCP bilayer into density doubled dots has also been shown by Wu and co-workers, but the results may not be generalizable as they are complicated by non-uniform dot heights and sizes.[178] Line frequency doubling of BCP-derived nanostructures has also been demonstrated *via* application of the

self-aligned double patterning (SADP) process to produce density-doubled metal lines.[222] In this chapter, we describe a fully bottom-up approach that attempts to surpass the intrinsic or native density of a given single layer nanopattern of dots using strongly segregating BCPs that yield ordered nanopatterns over large areas. Through two or three identical self-assembly steps, density-doubled or density-tripled nanopatterns, respectively, can be achieved. The processing for each layer is straightforward and repetitive, which simplifies the overall procedure.

4.2 Methods

4.2.1 Materials

PS-*b*-PDMS (31k-14.5k, N_{PS}: 295, N_{PDMS}: 196, f_{PDMS} = 0.34), PS-*b*-PDMS (43K-8.5k, N_{PS}: 410, N_{PDMS}: 115, f_{PDMS} = 0.18), PS-*b*-PDMS (22.5k-4.5k, N_{PS}: 214, N_{PDMS}: 61, f_{PDMS} = 0.18), PS-*b*-PDMS (34k-5.5k, N_{PS}: 324, N_{PDMS}: 74, f_{PDMS} = 0.15), and polystyrene (PS) (M_n = 10,000 g/mol and M_n = 5,000 g/mol) were purchased from Polymer Source Inc. The polydispersity index (PDI), as measured by size exclusion chromatography of PS-*b*-PDMS (31k-14.5k), PS-*b*-PDMS (43k-8.5k), PS-*b*-PDMS (22.5k-4.5k), and PS-*b*-PDMS (34k-5.5k) were 1.15, 1.04, 1.09, and 1.09, respectively, (data provided by the Polymer Source Inc., for the specific batches). Sulphuric acid (96%) and hydrogen peroxide (30%) were purchased from Avantor Performance Materials, Inc.. Toluene and THF were obtained from Fisher Scientific; Silicon wafers ($\langle 100 \rangle$, intrinsic, thickness: 525 $\pm$ 25 μm) were obtained from WRS Materials.

4.2.2 Substrate Preparation

Silicon wafers were cut into 1 cm $\times$ 1 cm squares with a dicing saw (Disco DAD 321). Diced silicon wafers and samples after the first or second annealing and etching steps were cleaned using a piranha solution [3:1 v/v sulfuric acid (96 %):hydrogen peroxide (30 %)]. Substrates and samples were immersed in piranha solution for 15 min, rinsed by DI water, and dried with a nitrogen stream.

4.2.3 BCP Thin Film Self-Assembly

Individual solutions of PS-*b*-PDMS (31k-14.5k), PS-*b*-PDMS (43k-8.5k), PS-*b*-PDMS (34k-5.5k), PS-*b*-PDMS (22.5k-4.5k), and PS (M_n= 10,000 g/mol, M_n= 5,000 g/mol) were prepared by dissolution in toluene to make 1 wt % solutions. For solutions of mixtures of polymers, PS-*b*-PDMS (22.5k-4.5k, 1 wt %) was mixed with PS (M_n= 5000 g/mol, 1 wt %) at 10 %, 12.5 %, 15 %, 17.5 %, 20 %, and 30 % fractions of the total polymer weight. PS-*b*-PDMS (31k-14.5k, 1 wt %) was mixed with PS (M_n= 10,000 g/mol, 1 wt %) at 30 %, 40 %, and 50 % fractions of the total polymer weight. PS-*b*-PDMS (34k-5.5k, 1 wt %) was mixed with PS (Mn= 10,000 g/mol, 1 wt %) at 15 % fractions of the total polymer weight. Block copolymer blends were stirred for 24 h before use. The polymer solution, 17 μL, was spin cast (Spin-coater: Model WS-400BZ-6NPP/LITE, Laurell Technologies Corporation) on a piranha solution-cleaned silicon substrate at 8500 rpm for PS-*b*-PDMS (34k-5.5k) blend, PS-*b*-PDMS (22.5k-4.5k), and PS-*b*-PDMS (22.5k-4.5k) blends, and 7000 rpm for the rest of the samples. The spinning time was 40 s for every polymer sample. The film thickness was measured by ellipsometry and was 26 $\pm$ 1 nm for PS-*b*-PDMS (34k-5.5k), PS-*b*-PDMS (22.5k-4.5k), and PS-*b*-PDMS (22.5k-4.5k) blends, and 30 $\pm$ 1 nm for the rest of the samples.

These as-cast samples were then placed in a custom-designed chamber for solvent annealing in THF vapour (see Figure 4.1), in which film thickness was

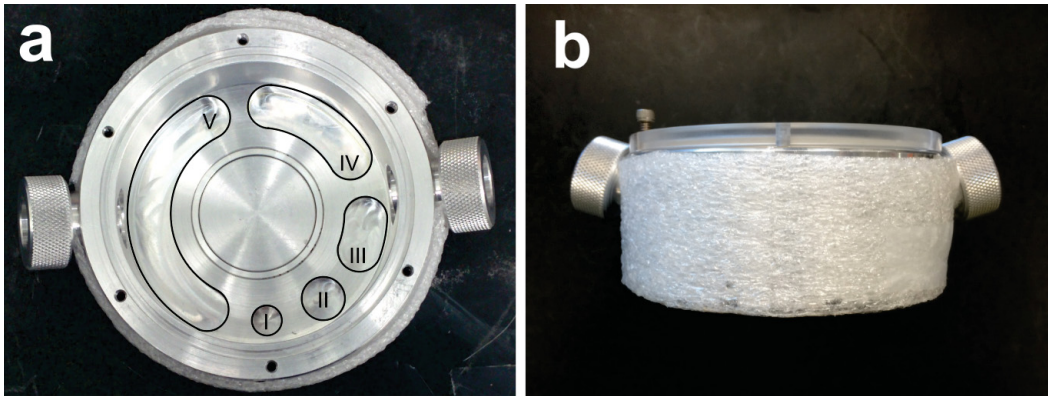

Figure 4.1: *Top-down (a) and side view (b) of chamber used for BCP thin film annealing. There are a total of 5 solvent reservoirs (outlined in black), which are labeled I,II,III,IV and V, having surface areas of 0.771, 1.60, 1.99, 2.67, and 3.89 cm^2 respectively. The depth of each solvent reservoir is 0.953 cm and the total volume of the chamber is 173 cm^3. This configuration of solvent reservoirs allows for 31 different configurations of solvent surface areas (and consequent vapour pressures), ranging from 0.771 to 10.9 cm^2. Reprinted with permission from ref. [30]. Copyright © 2016 American Chemical Society.*

measured *in situ* by ellipsometry. To determine the best solvent annealing conditions for each different type of BCP, for a given initial thickness, the swelling ratios of the films during annealing were adjusted by varying the steady-state vapour pressure of THF in the chamber. The THF vapour pressure was controlled by filling different combinations of solvent reservoirs with THF, allowing the solvent surface area (and consequent vapour pressure) to be adjusted. This process was found to be highly repeatable, as determined by the measured swelling ratios from ellipsometry. Following solvent annealing, the BCP films were converted to SiO_x and inspected using SEM. From these data, the annealing conditions producing the most highly ordered dot arrays were chosen. For the PS-*b*-PDMS (34k-5.5k) blend, PS-*b*-PDMS (22.5k-4.5k), and PS-*b*-PDMS (22.5k-4.5k) blends thin films, it was found that filling reservoir III (Figure 4.1, total surface area = 1.99 cm^2, with 0.5 mL THF) resulted in optimal films, while for the other PS-*b*-PDMS films, filling reservoir IV (total surface area = 2.67 cm^2) with 1 mL THF resulted in optimally ordered dot arrays. The swelling degree of the PS-*b*-PDMS (34k-5.5k) blend, PS-*b*-PDMS (22.5k-4.5k), and PS-*b*-PDMS (22.5k-4.5k) blend films was $\sim$1.6, while the other PS-*b*-PDMS films had swelling degrees of $\sim$2.0. The system was allowed to reach the equilibrium vapour pressure of the solvent, which is influenced by the total surface area of filled reservoirs. The thickness monitoring was used to quantitatively monitor the process and determine annealing time needed for the film to become fully saturated. A typical swelling ratio curve in Figure 4.2 is shown as an example. All solvent annealing was performed at room temperature, but it is noted that long period fluctuations in swelling ratio (Figure 4.2) are a result of room temperature fluctuations.[28]

These BCPs/BCP blends form hexagonal packed spherical domain structures in annealed single layer films. Annealed BCP films were then plasma-etched using a PlasmaLab μETCH. Plasma etching of samples was optimized for each polymer in the following manner. First, a CF_4 plasma was applied (10 s, 100 mTorr, 50 watt RF power) followed by a mixed CF_4/O_2 plasma. Following this step, a second plasma etching step was used as modified for different polymer samples: A single annealed

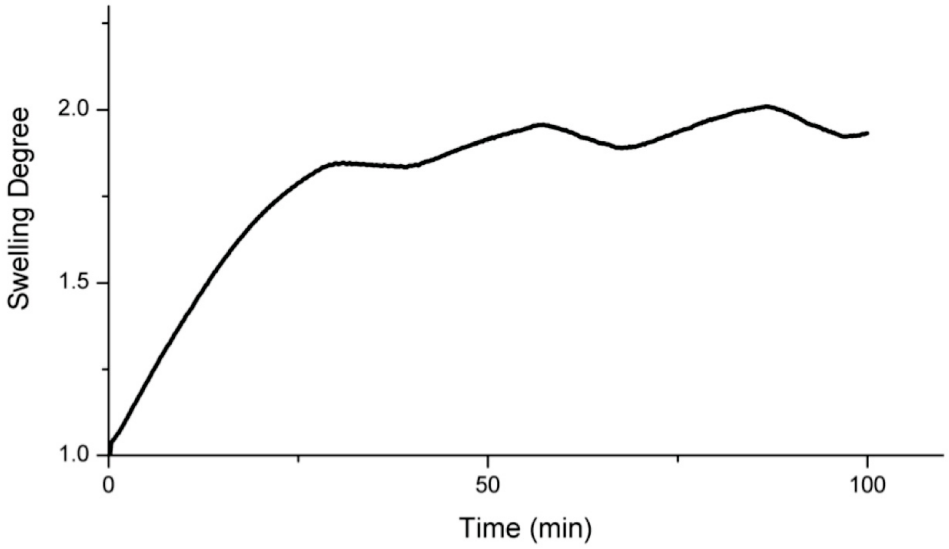

Figure 4.2: *Swelling curve of a BCP thin film during THF solvent annealing. Swelling degree is tracked in situ using ellipsometry. The fluctuations in the degree of swelling are a result of background fluctuations in room temperature. Reprinted with permission from ref.[30]. Copyright © 2016 American Chemical Society.*

sample is cleaved into four different chips and etched using different etching times or gas pressures, and then checked by SEM. An etching recipe is considered good if it yields clean dot patterns, has no under-etch (no polymer residue left in between dots) and no over-etch (clear dot pattern under SEM, strong signal). For PS-*b*-PDMS (43k-8.5k), and all PS-*b*-PDMS(31k-14.5k) blends, a mixed CF_4/O_2 plasma of 40 s, 80% O_2 and 20 % CF_2, 145 mTorr and 30 W RF power was used. For PS-*b*-PDMS (22.5k-4.5k), PS-*b*-PDMS (22.5k-4.5k) blends, and PS-*b*-PDMS (34k-5.5k) with 15 wt % PS, a O_2 plasma of 60 s, 135 mTorr and 30 W RF power was used. After preparation of a layer of silica dots, the samples were analyzed by SEM before preparation of a subsequent layer. After SEM analysis, the sample was first piranha-cleaned (*vide infra*), and then subjected to an identical process to form the next layer. All of the conditions described here are identical for the single-, double-, and triple-layer films; no modifications are needed.

4.2.4 Characterization

All SEM images were taken using a Hitachi S4800 scanning electron microscope at 15 kV, 20 μA. Tilted SEM images were taken at a 70° tilt angle for single layer samples and 60° for double and triple density samples. All SEM images were processed in Gwyddion, which is an open-source software for scanning probe microscopy data visualization and analysis.[223] .

4.2.5 Data Processing

In order to determine various parameters of the dot pattern lattices ($\bar{\epsilon}$, $\sigma_{\bar{\epsilon}}$, β, L_0, d_0) it was necessary to first find the positions of the dot centers from SEM micrographs. In single layer patterns this was a trivial task, as each dot was well defined and there was zero dot overlap. This was done by importing SEM micrographs into Gwyddion. Shown in Figure 4.3 and Figure 4.4 is a step-by-step example of the

process used to determine the dot centers in a double layer pattern.

In order to calculate the mean hydrostatic strain of any dot within a double layer honeycomb lattice, it was first necessary to determine which dots comprise the coordination shell. In a perfectly undeformed honeycomb lattice, the first three nearest neighbours to each dot belong to dots from the other layer, and the next 6 nearest neighbours were the set of 6 coordinating dots from the center dot's own layer. However, even when small perturbations in the dot positions occurred, nearest neighbour distances could not always be used to determine the coordination shell. As such, the following process was used to determine the six-fold coordination shell of each dot.

Firstly, the 3 coordinating dots from the other layer were determined (i.e. the set of dots from the other layer whose interstitial was occupied by the dot of interest). This was done by first finding the 12 nearest neighbours of each dot. From this set of 12 dots the Delaunay triangulation was computed and the dots forming the triangle that encloses the dot of interest were marked as dots from the other layer. This was shown in Figure 4.5a, where the Delaunay triangulation was shown for the 12 nearest neighbours and the 3 enclosing closing dots were marked in blue, the remaining 9 in green and the central dot of interest in red.

Next, the six-fold coordination shell from the remaining 9 dots was determined (green in Figure 4.5a). This coordination shell was determined by calculating the centrosymmetry parameter[224] of each different combination of 6 dots from this set of 9 dots (total of 84 different configurations), where the set of 6 dots with the minimum centrosymmetry parameter was taken at the six-fold coordination shell. Shown in Figure 4.5b was the six-fold coordination shell determined using this method, where the 6 nearest neighbours were colored green and the next 3 nearest neighbours were colored orange. It was noted that the 6 nearest neighbours were not necessarily identical the six-fold coordination shell with minimum centrosymmetry parameter. This was due to the fact that in a perfect honeycomb lattice the first coordination shell had a distance of $L_0/\sqrt{3}$, the second coordination shell has a

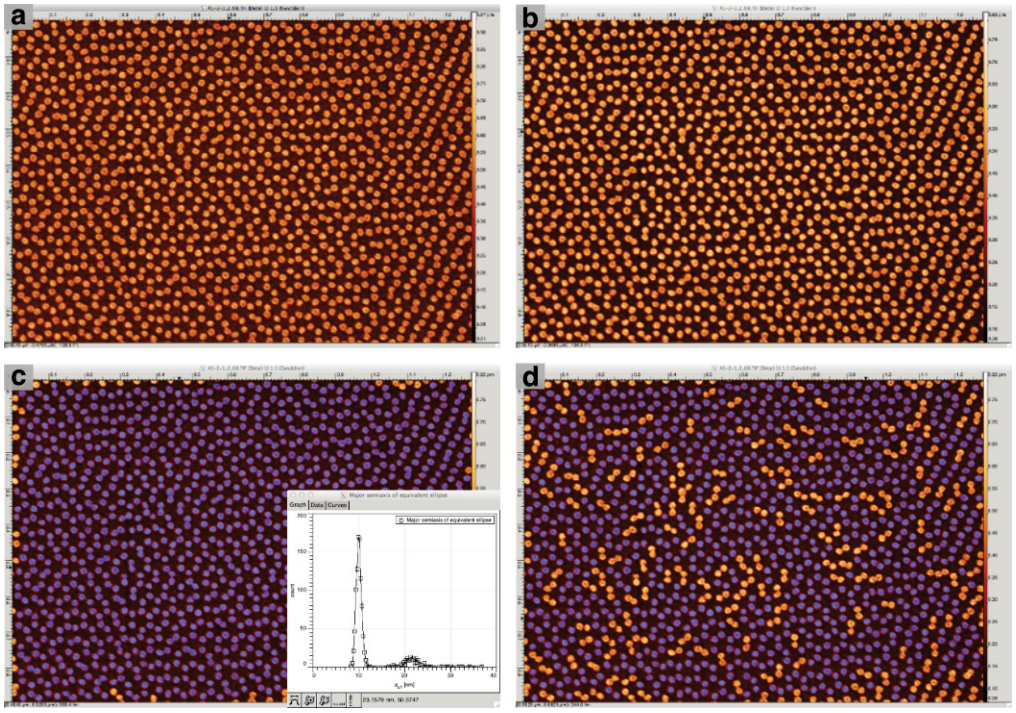

Figure 4.3: *(a) Raw SEM micrograph. (b) Convolution filter was used to remove high frequency noise in the SEM micrograph. (c) Particles were automatically identified using a clustering-based image thresholding algorithm known as Ostu's method. Marked particles were shown in blue. Inset: distribution of dot sizes (by major semiaxis of equivalent ellipse) was calculated. Here, the dot sizes were bimodally distributed; the dots at small sizes represented single dots, while the larger sizes were multi-dot clusters which could not be individually distinguished using Otsu thresholding. (d) The multi-dot clusters were removed from the thresholding mask and the mean dot diameter was calculated. This was used for* d_0 *when calculating* β*. Reprinted with permission from ref. [30]. Copyright © 2016 American Chemical Society.*

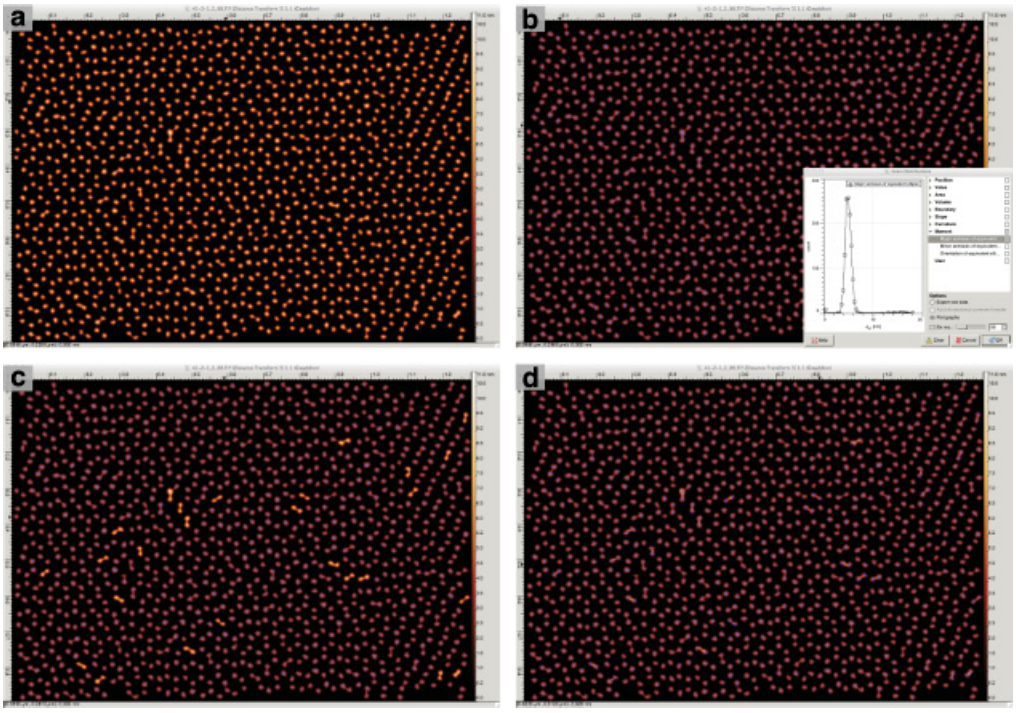

Figure 4.4: *(a) Euclidean distance transform was then applied to the unfiltered threshold mask in Figure 4.3c. (b) Ostu's method was now applied to the euclidean distance transformed micrograph. This was followed by shrinking the threshold mask from the border until the majority of thin necks connecting double dots disappear. Inset: distribution of dot sizes are now calculated (again by major equivalent ellipse axis). This time the majority of dots were single dots, however a few double dots remained. (c) Dots with large equivalent major ellipse axis were removed. (d) The dot centers of removed large dots were manually marked by hand. Finally the center positions of the dots were exported to a text file and used for analysis. Reprinted with permission from ref. [30]. Copyright © 2016 American Chemical Society.*

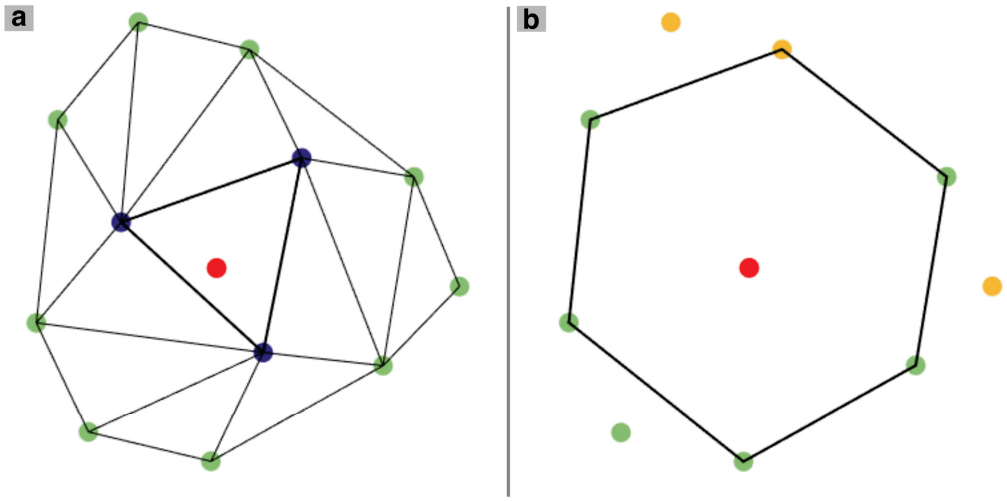

Figure 4.5: *(a) Delaunay triangulation of a dot and its 12 nearest neighbours in a honeycomb double layer dot pattern (taken from real data). The 3 nearest neighbour dots from the other layer were marked in blue and were determined from the triangulation that enclosed the central dot (red). (b) Six-fold coordination shell of dots with minimum centrosymmetry parameter surrounding the central dot (red). The 6 nearest neighbours were colored green and the next 3 nearest neighbours were colored orange. Reprinted with permission from ref. [30]. Copyright © 2016 American Chemical Society.*

distance of L_0 and the third coordination shell has a distance of $2/\sqrt{3}L_0 \simeq 1.15L_0$, as such small perturbations might result in dots from the third coordination shell (which belong to a different layer than the central dot) being closer than those from the second coordination shell.

The deformation and disorder of the hexagonal BCP dot patterns were quantified using finite strain theory. The amount of deformation of a given hexagonal coordination shell, which has experienced relative to the reference configuration of dots forming a perfect hexagonal shell, need to be described. The positions of the dots in the reference configuration are given by d_i^0, while the (measured) positions of the deformed configuration are given by d_i^N (all positions were measured relative to the centroid of the coordination shell). Therefore, a transformation matrix F_N can be described as,

$$d_i^N = F_N d_i^0$$

where F_N is the deformation gradient tensor. F_N is estimated *via* least-squares minimization of

$$\sum_i |d_i^N - F_N d_i^0|^2$$

which is shown to be [225]

$$F_N = \left(\sum_i d_i^0 \otimes d_i^0 \right)^{-1} \left(\sum_i d_i^0 \otimes d_i^N \right)$$

Here, F_N is factorized using polar decomposition in the form $F_N = RU$, where R is a rotation matrix and U is the deformation gradient tensor in the principal axes coordinate system. Therefore, the eigenvalues of U are the principal stretch ratios $\lambda_i = d_i^N/d_i^0$ along the principal axes.[226] Finally, the mean hydrostatic strain $\bar{\epsilon}_N$,

is given by

$$\bar{\epsilon} = \frac{1}{2}(\lambda_1 + \lambda_2) - 1$$

In practice, the stretch ratios is directly taken as the singular values of F_N, which are computed *via* singular value decomposition. Also, it is important to note that the relative orientation of the deformed configuration to the reference configuration didn't matter, since the principal stretch ratios are invariant under rotation. But it is critical that the positions of the dots in each configuration are angularly sorted (i.e. the dot positions of d_i^0 and d_i^N are both ordered in a clockwise or counter-clockwise direction).

In order to predict the amount of overlap a given double layer pattern, we constructed honeycomb lattices, where a dot was perturbed by a displacement Δd, where the magnitude of Δd was a pseudorandom number drawn from the standard normal distribution having a standard deviation of σ_d. Unfortunately, σ_d was not a measurable parameter, however, it was found that a simple relationship between σ_d and $\sigma_{\bar{\epsilon}}$ exists. This relationship was determined by generating a large number of configurations ($N = 300$) for a given σ_d measuring $\sigma_{\bar{\epsilon}}$ for each configuration. The mean value of $\sigma_{\bar{\epsilon}}$ was then taken. This process was then repeated for a range of σ_d and was plotted in Figure 4.6. We see that σ_d and $\sigma_{\bar{\epsilon}}$ have a simple linear relationship up to $\sigma_d \simeq 13\%$, which is given by $\sigma_{\bar{\epsilon}} = 0.2875\sigma_d$.

The map of dot overlap as a function of $\sigma_{\bar{\epsilon}}$ and β for both double and triple layers (Figure 4.20, 4.21 and 4.22) was done in the following way. First, a honeycomb (or triple density) lattice was generated with a total of 8479 dots (12688 dots for the triple layer). Next, each dot was perturbed by a distance that is selected from a normal distribution, with standard deviation $\sigma_d = \sigma_{\bar{\epsilon}}/0.2875$. Following this the total amount of dot overlap was measured for the range of β. This process was repeated for 1000 randomly generated configurations, which was then averaged to determine the total amount of dot overlap for each pair of $\sigma_{\bar{\epsilon}}$ and β.

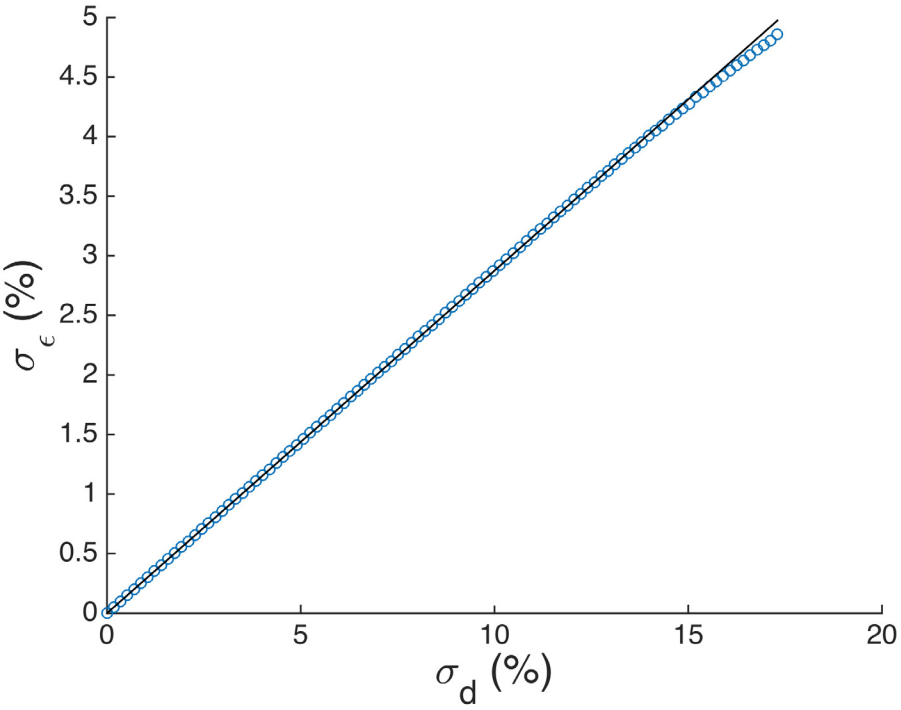

Figure 4.6: *(a) Relationship between σ_d and $\sigma_{\bar{\epsilon}}$. Open circles were determined from the average of 300 configurations each, and the solid line was best fit up to $\sigma_d = 13\%$, giving the linear relation $\sigma_{\bar{\epsilon}} = 0.2875\sigma_d$ Reprinted with permission from ref. [30]. Copyright © 2016 American Chemical Society.*

4.3 Homopolymer Percentage and Dot Separation

A scheme illustrating sequential layer deposition is shown in Figure 4.7. A highly ordered single layer of hexagonally packed dots was prepared by spin-casting a PS-*b*-PDMS thin film onto a native oxide-capped silicon surface. The as-cast film was solvent annealed and plasma treated, resulting in formation of silica dots on the silicon surface (Figure 4.7a).[227] Deposition of a second layer on top of the first layer, using identical processing conditions, results in the formation of a combined dot pattern possessing a honeycomb lattice (Figure 4.7b). The spatial position of the dots in the second layer is coincident to the triangular interstitial positions of the first layer. The density of the dot pattern can be further increased if a subsequent layer of BCP is deposited on the honeycomb lattice template. The dots of this third layer are registered to the hexagonal lattice positions, forming a triple density hexagonal lattice dot pattern (Figures 4.7c). Because the surfaces are chemically homogeneous (uniformly SiO_x), the registration is driven by the topology of the resulting dot pattern.

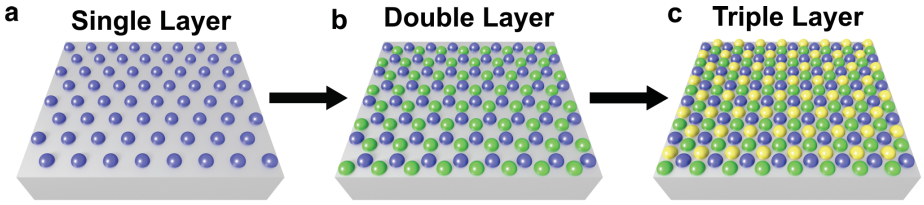

Figure 4.7: *Schematic of sequential layer deposition: (a) a single layer hexagonal dot pattern (blue) is deposited via spin-casting of a BCP thin film, followed by annealing and plasma treatment. (b) A second layer (green) is then deposited via the same process to form a honeycomb dot pattern. (c) Finally, a third layer of BCP (yellow) is deposited on top of the honeycomb dot pattern, resulting in a triple density hexagonal dot pattern. Reprinted with permission from ref. [30]. Copyright © 2016 American Chemical Society.*

Generalization of the approach to a BCP that has approximately half the

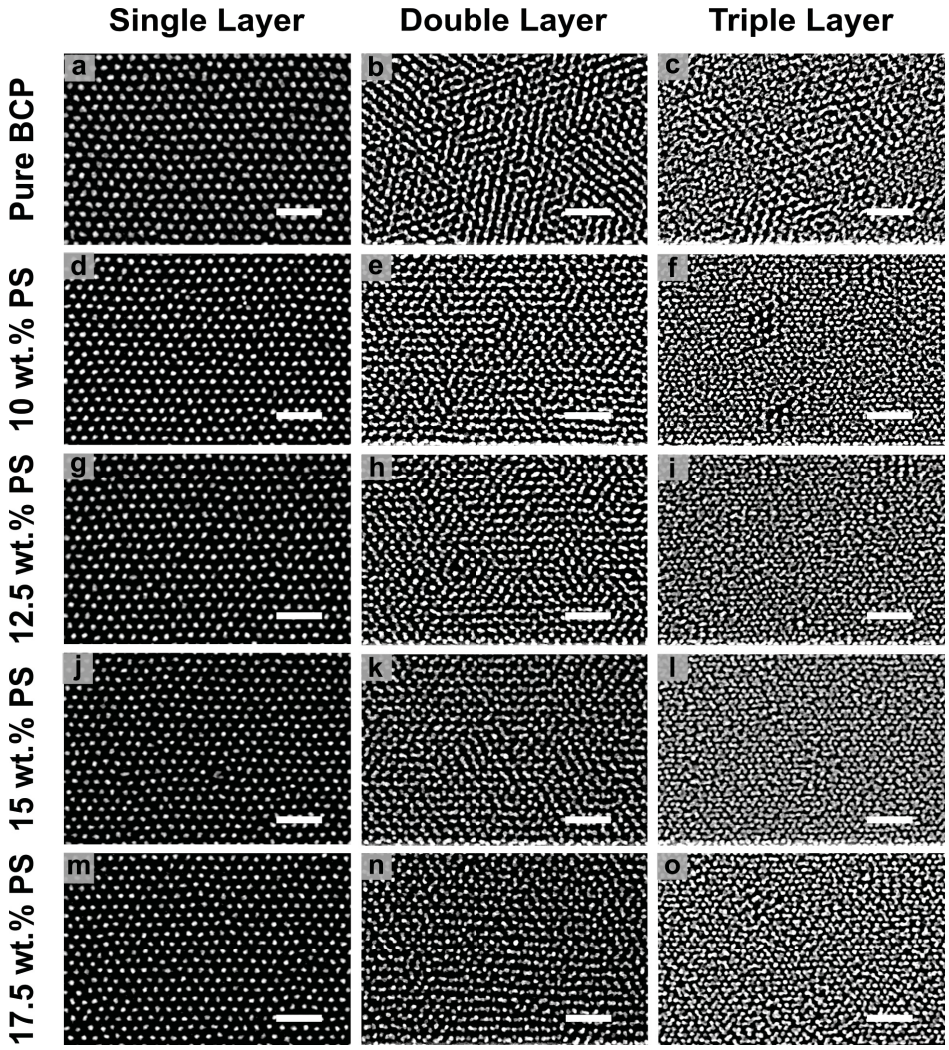

Figure 4.8: *Plan view SEM micrographs of single, double, and triple layer nanopatterns formed from PS-b-PDMS (22.5k-4.5k), blended with different quantities of PS (5k). (a-c) Neat PS-b-PDMS (22.5k-4.5k). (d-f) 10 wt % of PS (5k). (g-i) 12.5 wt % of PS (5k). (j-l) 15 wt % of PS (5k). (m-o) 17.5 wt % of PS (5k). All scale bars are 100 nm. Reprinted with permission from ref. [30]. Copyright © 2016 American Chemical Society.*

molecular weight, and thus corresponding smaller features, leads to formation of the single-layer pattern shown in Figure 4.8a. The lattice parameter for this BCP is 25.1 $\pm$ 2.3 nm, with a dot diameter of 12.4 $\pm$ 0.9 nm. As in the double layer pattern in Figure 4.8b, there is substantial dot overlap as few of the dots are isolated and distinct. Application of a third layer, Figure 4.8c, results in a poorly defined pattern due to considerable dot overlap, and indistinguishable dot boundaries (*vide infra*). Spatially separation of the dots derived from the different layers is fundamental to enabling density multiplication.[28] In an attempt to improve dot separation, polystyrene (PS, 5k) was added to the PS-*b*-PDMS (22.5k-4.5k) BCP to increase the notional molecular weight of the PS block.[173, 228] The effect of the added PS on the resulting patterns is summarized in Figures 4.8d-l. The addition of PS, up to 15 wt % to the PS-*b*-PDMS (22.5k-4.5k) BCP, results in the dots becoming more clearly distinguishable in both the double and triple layer patterns, which can be seen upon close inspection. The effect becomes more obvious in the higher contrast micrographs of the triple density patterns shown in Figure 4.9. The triple layer BCP pattern with 15 wt % PS (Figure 4.9b) is more regular with respect to registration and dot separation than the neat PS-*b*-PDMS (22.5k-4.5k) BCP (Figure 4.9a) due to the subtle decrease in dot size relative to the spacing.

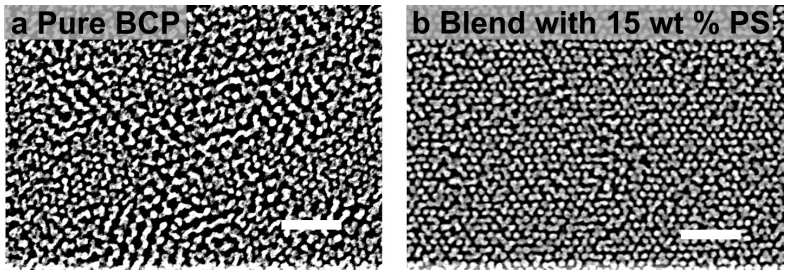

Figure 4.9: *Higher contrast and resolution SEM micrographs of the triple layer patterns from Figure 4.8, formed from (a) PS-b-PDMS (22.5k-4.5k), and (b) PS-b-PDMS (22.5k-4.5k) blended with 15 wt % PS. Scale bars are 100 nm. Reprinted with permission from ref. [30]. Copyright © 2016 American Chemical Society.*

Quantification of the effect of adding PS, within the patterns shown in

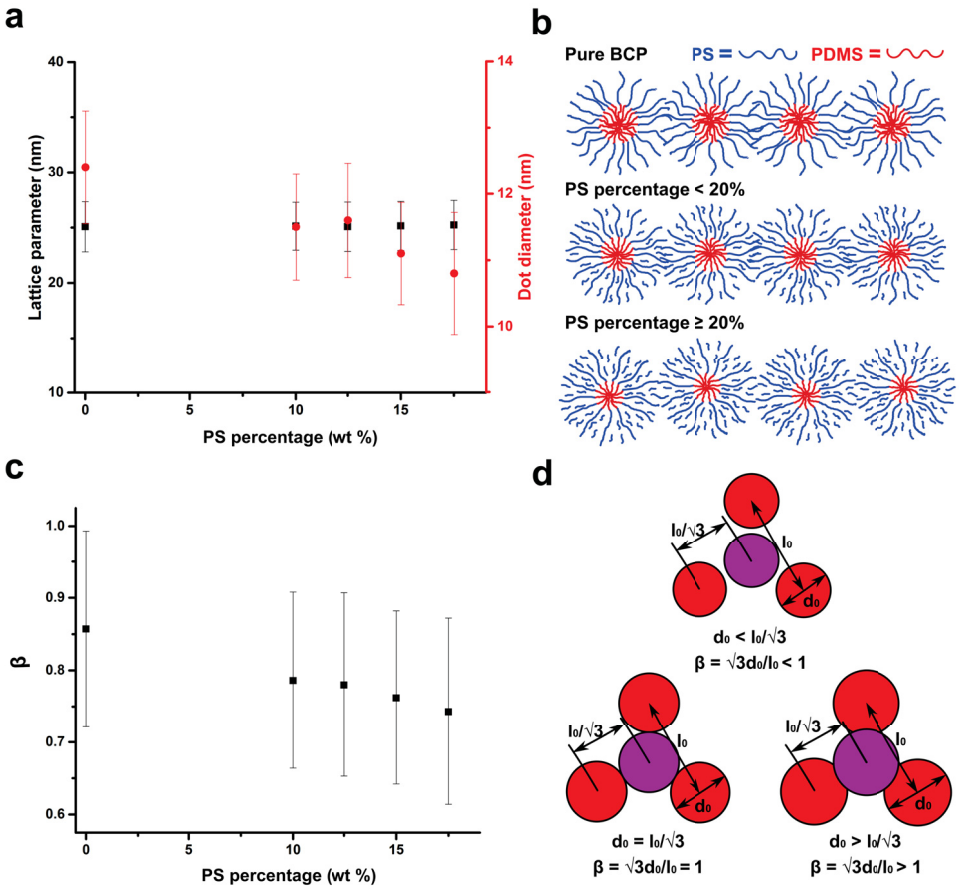

Figure 4.10: *(a) Lattice parameter and silica dot diameter, versus the percentage of blended PS for PS-b-PDMS (22.5k-4.5k), as calculated from the shown in Figure 4.8, and the Supplementary Information. (b) Schematic representation of the BCP micelles upon increasing the weight percentage of added (PS in blue, PDMS in red). (c) The calculated value of β versus the weight percentage of blended PS. (d) Geometric values of interest within a perfect hexagonal lattice, showing three different scenarios of dot-to-dot contact within a lattice, from dot overlap (β > 1), to touching of the edges (β = 1), to no contact (β < 1). Reprinted with permission from ref. [30]. Copyright © 2016 American Chemical Society.*

Table 4.1: *Values of Mean Dot Diameter d_0, Lattice Parameter L_0, β Parameter, Standard Deviation of Hydrostatic Strain $\sigma_{\bar{\epsilon}}$, Measured Double-Layer Dot Overlap, and Measured Triple-Layer Dot Overlap for PS-b-PDMS (22.5k−4.5k) and its PS Blends.*

wt % of PS	d_0 (nm)	L_0 (nm)	β (%)	$\sigma_{\bar{\epsilon}}$ (%)	Double Layer Overlap (%)	Triple Layer Overlap (%)
0	12.4±0.9	25.1±2.3	0.857	2.88	42	64
10	11.5±0.8	25.1±2.2	0.786	2.71	22	37
12.5	11.6±0.9	25.1±2.2	0.780	2.75	21	36
15	11.4±0.8	25.2±2.2	0.762	2.75	18	30
17.5	10.8±0.9	25.2±2.2	0.743	2.82	15	27

Figures 4.8 and 4.9, is described in Figure 4.10. The plots in Figures 4.10a,b graphically show the role of added PS on the lattice parameter of the resulting hexagonal nanopattern, as well as the dot diameter. The lattice parameter remains constant over this range of added PS, but the dot diameter decreases as a percentage of added PS homopolymer from 12.4 ± 0.9 nm to 10.8 ± 0.9 nm and from 0 % to 17.5 % added PS, respectively.[173, 228] Since the same volume of polymer blend in toluene is used to generate the films, addition of PS results in a decrease in the quantity of PDMS, thus leading to smaller dot diameters. At 20 wt % PS and greater, when added to this BCP, the hexagonal dot patterns become substantially disordered, as shown in Figure 4.11, and thus these patterns were not studied for sequential BCP assembly. For there to be no overlap in a perfect lattice, the value of β, as defined in Figures 4.10c,d, needs to be less than 1. Physically, β is the fraction of empty space between a dot residing in the interstitial position of the host hexagonal lattice. Figure 4.10c shows that β, as calculated from multiple SEM micrographs of hexagonal nanopatterns, decreased with added PS from 0.857 to 0.743. The standard deviations shown in Figure 4.10c are large and result from considerable fluctuation of the hexagonal dot pattern from a perfect lattice, meaning

that a smaller value of β is preferable to allow for additional space, or wiggle-room, for the dots within the pattern. As seen in Figures 4.8 and 4.9, the dot patterns formed by BCP self-assembly are not idealized perfect hexagonal lattices, as they have point defects (dislocations and vacancies, etc.), grain boundaries, and localized fluctuations from ideal positions.[229] If there are sufficiently large positional fluctuations or point defects, perfect registration of dots in the upper layer will be compromised, resulting in overlap between dots and a reduction of the maximum achievable density.

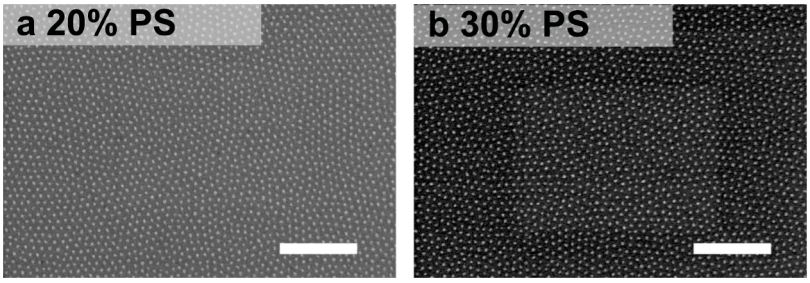

Figure 4.11: *Single layer plan-view SEM micrographs of PS-b-PDMS (22.5k-4.5k) with 20 wt % PS (a), and 30 wt % PS. All scale bars are 250 nm. Reprinted with permission from ref. [30]. Copyright © 2016 American Chemical Society.*

4.4 Analysis of Dot Overlap in Double- and Triple-Layer Patterns

Although visual analysis of an SEM micrograph can provide qualitative information regarding the degree of order, a better method to quantify the level of defects and deformation in the observed dot pattern is required to rationally optimize a given system. A formalism of finite strain theory was applied as follows. Briefly, from SEM micrographs of honeycomb dot patterns formed from two layers, the intra-layer coordination shell of each dot was determined by identifying the set of coordinating dots of minimum centrosymmetry parameter 1[224] (see Methods

section for more detail). The deviation of each coordination shell, relative to a perfectly regular hexagonal coordination shell, can be quantified *via* the deformation gradient tensor F_N,[226] which is given by[225]

$$F_N = (\sum_{i=1}^{6} d_i^0 \bigotimes d_i^0)^{-1} (\sum_{i=1}^{6} d_i^0 \bigotimes d_i^N) \tag{4.4.1}$$

where d_i^N and d_i^0 are the vectors connecting the central dot to coordinating dots in the deformed and undeformed configurations, respectively. Finally, the singular values of F_N are used to calculate the mean hydrostatic strain $\bar{\epsilon}$, of each coordination shell (see Methods section for more detail). It is noted that the hydrostatic strain is simply a measure of how different the local environment of each dot is from a perfect hexagonal lattice.[230] This should not be confused with mechanical stress (that results in the deformation of the lattice).

A demonstration of this approach is shown in Figure 4.12a, an SEM micrograph of a sequentially processed double layer honeycomb pattern made from a blend of PS-*b*-PDMS (31k-14.5k) with 30 wt % PS. This BCP has a higher molecular weight than the PS-*b*-PDMS (22.5k-4.5k) used in Figures 4.8-4.10, and the resulting dot pattern is of considerably higher quality. The dots within the pattern in Figure 4.12a are distinct with little overlap, and can be easily differentiated based on their layer of origin (Figure 4.12b), where each dot is colored by $\bar{\epsilon}$ and the coordination shell is visualized *via* Voronoi tessellation. Both layers are highly ordered hexagonal lattices, in which each dot has hexagonal intra-layer coordination (it should noted that there is a non-zero point defect density, but in all samples the defect density of the individual single layers is found to be less than 1 % of all dots, see Figure 4.13). Moreover, both layers possess identical lattice parameters (44.3 $\pm$ 0.1 nm), and distributions of $\bar{\epsilon}$ for each layer (Figure 4.14) are both found to be normally distributed (see Figure 4.15 for large scale statistics), with standard deviations of $\sigma_{\bar{\epsilon}}$ = 1.8 %. A representation of the dot positions is shown in Figure 4.12a, where each dot is colored by the difference of closest nearest neighbour center-to-center

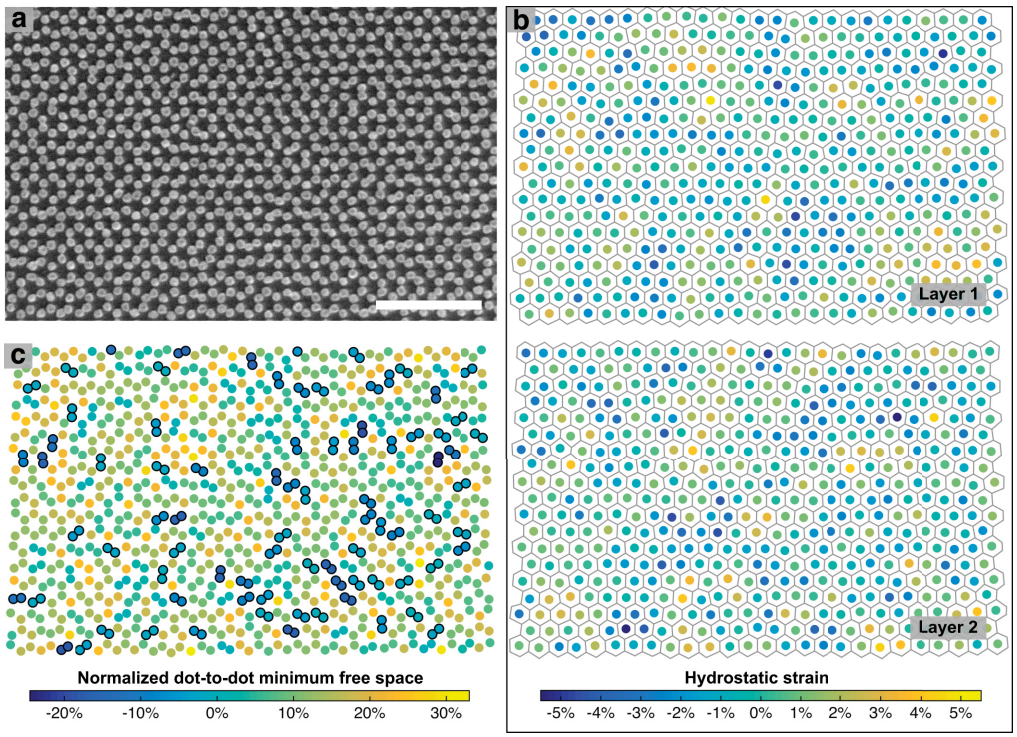

Figure 4.12: *Analysis of double layer dot patterns. (a) SEM micrograph of double layer honeycomb dot pattern formed via sequential layer deposition of PS-b-PDMS (31k-14.5k) with 30 wt % PS (scale bar = 250 nm), which is separated into (b) individual single layers patterns, where each dot is colored by its mean hydrostatic strain. The deformation of the local coordination shell is visualized by Voronoi tessellation. (c) Dot pattern in (a) colored by the difference of closest neighbour center-to-center dot spacing and dot diameter (normalized by the average dot diameter) where overlapping dots are marked with a black border. Reprinted with permission from ref. [30]. Copyright © 2016 American Chemical Society.*

dot spacing and dot diameter (normalized by the average dot diameter), where overlapping dots are marked with a black border. Despite both individual layers being highly ordered and parametrically indistinguishable from each other, we see that there is a significant percentage of dots that are overlapping with dots from another layer (17 % dot overlap, where two dots are defined to overlap if their center-to-center distance is less than the average dot diameter).

To approach the theoretical limits for density multiplication *via* sequential layer deposition, it is necessary to design material systems and methods that minimize dot overlap between layers. To this end, we have developed an empirical model that can be used to describe and predict the amount of dot overlap produced by sequential layer deposition of BCP dot patterns. In this model, the amount of dot overlap can be predicted from only two material parameters: the standard deviation in hydrostatic strain, $\sigma_{\bar{\epsilon}}$, and the dimensionless constant, $\beta = \sqrt{3}d_0/L_0$, where d_0 is the mean dot diameter and L_0 is the lattice parameter. From the results shown in Figure 4.10 it was found that the combined layer dot pattern could be described by the superposition of two single layer hexagonal lattices, where the dots are registered to interstitial positions with a random perturbation set by the value of $\sigma_{\bar{\epsilon}}$. The predictions of this model are shown in Figure 4.20 and 4.21, which is a contour map of dot overlap as a function of β and $\sigma_{\bar{\epsilon}}$. As expected, this model predicts that the total amount of overlap decreases with both β and $\sigma_{\bar{\epsilon}}$.

In order to validate the predictions of this model, a series of sequentially deposited honeycomb dot lattices were fabricated using different β and $\sigma_{\bar{\epsilon}}$ parameters. These parameters are systematically varied by adjusting the fraction of polystyrene blended with PS-*b*-PDMS (31k-14.5k), ranging from 30 wt % PS to 50 wt % PS (see Figure 4.16, 4.17, and 4.18) The values of β, $\sigma_{\bar{\epsilon}}$ and dot overlap are measured from the double layer dot patterns (Figures 4.21) for each polymer blend. It was found that the measured overlap for each polymer blend agrees within error of the values predicted in Figure 4.20 (see Table 4.2). Specifically, the overlaps are found to be 17 $\pm$ 3 %, 6 $\pm$ 1%, and 9 $\pm$ 1 % for PS fractions of 30 wt %, 40 wt

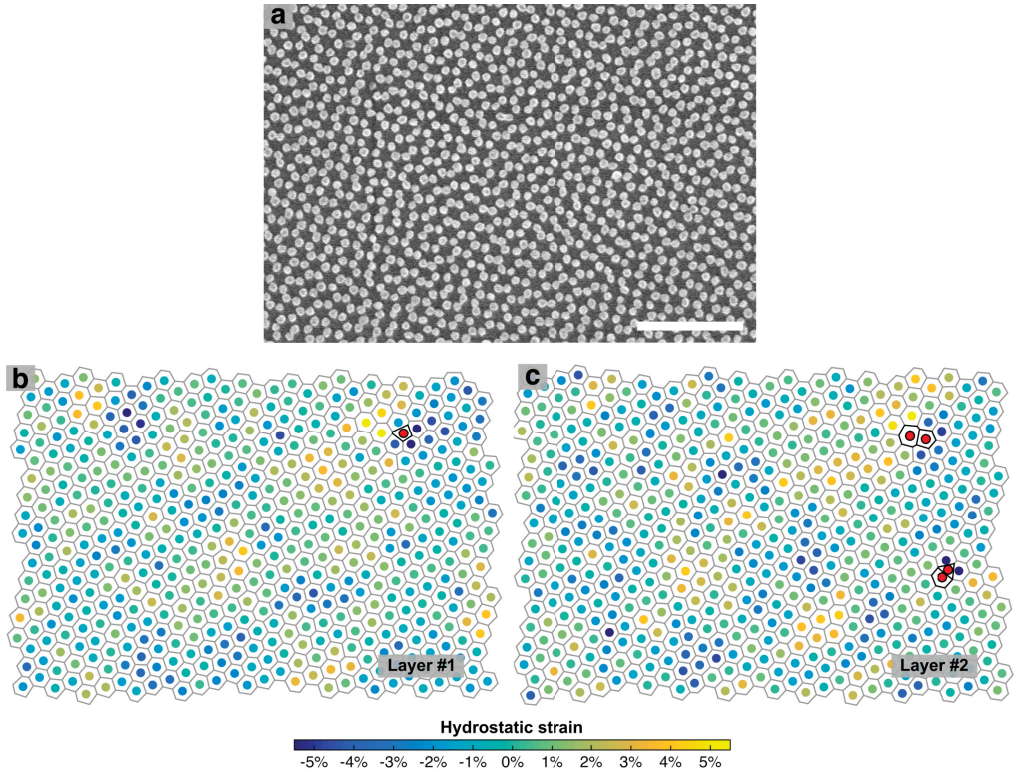

Figure 4.13: *Representative example of point defects in double layer patterns. (a) SEM micrograph of double layer honeycomb dot pattern formed via sequential processing of PS-b-PDMS (31k-14.5k) with 30 wt % PS (scale bar = 250 nm), which is separated into individual single layers patterns (b,c), where each dot is colored by its mean hydrostatic strain. In both (b and c), point defects are identified in red, which are dots possessing coordination numbers not equal to 6. As seen in this example, all defect densities were found to be less than 1 % of all dots. Reprinted with permission from ref. [30]. Copyright © 2016 American Chemical Society.*

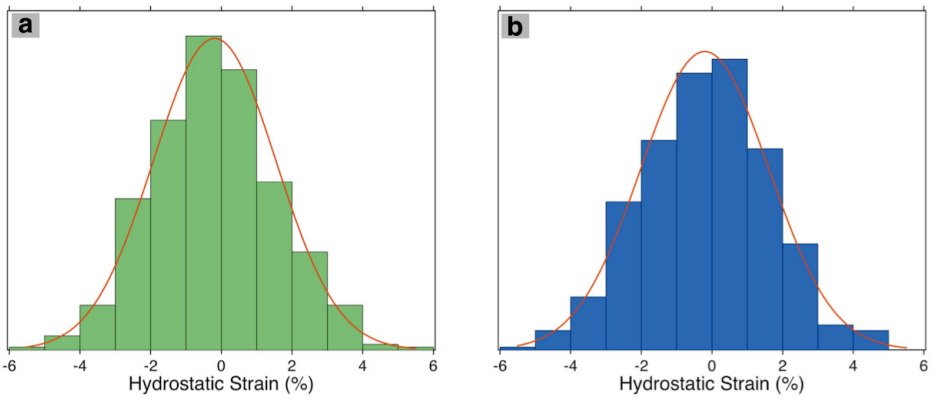

Figure 4.14: *Distribution of hydrostatic strains for the separated single layers of a double layer pattern of PS-b-PDMS (31k-14.5k) with 40 wt % PS. Overlaid on each histogram is a Gaussian with standard deviation and mean of the respective strain distribution. (a) and (b) correspond to layer 1 and layer 2 in Figure 4.12. Reprinted with permission from ref. [30]. Copyright © 2016 American Chemical Society.*

%, and 50 wt % respectively. The minimal overlap observed at a PS fraction of 40 wt % can be physically understood *via* inspection of the SEM micrographs in Figure 4.20 and 4.21, where it is seen that as the PS fraction becomes too large, the deviation of dots from a perfect hexagonal coordination shell becomes significant and begins to outweigh the increased amount of free space between dots (reduction in β), resulting in a large amount of overlap.

Minimizing the amount of dot overlap is clearly of primary concern when selecting polymers to be used for the fabrication of highly ordered, sequentially deposited dot patterns. However, if this technique is to be used for increasing absolute dot density, it is also necessary to minimize both dot overlap and the dot pattern lattice parameter. As such, a polymer, PS-*b*-PDMS (43k-8.5k), with a 25 % smaller lattice parameter (35.8 $\pm$ 0.5 nm) and slightly smaller values of β, $\sigma_{\bar{\epsilon}}$ parameters (0.71 $\pm$ 0.02 and 2.1 $\pm$ 0.1 %, respectively) was used for sequential layer deposition instead of the PS-*b*-PDMS (31k-14.5k) with 40 wt % PS (Figure 4.19). Shown in Figure 4.21d is an SEM micrograph of a double layer dot pattern formed

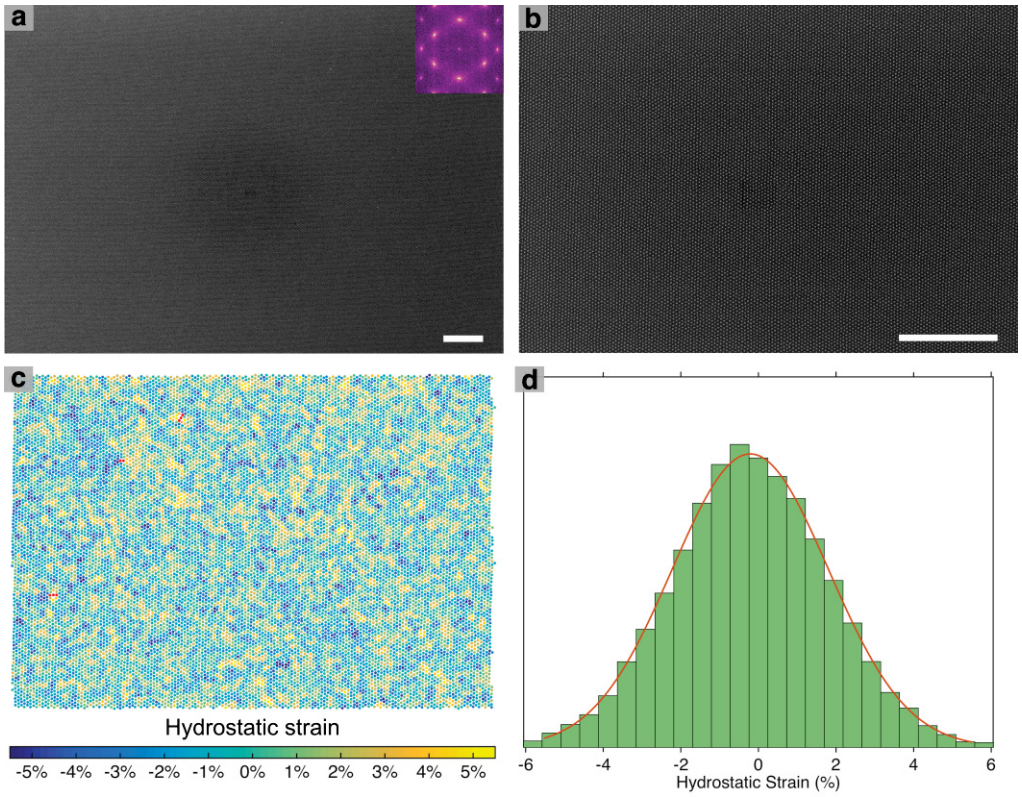

Figure 4.15: *(a) Large area (12.7 μm × 8.9 μm) SEM micrograph of PS-b-PDMS (43k-8.5k) dot pattern with FFT inset, which shows that this large region is composed of a single grain. (b) Zoomed-in view of (a) showing dots in more detail (all scale bars are 1μm). (c) Dots in (b) colored by hydrostatic strain and defected dots (non-sixfold coordination) are shown in red. (d) Distribution of hydrostatic strains in (d), overlaid curve is a Gaussian with standard deviation and mean of the strain distribution. Reprinted with permission from ref. [30]. Copyright © 2016 American Chemical Society.*

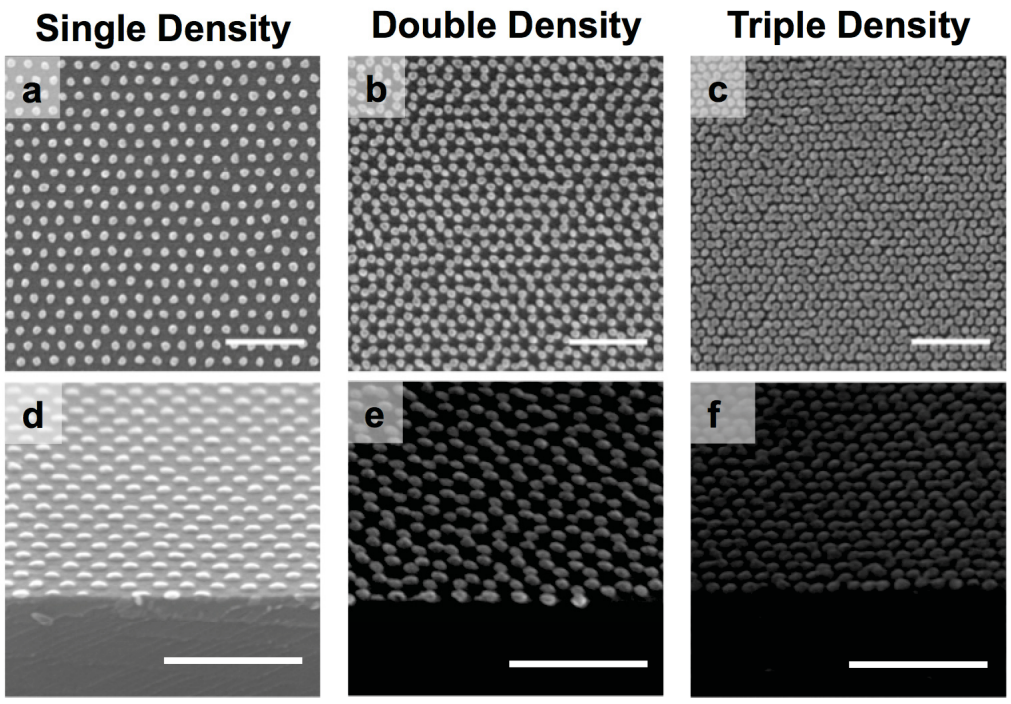

Figure 4.16: *(a-c) Single, double, and triple layer plan-view and (d-f) tilted SEM micrographs of PS-b-PDMS (31k-14.5k) with 30 wt % PS. All scale bars are 200 nm. Reprinted with permission from ref. [30]. Copyright © 2016 American Chemical Society.*

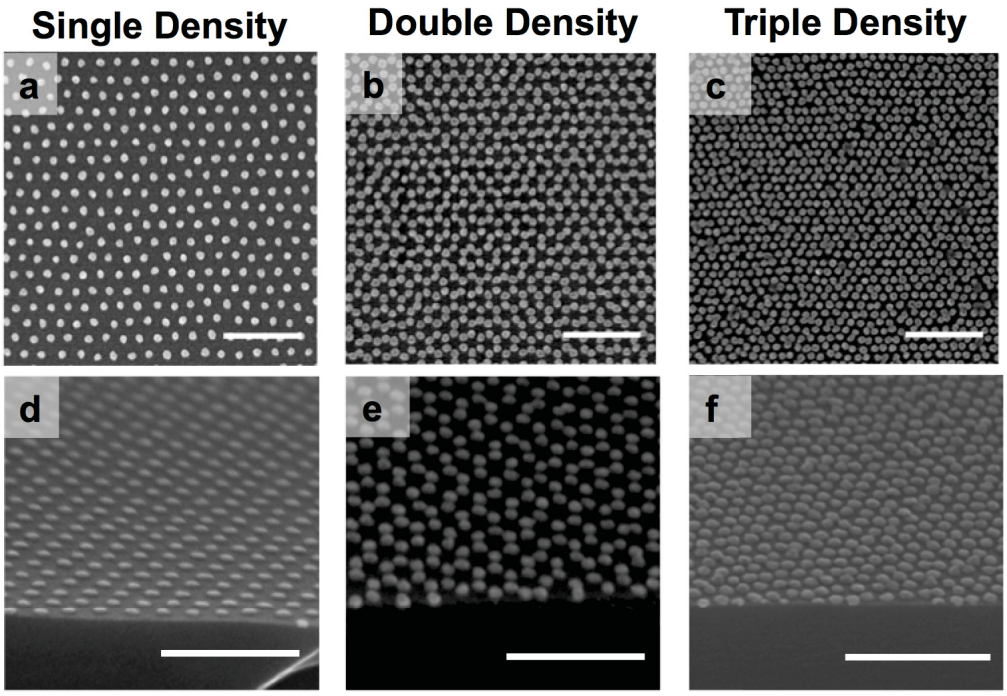

Figure 4.17: *(a-c) Single, double, and triple layer plan-view and (d-f) tilted SEM micrographs of PS-b-PDMS (31k-14.5k) with 40 wt % PS. All scale bars are 200 nm. Reprinted with permission from ref. [30]. Copyright © 2016 American Chemical Society.*

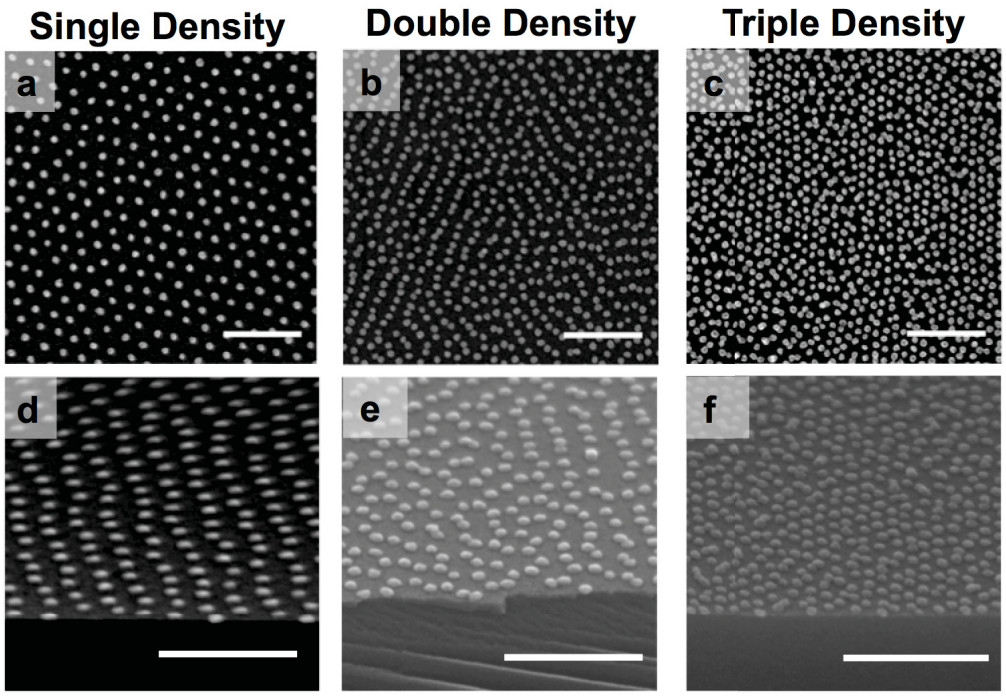

Figure 4.18: *(a-c) Single, double, and triple layer plan-view and (d-f) tilted SEM micrographs of PS-b-PDMS (31k-14.5k) with 50 wt % PS. All scale bars are 200 nm. Reprinted with permission from ref. [30]. Copyright © 2016 American Chemical Society.*

via the sequential layer deposition of PS-*b*-PDMS (43k-8.5k), resulting in a highly ordered lattice with a dot overlap of 3 ± 1 % (predicted overlap of 2.9 ± 0.8 %). Moreover, the dot density is found to be 1.1 Teradots/in^2, which is 60 % greater than the densities achieved with PS-*b*-PDMS (31k-14.5k) and 40 wt % PS.

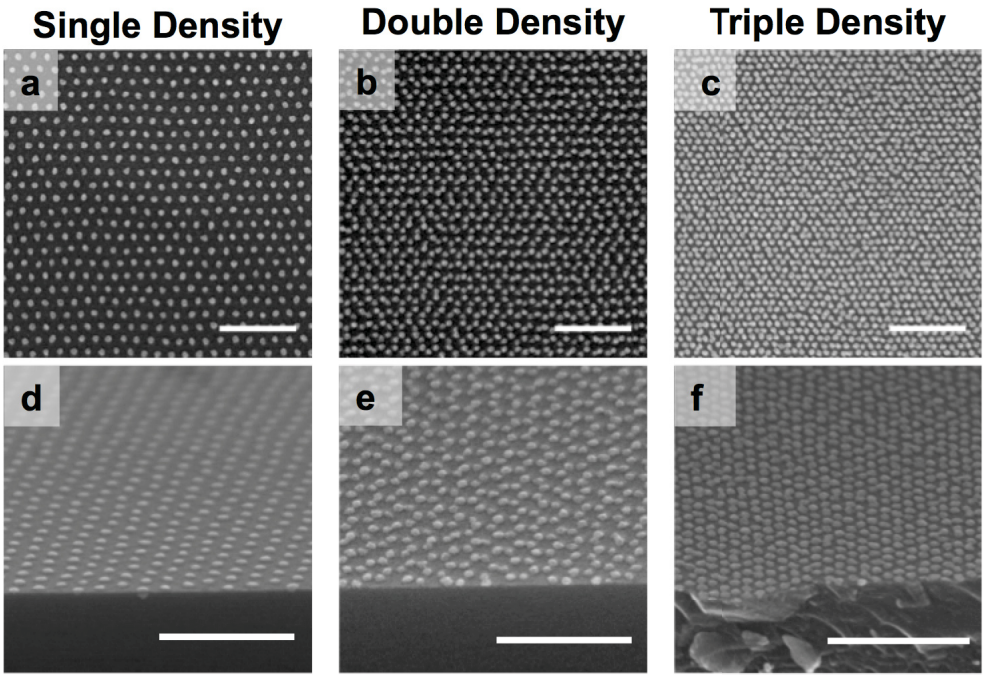

Figure 4.19: *(a-c) Single, double, and triple layer plan-view and (d-f) tilted SEM micrographs of PS-b-PDMS (43k-8.5k). All scale bars are 200 nm. Reprinted with permission from ref. [30]. Copyright © 2016 American Chemical Society.*

Shown in Figure 4.22a is the map of predicted overlap for triple layer dot patterns, which is very similar to the double layer overlap map, with the primary difference being greater amounts of overlap for identical β and $\sigma_{\bar{\epsilon}}$ parameters. As such, given these stricter requirements on β and $\sigma_{\bar{\epsilon}}$, triple layer dot patterns are made using PS-*b*-PDMS (43k-8.5k). The triple layer dot pattern of PS-*b*-PDMS (43k-8.5k) is shown in Figure 4.22b, which is found to have a 3 % defect density, 13 ± 3 % overlap (predicted overlap of 8 ± 3 %) and a dot density of 1.58 ± 0.05

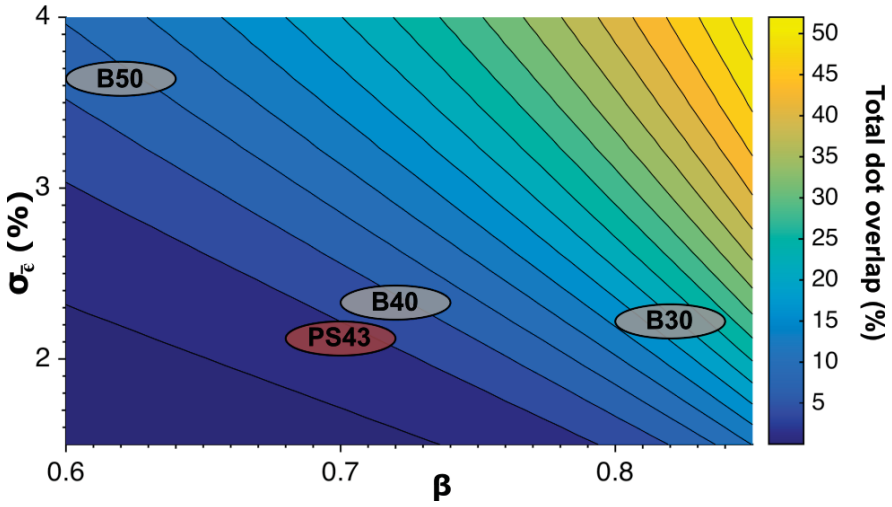

Figure 4.20: *Map of the predicted dot overlap for double layer dot patterns as a function of BCP material parameters β and σϵ. Contours are separated by 3 % overlap, with the lowest contour shown at 1 % overlap. The β and $\sigma_{\bar{\epsilon}}$ parameters for each of these polymers are marked on the dot overlap map, showing the predicted overlap expected for each of these polymers. Reprinted with permission from ref. [30]. Copyright © 2016 American Chemical Society.*

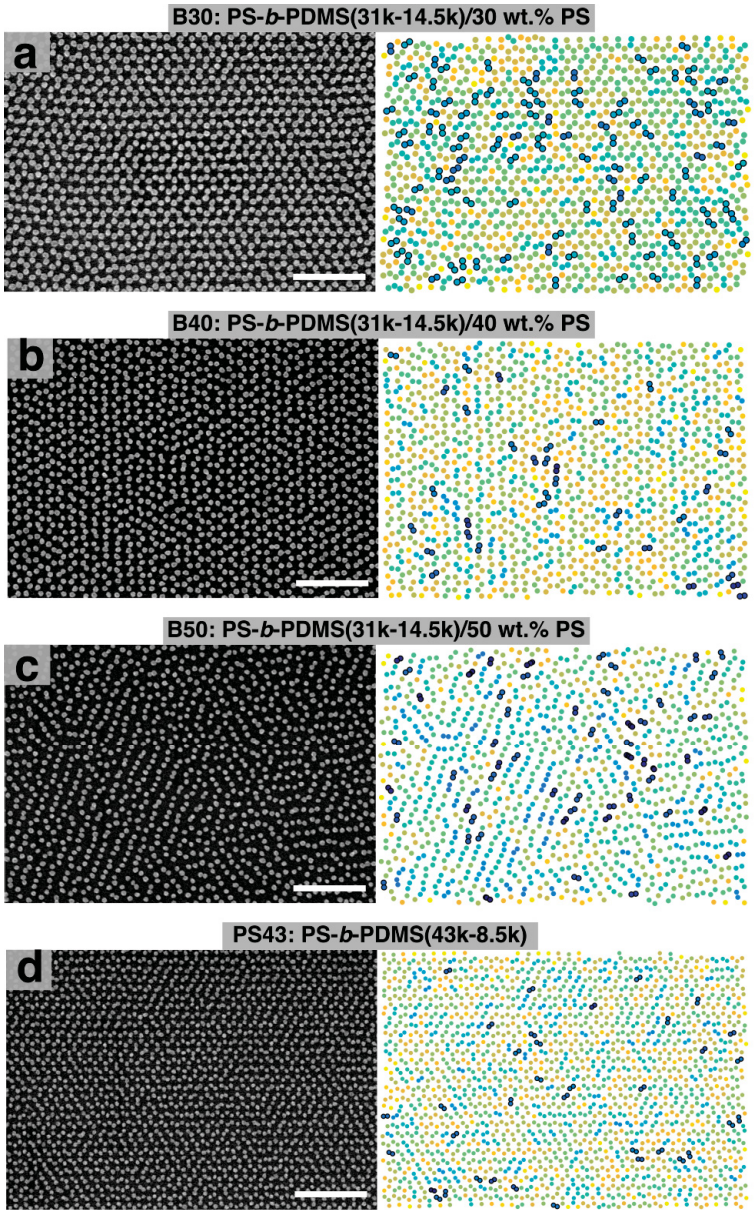

Figure 4.21: *SEM micrographs (left) of double layer dot patterns of PS-b-PDMS (31k-14.5k) with varying wt % PS (30, 40, 50) and PS-b-PDMS (43k-8.5k) respectively. Corresponding dot pattern colored by closest nearest neighbor distance (right), where overlapping dots are marked with a black border. All scale bars are 250 nm. Reprinted with permission from ref. [30]. Copyright © 2016 American Chemical Society.*

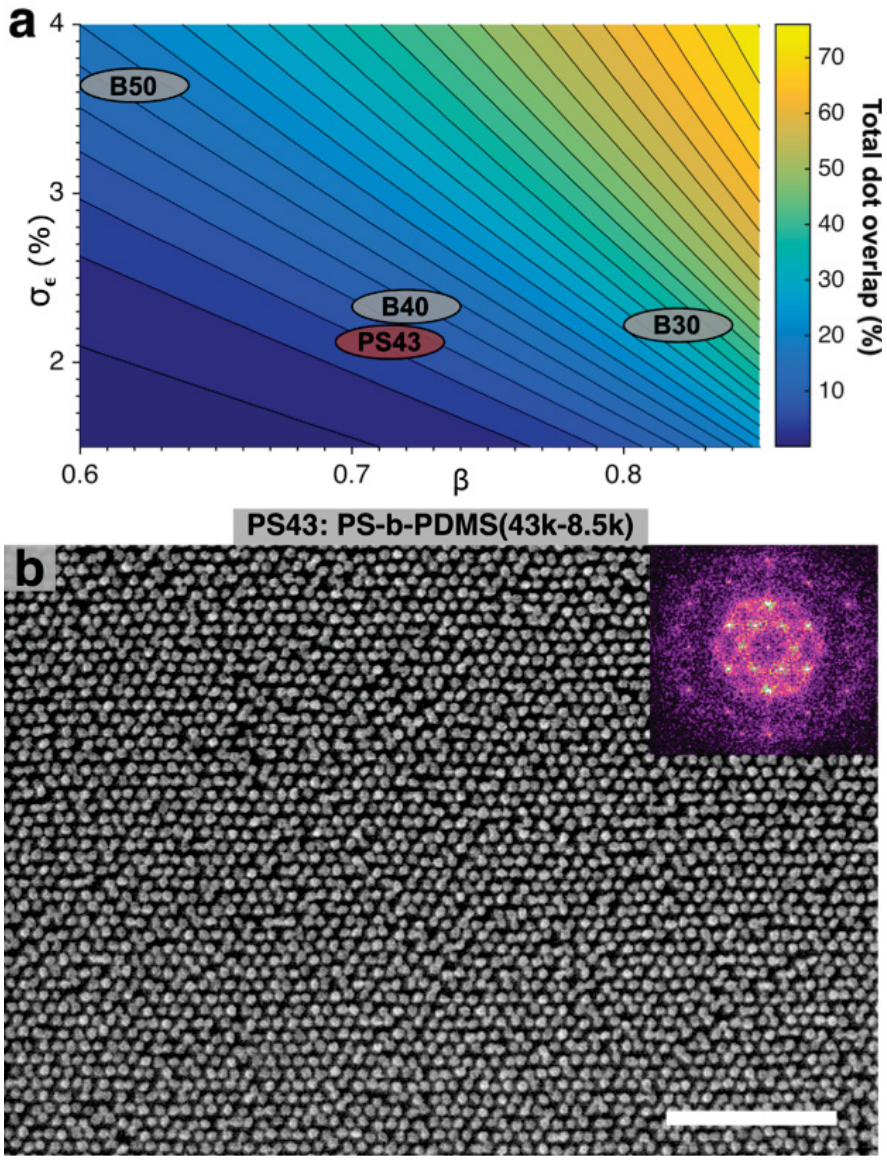

Figure 4.22: *Map of dot overlap for triple layer dot patterns. Contours are separated by 3 % overlap, with the lowest contour shown at 1 % overlap. (b) SEM micrograph of a triple layer dot pattern of PS-b-PDMS (43k-8.5k). The abbreviations PS43, B30, B40, and B50 are defined in Figure 4.20 and 4.21. Scale bar is 250 nm. Inset: FFT. Reprinted with permission from ref. [30]. Copyright © 2016 American Chemical Society.*

Table 4.2: *Values of Mean Dot Diameter d_0, Lattice Parameter L_0, β Parameter, Standard Deviation of Hydrostatic Strain $\sigma_{\bar{\epsilon}}$, Measured dot overlap, and Predicted Dot Overlap for Double Layer Patterns.*

BCP Sample	d_0 (nm)	L_0 (nm)	β	$\sigma_{\bar{\epsilon}}$	Measured Overlap (%)	Predicted Overlap (%)
PS-*b*-PDMS (31K-14.5K)+30 wt %	20.6±0.5	43.9	0.81±0.02	2.0	17±3	17±2
PS-*b*-PDMS (31K-14.5K)+40 wt %	18.8±0.5	44.9	0.73±0.02	2.3	6±1	7±1
PS-*b*-PDMS (31K-14.5K)+50 wt%	17.4±0.5	48.1	0.63±0.02	3.7	9±1	10±1
PS-*b*-PDMS (43K-8.5K)	14.7±0.5	36.0	0.71±0.02	2.1	3±1	3±0.6

Td/in^2. Inspection of the FFT (Figure 4.22b) of this triple layer pattern reveals a well-defined spot pattern, indicating long-range periodic ordering. To contrast, the triple density pattern shown in Figures 4.8 and 4.9, formed from the smaller BCP, PS-*b*-PDMS (22.5k-4.5k), has 64 % of overlap. Addition of 15 wt % PS, which resulted in smaller dot diameters and a corresponding decrease of β (Figure 4.8l and 4.9d), led to a lower overlap of 30 % in the resulting pattern (Table 4.1).

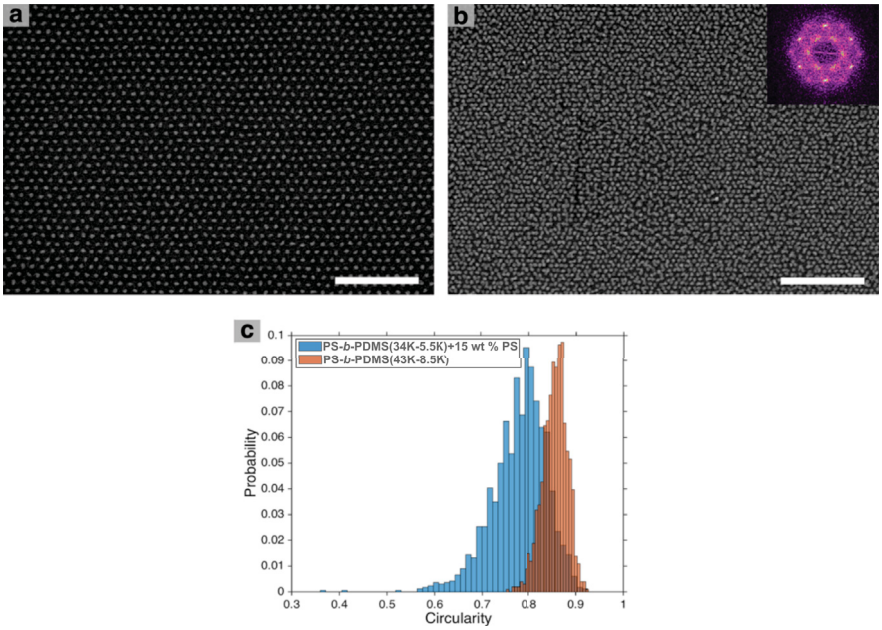

Figure 4.23: *SEM micrographs of (a) single layer and (b) triple layer nanopatterns formed using PS-b-PDMS (34k-5.5k) and 15 wt % PS. Inset: FFT. (c) Histograms of dot circularity for single layer patterns of PS-b-PDMS (43k-8.5k) and PS-b-PDMS (34k-5.5k) with 15 wt % PS. Circularity is calculated as 4π[area]/[perimeter]^2. Scale bars are 250 nm. Reprinted with permission from ref. [30]. Copyright © 2016 American Chemical Society.*

To further explore the utility of this density multiplication technique, it was applied to PS-*b*-PDMS (34k-5.5k) with 15 wt % PS, which has a smaller lattice parameter of 28.1 nm, and single layer parameters of β = 0.72 and $\sigma_{\bar{\epsilon}}$ = 2.5 % (predicted overlap of 16 $\pm$ 6 %), giving a measured single layer dot density of 0.97

Td/in^2 (Figure 4.23a). These triple layer patterns of PS-*b*-PDMS (34k-5.5k) with 15 wt % PS were found to have a defect density of 17 %, dot density of 1.9 $\pm$ 0.2 Td/in^2 after accounting for 35 $\pm$ 6 % overlap (Figure 4.23b). It is noted that this measured overlap is much larger than the predicted overlap of 16 %. Inspection of the PS-*b*-PDMS (34k-5.5k) with 15 wt % PS dot patterns (Figure 4.23a) reveals that the individual dots are irregularly shaped and non-circular, indicating that further optimization of the solvent annealing conditions need to be performed. The non-circular shape of these dots is quantified by measuring the circularity of the dots, where a perfect circle has circularity of 1 and infinitely thin rod has a circularity of 0. It is found that the dots of PS-*b*-PDMS (34k-5.5k) with 15 wt % PS have a mean circularity of 0.78 with a standard deviation of 0.06; when compared to the dots from PS-*b*-PDMS (43k-8.5k), which have a circularity of 0.86 and standard deviation of 0.03. We see that the dots from PS-*b*-PDMS (34k-5.5k) with 15 wt % PS are significantly less circular and twice as polydisperse, Figure 4.23c. As such, the poor circularity and large shape dispersity is the likely cause for the discrepancy between predicted and observed overlap values, as it is assumed in the model that the dots are monodisperse circles.

4.5 Discussion

Despite achieving $\sim$2 Td/in^2 using this density multiplication technique, other groups have reported dot densities greater than 5 Td/in^2 using only bottom-up methods on planar substrates.[31, 32, 218] However, if these high density dot patterns are viable candidates for bit-patterned media recording, it is necessary to characterize their degree of disorder. Specifically, it has been shown that for areal densities of $\sim$5 Td/in^2 it is necessary for the fluctuations in dot spacing be less than 5 %.[231] Therefore, the areal density of dots with less than 5 % hydrostatic strain, $\rho_{\bar{\epsilon}}$, can be used as a metric to assess the potential viability of BCP dot patterns for high density bit-patterned media recording.

Shown in Figure 4.24 is a plot of $\rho_{\bar{\epsilon}}$ vs χN for previously reported PS-*b*-PDMS BCP dot patterns taken from literature.[8, 31–34, 36–39] We see that as N decreases (starting from large N) the value of $\rho_{\bar{\epsilon}}$ increases monotonically, following the expected $N^{-4/3}$ relation for dot density.[57] However, as N is further decreased $\rho_{\bar{\epsilon}}$ begins to deviate from the $N^{-4/3}$ density relation, eventually reaching a maximum at χN ~45 of $\rho_{\bar{\epsilon}}$ ~2 Td/in^2. At lower N, we see that the $\rho_{\bar{\epsilon}}$ begins decreasing and is already below 1 Td/in^2 at χN = 20. This behaviour of $\rho_{\bar{\epsilon}}$ with N can be better understood by inspection of the inset dot patterns in Figure 4.24, which are images of dot patterns of for χN = 22.6, 44.5 and 148.3. At large N, we see that the defect density (number of points with non six-fold symmetry) is very low, and the majority of non-defected dots (~90 %) have less than 5 % hydrostatic strain. As such, $\rho_{\bar{\epsilon}}$ is very close to the raw dot density and follows a $N^{-4/3}$ relation. At intermediate N we see that there is an increase in both defect density and $\sigma_{\bar{\epsilon}}$, which is responsible for lower values of $\rho_{\bar{\epsilon}}$ relative to the expected $N^{-4/3}$. Finally, at low N, where the raw dot densities are ~5 Td/in^2, $\rho_{\bar{\epsilon}}$ is comparatively much less (~1 Td/in^2), which is a primarily due to a very large increase in defect density.

From this analysis, we see that when using traditional single layer methods on a planar surface, the value of of $\rho_{\bar{\epsilon}}$ for PS-*b*-PDMS dot patterns appears to be limited to be less than 2 Td/in^2. Now, if $\rho_{\bar{\epsilon}}$ is computed for the triple layer patterns of PS-*b*-PDMS (34k-5.5k)/15 wt % PS and PS-*b*-PDMS (43k-8.5k), (1.8 and 1.5 Td/in^2 respectively) we see that these values compare quite favorably to the maximum value of $\rho_{\bar{\epsilon}}$ for single layers. These results demonstrate that triple layer patterning can used to achieve state-of-the-art dot pattern densities, when adjusting for the degree of ordering/defectivity. It is however important to note that the equilibrium defect density of a self-assembled BCP pattern is vanishingly small.[229] As such, the calculated values of $\rho_{\bar{\epsilon}}$ for low N polymers does not necessarily represent some fundamental limit, but are instead likely limited by a non-optimized annealing process. This trend of increasing defectivity with decreasing N is likely the result of the extremely narrow processing window (polymer to solvent ratio) during solvent annealing of low N polymers.[207, 232] As such, this density tripling method is

potentially attractive from a processing perspective, where similar densities can be achieved, but a much larger tolerance for fluctuations in the solvent annealing parameters are permissible due to the fact that larger N polymers can be used.

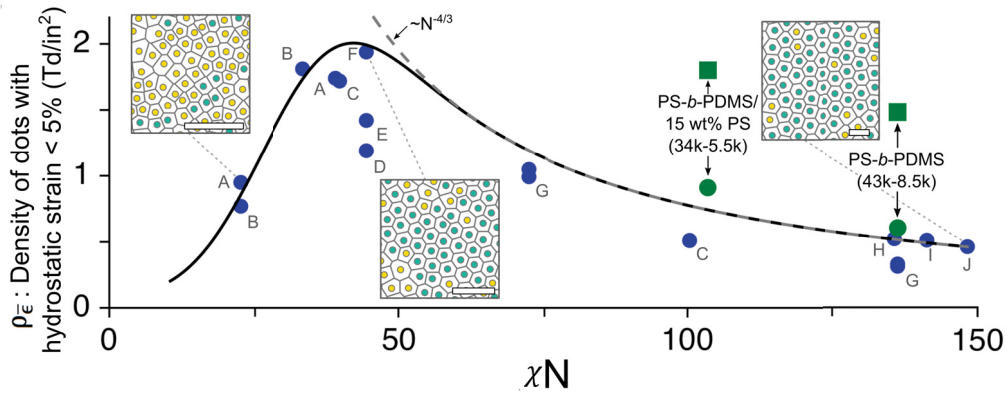

Figure 4.24: *Areal density of dots with less than 5 % hydrostatic strain ($\rho_{\bar{\epsilon}}$) of various PS-b-PDMS BCP single layer patterns taken from literature (blue circles), this work (green circles) and the corresponding triple layer patterns (green squares). Embedded are images of dot patterns of for χN = 22.6, 44.5 and 148.3; dots with less than 5 % hydrostatic strain are colored in cyan, while dots with hydrostatic strain greater than 5 % are colored in yellow. Voronoi tessellation is also shown to visualize local deviations from a perfect hexagonal lattice. Each point on the plot is from the following sources (A, [31]; B, [32]; C, [33]; D, [34]; E, [35]; F, [36]; G, [37]; H, [8]; I, [38] and J,[39]). The solid curve is simply an envelope of the maximum effective density as a function of χN.*

From the data presented in this work, through judicious selection of BCP properties and careful optimization of the annealing process,[207] this density multiplication approach could be potentially surpass the current density limit of highly ordered dot arrays. Specifically, reduction in the β parameter could be achieved by tuning the respective volume fractions of each block. For instance, in the case of PS-*b*-PDMS, increasing the volume fraction of PS to PDMS could reduce the value of β. Secondly, fluctuations in dot spacing, dot size and $\sigma_{\bar{\epsilon}}$, result

from variations of the BCP film morphology, the degree of phase separation, and polydispersity (composition and N) of the BCP.[233] The polydispersity can be minimized *via* synthetic control,[234] the degree of phase separation is determined by the segregation strength χN, and the BCP film morphology can be contolled by the annealing conditions.[232] It is also noted that the swelling ratio of the films during the annealing process is subject to room temperature fluctuations,[28] where the swelling ratio can change from 1.8 to 2.0 (see Figure 4.2). Therefore, differences in the swelling ratio of films between subsequent layers may change the dot morphology and spacing. These differences between successive layers will likely degrade the quality of these density-multiplied patterns. As such, improvements in annealing chamber design, such as temperature control and computer control feedback to solvent vapour flow to maintain a constant swelling ratio, could be used to alleviate this problem and further optimize this approach towards density multiplication.[122, 133]

4.6 Conclusions

In this work, we suggest a straightforward method for sequential patterning of BCP hexagonal nanodot arrays using a bottom-up, self-assembly approach. The quality of the resulting patterns is dependent upon the lattice parameter of the hexagonal pattern, and the diameter and circularity of the dots, factors that can be controlled *via* manipulation of the polymer composition and annealing conditions, among others. Given the wide applicability of this method to other dot forming BCP systems, density multiplication approach could be extended to other BCP systems, notably recent efforts towards the synthesis of new families of high χ parameter, low N and low polydispersity BCPs to yield tightly packed nanopatterned arrays.

5

Incommensurate Block Copolymer Epitaxy for Moiré Pattern Fabrication

In this chapter, we demonstrate a new method of fabricating Moiré nanopatterns *via* block copolymer (BCP) self-assembly. Briefly, a layer of hexagonal packed silica dot patterns was obtained *via* annealing and etching polystyrene-*block*-polydimethylsiloxane (PS-*b*-PDMS) thin film on a silicon chip. Next, another thin film of dot-forming PS-*b*-PDMS with different periodicity was annealed and etched on top, resulting in a Moiré superstructure. Four distinct Moiré superstructures were demonstrated through different BCP combinations and different annealing order. The registration force of shallow BCP dots in the bottom layer is sufficient to direct the self-assembly of the top layer and take on a preferred relative angle of rotation. Large-area helium ion microscopy (HIM) imaging enabled quantification of the distributions of relative rotations between the two lattices in the Moiré superstructures, yielding statistically meaningful results for each combination. The effect of bottom layer dot size and pitch to the registration of top layer BCP dots was also studied.

5.1 Moiré Patterns and Their Applications in Nanoscience

Moiré patterns are a type of higher order pattern formed from superimposing two or more periodic arrays of different size, periodicity, or angle. For example, Figure 5.1a and b are two Moiré patterns composed of two hexagonal packed dot patterns with different rotation angles and center-to-center spacings, respectively. It is a common phenomenon in daily life, and has been used in art, security, strain analysis, holography, and defect measurement for decades.[235–239] In nanoscience, Moiré nanopatterns are often reported in transmission electron microscope (TEM) micrographs of polycrystalline nanoparticles.[240] It serves as a useful tool to understand the structure or quality of nanoparticles. Moiré patterns are also reported in scanning tunneling microscope (STM) study of graphene bilayers. In this case, Moiré patterns are electron wave maps caused by misaligned graphene layers.[241, 242] Various methods, such as electron beam lithography (EBL),[243] nanoimprint lithography,[244] self-assembly of PS spheres,[245] anodic aluminum oxide,[246] and photolithography,[247] have been demonstrated to produce Moiré patterns. Plasmonic crystals made with Moiré patterns exhibited more surface plasma polarization modes compared to regular plasmonic crystals.[248] Moiré photonic crystals showed richer band gaps and may help to improve performance of photonic devices.[245, 247]. Additionally, Moiré nanopatterns also find applications in guiding scanning probe microscopes.[243]

In BCP self-assembly, Moiré patterns are commonly observed in imaging large scale BCP patterns, which is caused by the interference of periodic BCP nanopatterns and the resolution of the micrograph.[249] This unique phenomenon has been proven to be a fast analysis method to measure shape, size, orientation, grain boundaries, lattice parameters, and even defects of grains in the resulting BCP nanopatterns.[249, 250] So far, utilizing self-assembled block copolymer patterns as templates to fabricate Moiré nanopatterns was only reported by Luchnikov

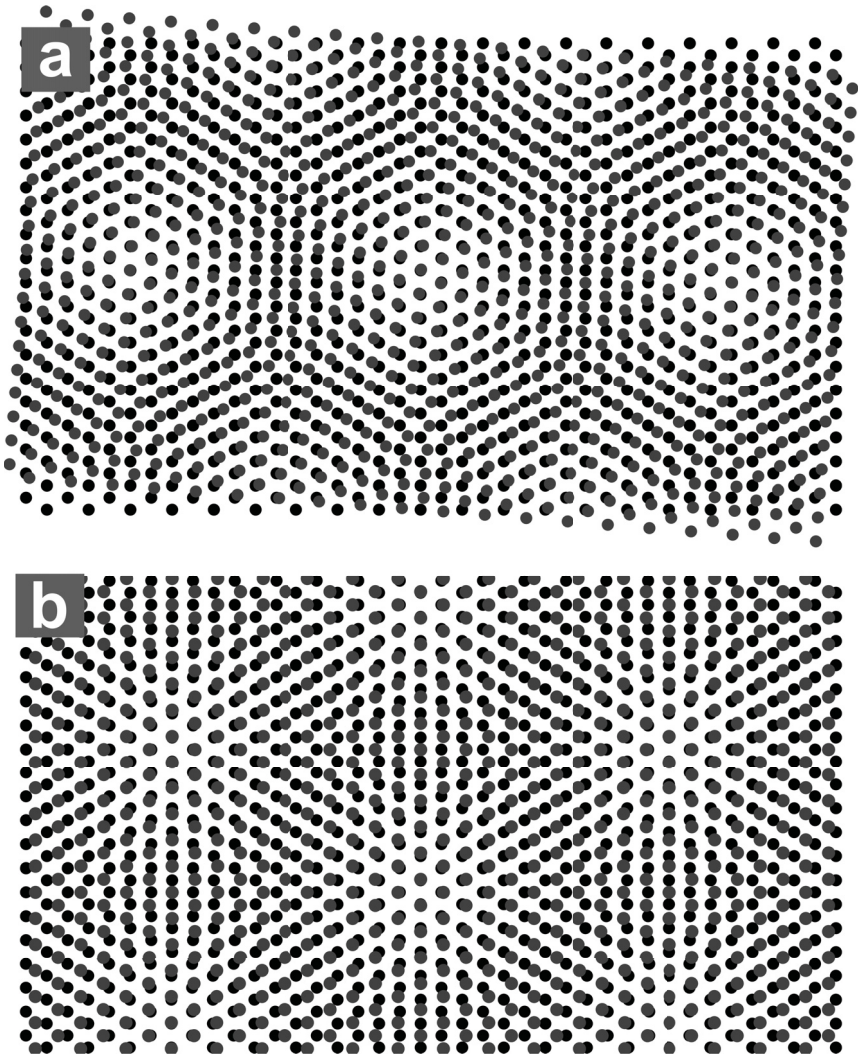

Figure 5.1: *Schematic illustrating of two Moiré patterns formed via superimposing two hexagonal packed dot arrays with different rotation angle (a) and pitch (b).*

and co-workers in 2007.[251] Arbitrarily oriented Moiré structures and labyrinth-like nanopatterns were observed by TEM when free-standing monolayers of self-assembled hexagonal dot array BCP films were folded onto themselves, forming a bilayer.[251] Unfortunately, this fabrication process had no control in the folding process of self-assembled BCP films and the resulting Moiré patterns.

5.2 Full Bottom-Up Directed Self-Assembly of Block Copolymer Thin Films

Directed self-assembly (DSA) is of great interest to induce long-range order, orientation, and registry of BCP nanopatterns, and to reduce the incidence of defects.[52, 55, 56, 107, 108, 126, 146, 218, 220, 252–259] DSA is an epitaxial approach that relies upon sparse prepatterning of a substrate with chemical or topological features to guide the process of BCP self-assembly in a spatially-defined manner.[16, 20, 53] DSA has been demonstrated to yield low-defect, periodic patterns with long range order,[8, 107, 108, 143, 260] as well as complex patterns such as bands,[106] jogs,[12] T-junctions,[12] concentric circles,[11] square arrays,[92, 145] and some 3D nanopatterns.[145] With respect to the application of DSA to dot patterns, arrays of chemical and topological dot patterns, prepared by EBL, have been most commonly used.[8, 107, 261] For instance, chemical patterns with varying feature densities from 1:1 to more sparse arrangements have been shown to exert control over orientational order.[108, 148, 262] Ross and co-workers showed that hexagonal arrays of 30 nm-high pillars of silica could substitute (act as surrogates) for minority domains within hexagonal ordered BCPs,[8] if the pillars had a spacing that was a multiple of the periodicity of the BCP pattern (an integral multiple of BCP pitch).[149, 263] Trenches and other hole arrays, also produced *via* EBL, have been used to direct the long range order of BCP dot patterns,[23, 32, 263–265] as well as the use of nanoimprint lithography stamps.[16]

Using only bottom-up methods, commensurate assembly of a second BCP pattern directed by a first pattern can produce hierarchical topographical nanopatterns[35, 266] or metal/metal-oxide binary nanoarrays.[198, 221, 267] The full bottom-up directed self-assembly of BCP own several advantages compared to common directed self-assembly process. Ross and co-workers demonstrated that a 34 nm pitch line pattern from a bigger PS-*b*-PDMS BCP could be used to direct self-assembly of a smaller line-forming PS-*b*-PDMS with 17 nm pitch, which enable them to use relative large features to direct self-assembly of sub-20 nm BCPs pattern.[266] Later, they demonstrated this idea with a line or dot forming BCP onto the patterns fabricated from bigger line or dot forming BCP patterns. Kim and co-workers showed that sequential annealing of different PS-*b*-P4VP thin films enabled fabrication of multicomponent binary nanopattern arrays on silicon surface.[198] Sub-10 nm metal nanopatterns, such as line-line, line-dots, and dot-dot patterns, were demonstrated with metal composition of Au, Pt, Fe, Pd, and Co. These patterns showed potential in charge-trap memory devices and plasmonic applications. Spatz and co-workers and Yager and their co-workers also reported hierarchical BCP nanopatterns by sequentially annealing BCP on surface.[221, 267] However, little work has been done to statistically quantify the epitaxially alignment produced using these bottom-up methods. In last chapter, we described the use of an array of hexagonal silica dots, prepared *via* self-assembly of BCPs of PS-*b*-PDMS, to direct the self-assembly of a top layer of a thin film of the same PS-*b*-PDMS BCP. The commensurate, two-layered pattern was converted to a honeycomb pattern of silica dots with a concomitant doubling of the density of the dots. In this chapter, nanoscale structures produced *via* sequential deposition of self-assembled BCP hexagonal dot arrays with incommensurate periodicity is investigated. It is found that a unique set of preferential orientation relationship(s) exist between the two BCP dot arrays, leading to formation of Moiré superstructures not previously observed in directed self-assembly. The resulting Moiré superstructures, are driven by registration of the top layers by the bottom layers, leading to large multi-micron-sized grains with preferred, majority phases.

5.3 Methods

5.3.1 Materials

PS-*b*-PDMS (31k-14.5k, PDI: 1.15, N_{PS}: 295, N_{PDMS}: 196, f_{PDMS} = 0.34), PS-*b*-PDMS (43k-8.5k, PDI: 1.04, N_{PS}: 410, N_{PDMS}: 115, f_{PDMS} = 0.18), PS-*b*-PDMS (22.5k-4.5k, PDI: 1.09, N_{PS}: 214, N_{PDMS}: 61, f_{PDMS} = 0.18), and polystyrene (PS) (10k, PDI: 1.09) were obtained from Polymer Source Inc. Toluene and THF were purchased from Fisher Scientific. Silicon wafers ($\langle 100 \rangle$, 4 inch diameter, thickness: 525 $\pm$ 25 μm, p-type, boron doped, 0.005 Ω·cm in resistivity) were purchased from WRS Materials. Sulfuric acid (96 %) and hydrogen peroxide (30 %) were purchased from Avantor Performance Materials.

5.3.2 Silicon Wafer Dicing and Cleaning

Silicon wafers were diced into 1 cm $\times$ 1 cm squares by a DSA 321 dicing saw and cleaned with piranha solution [3:1 v/v sulfuric acid (96 %)/hydrogen peroxide (30 %)].

5.3.3 EBL Pillar Array Fabrication

A 15-nm-thick HSQ thin film was spin cast from a 1 % hydrogen silsesquioxane (HSQ) (methyl isobutyl ketone as solvent) at 8000 rpm for 60 s onto a piranha cleaned 1 cm $\times$ 1 cm silicon chip. The samples were then transferred into Raith 150-two EBL system for pattern writing (30 kV, 10 μm aperture, 9 mm working distance, and 0.02 μC dosage). The samples were then immersed into a 25 % tetramethylammonium hydroxide for 60 s and then rinsed in deionized water and dried in nitrogen stream.

5.3.4 Sample Preparation

The general experimental procedure used in this work of sequential annealing of block copolymer thin films, and conversion into silica dot patterns, is shown in Figure 5.2. A detailed description of BCP thin film preparation, annealing procedure, annealing conditions, etching recipes for each BCP sample, and sequential annealing procedures can be found in previous chapter and it can also be found in reference [27, 30]. Briefly, the fabrication process begins by spin casting a dot-forming BCP or BCP/PS blend thin film (bottom layer) on piranha-cleaned 1 cm $\times$ 1 cm silicon chips from a 1 wt % toluene solution. For each BCP or BCP/PS blend, the film thickness was optimized to form a single layer dot pattern after solvent annealing. In this chapter, three different BCP or BCP/PS blends were used, PS-*b*-PDMS (13k-14.5k)/30 wt % PS (denoted as B30), PS-*b*-PDMS (43k-8.5k) (denoted as P43), and PS-*b*-PDMS (22.5k-4.5k) (denoted as P22). The optimised film thicknesses for B30, P43, and P22 were $\sim$32 nm, $\sim$30 nm, and $\sim$25 nm respectively. The BCP or BCP/PS blended films were annealed in a custom made solvent annealing chamber, where THF was used as the annealing solvent.[27, 30] Film thickness was monitored *in situ* during the annealing process using ellipsometry ($\lambda = 632.8$ nm, $\theta = 70°$). The optimised final degrees of swelling (swollen film thickness/initial film thickness) of each sample were 2.0 for B30 and P43, and $\sim$1.6 for P22. After annealing, hexagonally packed spherical PDMS domains were bound within the PS matrix. The annealed BCP or BCP/PS blend films were then converted to a silica dot array by applying a CF_4/O_2 RIE treatment (Figure 5.2a). The etching recipe for each BCP film is described in previous chapter and can also be found in reference. [30] During RIE etching, the PDMS domains are oxidized to SiO_x and PS domains are etched away. Following the first patterning step, the top layer of the BCP or BCP/PS blend thin film was then spin-cast onto the now-patterned silicon substrate (Figure 5.2b). The top layer of the BCP film was annealed and converted to silica dots using identical annealing and RIE conditions as those of the bottom layer.

5.3.5 Imaging and Data Processing

All images were taken with a Hitachi S4800 scanning electron microscope (15 kV, 20 μA), a Zeiss scanning helium ion beam microscope (30.8 kV, 10 μm aperture, spot size 4) or atomic force microscope (AFM) (Digital Instruments/Veeco, tapping mode under ambient condition). Statistical analyses of lattice angles and dot pitch were taken from a collection of HIM micrographs with a 15 μm or 20 μm field of view and a resolution of 8192 $\times$ 8192 pixels (1.8 or 2.4 nm/pixel respectively). The statistical analysis of P22(bottom)+P43(top) was carried out using 8 HIM micrographs (15 μm $\times$ 15 μm) from 3 different samples comprising over 1.6 million dots. P43(bottom)+P22(top) statistics were collected from 10 HIM micrographs (15 μm $\times$ 15 μm) from 3 different samples comprising over 1.9 million dots. P43(bottom)+B30(top) statistics were collected from 5 HIM micrographs (20 μm $\times$ 20 μm) from one sample comprising over 0.9 million dots. P43(bottom)+B30(top) statistics were collected from 4 HIM micrographs (20 μm $\times$ 20 μm) from one sample comprising over 0.7 million dots. The dot positions corresponding to the top and bottom BCP layers were separated *via* Fourier filtering using Gwyddion analysis software.[223] Specifically, due to the differences in dot pitch (L_0) of each layer, the dots from a single layer (either top or bottom) can be revealed by application of a bandpass filter centered on the fundamental frequency of each lattice ($k \simeq 2/\sqrt{3}L_0^{-1}$). Dot positions were then determined by a thresholding algorithm (Ostu's method). It is noted that this type of separation is only possible on patterns that do not have overlapping fundamental frequencies.

To measure the pitch and angle of each dot, the positions of the 6 nearest-neighbours of each dot were first determined. The pitch of each dot was then taken as the mean distance between the central dot and its 6 nearest-neighbours. The lattice angle of each dot was defined as the orientation of the corresponding coordination shell of each dot, relative to the horizontal axis of the image; this was determined by calculating the angle between the central dot and each of its coordinating dots (modulo 60°). The circular mean of these 6 angles was then used to calculate the

lattice orientation.

5.4 Incommensurate Block Copolymer Epitaxy

The general scheme for the self-assembly of incommensurate BCP double layers is shown in Figure 5.2. The bottom layer of hexagonal dots is formed *via* self-assembly of a PS-*b*-PDMS BCP, followed by solvent annealing and reactive ion etching (RIE) to transform the BCP into the nanopattern of silica dots (Figure 5.2a). A second layer of a PS-*b*-PDMS BCP, which has a different molecular weight and thus a different periodicity, is then spin-coated onto the initial pattern of silica dots (bottom layer). Upon a second solvent anneal (Figure 5.2c) and RIE treatment, the top layer of the PS-*b*-PDMS BCP is converted into another array of dots (Figure 5.2). The resulting nanopattern is generally a Moiré superstructure.

In this work, the two different PS-*b*-PDMS BCPs and BCP blend used in this study, and their abbreviations, are summarized in Table 5.1. These BCPs were chosen in order to explore a large range of array pitches and pitch ratios. The B30 blend was specifically chosen to achieve a large pitch of 43 nm (blending was necessary to produce dot arrays instead of cylindrical arrays).[28] The plan view scanning electron micrographs (SEM) and atomic force micrographs (AFM) of single-layer silica dot patterns fabricated from B30, P43, and P22 on flat silicon substrates are shown in Figures 5.3 and 5.4 respectively, and the dot diameter, pitch, and height of each silica dot array are listed in Table 5.1. The layered structures are denoted by their deposition sequence. For example, P22(bottom)+P43(top) is a sample where P22 is used as the bottom layer and P43 used as the top layer. The layered structures produced in this work are P22(bottom)+P43(top), P43(bottom)+P22(top), P43(bottom)+B30(top), and B30(bottom)+P43(top).

Examples of three Moiré superstructures on flat silicon substrates, resulting from combinations of the BCPs listed in Table 5.1, are shown in Figure 5.5.

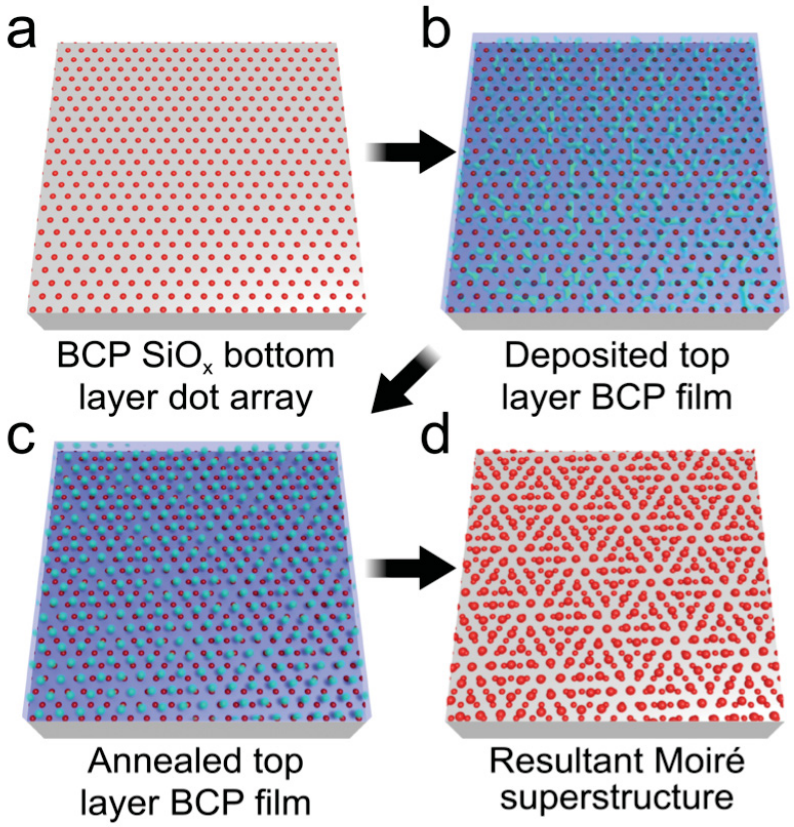

Figure 5.2: *Schematic illustrating the method for formation of BCP dot-array-based Moiré superstructures. (a) Formation of a bottom layer of hexagonal dots via self-assembly of a BCP, followed by solvent annealing and reactive ion etching (RIE) to transform the BCP into a hexagonal lattice of silica dots. (b) Deposition of a top layer BCP film on the preformed nanopattern of silica dots from (a). (c) Annealing of top layer BCP films results in orientational alignment of the top layer BCP dot array. (d) RIE of the top layer converts the BCP to silica dots, resulting in a Moiré superstructure.Reprinted with permission from ref. [40]. Copyright © 2017 American Chemical Society.*

Table 5.1: *Pitch, dot diameter, and height of silica nanodot arrays converted from the annealed BCPs/BCP blends used in this study.*

Abbreviation	Composition	Pitch/nm	Diameter/nm	Height/nm
P22	PS-*b*-PDMS (22.5k-4.5k)	23.4(5)	12.0(1.6)	2.9(4)
P43	PS-*b*-PDMS (43k-8.5k)	34.1(6)	15.9(7)	5.0(4)
B30	PS-*b*-PDMS (31.5k-14.5k) + 30 wt % PS (10k)	42.5(5)	21.8(8)	7.3(5)

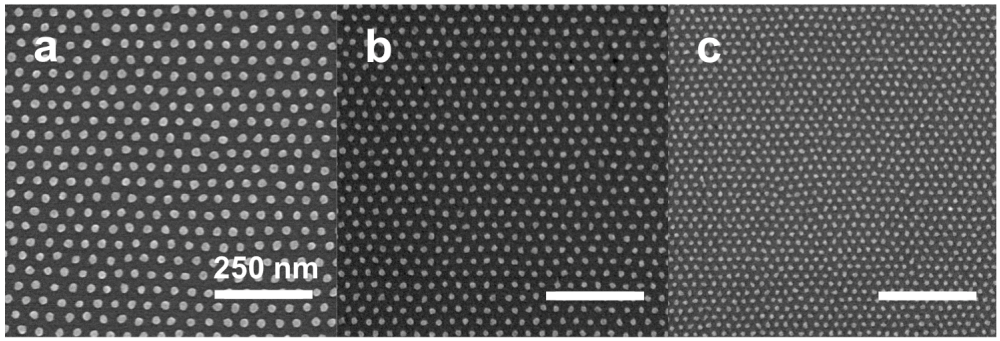

Figure 5.3: *SEM micrographs of single layer silicon dot patterns converted from annealed (a) B30, (b) P43, and (c) P22. All scale bars are 250 nm. Reprinted with permission from ref. [40]. Copyright © 2017 American Chemical Society.*

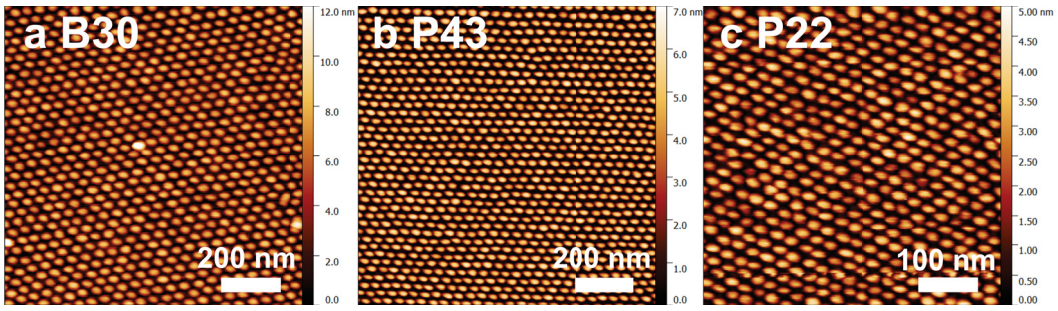

Figure 5.4: *AFM micrographs of single layer silicon dot patterns converted from annealed (a) B30, (b) P43, and (c) P22. Reprinted with permission from ref. [40]. Copyright © 2017 American Chemical Society.*

Figures 5.5a, c, and e show SEM micrographs of the three Moiré superstructures, and Figures 5.5b, d, and f are schematic illustrations indicating the relative rotation of the individual dot arrays in the three Moiré superstructures. Figure 5.5a and c utilize the same pair of BCPs, but in reverse order, and Figure 5.5e examines a higher molecular weight BCP and a BCP/homopolymer blend. In Figure 5.5a the BCP with the lower molecular weight, P22 (PS-*b*-PDMS) (22.5k-4.5k), was applied as the bottom layer of dots, having a pitch of ∼23-24 nm (Table 5.1). The top layer of dots was formed from a higher molecular weight BCP, P43 (PS-b-PDMS) (43k-8.5k), which consequently has a larger pitch of ∼34 nm (Table 5.1). The resulting majority phase is shown in Figure 5.5a (*vide infra* for discussion of determination of majority phase). The relative rotation angle between the first and second layers is 30°. When carried out in the reverse order, with the bottom dot pattern formed from P43 formed, followed by P22 as the top layer, a different Moiré superstructure is observed (majority phase, Figure 5.5c). The relative rotation angle between the two layers in this case is about 11°. Starting with P43 (pitch of 34 nm) as the bottom dot pattern, B30, which has a pitch of ∼43 nm (Table 5.1), was used to form the top layer of dots; the majority phase of the resulting Moiré superstructure is shown in Figure 5.5e. In this latter case, the relative rotation angle between the two layers is near 3°.

Figure 5.6 shows a representation of the individual layers in the three distinct majority phase Moiré superstructures, as observed by SEM, in Figures 5.6a-c. The dots in Figure 5.6d-i were manually separated based on the differences in dot sizes between the two layers; the sizes of the dots are displayed as the average size of the corresponding BCP pattern determined from the SEM micrograph. The bottom layer dot nanopatterns, Figures 5.6d-f, displays long range hexagonal ordering within the 850 nm × 850 nm area of the micrograph. The top layers, Figures 5.6g-i, also show long range hexagonal ordering despite undergoing self-assembly on a surface with protruding silica dots of a different spacing. Figures 5.6j-l correspond to the original SEM micrographs in Figures 5.6a-c, with the layers stacked according to the annealing sequence: blue dots comprise the bottom layer, and the red dots

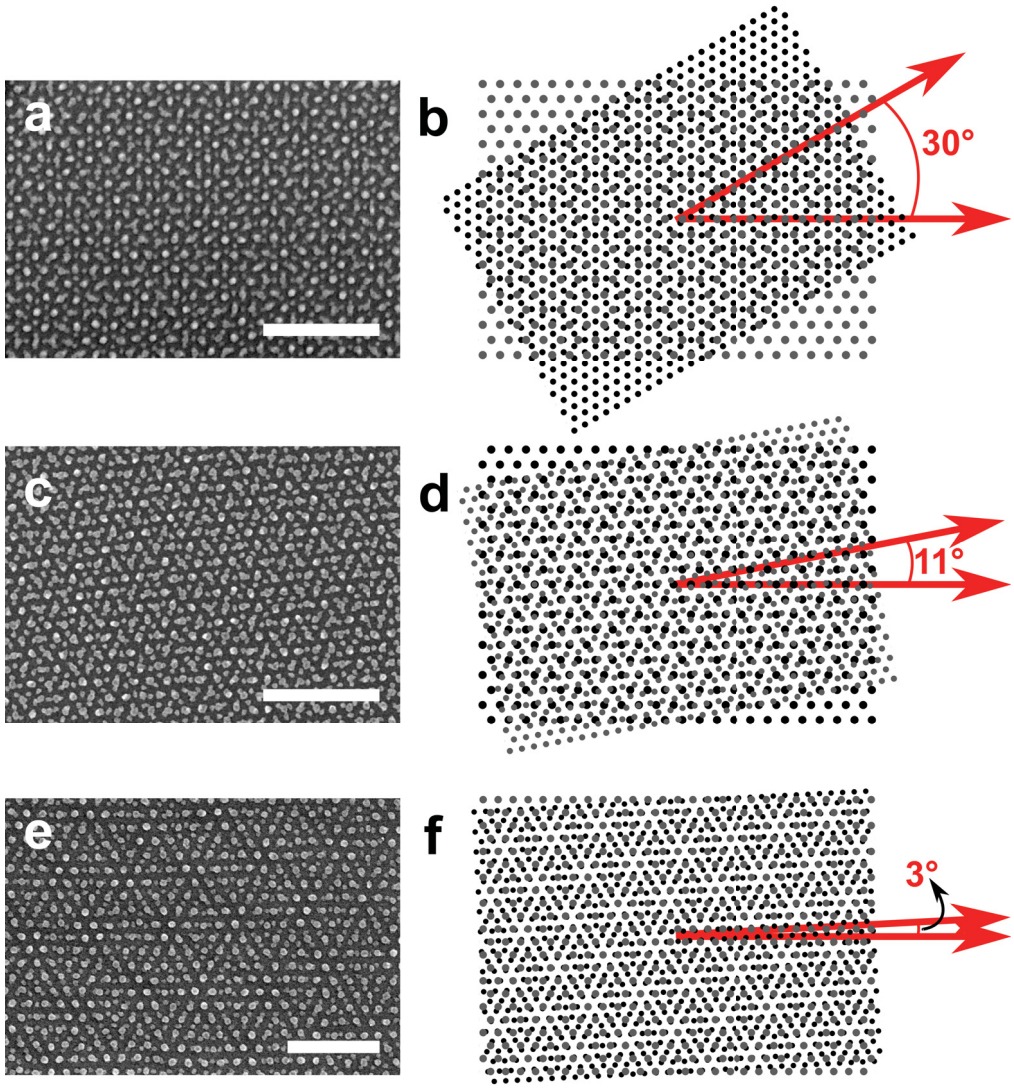

Figure 5.5: *Left column: SEM micrographs of Moiré superstructures formed from sequential annealing of two incommensurate BCP combinations. Right column: corresponding schematic representation.(a, b) P22(bottom)+P43(top). (c, d) P43(bottom)+P22(top). (e, f) P43(bottom)+B30(top). In (b), (d), and (f), the bottom layers are portrayed in black, and the top layers in gray. All scale bars are 250 nm. Reprinted with permission from ref. [40]. Copyright © 2017 American Chemical Society.*

the top layer. Random sampling *via* high-magnification SEM generally revealed a consistent Moiré superstructure (majority phase) across the substrate. From these observations it was hypothesized that a unique set of preferential orientation relationship(s) exists between any two BCP dot arrays. However, from these micrographs it was also observed that there was some variance in the relative orientation of the lattices, as well as a sparse amount of other configurations.

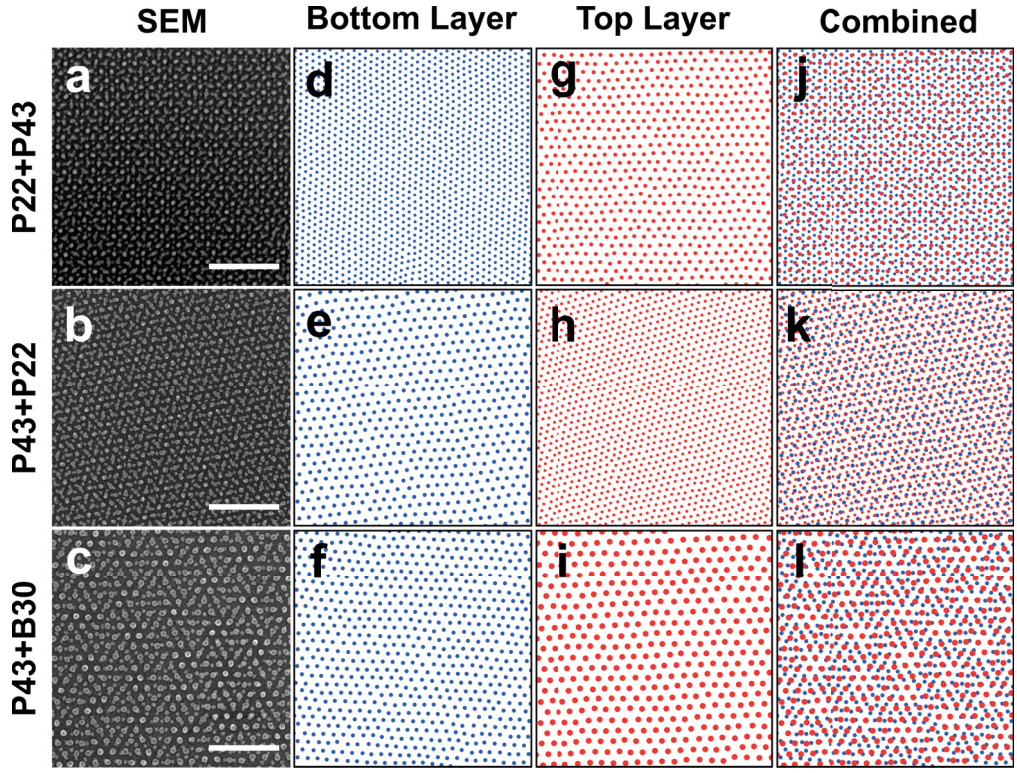

Figure 5.6: *Separation of BCP Moiré Superstructures into top and bottom layers. (a-c) SEM micrographs, (d-f) dot patterns of the bottom layer, (g-i) dot patterns of the top layer, (j-l) combined bottom and top layers of the three Moiré superstructures. All scale bars are 250 nm. Reprinted with permission from ref. [40]. Copyright © 2017 American Chemical Society.*

In order to test the hypothesis of preferential lattice orientations, it was necessary to perform high-resolution large-area imaging of multiple films (made under identical processing conditions) in order quantify the distributions of relative

rotation between the two lattices, yielding statistically meaningful results. Helium ion microscopy (HIM) was used to acquire the high-resolution (8192 × 8192 pixels) large-scale micrographs [20 μm × 20 μm for P43(bottom)+B30(top), 15 μm × 15 μm for P22(bottom)+P43(top) and P43(bottom)+P22(top)]. From these micrographs, dot positions of the two layers in the Moiré superstructures were separated using FFT filtering of the HIM images (see Methods section), and the orientations of each individual layer were calculated at each dot position using the data processing analyses, described in Methods section. The relative orientations of the top and bottom layers were then calculated by taking the difference of these angles. Since the relative rotation angles are calculated per dot, those angles can be color mapped and plotted on the dot positions to form an image over the entire micrograph to reveal preferred domains, as well as other distinct superstructures. Examples of these processed images are shown in Figure 5.7, along with labelled details of these high-magnification images (Figures 5.7b-e and g-j) to reveal the nature of the Moiré superstructures. Figure 5.7a and f are processed HIM micrographs of P43(bottom)+P22(top), and P43(bottom)+B30(top), respectively. As the hexagonal dot pattern has six-fold circular symmetry, the relative rotation angle has been mapped on a cyclical color scale with a range of -30° to +30°. As can be seen upon close inspection of Figure 5.7, the areas that have the same relative rotation, represented by the same colors, correspond to areas with the same patterns. These patterns have the same structure and relative rotation between the layers, although they do not have the same absolute rotation. It can be seen that these data are evidence of a preferential orientational relationship between the two layers.

Shown in Figure 5.8 are spatial mappings of the lattice orientations for different bottom layers (a-c) and corresponding top layers (d-f). From these lattice orientation maps of the bottom and top layers, the relative rotation maps are calculated and shown in Figures 5.8g-i. The maps portray a 15 μm × 15 μm area of P22(bottom)+P43(top) and P43(bottom)+P22(top), and a 20 μm × 20 μm area of P43(bottom)+B30(top). The lattice angles are measured as described in the Methods

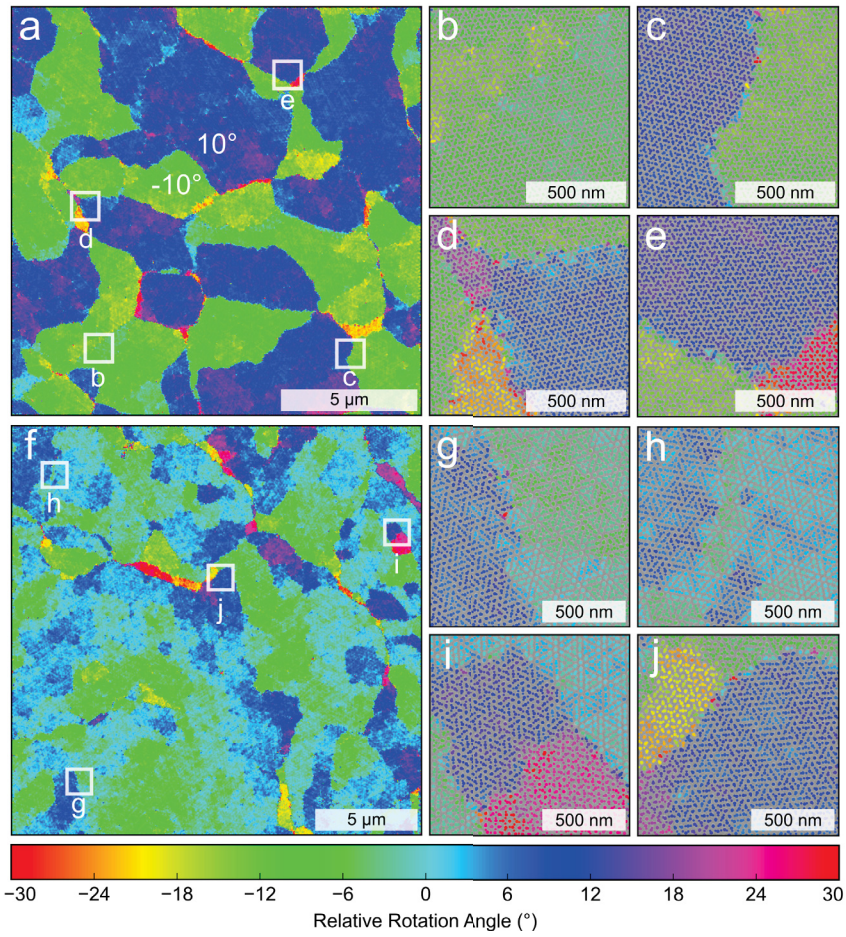

Figure 5.7: *Large-area high-magnification map of relative lattice orientation between top and bottom BCP dot arrays. (a) Relative rotation angles of the bottom and top dot layers, derived from P43(bottom)+P22(top), as defined as the angular difference between the lattice orientation of the two dot patterns. In this map, a single color corresponds to a particular Moiré superstructure. (b-e) Higher magnification of (a) as labelled. (f) Dot lattice relative rotation angles angles in the combination of P43(bottom)+B30(top). (g-j) Higher magnification of (f) as labelled. Reprinted with permission from ref. [40]. Copyright © 2017 American Chemical Society.*

section from the horizontal axis of the image, where a color represents the lattice orientation as indicated by the cyclical color map, with a range of -30° to 30°. From these maps, the BCP dot pattern grains, grain orientations, and their associated grain boundaries are easily differentiated.

The relative rotation map for P43(bottom)+P22(top), shown in Figure 5.8h, indicates the presence of two phases with preferential rotation angles of -10 and +10°. These patterns share the same Moiré structure but have opposite chirality as seen in the detailed dot patterns found in Figures 5.7c and g. Every preferential relative rotation angle at angles other than 0° or 30° will exhibit a selection between two degenerate lattice orientations, resulting in left- and right-handed domains of the same Moiré structure, which on the chosen scale are seen as positive and negative angles of equal magnitude.[8] To clearly show the preferential relative rotation angles/lowest energy configuration of each sample, the absolute values of the relative rotation angles were plotted in Figures 5.8j-l. After accounting for the left and right handed domains, only the blue color, corresponding to an angle of about 10°, appears in the absolute relative rotation angle map in Figure 5.8k, revealing that the pattern has only one preferential dot configuration/Moiré superstructure. Upon close inspection, all three samples show a preferred relative rotation angle, and thus a preferred Moiré superstructure. The preferential relative rotation angle between the two BCP layers of P22(bottom)+P43(top) is about 30° (Figure 5.8g and j). Figure 5.9 is a defect-free low magnification SEM micrograph taken from a P22(bottom)+P43(top) sample and the insert FFT also confirmed that a 30° relative rotation angle between two hexagonal dot lattice. The relative rotation angle map and the absolute relative rotation map of P43(bottom)+B30(top) show a preferential relative rotation angle around 0°.

Inspection of the individual layers in Figures 5.8a-f shows that the grains of the top layer generally align with the bottom layer. However, as seen in the relative rotation maps (Figures 5.8g-i), the overlap of the grains is not perfect, as there are thin regions with very different relative lattice orientations. It is these grain

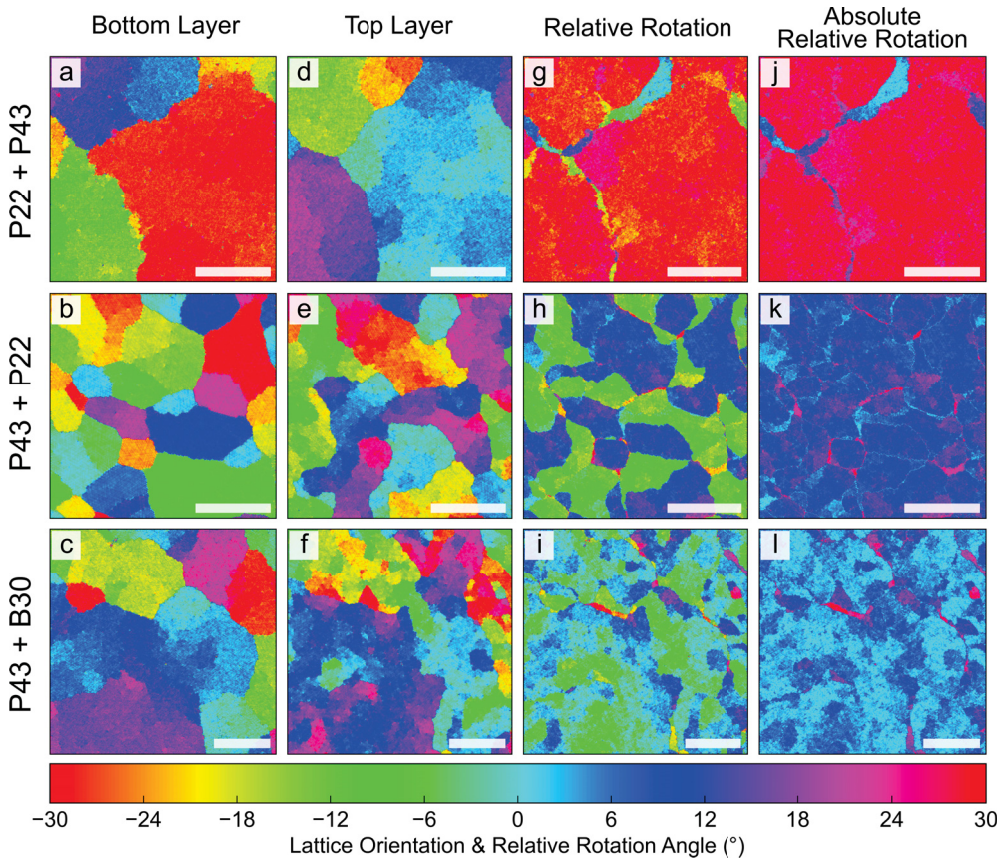

Figure 5.8: *Grain structures of top and bottom layers and corresponding relative orientations between layers. (a-f) Bottom and top layer dot-pattern lattice orientations (relative to the horizontal axis of the image). (g-i) The relative rotation angle between dot-patterns of the first and second layers as described in Figure 5.7. (j-l) The absolute values of previous relative rotation angles showing the chiral symmetry resulting from the degenerate lattice orientations in the double layer patterns. All scale bars are 5 μm in length. Interactive and full-resolution images of all of these maps can be found online at* `http://maverick.chem.ualberta.ca/bcp_micrographs/` *using the Web Deep Zoom Toolkit developed at NIST.[41] Reprinted with permission from ref. [40]. Copyright © 2017 American Chemical Society.*

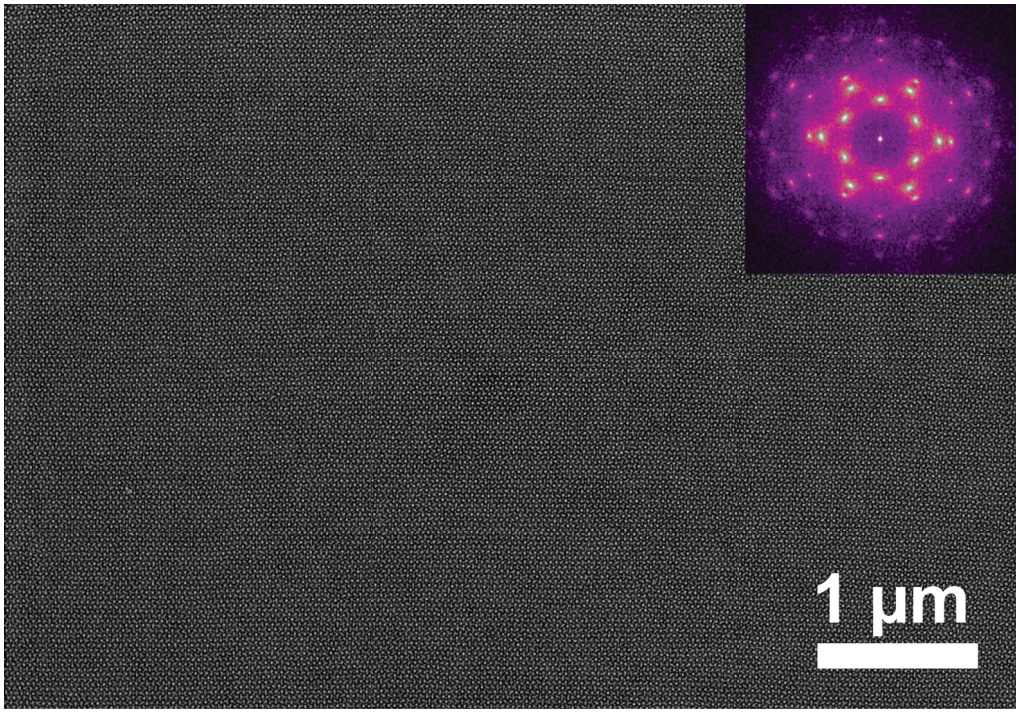

Figure 5.9: *Large-scale SEM micrograph of P22 (bottom)+P43 (top). Insert: FFT. Reprinted with permission from ref. [40]. Copyright © 2017 American Chemical Society.*

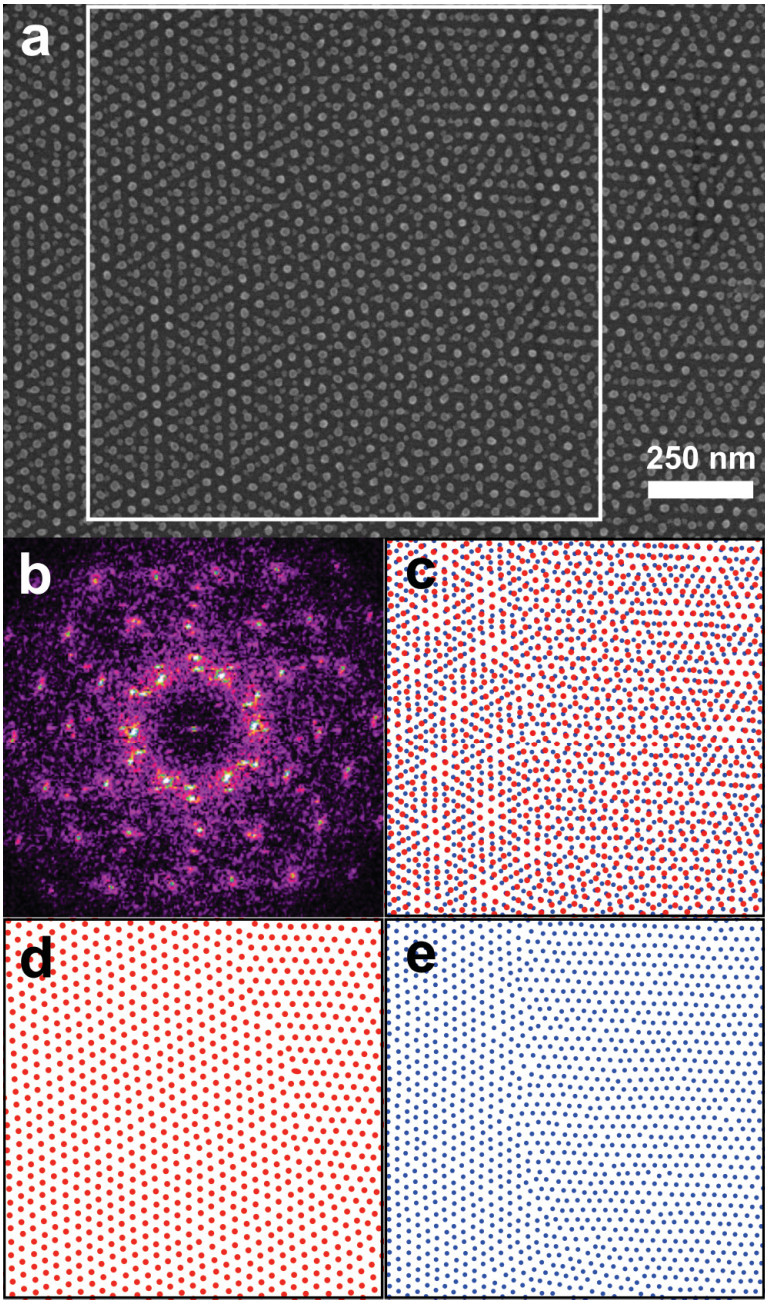

Figure 5.10: *Grain boundary of P43 (bottom)+B30 (top). (a) SEM micrograph of grain boundary area. (b) FFT of white square area of (a). (c) Combined B30 (red dots) and P43 (blue dots). (d,e) Separated B30 and P43 arrays, respectively. Reprinted with permission from ref. [40]. Copyright © 2017 American Chemical Society.*

boundary transition regions between the top and bottom layers that account for the different Moiré superstructures occasionally observed in SEM (Figure 5.10a).

Figure 5.10d and e are referred to dot patterns in the bottom layer and top layer of white square area of Figure 5.10a. Both of them showed a grain boundary in single layer dot patterns and a angle at around 30° at grain boundary. FFT (Figure 5.10b) of the white area also shows two set of arrays with two different grains in each array. Figure 5.10c is superimposed image of Figure 5.10d and e. It clearly shows that the grain boundary area is caused by the misalignment of grain boundary of two hexagonal dot arrays.

A Moiré superstructure is uniquely defined by a pitch ratio (defined as the ratio of the dot pitch of the top layer divided by that of the bottom layer) and a relative rotation between the layers. As such, in order to analyze the Moiré structures found in these samples, the distributions of these quantities are shown in Figure 5.12, which are calculated using a 2D and 1D kernel density estimation (KDE).[268] Each chart is an ensemble of statistics from multiple HIM micrographs and samples, with the total number of dots indicated in the KDE as N. The median pitch ratios and relative rotation angles of five different configurations of sequentially deposited BCP bilayers are summarised in Table 5.2. The native pitch ratio is also listed, which is defined as the ratio of dot spacings found in the corresponding single (or bottom) layer patterns. The dot pitch distributions of the dot patterns from the separated layers can be seen in Figure 5.11. Two additional configurations are listed in the table, B30(bottom)+P43(top), and $B30_{oe}$(bottom)+P43(top), which will be discussed later.

Several observations can be made from these KDEs. Firstly, for any given configuration, it is seen that all relative rotations are clustered around an angle of Θ° and -Θ° (which corresponds to the chiral but degenerate Moiré superstructure), with standard deviations on the order of 3.5°. These data substantiates the hypothesis that preferred Moiré superstructure(s) can be formed for a given pair of incommensurate BCP lattices, further suggesting that these Moiré superstructures represent a minima

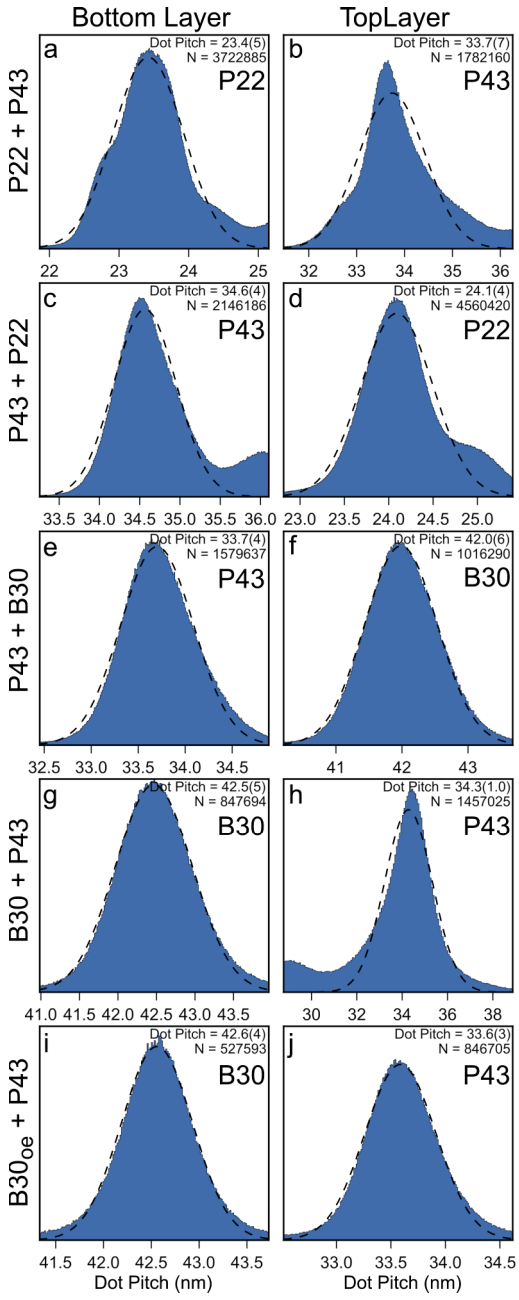

Figure 5.11: *Distributions of dot pitches for all 5 different BCP combinations used in this work. Dot pitch is calculated as the mean dot pitch of the first coordination shell around each dot. Gaussian fits are used to determine the standard deviation in dot pitch. Reprinted with permission from ref. [40]. Copyright © 2017 American Chemical Society.*

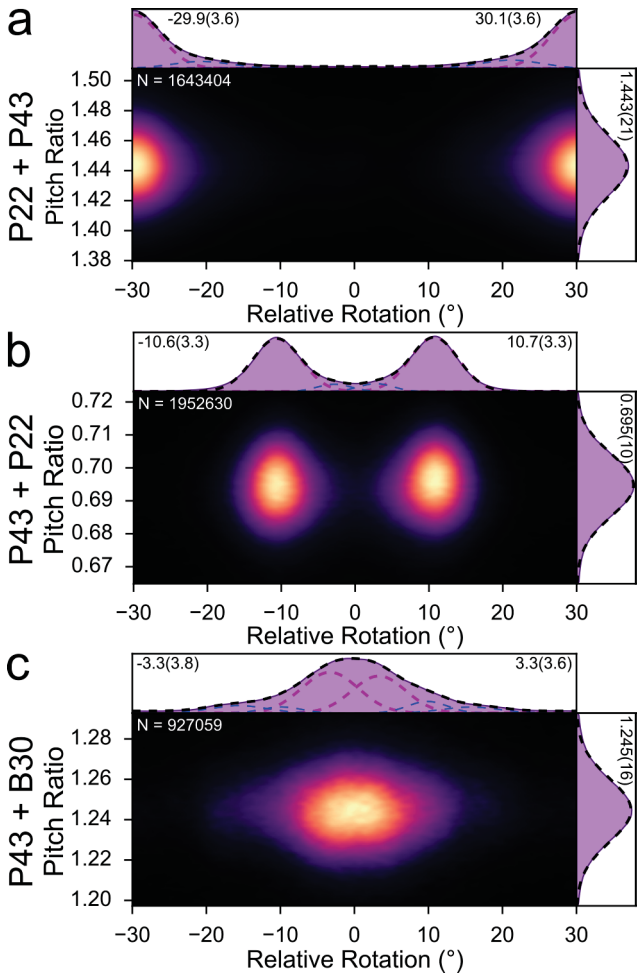

Figure 5.12: *2D and 1D kernel density estimations (KDE) showing the distribution of pitch ratios(L2/L1) and relative rotation angles found in the Moiré superstructures. (a) Statistical representation of P22(bottom)+P43(top) comprising 8 HIM micrographs (15 μm × 15 μm) from 3 different samples, sampling a total of over 1.6 million dots. (b) Statistical representation of P43(bottom)+P22(top) comprising 10 HIM micrographs (15 μm × 15 μm) from 3 different samples, sampling a total of over 1.9 million dots. (c) Statistical representation of P43(bottom)+B30(top) comprising 5 HIM micrographs (20 μm × 20 μm) from one sample, containing over 0.9 million dots. Reprinted with permission from ref. [40]. Copyright © 2017 American Chemical Society.*

Table 5.2: *Pitch, dot diameter, and height of silica nanodot arrays converted from the annealed BCPs/BCP blends used in this study.*

BCP Layers (bottom+top)	Native Pitch Ratio (L2/L1)	Measured Pitch Ratio (L2/L1)	Relative Rotation (°)	Correlation Coefficient
P22+P43	1.46(4)	1.443(21)	29.9(3.6)	0.007
P43+P22	0.687(19)	0.695(10)	10.7(3.3)	0.018
P43+B30	1.245(27)	1.245(16)	3.3(3.8)	0.045
B30+P43	0.803(17)	0.813(19)	2.6(5.0)	-0.004
$B30_{oe}$+P43	0.803(17)	0.789(9)	4.8(2.9)	-0.007

in the energy landscape of these incommensurate BCP lattices. Inspection of Table 5.2 reveals that differences in native and measured pitch ratio are between 0-2 %. These data imply that the registration force from the bottom layer is insufficiently strong to induce a large global strain of the top layer lattice spacing. Lastly, the 2D KDEs show little correlation between the measured pitch ratio and the relative rotation, seen by the on-axial orientation of the elliptical peak shape and the near-zero Pearson product-moment correlation coefficients found in Table 5.2. This result suggests that local variations in relative lattice orientation do not significantly modify the local pitch ratio.

5.5 Influence of Bottom Layer Pattern Size

In addition to the previous three BCP combinations, B30(bottom)+P43(top) was also produced. However, the resulting pattern formed by this combination, shown in Figures 5.13a-d, Figures 5.15a-d and Figures 5.16 a-d differs significantly. In contrast to the other three examples analyzed, the spherical PDMS domains of the top layer, P43, tend to deviate from their equilibrium lattice positions, which

can be clearly seen *via* the dot separation in Figure 5.13b. Figure 5.14 also showed strong deviation of top dot layer, P43. In contrast to the grain boundary area of P43(top)+B30(bottom) (Figure 5.10), there is no grain boundary in the B30(bottom)+P43(top) sample, which indicated the bottom layer, B30 has strong registration force on the top layer, P43.

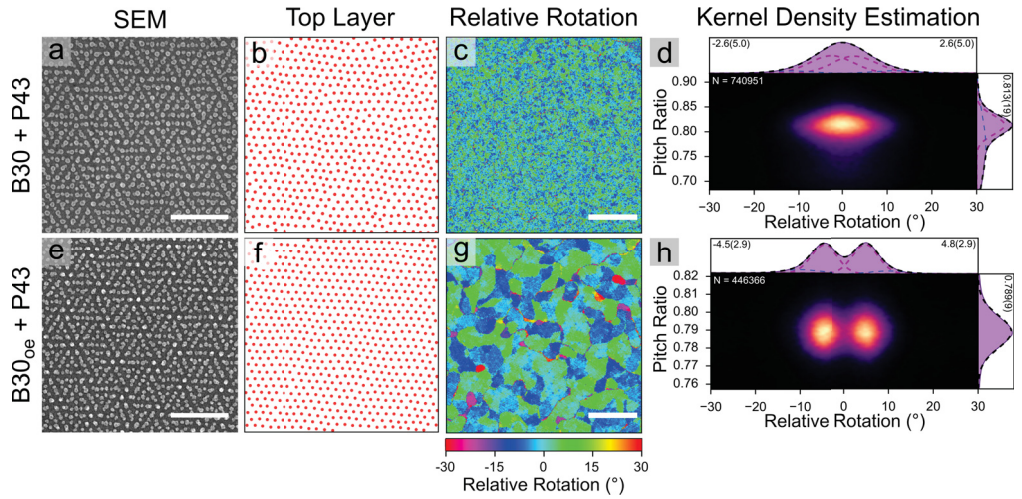

Figure 5.13: *The effect of bottom layer dot size on the resulting Moiré superstructures. (a-d) Data for the B30(bottom)+P43(top) BCP Moiré superstructures. (e-h) Data for a $B30_{oe}$(bottom)+P43(top) Moiré superstructures where the bottom B30 BCP layer was etched by RIE for an extra 5 s, resulting in the formation of smaller silica dots. Scale bars in SEM micrographs (a, b, e and f) are 250 nm, and scale bars in the relative rotation angle maps (c and g) are 5 μm in length. Reprinted with permission from ref. [40]. Copyright © 2017 American Chemical Society.*

Interestingly, despite the higher defect density in the top layer of P43, there is still a preferential orientational relationship between the top and bottom layers. As seen in Figure 5.13d the distribution of relative rotation angles is consistently centered around 0°, although quite broad with respect to both pitch and angle. The relative rotation is fit with two peaks at angles of ± 2.6(5.0)°. Two peaks were used because the resulting pattern has areas that twist from ∼0° to ∼+5°, and others that twist from ∼0° to ∼-5°, as can ben clearly seen in Figure 5.13c, where there are

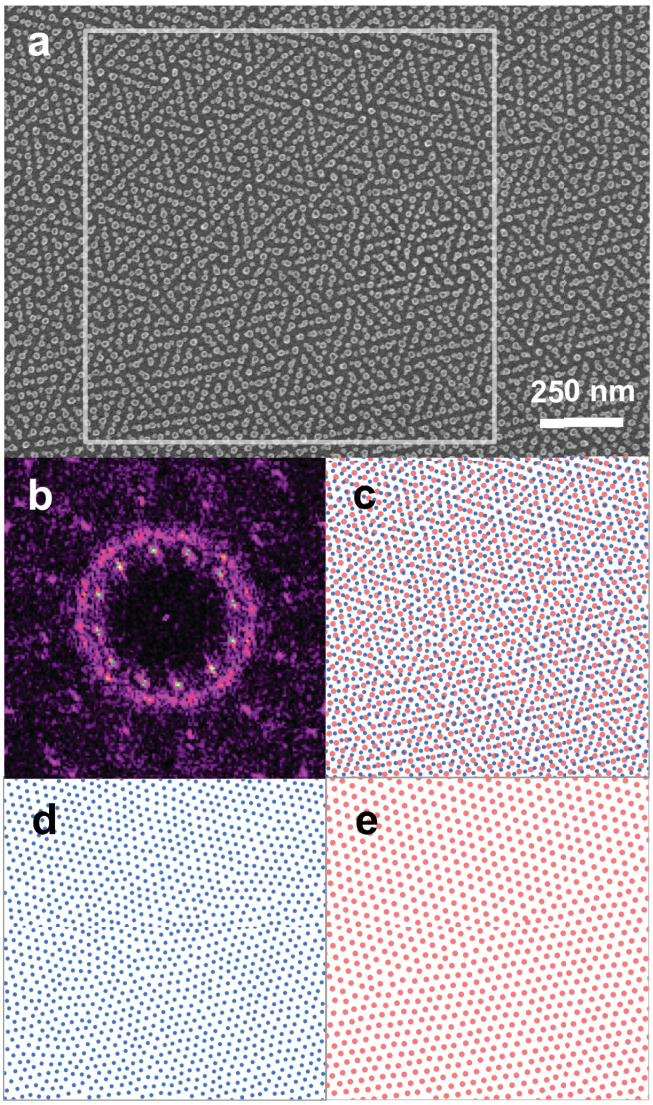

Figure 5.14: *Grain boundary of B30 (bottom)+P43 (top). (a) SEM micrograph of grain boundary area. (b) FFT of white square area of (a). (c) Combined B30 (red dots) and P43 (blue dots). (d,e) Separated P43 and B30 arrays, respectively. Reprinted with permission from ref. [40]. Copyright © 2017 American Chemical Society.*

distinct regions of green and blue, opposed to a uniform mixture of the two colors. The different registration observed in this system may be due to the size of the silica dots derived from the B30 BCP blend, which produces dots with a height of 7.3 nm, and a rather large diameter of 21.8 nm, compared to the dots derived from P43, which have a height of 5 nm (Figure 5.17 and a diameter of 15.9 nm.

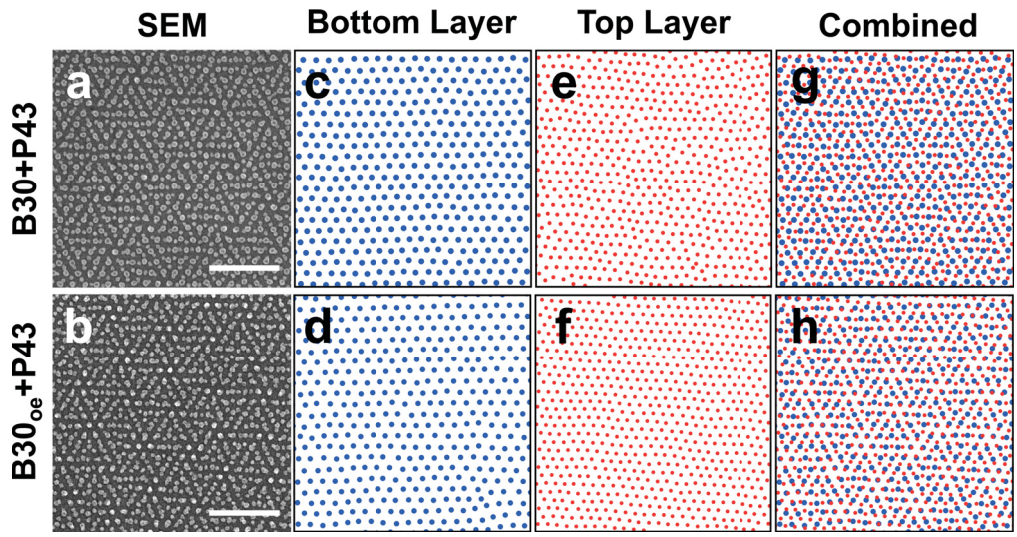

Figure 5.15: *SEM micrographs (a, b), separated first layer pattern (e, d), second layer pattern (e, f), combined double layer pattern (g, h) of B30 (bottom)+P43 (top) Moiré superstructure and B30$_{oe}$ (bottom)+P43 (top) Moiré superstructure. All scale bars are 250 nm. Reprinted with permission from ref. [40]. Copyright © 2017 American Chemical Society.*

To further study the effects of bottom layer dot size on the epitaxy of the top layer, the first layer of the B30 silica dots was etched by RIE with an extra 5 s of CF_4 (100 mT, 50 W), to reduce the dot size to 5.2 nm in height and 18.2 mm in diameter (Figure 5.17). This configuration is defined as B30$_{oe}$(bottom)+P43(top). Figures 5.13e-h shows the resulting pattern and analysis of the registration of the top layer formed from P43 on B30$_{oe}$. The epitaxial registration of the top layer on B30$_{oe}$ is remarkably different when compared the previous B30(bottom)+P43(top) sample. One of the most striking differences is the dramatic increase of long-

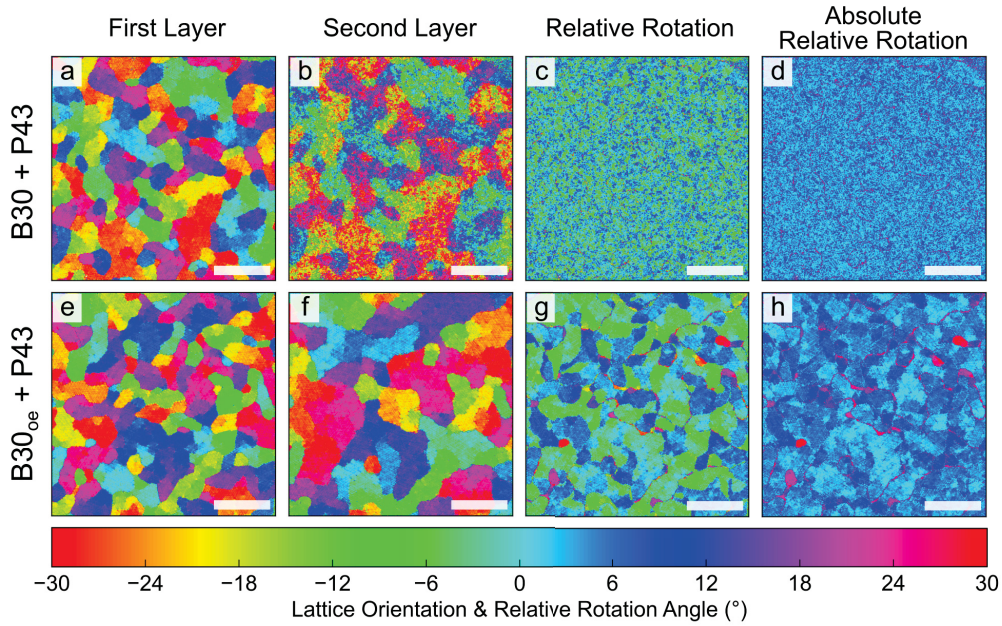

Figure 5.16: *Dot pattern maps as described in Figure 5.8 for B30+P43 (a-d) and $B30_{oe}$+P43 (e-h) where the B30 was etched longer to decrease the particle size ($B30_{oe}$). All scale bars are 5 μm in length. Reprinted with permission from ref. [40]. Copyright © 2017 American Chemical Society.*

range ordering observed in the top layer (compare Figures 5.13b and f). Secondly, the distribution of the relative rotation angles between the top and bottom layers has two clearly defined peaks centered at +5° and -5° (Figures 5.13d and h). Moreover, the relative rotation map of B30$_{oe}$(bottom)+P43(top) (Figure 5.13g) appears to be much more similar to the other BCP combinations used in this work (Figure 5.8), where there are large micron-sized regions possessing a single relative orientation, which are delineated by grain boundaries of either the top of bottom layer. Unlike B30(bottom)+P43(top), the 2D KDE of B30$_{oe}$(bottom)+P43(top) (Figure 5.13h) shows two well resolved peaks. The relative rotation angle between the top P43 layer and the bottom B30$_{oe}$ is fit to 4.8(2.9)°. The pitch ratio of B30$_{oe}$(bottom)+P43(top) was measured to be 0.803(17), which is very close to the native pitch ratio (Table 5.2). These results indicate that pitch ratio is not the only parameter that determines that resultant structure, as the relative dot sizes can also strongly influence the final morphology. In this case, as the dot size of the bottom layer is reduced, the registration with the top layer weakens. At these smaller dot sizes, the registration is insufficient to create point defects in the top layer, but is sufficiently strong such that the configurational energy is minimized with a relative rotation of $\pm$ 5°. Similar observations have also been reported in a study of self-assembly of PS-*b*-PDMS cylinders over silica pillar arrays, formed *via* EBL of HSQ.[269] In that work, differences in the silica post height of as little as 3 nm, in the range of 12 to 26 nm, induced substantial changes in the morphology and orientation of the self-assembled microdomains of the PS-*b*-PDMS BCP.

5.6 Influence of Bottom Layer Pitch

In order to systematically study the effect of bottom layer pitch size (center-to-center spacing) to the resulting Moiré patterns, hexagonal packed silica pillar arrays with pitch ranging from 36 nm to 90 nm were fabricated by EBL on a 1 $\times$ 1 cm^2 silicon chip. All gains were in circular shape (Figure 5.18) and EBL pillars were about 15

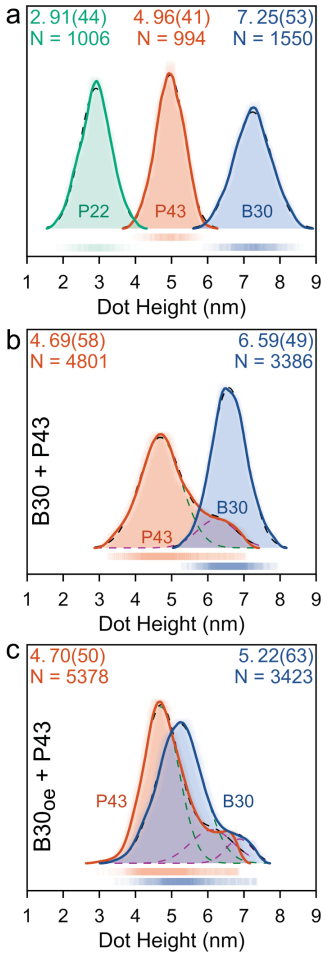

Figure 5.17: *ASH plots for RIE-treated dot heights obtained from AFM. (a) Dot height distributions for single layers of P22, P43, and B30 (b) Dot height distributions for B30(bottom)+P43(top). Since the AFM tip was unable to reach the flat silicon substrate, dot heights were shifted to match the mean height of P43 from (c). The shoulder of the main peak in P43 is a consequence of taller B30 layer dot included in the P43 height distribution due to dot proximity. (c) Dot height distributions for $B30_{oe}$(bottom)+P43(top). The second peak of B30 is a consequence of dots from the B30 layer that have additional height due to dot overlap. Reprinted with permission from ref. [40]. Copyright © 2017 American Chemical Society.*

nm in height and about 15 nm in diameter. In the following text, the EBL pillar grains will be denoted at EBL-xx, where xx is the pitch of related EBL pillar grain. A 32-nm-thick B30 thin film was then spin casted onto EBL patterned silicon chip and annealed in THF vapor for 100 min to the degree of swelling of 2. The native pitch of B30 dot patterns on this sample was measured to be 44.9 nm.

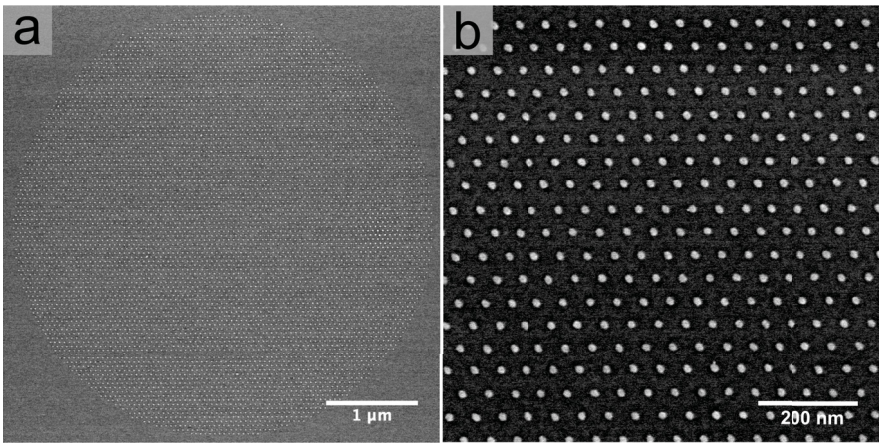

Figure 5.18: *A low-magnification SEM micrograph (a) and a high-magnification micrograph (b) of a 52 nm pitch EBL grain.*

Figure 5.19, 5.20, and 5.21 are high-magnification SEM micrographs of double layer nanopatterns of self-assembling B30 on EBL pillar arrays. The white dots in SEM micrographs are EBL pillars and the gray ones are B30 nanopatterns. The relative rotation angles of Moiré superstructures at EBL pillar pitch ranging from 36 nm to 52 nm area are around 0° (Figure 5.19). EBL-36(bottom)+B30(top) and EBL-38(bottom)+B30(top) Moiré superstructures show 'triangular' superstructures and the size of 'triangular' superstructure increase as the EBL pillar pitch increase (Figure 5.19a and b). When the EBL pillar pitch almost matched the B30 pitch (Figure 5.19c), honeycomb structures with a very small amount of 'line' patterns appear, which is similar to BCP double-density patterns discussed in Chapter 4. The formation of 'line' patterns is due to the slightly mismatch between EBL pillar pitch (44 nm) and the B30 dot pitch (44.9 nm). The Moiré superstructures formed by annealing B30 on EBL-46, EBL-50, and EBL-52 pillar arrays show 'triangular'

patterns again (Figure 5.19d, e, and f). The size of 'triangular' patterns decrease as the EBL pitch increase. Figure 5.20 shows Moiré superstructures at areas of EBL pitch ranging from 70 nm to 84 nm. The relative rotation angles are measured to be at around 30° and all six SEM micrographs show similar Moiré super structures. For the EBL pitch at 88 nm and 90 nm, 0° relative rotation angles appears again (Figure 5.21).

The native pitch ratios, measured pitch ratios, and relative rotation angles are shown in Table 5.3 . Here, native pitch ratios were calculated by dividing the pitch of B30 by that of EBL pillar arrays. For each Moireś supersturcture, measured pitch ratios and relative rotation angles were measured from at least three SEM micrographs of related sample by Gwyddium. "N/A" means the EBL pitch and BCP pitch are too close and hence the relative value and relative angle cannot be measured. Similar to the resulted observed in BCP+BCP Moiré superstructures, the bottom EBL pillar pitch have no influence to the pitch of top B30 nanopatterns. When the pitch ratio close to 1:1 or 2:1 (EBL pitch ranging from 36 nm to 52 nm and 88 nm to 90 nm), the relative rotation angle appears to be at 0° (Figure 5.22a and c). When the pitch ratio close to $\sqrt{3}$:1 (EBL pitch ranging from 70 nm to 84 nm), the relative rotation angles are shown to be at around 30° (Figure 5.22b).

5.7 Conclusions

Sequential self-assembly of incommensurate BCP dot arrays leads to preferred orientations, thus providing a route towards a unique set of large area, single-grain Moiré superstructures. The registration force of the bottom layer of dots is sufficiently strong to bring about registration of top layer, resulting in formation of a majority phase. The advantages of nanolithography *via* self-assembly of BCPs are multifold, and include the low cost of processing, their high resolution, and well developed methods to transfer the BCP nanopattern to the underlying substrate. This class of registration between BCP layers opens up an avenue to access a new family

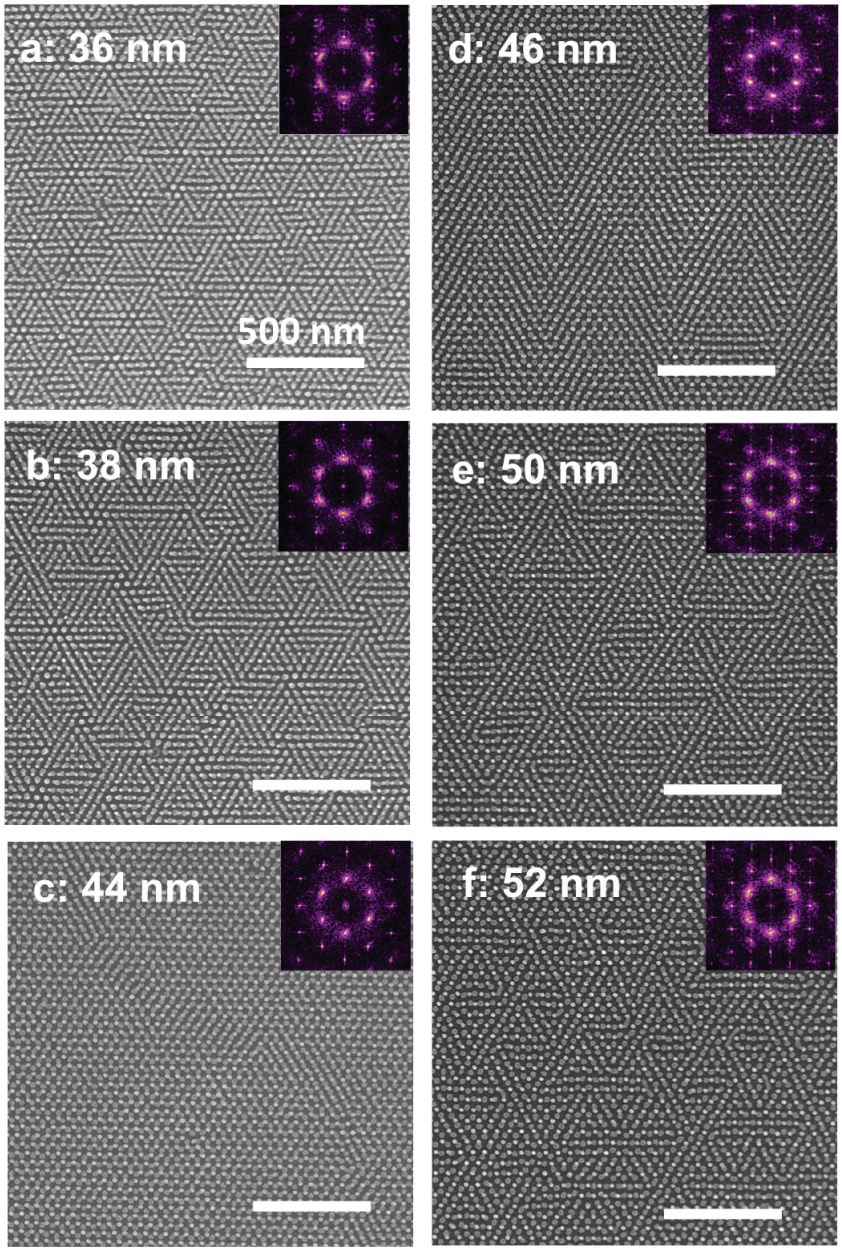

Figure 5.19: *SEM micrographs of Moiré superstructures formed from annealing of B30 on EBL patterned silica grains with pitch of 36 nm (a), 38 nm (b), 44 nm (c), 46 nm (d), 50 nm (e), and 52 nm (f). Inserted image are 2D FFT.*

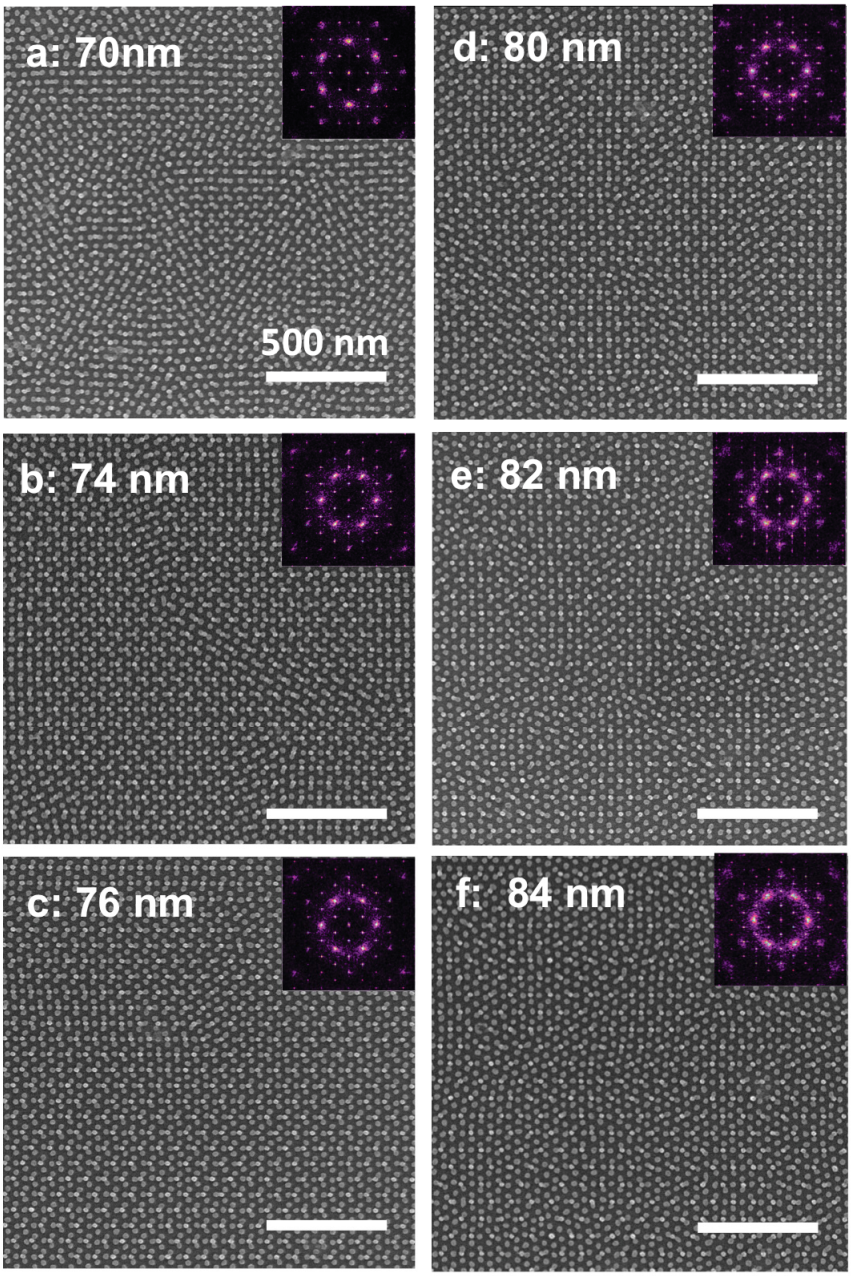

Figure 5.20: *SEM micrographs of Moiré superstructures formed from annealing of B30 on EBL patterned silica grains with pitch of 70 nm (a), 74 nm (b), 76 nm (c), 80 nm (d), 82 nm (e), and 84 nm (f). Inserted image are 2D FFT.*

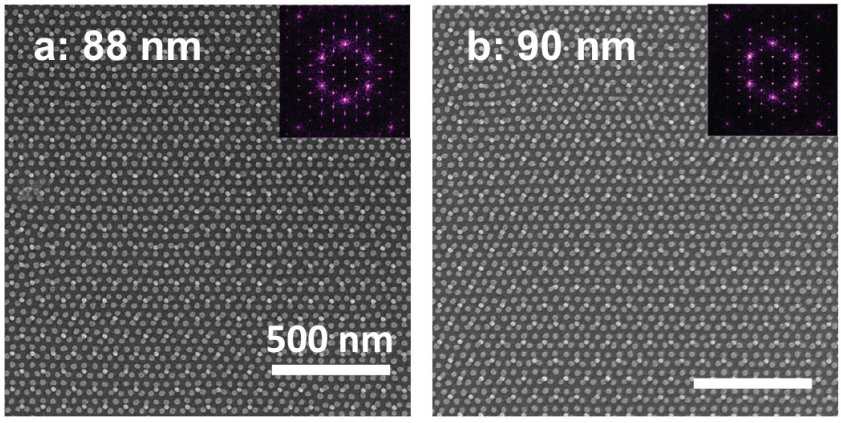

Figure 5.21: *SEM micrographs of Moiré superstructures formed from annealing of B30 on EBL patterned silica grains with pitch of 88 nm (a) and 90 nm (b). Inserted image are 2D FFT.*

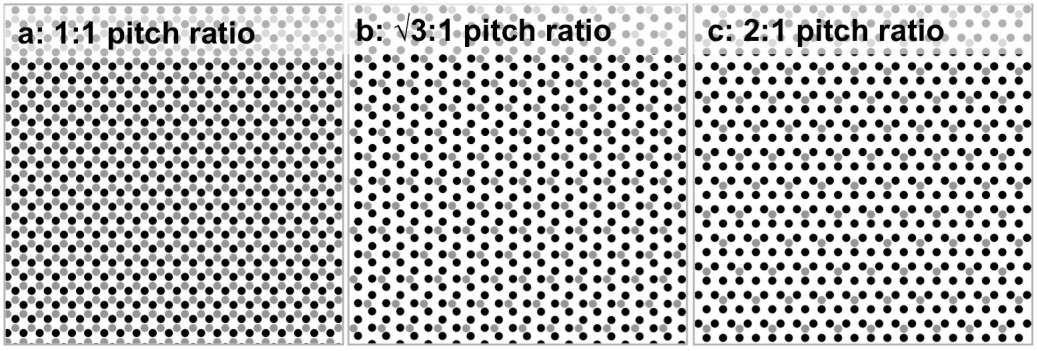

Figure 5.22: *Summary of three types of Moiré superstructures formed with EBL pitch: B30 pitch of (a) 1:1, (b) $\sqrt{3}$:1, and (c)2:1.*

Table 5.3: *Native pitch ratios (native BCP pitch/EBL pillar pitch), measured pitch ratios, and relative rotation angles of for the resulting Moiré superstructures.*

EBL Pillar Pitch	Native Pitch Ratio	Measured Pitch Ratio	Relative Rotation Angle (°)
36	1.25	1.21	2.2±0.1
38	1.18	1.14	0.7±0.3
44	1.02	N/A (∼1)	N/A (∼0)
46	0.98	0.95	N/A (∼0)
50	0.90	0.89	1.0±0.4
52	0.86	0.85	0.9 ± 0.6
70	0.64	0.62	28.7 ± 1.3
74	0.61	0.61	29.7 ± 0.2
76	0.59	0.58	29.5 ± 0.5
80	0.56	0.56	29.9 ± 0.1
82	0.55	0.53	29.5 ± 0.3
84	0.53	0.52	29.5 ± 0.2
88	0.51	0.50	0.6 ± 0.2
90	0.50	0.49	0.9 ± 0.3

of patterns and motifs, through an entirely bottom-up process. As is always the case with nanopatterning *via* self-assembly of BCPs, subtle effects are important, including the critical role of dot size, grain boundaries between dot domains, and the annealing process. Further investigation into the fundamental aspects of self-assembly of the second layer during the annealing step, coupled with large-scale statistical analysis of the resulting patterns, will lead to better understanding of registration, and hence reduce the level of defects in the resulting nanopatterns.

6

Conclusions

6.1 Thesis Summary

The primary goal of this thesis was to understand the mechanism of microwave annealing and solvent vapor annealing of block copolymer thin films and to explore the usage of fully bottom-up sequential annealing methods for density multiplying and Moiré pattern fabrication. *In situ* monitoring techniques, such as ellipsometry, optical microscopy, and/or thermal measurements, were applied to monitor and control annealing processes. Highlights and breakthroughs of each chapter are summarized in following sections.

6.1.1 Chapter 1

Chapter 1 gave a brief introduction of BCPs and their applications in the semiconductor industry. This chapter begins with a discussion of the current

challenges facing photolithography for future semiconductor fabrication. Next, the chapter briefly introduced the basic of polymer science and BCPs followed by microphase segregation of BCPs. Theoretical and experimental research of BCP microphase segregation were reviewed. The influence of film thickness, surface chemistry, annealing conditions, and surface guiding patterns were all discussed, and finally, various pattern transfer strategies were discussed. At the end of the chapter, potential applications of BCP self-assembly in the semiconductor industry were introduced and the challenges were discussed.

6.1.2 Chapter 2

Chapter 2 aimed to uncover the mechanism of microphase segregation of BCP thin films in microwave-driven annealing. An *in situ* fiber optic probe was used to in direct contact with samples and measured the temperature profiles of BCP thin films during microwave irradiation. The doping and size of silicon chips were shown to have a strong influence of the heating rate during microwave irradiation. Silicon chips with higher resistivity heated up faster compared with low resistivity ones, and the heating rates increased as the silicon chips size increased. Thick films of PS, PMMA, P2VP, and their mixtures also showed no significant heating effect under microwave irradiation. PS-*b*-P2VP and PS-*b*-PMMA thin films were spin-cast on a 1 cm $\times$ 1 cm low resistivity silicon substrate (non-microwave-responsive) and annealed in a domestic microwave oven (2.45 GHz, $\sim$600 W). BCP thin film samples were not hot enough to reach T_g after 60 s of irradiation and did not shown signs of microphase segregation and ordering. When BCP thin film samples were placed on a 1.5 cm $\times$ 1.5 cm high resistivity silicon chip (used as a heating element), ordered cylindrical patterns were formed after 60 s of microwave irradiation, and the defect density of resulting BCP thin films decreased as the annealing temperature increased. This evidence proved that the heating from the heating element induced the microphase segregation. As the heating element was decoupled from BCP substrate, fast annealing of BCP thin films on microwave a neutral substrate, such as

ITO-coated glass, glass, and kapton, was successfully carried out using microwave irradiation in about 60 s.

6.1.3 Chapter 3

In Chapter 3, a controlled solvent vapor flow annealing system was introduced. This system was integrated with *in situ* laser reflectometry, *in situ* optical microscopy, temperature control, and a feedback loop that controlled the real-time degree of film swelling by adjusting the solvent vapor flow rate. Precise control of swelling and deswelling rate, degree of swelling, and dwelling time of BCP thin films during annealing period was demonstrated. A multi-step annealing process with two swelling and deswelling processes was also carried out. The *in situ* optical microscope was able to monitor macroscopic BCP thin film morphological evolution during solvent annealing , as dewetting and double layers that commonly form in annealed BCP thin film, which is problematic for large scale patterning applications. However, it was also found that the formation of dewetted regions and double layers was reversible. Highly ordered hexagonally packed grains with sizes over 50 μm^2 was achieved by annealing PS-*b*-PDMS thin films with precise control over the degree of swelling.

6.1.4 Chapter 4

In Chapter 4, a fullly bottom-up sequential patterning approach was developed for BCP density multiplication. Briefly, a layer of hexagonally packed silica dots was obtained from spin-casting, annealing, and etching of a dot-forming PS-*b*-PDMS on a silicon substrate. Then, this process was repeated on the same substrate with the same PS-*b*-PDMS BCP one or two more times, resulting in density-doubled honeycomb dot structures or density tripled hexagonally packed dot structures.This approach was able to surpass the native dot density of a given dot-forming BCP.

The center-to-center spacing and dot diameter of BCP dot nanopatterns was critical to form highly ordered double or triple density patterns. It was also shown that by blending of a PS homopolymer into PS-*b*-PDMS the center-to-center spacing of the resulting dot patterns could be adjusted. The quality of double and triple density nanopatterns was successfully predicted by only using the standard deviation of the hydrostatic strain and the ratio between dot diameter and center-to-center spacing. A hexagonally packed silica dot pattern with a density of 2 Teradot/in^2 was demonstrated. This method provided an alternative approach to use well-established high molecular weight BCPs with highly ordered single layer dot patterns to form high density nanopatterns instead of using low molecular weight BCPs.

6.1.5 Chapter 5

In Chapter 5, a new bottom-up method of fabricating Moirè nanopatterns *via* BCP self-assembly was demonstrated. Similar to the sequential annealing process described in Chapter 4, a thin film of a dot-forming PS-*b*-PDMS was self-assembled on a hexagonally packed silica dot pattern obtained from annealing of another PS-*b*-PDMS. The native pitch difference between the two BCPs resulted in Moiré superstructures. Four distinct Moiré superstructures with mismatch angles of 3°, 5°, 11°, and 30° were demonstrated through different BCPs combinations and different annealing orders. The registration force of shallow BCP dots in the bottom layer was sufficient to direct the self-assembly of the top layer to take on a preferred relative angle of rotation. Large-area helium ion microscopy (HIM) imaging with a field view of 15 μm $\times$ 15 μm or 20 μm $\times$ 20 μm enabled quantification of the distributions of relative rotations between the two lattices in the Moiré superstructures, yielding statistically meaningful results for each combination. The influence of bottom layer dot size and pitch to the registration of top BCP dots were also studied.

6.2 Future Work

6.2.1 Microwave Thermal Annealing on Patterned Surfaces

Chapter 2 demonstrated sub-1 min microwave thermal annealing of BCP thin films on flat surfaces. However, the lowest defect density obtained from annealed BCP thin films was about 18 pairs/μm^2 at 240 °C, which is 2×10^9 times larger than the target value according to ITRS.[199] Graphoepitaxy and multiple heating cycles can help to further decrease the defect density of annealed BCP thin films. Initial tests have been done by annealing PS-*b*-P2VP (23.6k-10.4k) thin films and PS-*b*-PMMA (45k-20k) thin films on silicon substrates patterned with 35 nm tall silica walls. Experimental procedures, including BCP thin film preparation, annealing, metalization, and etching were all described in Chapter 2. The silica patterns were fabricated with electron beam lithography (EBL) using hydrogen silsesquioxane (HSQ) as photoresist. As shown in Figure 6.1, the quality of the parallel line patterns in PS-*b*-P2VP thin film was much improved on patterned substrates. In multiple annealing tests, PS-*b*-PMMA thin films were spin-cast on silica patterned substrates and annealed in a domestic microwave oven for 1, 3, and 6 heating cycles. Multiple heating cycles tests were done by turning off and on the microwave oven at 240 °C and 100 °C, respectively. Annealed PS-*b*-PMMA thin films on two different patterned areas were shown in Figure 6.2. Highly ordered parallel cylinder patterns were successfully obtained after 6 heating cycles. Interestingly, PS-*b*-PMMA thin films formed perpendicular hexagonal packed cylinder patterns (hexagonally packed dot patterns) instead of horizontal cylinder pattern after 1 annealing cycle on a 250 nm-silica wall patterned substrate, shown Figure 6.2a. The perpendicular hexagonal packed cylinder patterns convert to parallel cylinder patterns as the number of annealing cycles increases (Figure 6.2a-c). Similar trends could also be found in BCP thin films with 500 nm-pitch silica wall patterned substrates (Figure 6.2d-f). For future research, the influence of silica wall pitch, height, and annealing temperature need to be further optimized to achieve better

pattern quality. The transition from perpendicular cylinder patterns to horizontal cylinder patterns in different annealing cycles is very interesting. More work on controlled experiments and theoretical simulation work need to be done in order to understand the mechanism of this order-to-order transition process.

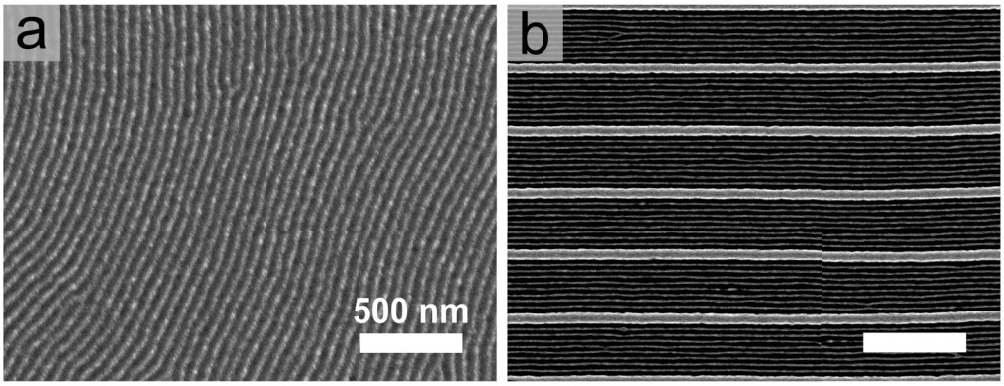

Figure 6.1: *SEM micrographs of Pt nanopatterns templated from microwave thermal annealed PS-b-P2VP (23.6k-10.4k) to 240 °C on flat surface (a) and on SiO_x walls surface (b).*

Moreover, PS-*b*-PMMA thin films on substrates with silica pillar patterns (50 nm center-to-center spacing) were also annealed in a microwave to 240 °C. As shown in Figure 6.3, PS-*b*-PMMA thin films form perpendicular cylinder patterns (gray dots) in silica pillar area instead of horizontal cylinder pattern on free surface. This is a new approach to control the orientation of cylinder forming BCPs and can be used to pattern dot arrays on surfaces. For the future work, center-to-center spacing, diameter, height, and geometry of silica pillar arrays need to be further optimized.

Additionally, a feedback loop that can adjust the microwave power output according to real time sample temperature, and a setpoint can be added into the annealing system. This feature would be able to maintain a constant temperature during annealing and allows for systematic study of the effects of annealing time, heating rate, and annealing temperature on the resulting morphology of BCP thin

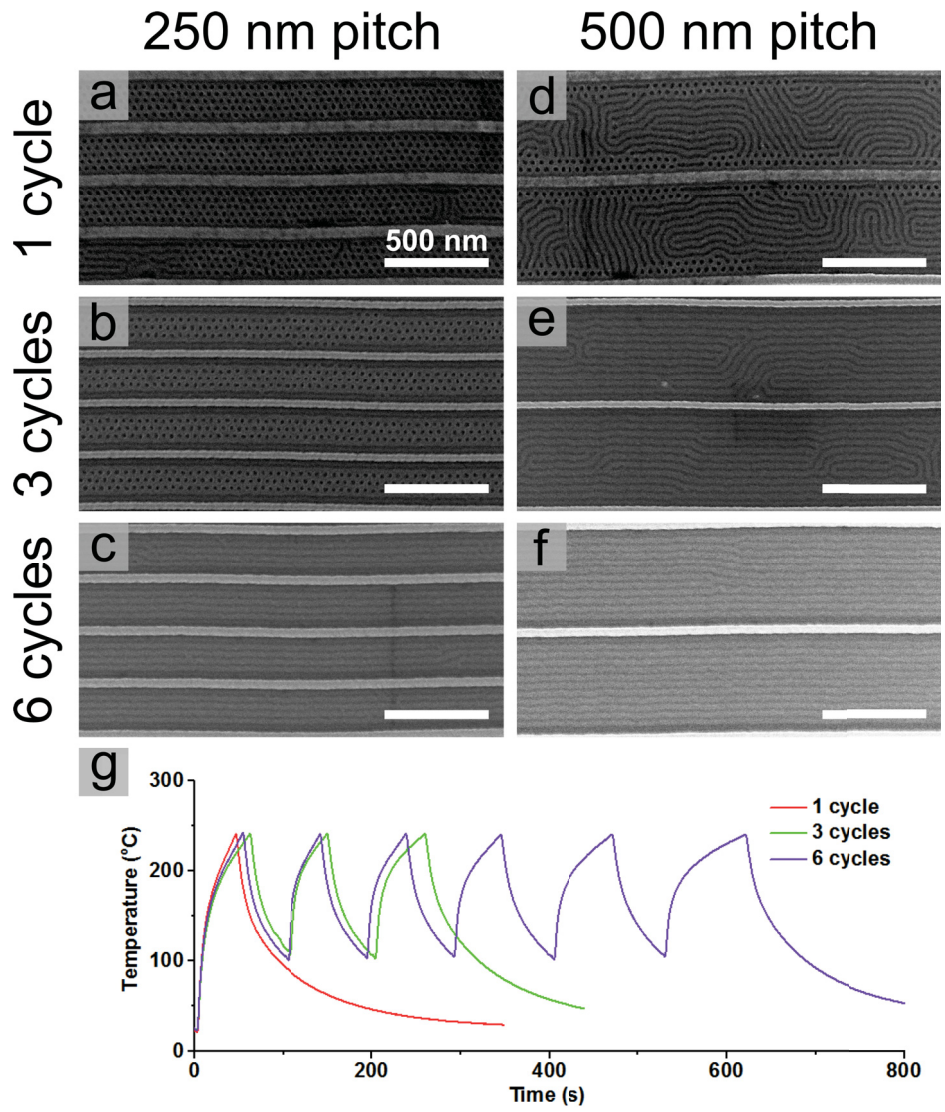

Figure 6.2: *Multi-cycle annealing of a PS-b-PMMA (45k-20k) thin film in microwave irradiation. (a-c) SEM micrographs of PS-b-PMMA thin film in SiO_x walls with a 250 nm separation annealed in 1, 3, and 6 heating cycles, respectively. (d-f) SEM micrographs of a PS-b-PMMA thin film between SiO_x walls with a 500 nm separation annealed in 1, 3, and 6 heating cycles, respectively. (g) Temperature profiles of 1, 3, and 6 microwave heating cycles.*

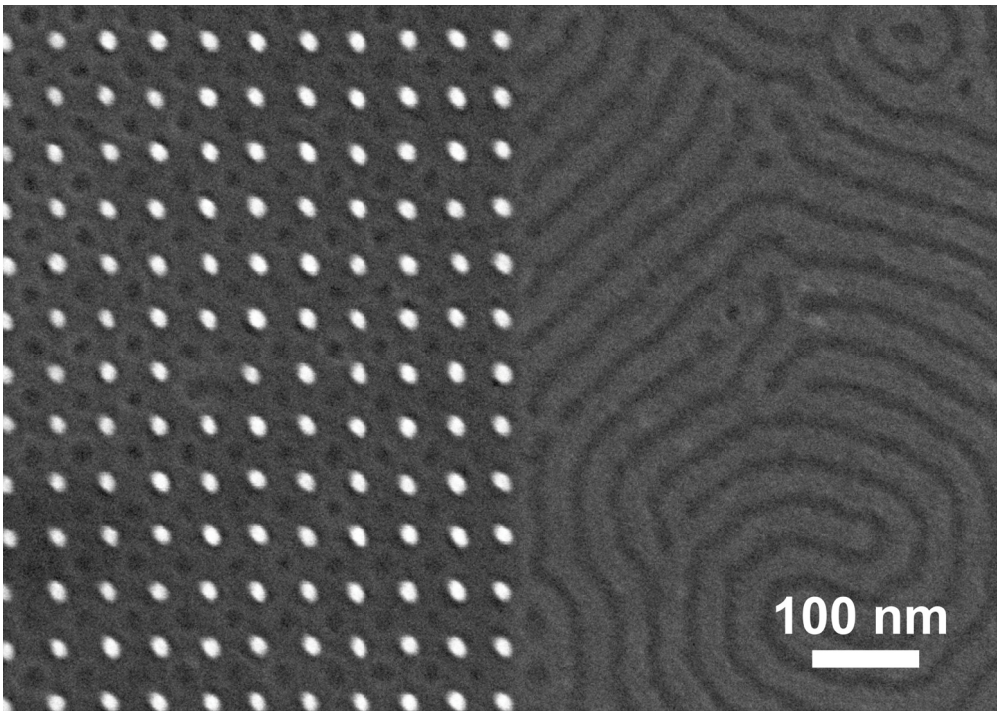

Figure 6.3: *SEM micrograph of PS-b-PMMA (45k-20k) thin film annealed using microwave irradiation on a patterned substrate of silica pillars (white dots). The silica pillars are about 35 nm in height, 16 nm in diameter and 50 nm in pitch.*

films.

6.2.2 Localized Thermal Annealing using Microwave Irradiation

The selective heating capability of microwave irradiation can be used to anneal BCP thin films locally. As shown in Figure 6.4, a microwave absorber with a high aspect ratio of nano- or micro-patterns would have direct contact with the BCP thin film in selective locations. These contact areas would be heated during microwave irradiation and annealing. The microwave absorber could be fabricated with a high resistivity silicon chip using lithography and high aspect silicon etching processes. Additionally, in order to achieve localized thermal annealing, the BCP substrate needs to be microwave neutral (can't heated up during microwave annealing) and possess low thermal conductivity.

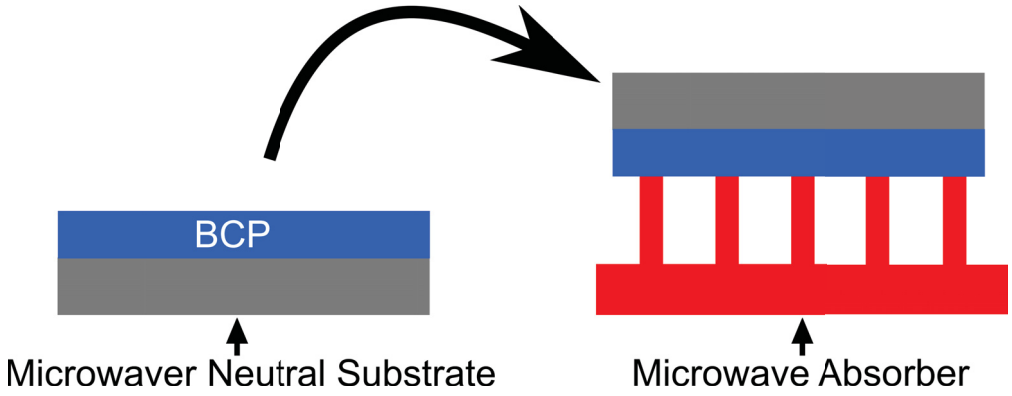

Figure 6.4: *Schematic representation of a sandwich structure for microwave localized thermal annealing.*

A rough test has been conducted by placing a 500 μm thick microwave absorber (1.5 cm $\times$ 1.5 cm in size) vertically on PS-*b*-P2VP (23.6k-10.4k) thin film samples on ITO-coated glass substrate (1 cm $\times$ 1 cm) and a low resistivity silicon substrate (1 cm $\times$ 1 cm). The 500 μm thick line area on the BCP thin films are in direct

contact with the microwave absorber and the microwave absorber was heated in microwave irradiation to around 240 °C in about 10 s. Both the ITO-coated glass substrate and low resistivity silicon substrate were microwave neutral substrates. As shown in Figure 6.5, the PS-*b*-P2VP thin film has equally ordered fingerprint patterns in all regions on the film, independent of the microwave absorber location. This is due to the high thermal conductivity of silicon. During annealing, the heat was efficiently transferred from heated area to the whole film. In contrast, PS-*b*-P2VP thin film on low thermal conductivity substrate, ITO-coated glass, was locally annealed (Figure 6.6), where ordered line patterns are only observed in the heated area. These results suggest that localized thermal annealing with microwave irradiation can be achieved.

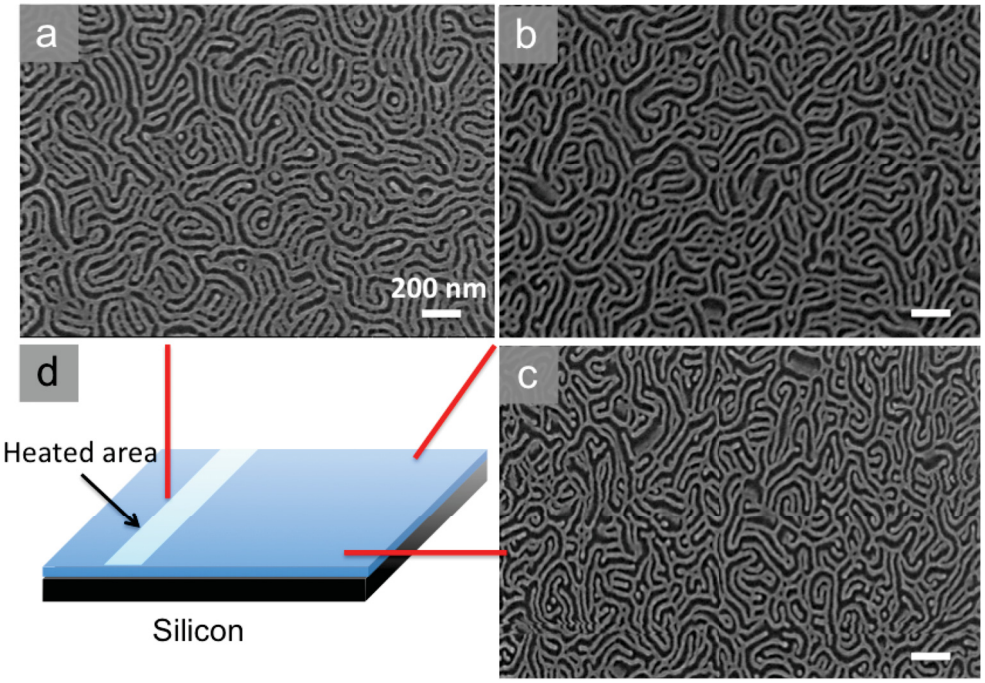

Figure 6.5: *SEM micrographs of Pt nanopatterns converted from a locally heated PS-b-P2VP thin film on a silicon substrate. All scale bars are 200 nm.*

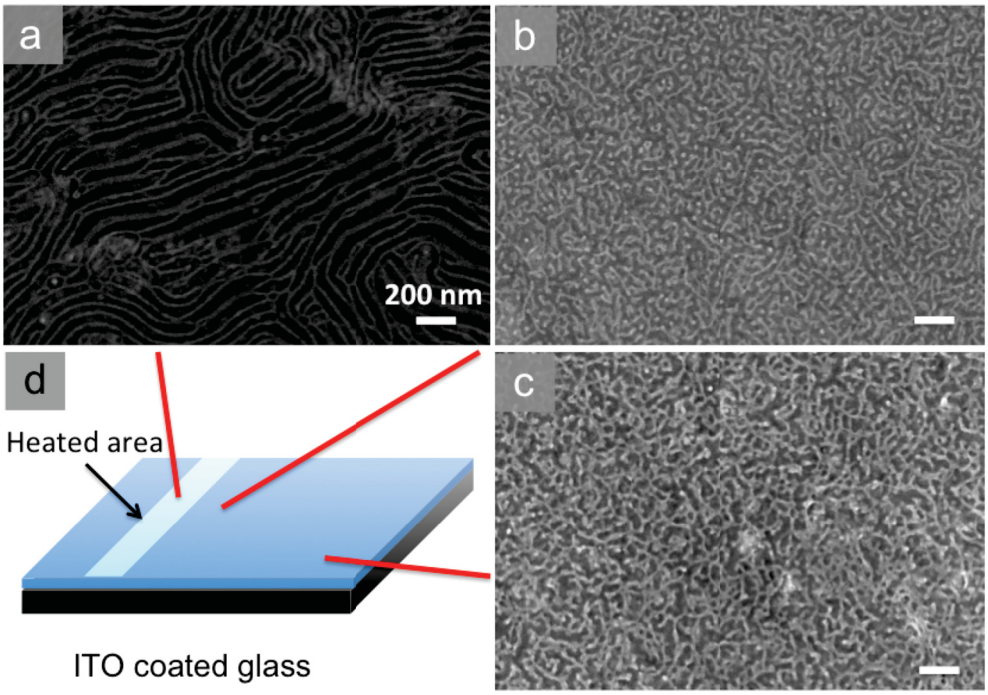

Figure 6.6: *SEM micrographs of Pt nanopatterns converted from a locally heated PS-b-P2VP thin film on a ITO-coated glass substrate. All scale bars are 200 nm.*

6.2.3 Self-Assembly Study in Controlled Solvent Vapor Flow Annealing

Controlled solvent vapor flow annealing is a great approach to systematically study the nano- and microscale morphology of BCP thin films during the solvent annealing process. The feedback loop allows the annealing system to precisely control the swelling, deswelling, and the degree of swelling. Multiple annealing cycles with multiple swelling and desweeling processes can be achieved. In future research, the influence of swelling rate, deswelling rate, degree of swelling, and dwelling time to the resulting BCP thin films (defect density, grain size, grain orientation, line edge roughness, line width roughness) can be studied. High resolution large scale images (over 40 μm $\times$ 40 μm) obtained by HIM provide a good way to analyze the ordering of BCP nanopatterns both in the nano- and macroscale. The optimized annealing process needs to be developed in order to obtain high quality BCP nanopatterns in short annealing times.

Double layer and dewetting areas are common annealed BCP thin films and often cause microscale defect areas. However, little work has been done to study the formation and growth of double layer and wetting areas during annealing. The use of an *in situ* optical microscope and feedback loop in our solvent flow annealing system enables capturing the formation and growth process of double layer and wetting areas. It was also shown that the formation of double layer areas and wetting areas are reversible in multi-cycle annealing tests (see Chapter 3 for more detail). More systematic work needs to be done in order to understand "nucleation" and "growth" of double layers and wetting areas, which may help to develop strategies to decrease or eliminate their formation.

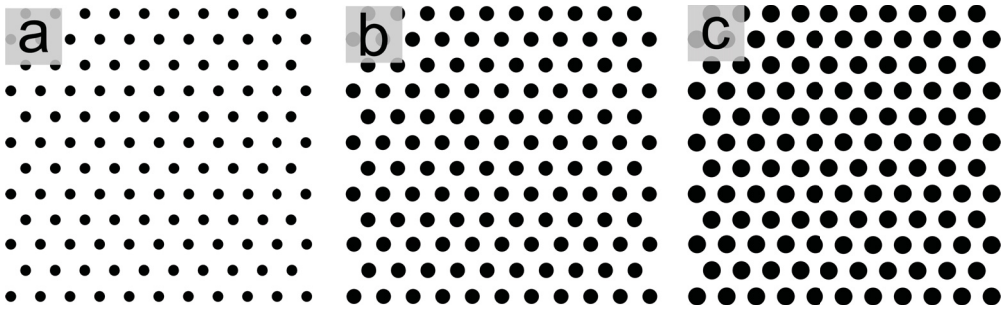

Figure 6.7: *Schematic diagram of EBL pillars with different diameters.*

6.2.4 Moiré Superstructure Formation

In order to study the incommensurate self-assembly of a dot-forming PS-*b*-PDMS nanopatterns on hexagonally packed dot arrays with a different pitch, 15 nm tall hexagonal packed silica pillar arrays with pitch range from 36 nm to 90 nm has been fabricated by EBL and the resulting Moiré patterns are shown in Chapter 5. As been shown in Chapter 5, the height of the bottom layer has a strong influence on the resulting Moiré superstructures. In future research, the effect of the height of the bottom layer on the resulting Moiré superstructures needs to be studied. Silicon pillar arrays with different heights can be fabricated with EBL and HSQ as photoresist. The pillar height can be adjusted by controlling the film thickness of photoresist and reactive ion etching after patterning. Additionally, the size of bottom layer pillars might be another aspect that will influence the resulting Moiré patterns (Figure 6.7). Hexagonal dot pillar arrays with the same pitch but different diameters can also be fabricated by EBL.

References

[1] Delachat, F.; Gharbi, A.; Pimenta Barros, P.; Argoud, M.; Lapeyre, C.; Bos, S.; Hazart, J.; Pain, L.; Monget, C.; Chevalier, X.; Nicolet, C.; Navarro, C.; Cayrefourcq, I.; Tiron, R. Advanced Surface Affinity Control for DSA Contact Hole Shrink Applications. Emerging Patterning Technologies. San Jose, California, 2017; p 101440O.

[2] Herr, D. J. *Journal of Materials Research* **2011**, *26*, 122–139.

[3] Bates, F. S.; Fredrickson, G. H. *Physics Today* **1999**, *52*, 32–38.

[4] Knoll, A.; Horvat, A.; Lyakhova, K. S.; Krausch, G.; Sevink, G. J. A.; Zvelindovsky, A. V.; Magerle, R. *Physical Review Letters* **2002**, *89*.

[5] Li, W.; Liu, M.; Qiu, F.; Shi, A.-C. *The Journal of Physical Chemistry B* **2013**, *117*, 5280–5288.

[6] Welander, A. M.; Kang, H.; Stuen, K. O.; Solak, H. H.; Müller, M.; de Pablo, J. J.; Nealey, P. F. *Macromolecules* **2008**, *41*, 2759–2761.

[7] Nandan, B.; Vyas, M. K.; Böhme, M.; Stamm, M. *Macromolecules* **2010**, *43*, 2463–2473.

[8] Bita, I.; Yang, J. K. W.; Jung, Y. S.; Ross, C. A.; Thomas, E. L.; Berggren, K. K. *Science* **2008**, *321*, 939–943.

[9] Yang, J. K. W.; Jung, Y. S.; Chang, J.-B.; Mickiewicz, R. A.; Alexander-Katz, A.; Ross, C. A.; Berggren, K. K. *Nature Nanotechnology* **2010**, *5*, 256–260.

[10] Chang, J.-B.; Choi, H. K.; Hannon, A. F.; Alexander-Katz, A.; Ross, C. A.; Berggren, K. K. *Nature Communications* **2014**, *5*, 3305.

[11] Chai, J.; Buriak, J. M. *ACS Nano* **2008**, *2*, 489–501.

[12] Stoykovich, M. P.; Kang, H.; Daoulas, K. C.; Liu, G.; Liu, C.-C.; de Pablo, J. J.; Müller, M.; Nealey, P. F. *ACS Nano* **2007**, *1*, 168–175.

References

[13] Farrell, R. A.; Petkov, N.; Shaw, M. T.; Djara, V.; Holmes, J. D.; Morris, M. A. *Macromolecules* **2010**, *43*, 8651–8655.

[14] Chai, J.; Wang, D.; Fan, X.; Buriak, J. M. *Nature Nanotechnology* **2007**, *2*, 500–506.

[15] Tsai, H.; Pitera, J. W.; Miyazoe, H.; Bangsaruntip, S.; Engelmann, S. U.; Liu, C.-C.; Cheng, J. Y.; Bucchignano, J. J.; Klaus, D. P.; Joseph, E. A.; Sanders, D. P.; Colburn, M. E.; Guillorn, M. A. *ACS Nano* **2014**, *8*, 5227–5232.

[16] Xiao, S.; Yang, X.; Steiner, P.; Hsu, Y.; Lee, K.; Wago, K.; Kuo, D. *ACS Nano* **2014**, *8*, 11854–11859.

[17] Ruiz, R.; Dobisz, E.; Albrecht, T. R. *ACS Nano* **2011**, *5*, 79–84.

[18] Servin, I. et al. *Japanese Journal of Applied Physics* **2014**, *53*, 06JC05.

[19] Bao, X.-Y.; He Yi,; Bencher, C.; Chang, L.-W.; Dai, H.; Chen, Y.; Chen, P.-T. J.; Wong, H.-S. P. SRAM, NAND, DRAM Contact Hole Patterning Using Block Copolymer Directed Self-Assembly Guided by Small Topographical Templates. Electron Devices Meeting. Washington DC, 2011; pp 7.7.1–7.7.4.

[20] Yi, H.; Bao, X.-Y.; Zhang, J.; Bencher, C.; Chang, L.-W.; Chen, X.; Tiberio, R.; Conway, J.; Dai, H.; Chen, Y.; Mitra, S.; Wong, H.-S. P. *Advanced Materials* **2012**, *24*, 3107–3114.

[21] Zhang, X.; Murphy, J. N.; Wu, N. L. Y.; Harris, K. D.; Buriak, J. M. *Macromolecules* **2011**, *44*, 9752–9757.

[22] Gotrik, K. W.; Ross, C. A. *Nano Letters* **2013**, *13*, 5117–5122.

[23] Park, W. I.; Kim, K.; Jang, H.-I.; Jeong, J. W.; Kim, J. M.; Choi, J.; Park, J. H.; Jung, Y. S. *Small* **2012**, *8*, 3762–3768.

[24] Singh, G.; Yager, K. G.; Berry, B.; Kim, H.-C.; Karim, A. *ACS Nano* **2012**, *6*, 10335–10342.

[25] Majewski, P. W.; Yager, K. G. *ACS Nano* **2015**, *9*, 3896–3906.

References

[26] Jin, C.; Murphy, J. N.; Harris, K. D.; Buriak, J. M. *ACS Nano* **2014**, *8*, 3979–3991.

[27] Jin, C.; Olsen, B. C.; Luber, E. J.; Buriak, J. M. *Chemistry of Materials* **2017**, *29*, 176–188.

[28] Wu, N. L. Y.; Harris, K. D.; Buriak, J. M. *ACS Nano* **2013**, *7*, 5595–5606.

[29] Knoll, A.; Magerle, R.; Krausch, G. *The Journal of Chemical Physics* **2004**, *120*, 1105–1116.

[30] Jin, C.; Olsen, B. C.; Wu, N. L. Y.; Luber, E. J.; Buriak, J. M. *Langmuir* **2016**, *32*, 5890–5898.

[31] Kihara, N.; Yamamoto, R.; Sasao, N.; Shimada, T.; Yuzawa, A.; Okino, T.; Ootera, Y.; Kamata, Y.; Kikitsu, A. *Journal of Vacuum Science & Technology B, Nanotechnology and Microelectronics: Materials, Processing, Measurement, and Phenomena* **2012**, *30*, 06FH02.

[32] Yang, X.; Xiao, S.; Hsu, Y.; Feldbaum, M.; Lee, K.; Kuo, D. *Journal of Nanomaterials* **2013**, *2013*, e615896.

[33] Yamamoto, R.; Yuzawa, A.; Shimada, T.; Ootera, Y.; Kamata, Y.; Kihara, N.; Kikitsu, A. *Japanese Journal of Applied Physics* **2012**, *51*, 046503.

[34] Son, J. G.; Chang, J.-B.; Berggren, K. K.; Ross, C. A. *Nano Letters* **2011**, *11*, 5079–5084.

[35] Son, J. G.; Hannon, A. F.; Gotrik, K. W.; Alexander-Katz, A.; Ross, C. A. *Advanced Materials* **2011**, *23*, 634–639.

[36] Ross, C. A.; Jung, Y. S.; Chuang, V. P.; Son, J. G.; Gotrik, K. W.; Mickiewicz, R. A.; Yang, J. K. W.; Chang, J. B.; Berggren, K. K.; Gwyther, J.; Manners, I. Templated Self-Assembly of Si-Containing Block Copolymers for Nanoscale Device Fabrication. Alternative Lithographic Technologies II. San Jose, CA, 2010; pp 76370H–76370H–7.

[37] Park, W. I.; Yoon, J. M.; Park, M.; Lee, J.; Kim, S. K.; Jeong, J. W.; Kim, K.;

Jeong, H. Y.; Jeon, S.; No, K. S.; Lee, J. Y.; Jung, Y. S. *Nano Letters* **2012**, *12*, 1235–1240.

[38] Park, W. I.; You, B. K.; Mun, B. H.; Seo, H. K.; Lee, J. Y.; Hosaka, S.; Yin, Y.; Ross, C. A.; Lee, K. J.; Jung, Y. S. *ACS Nano* **2013**, *7*, 2651–2658.

[39] Jeong, C. K.; Baek, K. M.; Niu, S.; Nam, T. W.; Hur, Y. H.; Park, D. Y.; Hwang, G.-T.; Byun, M.; Wang, Z. L.; Jung, Y. S.; Lee, K. J. *Nano Letters* **2014**, *14*, 7031–7038.

[40] Jin, C.; Olsen, B. C.; Luber, E. J.; Buriak, J. M. *ACS Nano* **2017**, *11*, 3237–3246.

[41] Vandecreme, A.; Blattner, T.; Majurski, M.; Bajcsy, P.; Scott, K.; Scott, J. H. J. *Microscopy and Microanalysis* **2015**, *21*, 89–90.

[42] Moore, G. E. *Electronics* **1965**, *86*, 114–117.

[43] Kim, N. S.; Austin, T.; Baauw, D.; Mudge, T.; Flautner, K.; Hu, J. S.; Irwin, M. J.; Kandemir, M.; Narayanan, V. *Computer* **2003**, *36*, 68–75.

[44] Levinson, H. J. *Principles of Lithography*; SPIE Press, 2005.

[45] Wallraff, G. M.; Hinsberg, W. D. *Chemical Reviews* **1999**, *99*, 1801–1822.

[46] Sanders, D. P. *Chemical Reviews* **2010**, *110*, 321–360.

[47] Trybula, W. J. *Journal of Micro/Nanolithography, MEMS, and MOEMS* **2005**, *4*, 011007.

[48] Abhari, R. S.; Rollinger, B.; Giovannini, A. Z.; Morris, O.; Henderson, I.; Ellwi, S. S. *Journal of Micro/Nanolithography, MEMS, and MOEMS* **2012**, *11*, 021114–1.

[49] *International Technology Roadmap for Semiconductors 2.0*, 2015th ed.; Semiconductor Industry Association: San Jose, CA, 2015.

[50] Oyama, K.; Nishimura, E.; Kushibiki, M.; Hasebe, K.; Nakajima, S.; Murakami, H.; Hara, A.; Yamauchi, S.; Natori, S.; Yabe, K.; Yamaji, T.; Nakatsuji, R.; Yaegashi, H. The Important Challenge to Extend Spacer DP Process towards 22nm and Beyond. Advances in Resist Materials and Processing Technology XXVII. San Jose, CA,

2010; p 763907.

[51] Yaegashi, H.; Oyama, K.; Hara, A.; Natori, S.; Yamauchi, S.; Yamato, M. Sustainable Scaling Technique on Double-Patterning Process. Advances in Resist Materials and Processing Technology XXX. San Jose, CA, 2013; pp 868204–868204–7.

[52] Darling, S. B. *Progress in Polymer Science* **2007**, *32*, 1152–1204.

[53] Jeong, S.-J.; Kim, J. Y.; Kim, B. H.; Moon, H.-S.; Kim, S. O. *Materials Today* **2013**, *16*, 468–476.

[54] Li, W.; Müller, M. *Annual Review of Chemical and Biomolecular Engineering* **2015**, *6*, 187–216.

[55] Morris, M. A. *Microelectronic Engineering* **2015**, *132*, 207–217.

[56] Ji, S.; Wan, L.; Liu, C.-C.; Nealey, P. F. *Progress in Polymer Science* **2016**, *54–55*, 76–127.

[57] Bates, F. S.; Fredrickson, G. H. *Annual Review of Physical Chemistry* **1990**, *41*, 525–557.

[58] *International Technology Roadmap for Semiconductors*, 2005th ed.; Semiconductor Industry Association: San Jose, CA, 2005.

[59] Szwarc, M. *Nature* **1956**, *178*, 1168–1169.

[60] Marcy, J.; Shalanski, A.; Yarmuch, M.; Patchett, B. *Journal of Materials Engineering and Performance* **2004**, *13*, 208–217.

[61] Dunn, A. S.; Melville, H. W. *Nature* **1952**, *169*, 699–700.

[62] Hicks, J. A.; Melville, H. W. *Nature* **1953**, *171*, 300–301.

[63] Dunn, A. S.; Stead, B. D.; Melville, H. W. *Transactions of the Faraday Society* **1954**, *50*, 279–290.

[64] Woodward, A. E.; Smets, G. *Journal of Polymer Science* **1955**, *17*, 51–64.

References

[65] Allen, P. E. M.; Downer, J. M.; Hastings, G. W.; Melville, H. W.; Molyneux, P.; Urwin, J. R. *Nature* **1956**, *177*, 910–912.

[66] Jackson, D. R.; Lundsted, L. G. Polyoxyalkylene Surface Active Agents. 1954.

[67] Schmolka, I. Polyoxyethylene-Polyoxypropylene Aqueous Gels. 1973.

[68] Alexandridis, P.; Alan Hatton, T. *Colloids and Surfaces A: Physicochemical and Engineering Aspects* **1995**, *96*, 1–46.

[69] Desmond Goddard, E., Gruber, J., Eds. *Principles of Polymer Science and Technology in Cosmetics and Personal Care*; Cosmetic Science and Technology; CRC Press, 1999; Vol. 19990883.

[70] Kabanov, A. V.; Alakhov, V. Y. *Critical Reviews in Therapeutic Drug Carrier Systems* **2002**, *19*, 1–73.

[71] Maitz, M. *Biosurface and Biotribology* **2015**, *1*, 161–176.

[72] Ahn, H.; Park, S.; Kim, S.-W.; Yoo, P. J.; Ryu, D. Y.; Russell, T. P. *ACS Nano* **2014**, *8*, 11745–11752.

[73] Wang, Y.; Li, F. *Advanced Materials* **2011**, *23*, 2134–2148.

[74] Bockstaller, M. R.; Mickiewicz, R. A.; Thomas, E. L. *Advanced Materials* **2005**, *17*, 1331–1349.

[75] Mizuno, H.; Buriak, J. M. *Journal of the American Chemical Society* **2008**, *130*, 17656–17657.

[76] Liu, F.; Luber, E. J.; Huck, L. A.; Olsen, B. C.; Buriak, J. M. *ACS Nano* **2015**, *9*, 2184–2193.

[77] Gu, X.; Gunkel, I.; Russell, T. P. *Philosophical Transactions of the Royal Society A: Mathematical, Physical and Engineering Sciences* **2013**, *371*, 20120306.

[78] Meier, D. J. *Journal of Polymer Science Part C: Polymer Symposia* **1969**, *26*, 81–98.

[79] Helfand, E. *Macromolecules* **1975**, *8*, 552–556.

[80] Leibler, L. *Macromolecules* **1980**, *13*, 1602–1617.

[81] Sinturel, C.; Bates, F. S.; Hillmyer, M. A. *ACS Macro Letters* **2015**, *4*, 1044–1050.

[82] Bates, C. M.; Maher, M. J.; Janes, D. W.; Ellison, C. J.; Willson, C. G. *Macromolecules* **2014**, *47*, 2–12.

[83] Luo, M.; Epps, T. H. *Macromolecules* **2013**, *46*, 7567–7579.

[84] Thomas, H. R.; O'Malley, J. J. *Macromolecules* **1979**, *12*, 323–329.

[85] Hasegawa, H.; Hashimoto, T. *Macromolecules* **1985**, *18*, 589–590.

[86] Fredrickson, G. H. *Macromolecules* **1987**, *20*, 2535–2542.

[87] Anastasiadis, S. H.; Russell, T. P.; Satija, S. K.; Majkrzak, C. F. *Physical Review Letters* **1989**, *62*, 1852–1855.

[88] Lyakhova, K. S.; Horvat, A.; Zvelindovsky, A. V.; Sevink, G. J. A. *Langmuir* **2006**, *22*, 5848–5855.

[89] Radzilowski, L. H.; Carvalho, B. L.; Thomas, E. L. *Journal of Polymer Science Part B: Polymer Physics* **1996**, *34*, 3081–3093.

[90] She, M.-S.; Lo, T.-Y.; Ho, R.-M. *ACS Nano* **2013**, *7*, 2000–2011.

[91] Gu, W.; Hong, S. W.; Russell, T. P. *ACS Nano* **2012**, *6*, 10250–10257.

[92] Park, S.-M.; Stoykovich, M. P.; Ruiz, R.; Zhang, Y.; Black, C. T.; Nealey, P. F. *Advanced Materials* **2007**, *19*, 607–611.

[93] Peters, R. D.; Yang, X. M.; Kim, T. K.; Nealey, P. F. *Langmuir* **2000**, *16*, 9620–9626.

[94] Niemz, A.; Bandyopadhyay, K.; Tan, E.; Cha, K.; Baker, S. M. *Langmuir* **2006**, *22*, 11092–11096.

[95] Bates, C. M.; Seshimo, T.; Maher, M. J.; Durand, W. J.; Cushen, J. D.; Dean, L. M.;

Blachut, G.; Ellison, C. J.; Willson, C. G. *Science* **2012**, *338*, 775–779.

[96] Maher, M. J.; Bates, C. M.; Blachut, G.; Sirard, S.; Self, J. L.; Carlson, M. C.; Dean, L. M.; Cushen, J. D.; Durand, W. J.; Hayes, C. O.; Ellison, C. J.; Willson, C. G. *Chemistry of Materials* **2014**, *26*, 1471–1479.

[97] Mastroianni, S. E.; Epps, T. H. *Langmuir* **2013**, *29*, 3864–3878.

[98] Zhang, J.; Clark, M. B.; Wu, C.; Li, M.; Trefonas, P.; Hustad, P. D. *Nano Letters* **2016**, *16*, 728–735.

[99] Han, E.; Leolukman, M.; Kim, M.; Gopalan, P. *ACS Nano* **2010**, *4*, 6527–6534.

[100] Zhang, X.; Harris, K. D.; Wu, N. L. Y.; Murphy, J. N.; Buriak, J. M. *ACS Nano* **2010**, *4*, 7021–7029.

[101] Majewski, P. W.; Yager, K. G. *Macromolecules* **2015**, *48*, 4591–4598.

[102] Jin, H. M.; Lee, S. H.; Kim, J. Y.; Son, S.-W.; Kim, B. H.; Lee, H. K.; Mun, J. H.; Cha, S. K.; Kim, J. S.; Nealey, P. F.; Lee, K. J.; Kim, S. O. *ACS Nano* **2016**, *10*, 3435–3442.

[103] Majewski, P. W.; Rahman, A.; Black, C. T.; Yager, K. G. *Nature Communications* **2015**, *6*, 7448.

[104] Berry, B. C.; Bosse, A. W.; Douglas, J. F.; Jones, R. L.; Karim, A. *Nano Letters* **2007**, *7*, 2789–2794.

[105] Park, W. I.; Kim, J. M.; Jeong, J. W.; Jung, Y. S. *ACS Nano* **2014**, *8*, 10009–10018.

[106] Stoykovich, M. P.; Müller, M.; Kim, S. O.; Solak, H. H.; Edwards, E. W.; de Pablo, J. J.; Nealey, P. F. *Science* **2005**, *308*, 1442–1446.

[107] Ouk Kim, S.; Solak, H. H.; Stoykovich, M. P.; Ferrier, N. J.; de Pablo, J. J.; Nealey, P. F. *Nature* **2003**, *424*, 411–414.

[108] Ruiz, R.; Kang, H.; Detcheverry, F. A.; Dobisz, E.; Kercher, D. S.; Albrecht, T. R.; de Pablo, J. J.; Nealey, P. F. *Science* **2008**, *321*, 936–939.

[109] Cheng, J. Y.; Rettner, C. T.; Sanders, D. P.; Kim, H.-C.; Hinsberg, W. D. *Advanced Materials* **2008**, *20*, 3155–3158.

[110] Giammaria, T. J.; Ferrarese Lupi, F.; Seguini, G.; Perego, M.; Vita, F.; Francescangeli, O.; Wenning, B.; Ober, C. K.; Sparnacci, K.; Antonioli, D.; Gianotti, V.; Laus, M. *ACS Applied Materials & Interfaces* **2016**, *8*, 9897–9908.

[111] Zha, W.; Han, C. D.; Lee, D. H.; Han, S. H.; Kim, J. K.; Kang, J. H.; Park, C. *Macromolecules* **2007**, *40*, 2109–2119.

[112] Chun, S. B.; Han, C. D. *Macromolecules* **1999**, *32*, 4030–4042.

[113] Russell, T. P.; Hjelm, R. P.; Seeger, P. A. *Macromolecules* **1990**, *23*, 890–893.

[114] Cushen, J. D.; Otsuka, I.; Bates, C. M.; Halila, S.; Fort, S.; Rochas, C.; Easley, J. A.; Rausch, E. L.; Thio, A.; Borsali, R.; Willson, C. G.; Ellison, C. J. *ACS Nano* **2012**, *6*, 3424–3433.

[115] Pitet, L. M.; Wuister, S. F.; Peeters, E.; Kramer, E. J.; Hawker, C. J.; Meijer, E. W. *Macromolecules* **2013**, *46*, 8289–8295.

[116] Welander, A. M.; Craig, G. S. W.; Tada, Y.; Yoshida, H.; Nealey, P. F. *Macromolecules* **2013**, *46*, 3915–3921.

[117] Borah, D.; Senthamaraikannan, R.; Rasappa, S.; Kosmala, B.; Holmes, J. D.; Morris, M. A. *ACS Nano* **2013**, *7*, 6583–6596.

[118] Borah, D.; Shaw, M. T.; Holmes, J. D.; Morris, M. A. *ACS Applied Materials & Interfaces* **2013**, *5*, 2004–2012.

[119] Ferrarese Lupi, F.; Giammaria, T. J.; Ceresoli, M.; Seguini, G.; Sparnacci, K.; Antonioli, D.; Gianotti, V.; Laus, M.; Perego, M. *Nanotechnology* **2013**, *24*, 315601.

[120] Black, C. T.; Ruiz, R.; Breyta, G.; Cheng, J. Y.; Colburn, M. E.; Guarini, K. W.; Kim, H.-C.; Zhang, Y. *IBM Journal of Research and Development* **2007**, *51*, 605–633.

[121] Durand, W. J.; Blachut, G.; Maher, M. J.; Sirard, S.; Tein, S.; Carlson, M. C.;

Asano, Y.; Zhou, S. X.; Lane, A. P.; Bates, C. M.; Ellison, C. J.; Willson, C. G. *Journal of Polymer Science Part A: Polymer Chemistry* **2015**, *53*, 344–352.

[122] Gotrik, K. W.; Hannon, A. F.; Son, J. G.; Keller, B.; Alexander-Katz, A.; Ross, C. A. *ACS Nano* **2012**, *6*, 8052–8059.

[123] Gu, X.; Gunkel, I.; Hexemer, A.; Russell, T. P. *Macromolecules* **2016**, *49*, 3373–3381.

[124] Gianotti, V.; Antonioli, D.; Sparnacci, K.; Laus, M.; Giammaria, T. J.; Ferrarese Lupi, F.; Seguini, G.; Perego, M. *Macromolecules* **2013**, *46*, 8224–8234.

[125] Albert, J. N. L.; Epps III, T. H. *Materials Today* **2010**, *13*, 24–33.

[126] Kim, E.; Ahn, H.; Park, S.; Lee, H.; Lee, M.; Lee, S.; Kim, T.; Kwak, E.-A.; Lee, J. H.; Lei, X.; Huh, J.; Bang, J.; Lee, B.; Ryu, D. Y. *ACS Nano* **2013**, *7*, 1952–1960.

[128] Albalak, R. J.; Capel, M. S.; Thomas, E. L. *Polymer* **1998**, *39*, 1647–1656.

[129] Kim, G.; Libera, M. *Macromolecules* **1998**, *31*, 2670–2672.

[130] Fukunaga, K.; Elbs, H.; Magerle, R.; Krausch, G. *Macromolecules* **2000**, *33*, 947–953.

[131] Kimura, M.; Misner, M. J.; Xu, T.; Kim, S. H.; Russell, T. P. *Langmuir* **2003**, *19*, 9910–9913.

[132] Kim, H., S. Misner, J., M. Xu, T.; Kimura, M.; Russell, P., T. *Advanced Materials* **2004**, *16*, 226–231.

[133] Sinturel, C.; Vayer, M.; Morris, M.; Hillmyer, M. A. *Macromolecules* **2013**, *46*, 5399–5415.

[134] Chao, H.; Koski, J.; Riggleman, R. A. *Soft Matter* **2017**, *13*, 239–249.

[135] Tung, S.-H.; Xu, T. *Macromolecules* **2009**, *42*, 5761–5765.

[136] Kao, J.; Tingsanchali, J.; Xu, T. *Macromolecules* **2011**, *44*, 4392–4400.

[137] Wan, L.; Ji, S.; Liu, C.-C.; Craig, G. S. W.; Nealey, P. F. *Soft Matter* **2016**, *12*, 2914–

2922.

[138] Bai, W.; Hannon, A. F.; Gotrik, K. W.; Choi, H. K.; Aissou, K.; Liontos, G.; Ntetsikas, K.; Alexander-Katz, A.; Avgeropoulos, A.; Ross, C. A. *Macromolecules* **2014**, *47*, 6000–6008.

[139] Dinachali, S. S.; Bai, W.; Tu, K.-H.; Choi, H. K.; Zhang, J.; Kreider, M. E.; Cheng, L.-C.; Ross, C. A. *ACS Macro Letters* **2015**, *4*, 500–504.

[140] Kim, K.; Park, S.; Kim, Y.; Bang, J.; Park, C.; Ryu, D. Y. *Macromolecules* **2016**, *49*, 1722–1730.

[141] Olszowka, V.; Hund, M.; Kuntermann, V.; Scherdel, S.; Tsarkova, L.; Böker, A. *ACS Nano* **2009**, *3*, 1091–1096.

[142] Jeong, J. W.; Hur, Y. H.; Kim, H.-j.; Kim, J. M.; Park, W. I.; Kim, M. J.; Kim, B. J.; Jung, Y. S. *ACS Nano* **2013**, *7*, 6747–6757.

[143] Hong, S. W.; Gu, X.; Huh, J.; Xiao, S.; Russell, T. P. *ACS Nano* **2011**, *5*, 2855–2860.

[144] Park, S.-M.; Craig, G. S. W.; La, Y.-H.; Solak, H. H.; Nealey, P. F. *Macromolecules* **2007**, *40*, 5084–5094.

[145] G, A. T. K.; Nicaise, S. M.; Gadelrab, K. R.; Alexander-Katz, A.; Ross, C. A.; Berggren, K. K. *Nature Communications* **2016**, *7*, 10518.

[146] Kim, S.; Shin, D. O.; Choi, D.-G.; Jeong, J.-R.; Mun, J. H.; Yang, Y.-B.; Kim, J. U.; Kim, S. O.; Jeong, J.-H. *Small* **2012**, *8*, 1563–1569.

[147] Park, M. *Science* **1997**, *276*, 1401–1404.

[148] Tada, Y.; Yoshida, H.; Ishida, Y.; Hirai, T.; Bosworth, J. K.; Dobisz, E.; Ruiz, R.; Takenaka, M.; Hayakawa, T.; Hasegawa, H. *Macromolecules* **2012**, *45*, 292–304.

[149] Son, J. G.; Gwyther, J.; Chang, J.-B.; Berggren, K. K.; Manners, I.; Ross, C. A. *Nano Letters* **2011**, *11*, 2849–2855.

[150] Cao, L.; Massey, J.; Winnik, M.; Manners, I.; Riethmüller, S.; Banhart, F.; Spatz, J.;

Möller, M. *Advanced Functional Materials* **2003**, *13*, 271–276.

[151] Cummins, C.; Gangnaik, A.; Kelly, R. A.; Borah, D.; O'Connell, J.; Petkov, N.; Georgiev, Y. M.; Holmes, J. D.; Morris, M. A. *Nanoscale* **2015**, *7*, 6712–6721.

[152] Peng, Q.; Tseng, Y.-C.; Darling, S. B.; Elam, J. W. *Advanced Materials* **2010**, *22*, 5129–5133.

[153] Peng, Q.; Tseng, Y.-C.; Darling, S. B.; Elam, J. W. *ACS Nano* **2011**, *5*, 4600–4606.

[154] Biswas, M.; Libera, J. A.; Darling, S. B.; Elam, J. W. *The Journal of Physical Chemistry C* **2015**, *119*, 14585–14592.

[155] Tang, C.; Lennon, E. M.; Fredrickson, G. H.; Kramer, E. J.; Hawker, C. J. *Science* **2008**, *322*, 429–432.

[156] Ruiz, R.; Sandstrom, L., R. Black, T., C. *Advanced Materials* **2007**, *19*, 587–591.

[157] Muramatsu, M. *Journal of Micro/Nanolithography, MEMS, and MOEMS* **2012**, *11*, 031305.

[158] Cheng, J. Y.; Sanders, D. P.; Truong, H. D.; Harrer, S.; Friz, A.; Holmes, S.; Colburn, M.; Hinsberg, W. D. *ACS Nano* **2010**, *4*, 4815–4823.

[159] Liu, C.-C. et al. Fin Formation Using Graphoepitaxy DSA for FinFET Device Fabrication. Alternative Lithographic Technologies VII. San Jose, CA, 2015; p 94230S.

[160] Liu, C.-C. C. et al. DSA Patterning Options for FinFET Formation at 7nm Node. Alternative Lithographic Technologies VIII. San Jose, CA, 2016; p 97770R.

[161] Ferain, I.; Colinge, C. A.; Colinge, J.-P. *Nature* **2011**, *479*, 310–316.

[162] Black, C. T. *Applied Physics Letters* **2005**, *87*, 163116.

[163] Tsai, H. et al. High Chi Block Copolymer DSA to Improve Pattern Quality for FinFET Device Fabrication. San Jose, CA, 2016; p 977910.

[164] Service, R. F. *Science* **2006**, *314*, 1868–1870.

[165] Griffiths, R. A.; Williams, A.; Oakland, C.; Roberts, J.; Vijayaraghavan, A.; Thomas Thomson, *Journal of Physics D: Applied Physics* **2013**, *46*, 503001.

[166] Hellwig, O.; Bosworth, J. K.; Dobisz, E.; Kercher, D.; Hauet, T.; Zeltzer, G.; Risner-Jamtgaard, J. D.; Yaney, D.; Ruiz, R. *Applied Physics Letters* **2010**, *96*, 052511.

[167] Schabes, M. E. *Journal of Magnetism and Magnetic Materials* **2008**, *320*, 2880–2884.

[168] Wan, L.; Ruiz, R.; Gao, H.; Patel, K. C.; Lille, J.; Zeltzer, G.; Dobisz, E. A.; Bogdanov, A.; Nealey, P. F.; Albrecht, T. R. *Journal of Micro/Nanolithography, MEMS, and MOEMS* **2012**, *11*, 031405–1.

[169] Miao, X.; Huli, L.; Chen, H.; Xu, X.; Woo, H.; Bencher, C.; Shu, J.; Ngai, C.; Borst, C. Double Patterning Combined with Shrink Technique to Extend ArF Lithography for Contact Holes to 22 Nm Node and Beyond. Optical Microlithography XXI. San Jose, CA, 2008; p 69240A.

[170] Kim, S. O.; Kim, B. H.; Kim, K.; Koo, C. M.; Stoykovich, M. P.; Nealey, P. F.; Solak, H. H. *Macromolecules* **2006**, *39*, 5466–5470.

[171] Coulon, G.; Ausserre, D.; Russell, T. *Journal de Physique* **1990**, *51*, 777–786.

[172] Goldacker, T.; Abetz, V.; Stadler, R.; Erukhimovich, I.; Leibler, L. *Nature* **1999**, *398*, 137–139.

[173] Jeong, U.; Kim, H.-C.; Rodriguez, R.; Tsai, I.; Stafford, C.; Kim, J.; Hawker, C.; Russell, T. *Advanced Materials* **2002**, *14*, 274–276.

[174] Jeong, U.; Ryu, D. Y.; Kim, J. K.; Kim, D. H.; Wu, X.; Russell, T. P. *Macromolecules* **2003**, *36*, 10126–10129.

[175] Koneripalli, N.; Levicky, R.; Bates, F. S.; Matsen, M. W.; Satija, S. K.; Ankner, J.; Kaiser, H. *Macromolecules* **1998**, *31*, 3498–3508.

[176] Winey, K. I.; Thomas, E. L.; Fetters, L. J. *Macromolecules* **1991**, *24*, 6182–6188.

[177] Mokarian-Tabari, P.; Collins, T. W.; Holmes, J. D.; Morris, M. A. *ACS Nano* **2011**, *5*, 4617–4623.

[178] Wu, N. L. Y.; Zhang, X.; Murphy, J. N.; Chai, J.; Harris, K. D.; Buriak, J. M. *Nano Letters* **2012**, *12*, 264–268.

[179] Misner, M.; Skaff, H.; Emrick, T.; Russell, T. *Advanced Materials* **2003**, *15*, 221–224.

[180] Jeong, J. W.; Park, W. I.; Kim, M.-J.; Ross, C. A.; Jung, Y. S. *Nano Letters* **2011**, *11*, 4095–4101.

[181] Albert, J. N. L.; Bogart, T. D.; Lewis, R. L.; Beers, K. L.; Fasolka, M. J.; Hutchison, J. B.; Vogt, B. D.; Epps, T. H. *Nano Letters* **2011**, *11*, 1351–1357.

[182] Skaug, M. J.; Coffey, B. M.; Schwartz, D. K. *ACS Applied Materials & Interfaces* **2013**, *5*, 12854–12859.

[183] Mansky, P.; Liu, Y.; Huang, E.; Russell, T. P.; Hawker, C. *Science* **1997**, *275*, 1458–1460.

[184] *International Technology Roadmap for Semiconductors*, 2007th ed.; Semiconductor Industry Association: San Jose, CA, 2007.

[185] *International Technology Roadmap for Semiconductors*, 2011th ed.; Semiconductor Industry Association: San Jose, CA, 2011.

[186] Park, W. I.; Choi, Y. J.; Yun, J. M.; Hong, S. W.; Jung, Y. S.; Kim, K. H. *ACS Applied Materials & Interfaces* **2015**, *7*, 25843–25850.

[187] Arias-Zapata, J.; Böhme, S.; Garnier, J.; Girardot, C.; Legrain, A.; Zelsmann, M. *Advanced Functional Materials* **2016**, *26*, 5690–5700.

[188] Black, C. T.; Guarini, K. W.; Ruiz, R.; Sikorski, E. M.; Babich, I. V.; Sandstrom, R. L.; Zhang, Y. Polymer Self Assembly in Semiconductor Microelectronics. 2006 International Electron Devices Meeting. San Francisco, CA, 2006; pp 1–4.

[189] Ko, C.-J.; Lin, Y.-K.; Chen, F.-C. *Advanced Materials* **2007**, *19*, 3520–3523.

[190] Kitchen, H. J.; Vallance, S. R.; Kennedy, J. L.; Tapia-Ruiz, N.; Carassiti, L.; Harrison, A.; Whittaker, A. G.; Drysdale, T. D.; Kingman, S. W.; Gregory, D. H. *Chemical Reviews* **2014**, *114*, 1170–1206.

[191] Kappe, C. O. *Accounts of Chemical Research* **2013**, *46*, 1579–1587.

[192] Clark, D. E.; Sutton, W. H. *Annual Review of Materials Science* **1996**, *26*, 299–331.

[193] Gedye, R.; Smith, F.; Westaway, K.; Ali, H.; Baldisera, L.; Laberge, L.; Rousell, J. *Tetrahedron Letters* **1986**, *27*, 279–282.

[194] Strauss, C.; Trainor, R. *Australian Journal of Chemistry* **1995**, *48*, 1665.

[195] James, R. B.; Bolton, P. R.; Alvarez, R. A.; Christie, W. H.; Valiga, R. E. *Journal of Applied Physics* **1988**, *64*, 3243–3253.

[196] Zohm, H.; Kasper, E.; Mehringer, P.; Müller, G. A. *Microelectronic Engineering* **2000**, *54*, 247–253.

[197] RESEARCH, M. I. O. T. C. L. F. I. *Tables of Dielectric Materials. Volume IV*; PN, 1953.

[198] Shin, D. O.; Mun, J. H.; Hwang, G.-T.; Yoon, J. M.; Kim, J. Y.; Yun, J. M.; Yang, Y.-B.; Oh, Y.; Lee, J. Y.; Shin, J.; Lee, K. J.; Park, S.; Kim, J. U.; Kim, S. O. *ACS Nano* **2013**, *7*, 8899–8907.

[199] *International Technology Roadmap for Semiconductors*, 2013th ed.; Semiconductor Industry Association: San Jose CA, 2013; 00032.

[200] Stoykovich, M. P.; Nealey, P. F. *Materials Today* **2006**, *9*, 20–29.

[201] Jeong, J. W.; Park, W. I.; Kim, M.-J.; Ross, C. A.; Jung, Y. S. *Nano Letters* **2011**, *11*, 4095–4101.

[202] Paik, M. Y.; Bosworth, J. K.; Smilges, D.-M.; Schwartz, E. L.; Andre, X.; Ober, C. K. *Macromolecules* **2010**, *43*, 4253–4260.

[203] Chavis, M. A.; Smilgies, D.-M.; Wiesner, U. B.; Ober, C. K. *Advanced Functional*

Materials **2015**, *25*, 3057–3065.

[204] Cavicchi, K. A.; Russell, T. P. *Macromolecules* **2007**, *40*, 1181–1186.

[205] Park, S.; Kim, B.; Xu, J.; Hofmann, T.; Ocko, B. M.; Russell, T. P. *Macromolecules* **2009**, *42*, 1278–1284, 00107.

[206] Albert, J. N. L.; Young, W.-S.; Lewis, R. L.; Bogart, T. D.; Smith, J. R.; Epps, T. H. *ACS Nano* **2012**, *6*, 459–466.

[207] Baruth, A.; Seo, M.; Lin, C. H.; Walster, K.; Shankar, A.; Hillmyer, M. A.; Leighton, C. *ACS Applied Materials & Interfaces* **2014**, *6*, 13770–13781.

[208] Zhang, J.; Posselt, D.; Sepe, A.; Shen, X.; Perlich, J.; Smilgies, D.-M.; Papadakis, C. M. *Macromolecular Rapid Communications* **2013**, *34*, 1289–1295.

[209] Zhang, J.; Posselt, D.; Smilgies, D.-M.; Perlich, J.; Kyriakos, K.; Jaksch, S.; Papadakis, C. M. *Macromolecules* **2014**, *47*, 5711–5718, 00012.

[210] Gu, X.; Gunkel, I.; Hexemer, A.; Gu, W.; Russell, T. P. *Advanced Materials* **2014**, *26*, 273–281.

[211] Gunkel, I.; Gu, X.; Sun, Z.; Schaible, E.; Hexemer, A.; Russell, T. P. *Journal of Polymer Science Part B: Polymer Physics* **2016**, *54*, 331–338.

[212] Bai, W.; Yager, K. G.; Ross, C. A. *Macromolecules* **2015**, *48*, 8574–8584.

[213] Murphy, J. N.; Harris, K. D.; Buriak, J. M. *PLOS ONE* **2015**, *10*, e0133088.

[214] Byrnes, S. J. *arXiv:1603.02720* **2016**,

[215] Williamson, L. D.; Seidel, R. N.; Chen, X.; Suh, H. S.; Rincon Delgadillo, P.; Gronheid, R.; Nealey, P. F. *ACS Applied Materials & Interfaces* **2016**, *8*, 2704–2712.

[216] Paradiso, S. P.; Delaney, K. T.; García-Cervera, C. J.; Ceniceros, H. D.; Fredrickson, G. H. *Macromolecules* **2016**, *49*, 1743–1751.

[217] Cabrini, S.; Kawata, S. *Nanofabrication Handbook*; CRC Press, 2012.

[218] Park, S.; Lee, D. H.; Xu, J.; Kim, B.; Hong, S. W.; Jeong, U.; Xu, T.; Russell, T. P. *Science* **2009**, *323*, 1030–1033.

[219] Kennemur, J. G.; Yao, L.; Bates, F. S.; Hillmyer, M. A. *Macromolecules* **2014**, *47*, 1411–1418.

[220] Maher, M. J.; Rettner, C. T.; Bates, C. M.; Blachut, G.; Carlson, M. C.; Durand, W. J.; Ellison, C. J.; Sanders, D. P.; Cheng, J. Y.; Willson, C. G. *ACS Applied Materials & Interfaces* **2015**, *7*, 3323–3328.

[221] Polleux, J.; Rasp, M.; Louban, I.; Plath, N.; Feldhoff, A.; Spatz, J. P. *ACS Nano* **2011**, *5*, 6355–6364.

[222] Patel, K. C.; Ruiz, R.; Lille, J.; Wan, L.; Dobiz, E.; Gao, H.; Robertson, N.; Albrecht, T. R. Line-Frequency Doubling of Directed Self-Assembly Patterns for Single-Digit Bit Pattern Media Lithography. Alternative Lithographic Technologies IV. San Jose, California, 2012; p 83230U.

[223] Něcas, D.; Klapetek, P. *Central European Journal of Physics* **2012**, *10*, 181–188.

[224] Kelchner, C. L.; Plimpton, S. J.; Hamilton, J. C. *Physical Review B* **1998**, *58*, 11085–11088.

[225] Falk, M. L.; Langer, J. S. *Physical Review E* **1998**, *57*, 7192–7205.

[226] Lubliner, J. *Plasticity Theory*; Dover Publications: Mineola, N.Y, 2008.

[227] Park, S.; Kim, B.; Wang, J.-Y.; Russell, P., T. *Advanced Materials* **2008**, *20*, 681–685.

[228] Hashimoto, T.; Tanaka, H.; Hasegawa, H. *Macromolecules* **1990**, *23*, 4378–4386.

[229] Takahashi, H.; Laachi, N.; Delaney, K. T.; Hur, S.-M.; Weinheimer, C. J.; Shykind, D.; Fredrickson, G. H. *Macromolecules* **2012**, *45*, 6253–6265.

[230] Dieter, G. *Mechanical Metallurgy*, 3rd ed.; McGraw-Hill Education: New York, 1986.

[231] Richter, H. J.; Dobin, A. Y.; Lynch, R. T.; Weller, D.; Brockie, R. M.; Heinonen, O.;

Gao, K. Z.; Xue, J.; v. d. Veerdonk, R. J. M.; Asselin, P.; Erden, M. F. *Applied Physics Letters* **2006**, *88*, 222512.

[232] Hur, S.-M.; Khaira, G. S.; Ramírez-Hernández, A.; Müller, M.; Nealey, P. F.; de Pablo, J. J. *ACS Macro Letters* **2015**, *4*, 11–15.

[233] Tsui, O. K. C.; Russell, T. P. *Polymer Thin Films*; World Scientific Publishing: Singapore ; Hackensack, NJ, 2008.

[234] Matyjaszewski, K. *Progress in Polymer Science* **2005**, *30*, 858–875.

[235] Liu, S.; Zhang, X.; Lai, H. *Applied Optics* **1995**, *34*, 4700.

[236] Amidror, I.; Chosson, S.; Hersch, R. D. *Journal of Physics: Conference Series* **2007**, *77*, 012001.

[237] Theocaris, P. S. *Moiré Fringes in Strain Analysis*; Elsevier, 2016.

[238] Collier, R. J.; Doherty, E. T.; Pennington, K. S. *Applied Physics Letters* **1965**, *7*, 223–225.

[239] Kishimoto, S.; Huimin, X.; Shinya, N. *Optics and Lasers in Engineering* **2000**, *34*, 1–14.

[240] Lichte, H.; Geiger, D.; Linck, M. *Phil. Trans. R. Soc. A* **2009**, *367*, 3773–3793.

[241] Kobayashi, K. *Physical Review B* **1996**, *53*, 11091–11099.

[242] Trambly de Laissardière, G.; Mayou, D.; Magaud, L. *Nano Letters* **2010**, *10*, 804–808.

[243] Semaltianos, N. G.; Scott, K.; Wilson, E. G. *Microelectronic Engineering* **2001**, *56*, 233–239.

[244] Choi, J.; Wehrspohn, R.; Gösele, U. *Advanced Materials* **2003**, *15*, 1531–1534.

[245] Chen, K.; Rajeeva, B. B.; Wu, Z.; Rukavina, M.; Dao, T. D.; Ishii, S.; Aono, M.; Nagao, T.; Zheng, Y. *ACS Nano* **2015**, *9*, 6031–6040.

[246] Chen, B.; Lu, K. *Langmuir* **2011**, *27*, 4117–4125.

[247] Lubin, S. M.; Zhou, W.; Hryn, A. J.; Huntington, M. D.; Odom, T. W. *Nano Letters* **2012**, *12*, 4948–4952.

[248] Lubin, S. M.; Hryn, A. J.; Huntington, M. D.; Engel, C. J.; Odom, T. W. *ACS Nano* **2013**, *7*, 11035–11042.

[249] Hexemer, A.; Stein, G. E.; Kramer, E. J.; Magonov, S. *Macromolecules* **2005**, *38*, 7083–7089.

[250] Angelescu, D. E.; Harrison, C. K.; Trawick, M. L.; Chaikin, P. M.; Register, R. A.; Adamson, D. H. *Applied Physics A* **2003**, *78*, 387–392.

[251] Luchnikov, V.; Kondyurin, A.; Formanek, P.; Lichte, H.; Stamm, M. *Nano Letters* **2007**, *7*, 3628–3632.

[252] Segalman, R. A. *Materials Science and Engineering: R: Reports* **2005**, *48*, 191–226.

[253] Cheng, J. Y.; Ross, C. A.; Smith, H. I.; Thomas, E. L. *Advanced Materials* **2006**, *18*, 2505–2521.

[254] Black, C. T. *Nature Nanotechnology* **2007**, *2*, 464–465.

[255] Kim, H.-C.; Park, S.-M.; Hinsberg, W. D. *Chemical Reviews* **2010**, *110*, 146–177.

[256] Hardy, C. G.; Tang, C. *Journal of Polymer Science Part B: Polymer Physics* **2013**, *51*, 2–15.

[257] Nunns, A.; Ross, C. A.; Manners, I. *Macromolecules* **2013**, *46*, 2628–2635.

[258] Ross, C. A.; Berggren, K. K.; Cheng, J. Y.; Jung, Y. S.; Chang, J.-B. *Advanced Materials* **2014**, *26*, 4386–4396.

[259] Deng, H.; Xie, N.; Li, W.; Qiu, F.; Shi, A.-C. *Macromolecules* **2015**, *48*, 4174–4182.

[260] Kim, J. Y.; Kim, H.; Kim, B. H.; Chang, T.; Lim, J.; Jin, H. M.; Mun, J. H.; Choi, Y. J.; Chung, K.; Shin, J.; Fan, S.; Kim, S. O. *Nature Communications* **2016**, *7*, 12911.

References

[261] Nicaise, S. M.; Amir Tavakkoli, K. G.; Berggren, K. K. In *Directed Self-Assembly of Block Co-Polymers for Nano-Manufacturing*; Nealey, P., Ed.; Woodhead Publishing Series in Electronic and Optical Materials; Woodhead Publishing, 2015; pp 199–232.

[262] Nagpal, U.; Kang, H.; Craig, G. S. W.; Nealey, P. F.; de Pablo, J. J. *ACS Nano* **2011**, *5*, 5673–5682.

[263] Xiao, S.; Yang, X.; Lee, K. Y.; Hwu, J. J.; Wago, K.; Kuo, D. *Journal of Micro/Nanolithography, MEMS, and MOEMS* **2013**, *12*, 031110–031110.

[264] Cheng, J. Y.; Mayes, A. M.; Ross, C. A. *Nature Materials* **2004**, *3*, 823–828.

[265] Salaun, M.; Zelsmann, M.; Archambault, S.; Borah, D.; Kehagias, N.; Simao, C.; Lorret, O.; Shaw, M. T.; Torres, C. M. S.; Morris, M. A. **2013**, *1*, 3544–3550.

[266] Jung, Y. S.; Chang, J. B.; Verploegen, E.; Berggren, K. K.; Ross, C. A. *Nano Letters* **2010**, *10*, 1000–1005.

[267] Rahman, A.; Majewski, P. W.; Doerk, G.; Black, C. T.; Yager, K. G. *Nature Communications* **2016**, *7*, 13988.

[268] Scott, D. W. *Multivariate Density Estimation: Theory, Practice, and Visualization*, 1st ed.; Wiley: New York, 1992.

[269] Chang, J.-B.; Son, J. G.; Hannon, A. F.; Alexander-Katz, A.; Ross, C. A.; Berggren, K. K. *ACS Nano* **2012**, *6*, 2071–2077.